Determining Charged Particle Residence Times: An SDE-based Modelling Approach

Dissertation
zur Erlangung des Doktorgrades
der Mathematisch-Naturwissenschaftlichen Fakultät
der Christian-Albrechts-Universität zu Kiel

vorgelegt von Adrian Vogt

Kiel, 2021

Erstgutachter:	**Prof. Dr. B. Heber**
Zweitgutachter:	**PD Dr. H. Fichtner**
Tag der mündlichen Prüfung:	**10. 8. 2021**

So lange die Alchimisten den Stein der Weisen suchten, die Kunst des Goldmachens anstrebten, waren alle ihre Versuche vergebens; erst die Beschränkung auf scheinbar wertlose Fragen schuf die Chemie.

As long as the Alchimists searched for the Philosopher's Stone, aimed for the art of making gold, all their trials were in vain; only the constraint to seemingly useless questions created the science of chemistry.

Ludwig Boltzmann

Contents

Reader's Guide

Since this thesis contributes to several aspects of charged particle propagation in the inner Heliosphere, it turns out to be necessary to present its results within the context of the field. Due to the extent of the text, this reader's guide aims to sort the content based on possible interests. Thereby this thesis can be roughly divided into two distinguishable parts: The first part introduced by Chapter 2 focuses on data analysis concerning the Jovian source spectrum and its physical properties as presented in Chapter 3. The second part introduced by Chapter 4 presents the results achieved by applying a stochastic differential equation (SDE) based simulation setup. The physical implications of these results are presented in Chapters 6 and 7. Generally speaking the Thesis therefore can be divided into an experimental part and a computational part in which also theoretical aspects are discussed.

List of Abbreviations

CIR corotating interaction region

CME coronal mass ejection

CPI Charged Particle Instrument

CPU central processing unit

CUDA Compute Unified Device Architecture

FPE Fokker-Planck equation

GCR Galactic cosmic ray

GPU graphic processing unit

HCS Heliospheric current sheet

HET High Energy Telescope

HMF Heliospheric magnetic field

IPM interplanetary medium

KET Kiel Electron Telescope

LET Low Energy Telescope

LIS local interstellar spectrum

LISM local interstellar medium

MHD magnetohydrodynamics

MSD mean square displacement

PDE probability density equation

PDF probability density function

SDE stochastic differential equation

SEP Solar energetic particle

TPE transport equation

QLT quasi linear theory

QTI quiet-time increases

Abstract

Since their discovery as the dominant population in the low-MeV energy range, Jovian electrons have been utilised as test particles in studies on charged particle transport phenomena in the inner Heliosphere. The decentral position of the Jovian source thereby uniquely allows to distinguish between times in which parallel or perpendicular diffusion dominates the transport to the observer. This thesis undertakes a re-evaluation of several aspects of Jovian electron transport research, which will lead to an improved understanding of diffusion within charged particle transport and as a consequence to the development of a realistic and self consistent estimation of residence times, both numerically and analytically. Therefore the spectral data available for Jovian electron during flybys and at Earth orbit is revisited and the for the first time, a source spectrum will be suggested, which is based entirely on *in situ* data obtained during Jovian flybys. Thus, eliminating the influence of possible transport effects from the estimation of the spectral shape. The second part of the thesis focuses on an SDE-based modelling approach utilising the newly developed Jovian source spectrum. Its influence on the resulting differential intensities as a boundary condition is investigated by analysing the distributions of phase-space trajectories obtained by the simulations with respect to the adiabatic energy changes and comparing these distributions to their actual contribution to the resulting differential intensities. Based on these result this work is able to suggest improved values for the parallel and perpendicular mean free paths and narrow the choices for the extent of the model Heliosphere and the size of the time increment utilised by SDE-based simulations to eliminate the influence of the simulation setup on the results. Further the influence of corotating the Heliospheric magnetic field during the simulation time was proven to be significant. These investigations subsequent motivate the development of a new estimation for charged particle residence times. The physical inconsistencies of the the previous estimations will be shown and new numerical and a new analytical estimation are derived and discussed. Finally a comparison with spacecraft data confirms that the results presented in this thesis are able to reproduce realistically the behaviour of Jovian electrons in the inner Heliosphere, thereby introducing the effects of the corotating Heliospheric magnetic field as a measure for the Jovian residence time.

Zusammenfassung

Seitdem sie als dominante Elektronenpopulation in niedrigen MeV-Bereich entdeckt wurden, sind Jupiterelektronen als Testteilchen in Studien zur Ausbreitung gelandener Teilchen in der inneren Heliosphäre eingesetzt worden. Die dezentrale Position der Jupiterquelle ermöglichte dabei auf einzigartige Weise zwischen Perioden zu unterscheiden, in denen entweder parellele oder senkrechte Diffusion den Transport der Teilchen zwischen Quelle und Beobachter dominiert. Diese Arbeit unternimmt eine Re-Evaluation diverser Aspekte der Forschung zur Ausbreitung von Jupiterelektronen, die zu einem vertieften Verständnis der Diffusion als Teil des Transports von geladenen Teilchen und in Konsequenz zu einer realistischen und selbstkonsistenten Abschätzung der Laufzeiten führen wird, sowohl numerisch, als auch analytisch. Deshalb wurden die Spektraldaten bezüglich der Jupiterelektronen, die während Vorbeiflügen und am Erdorbit aufgenommen wurden, ein weiteres Mal analysiert und so zum ersten Mal ein Quellspektrum vorgeschlagen, das ausschließlich auf Messungen basiert, die während Vorbeiflügen aufgenommen wurden. Auf diese Weise werden mögliche Einflüsse von Transporteffekten von der Ermittlung der spektralen Gestalt eliminiert. Der zweite Teil der Arbeit konzentriert sich auf die Modellierung des Jupiterelektronentransportes mit Hilfe des neu entwickelten Quellspektrums auf Basis Stochastischer Differentialgleichungen. Der Einfluss des Quellspektrums auf die resultierenden differentiellen Intensitäten vermittels der Randbedingungen wird untersucht, indem die Verteilungen der Phasenraumtrajektorien als Ergebnis der Simulationen in Bezug auf die adiabatischen Energieänderungen analysiert und mit ihrem tatsächlichen Einfluss auf die resultierend differentiellen Intensitäten verglichen werden. Aufbauend auf diesen Ergebnissen ist diese Arbeit in der Lage verbesserte Werte für die mittleren freien Weglängen, parallel und senkrecht zum interplanetaren Magnetfeld, vorzuschlagen und die Werte für das radiale Ausmaß der Modellheliosphäre und die Größe des Zeitschrittes einzuschränken, um Einfluss der Simulationsmethode auf die Ergebnisse zu vermeiden. Desweiteren wurde gezeigt, dass der Einfluss der Korotation des Magnetfeldes während des Simulationsprozesses signifikant ist. Diese Untersuchungen motivieren im Folgenden die Entwicklung einer neuen Abschätzung für die Laufzeiten geladener Teilchen. Dazu werden die physikalischen Inkonsistenzen bisheriger Vorschläge gezeigt und neue numerische und analytische Ansätze hergeleitet und diskutiert. Schließlich zeigt ein Vergleich mit Satellitendaten, dass die Ergebnisse dieser Arbeit in der Lage sind, das Verhalten von Jupiterelekronen in der inneren Heliosphäre realistisch wiederzugeben; dazu werden die Effekte der Korotation des heliosphären Magnetfeldes als Maß für die Laufzeiten der Jupiterelektronen eingeführt.

Chapter 1

Introduction

WITHIN the broad field of charged particle transport modelling, theory and observation, the investigation of residence times for a long time has served as a niche among niches. Although addressed as early as by Parker (1965) only a few studies have developed measures to answer the question how long charged particles need to to propagate between two points within the Heliosphere or from the heliopause inward to the Earth orbit. One reason for the absent of research on this topic could be the difficulties to validate the analytical and numerical estimations with observational evidence. Whereas this problem is obvious for Galactic cosmic rays (GCRs) an attempt to compare Jovian electron residence times with an indirect observational measure obtained by Strauss et al. (2013) lead to contradicting results for the transport parameter in order to reproduce realistic values for residence times and differential intensities. Throughout the course of this thesis, it will be shown why this approach lead to such ambiguous results and for the first time a realistic measure for charged particle residence times will be derived, self consistent with the derivation of differential intensities both for numerical and analytical solutions of the transport equation (TPE). Furthermore by investigating the parameter and setup dependences of the modelling approaches used within this thesis, a new method to validate residence times for Jovian electrons by comparison with *in situ* spacecraft data is introduced and shown to support the numerical and analytical estimations developed by this thesis.

First the Jovian electron source spectrum is revisited and improved according to a new analysis of the available flyby spectra. Jupiter is known as the source of the dominant electron population in the low-MeV range in the inner Heliosphere since the early 1970s. The unique qualities of the Jovian source, namely the dominance of the Jovian electron population within its energy range accompanied by the decentral position of the source which was proven to be point-like by Pyle and Simpson (1977) made Jovian electrons to a preferred test particle population for charged particle transport modelling studies. This of course gained interest in reliable estimations of the Jovian source spectrum as a boundary

condition and over the last 40 years several suggestions have been made, mostly based on a combination of selected flyby and Earth orbit data. In contrast this thesis based its estimations exclusively on flyby data thus eliminating possible influences of rigidity dependent transport effects and utilised the Earth orbit data in order to validate the consistency. In order to obtain the new source spectrum as published by Vogt et al. (2018) this thesis undertook a re-evaluation of the flyby spectrum measured by *Pioneer 10* and it could be proven that it shows intensities higher than the background Jovian electron intensities by a factor of ~ 20 due to the occurrence of a so-called Jovian jet, a phenomenon associated with short-term open field line connections to the Jovian magnetosphere. This discovery allowed to bring the fluxes measured by *Pioneer 10* to agreement with corresponding measurements by *Voyager 1* and *Ulysses* and to derive a reliable estimation of the Jovian electron source spectrum which proves to be in agreement with theoretical assumptions on electron acceleration and release within a planetary magnetosphere.

The second part of this thesis introduces the simulation setup which was utilised to perform the parameter studies discussed in the subsequent Sections: A SDE-based simulation code written in Compute Unified Device Architecture (CUDA) in order to perform the numerically calculations on parallelised graphic processing units (GPUs). According to Dunzlaff et al. (2015) this code thereby shows a performance increase up to a factor of ~ 50 compared to corresponding simulation codes operating on central processing units (CPUs). Therefore this work is partly devoted to perform extensive parameter studies in order to investigate the dependences of SDE modelling results on the different transport parameter as well as on the simulation parameter such as the radial extent of the model Heliosphere or the size of the time increment. Thereby this thesis contributes to the effort by e.g. Strauss and Effenberger (2017) to investigate the influence of the simulation setup on the simulation results within SDE approaches. Complementary to this more theory focused analysis, this thesis tests different settings within parameter studies and investigates them regarding a possible asymptotic behaviour in order to find ranges for these more technical parameters which balance the need for accuracy with the need to limit the complexity and temporal requirement of the setup. The major challenge thereby is the fact, that the performance increase due to the usage of GPUs demands a simplification of the transport model to fit the demands of the smaller memory on GPUs. In order to avoid to overstretch the possible limitations of the approach, a focus is set on the boundary conditions to evaluate the influence of the newly developed source spectrum. Therefore the individual phase-space trajectories as the primary results of the SDE-based modelling approach are investigated regarding their physical significance and their contribution to the resulting differential intensities after convolution with the Jovian source spectrum. Thereby this thesis contributes to our understanding concerning the significance of the influence of the boundary conditions. Furthermore this investigation proves that mono-energetic simulation setups such as the one used for this thesis are sufficient to test energy dependent transport parameters such as mean free paths, as it can be shown that only phase-space trajectories corresponding to a very limited range of adiabatic energy changes contribute to the resulting differential intensities. This discovery allows for the simplified and run-time optimised simulation setup used by this thesis to be applied to a parameter study on the parallel and perpendicular mean free paths which will be investigated for the whole energy range of interest for Jovian electron transport simulations. This work therefore derives from the improved Jovian source spectrum improved suggestions for the parallel and perpendicular mean free paths experienced by electrons within the energy range of the Jovian source spectrum and additionally secures the more technical parameters such as the radial extend or the time increment in order to avoid unnecessary systematic in future studies.

Subsequently this thesis presents a new approach to estimate residence times for charged particles propagation within the Heliosphere, which derivation is motivated by the inves-

tigations on the dependences of the Jovian electron differential intensities. Therefore a method will be derived to calculate residence times self consistently with the corresponding differential intensities, in the sense that the individual phase-space trajectories contribute with the same significance to the residence times as to the differential intensities. As a consequence the estimated residence times for Jovian electrons to reach the Earth orbit will decrease by almost two orders of magnitude with respect to previous suggestions applied to the simulation setup. This observations of course demands the discussion whether it is a consequence of the numerical setup to solve the TPE or refers to the way the TPE describes the physical processes within charged particle transport. By analysing the dependences between residence time and adiabatic energy changes it will be shown that the analytical estimates for the residence times tend to agree with the average of the phase-space trajectories durations. It will be discussed how these analytical estimates actually calculate the expectation value for the probability density function mathematically described by the TPE rather than describing the behaviour of the differential intensities derived from it. Therefore this thesis aims to derive a simple correction term which is able to reproduce the newly developed numerical estimate. Despite the unavoidable uncertainties in context with analytical estimates of this kind, it can be shown that the suggestion developed by this thesis is able to reproduce the numerical results. Finally the question whether these estimations can be validated by observational data, is answered by the introduction of a method to apply the effect of the Solar rotation and therefore the corotation of the Heliospheric magnetic field (HMF) to indirectly measure the residence times. Showing the general agreement between the data and the predictions from theory and numerical modelling this thesis therefore provides a new insights to all three aspects of charged particle transport research, observation, simulation and theory.

Chapter 2

The Sun And Inner Heliosphere

An introduction to the main concepts and phenomena of Solar physics and the physics of the inner Heliosphere as far as they are relevant for this thesis. After discussing the Solar cycle and the effects of Solar activity (Section 2.1), a focus is set on the Solar wind (Section 2.2). A brief overview on the structure of the Heliosphere as it is assumed today (Section 2.3) leads over to a detailed theoretical treatment of the Heliospheric magnetic field (HMF) including a sketched derivation from fundamental electrodynamic principles. These basics will be referred to e.g. in Chapter 3 regarding the significant and unique properties of the Jovian source and in Chapter 5 regarding the influence of the HMF on charged particle transport.

The exceptional role of the Sun has always been known to humankind and resulted to the Sun becoming supposedly one of the first deities. Archeological discoveries such as the Nebra Sky Disk as shown in Fig. 2.1 and the Neolithic circular enclosures such as Goseck proved further knowledge of astronomical phenomena often associated with the varying Sun path. The influence of Gods and Goddesses associated to the Sun is illustrated by the fact that the first monotheistic religion, enforced by Pharaoh Akhenaten around 1345 BC, developed from the cult of a local Egyptian Sun God called Aten. Throughout the Antics the Sun kept its divine status within mythology, recognised as the source of light, warmth and energy. This association still is reflected in the way that the absolutist King Louis XIV. of France is referred to as the Sun King. Also outside the western hemisphere, the Sun was associated with the concept of God-like kingship, most prominently the Ruler of the Inca empire referred to themselves as Sons of the Sun. The official title of the ancient Chinese emperors who were called Tianzi, meaning the Son of Heaven, may also reflects this rural traditions of Sun-centered religions.

For Christian theology, the Solar disk was the embodiment of divine perfection, hence the disbelief when Galileo Galilei discovered the first Sun spots in the early 17th century. The rise of science within the European civilisation also is strongly connected to understanding the Sun and its role. The Copernican Revolution not only changed our understanding of the planetary system and recognised that the Sun as the center but triggered through the discovery of Kepler's laws the development of modern theoretical physics. Famously Newton's gravitational force was inspired by the need to explain the ecliptical Kepler orbits. Therefore when we discuss how the Sun dominates its surrounding, we not only stand on the shoulders of giants according to the famous quote by Newton, but engage with mankind's oldest and probably most fascinating topic of thinking, which significantly influenced the transition from mythology over philosophy to quantitative science.

Figure 2.1: *The Nebra Sky Disc*[1]*, found in Sachsen-Anhalt, Germany, is the first known depiction of the night sky. It is believed to be the oldest form of an astrolabium, designed to calculate the main dates in the rural calendar.*

Building on that tradition this Chapter gives an overview on our present day knowledge of the Sun and the the Heliosphere as far as the investigation goals of this thesis are concerned. Valuing the history of scientific research in order to properly understand and estimate present concepts, the exposition occasional will cut back to past developments and portray how the theories discussed within this work were first introduced and why.

2.1 Solar Activity

The beginning of the scientific investigation of the Sun can be (at least in the western hemisphere attributed to the discovery of Sun spots by Thomas Harriot, Johannes Fabricius and Galileo Galilei in early 1611 independent from each other. As claimed by e.g. Xu Zhen-tao (1980) the earliest known record of Sun spot observations may be attributed to the ancient Chinese I Ching. As known by today the phenomenon of regions with reduced temperature in the Sun's photosphere, resulting in a darker appearance, is a consequence of Solar activity within a 11-year cycle. Since the understanding of Solar activity is important in order to estimate how the Sun may influence the propagation conditions for charged particles within the inner Heliosphere, it is necessary to give a short overview on Solar physics.

In astronomy the Sun is classified as a G-type main sequence star (G2V) and consists of approximately $m_{Sun} = 1.9884 \cdot 10^{30}$ kg hydrogen and helium, with $\sim 6 \cdot 10^{11}$ kg of hydrogen being converted into Helium every second by fusion. The nuclear fusion takes place in the core of the Sun, located within $0.2 - 0.25$ Solar radii. The subsequent layer according to the standard Solar model the so-called radiative zone, as the the energy is transferred outward through this layer by means of photonic radiation rather than convection. After

[1]Source: `https://upload.wikimedia.org/wikipedia/commons/7/7b/Nebra_Scheibe.jpg`

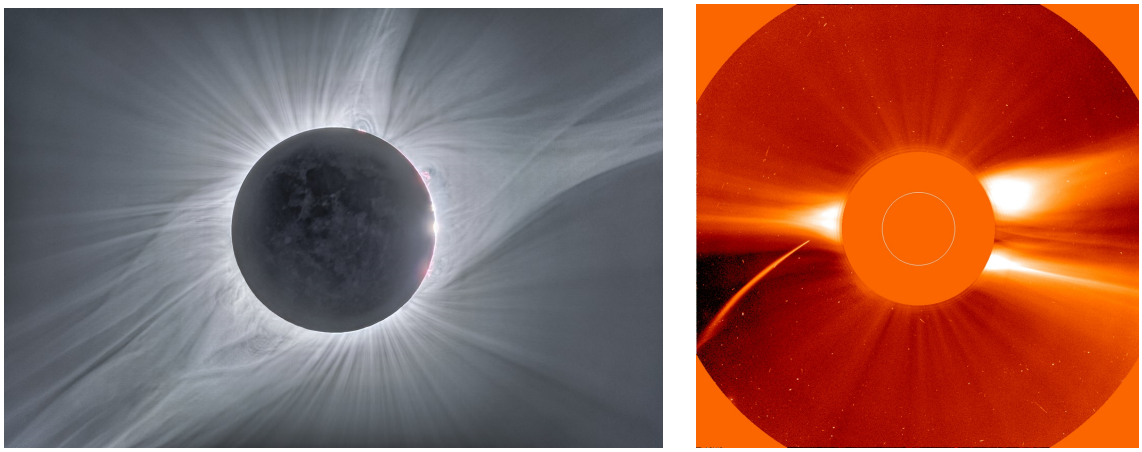

(a) **(b)**

Figure 2.2: *Figure 2.2a shows the structure of the Solar corona as seen during the total Solar eclipse of 21 August 2017, visible in the United States. The figure as published by the European Southern Observatory (see:* `https://www.eso.org/public/images/eso1822i` *) depicts the expanding of the corona resulting in the permanent outflow of Solar wind. A more dynamic situation is shown in Fig. 2.2b. Taken by the LASCO coronograph on board the SOHO spacecraft on 23 December 1996, it depicts a large coronal mass ejection (CME) on the right side of the Sun. For fürther information see e.g. the source of the figure at* `http://www.leibniz-kis.de/en/research/the-Sun/corona-and-Solar-wind`

the tachocline as the boundary between the radiative and the convective zone is called, the density of the Sun is low enough to enable the creation of convective current in the plasma, similar to weather cells in the Earths atmosphere. Outside of this region the photosphere is located, followed by the Solar corona as shown in Fig. 2.2a. The atmosphere of the Sun becomes visible e.g. during a Solar eclipse as shown in Fig. 2.2a. It consists of the chromosphere, the Solar transition region and the corona which expands into the Heliosphere as discussed in more detail in Section 2.3 and 2.4 with respect to the concept of the Solar wind as the radially expanding corona according to Parker (1958).

2.1.1 The Solar Cycle

As first suggested by Babcock (1961) the plasma convection within the convective zone builds up an magnetohydrodynamics (MHD) dynamo and therefore causes the Solar magnetic field. During Solar minimum condition this magnetic field is almost poloidal. Due to the Sun's differential rotation the structure of the field is twisted over time and becomes almost toroidal. As discussed by e.g. Kallenrode (2004) this results in the development of flux tubes, which are driven up into the photosphere and beyond due to the magnetic buoyancies. The intersections are visible as a pair of Sun spots with opposite magnetic polarities. The increasing distortion of the Sun's magnetic field subsequently increases the appearance of Sun spots closer to the Heliomagnetic equator as well as the wandering of Sun spots towards it. This phenomenon is commonly referred to as Spörer's law and illustrated by Fig. 2.3. The distortion of the magnetic field eventually changes the polarity of the Sun. After an 11 year period, the poloidal Solar minimum structure of the Solar magnetic field has reemerged but with a reversed polarity. A full Solar cycle in terms of

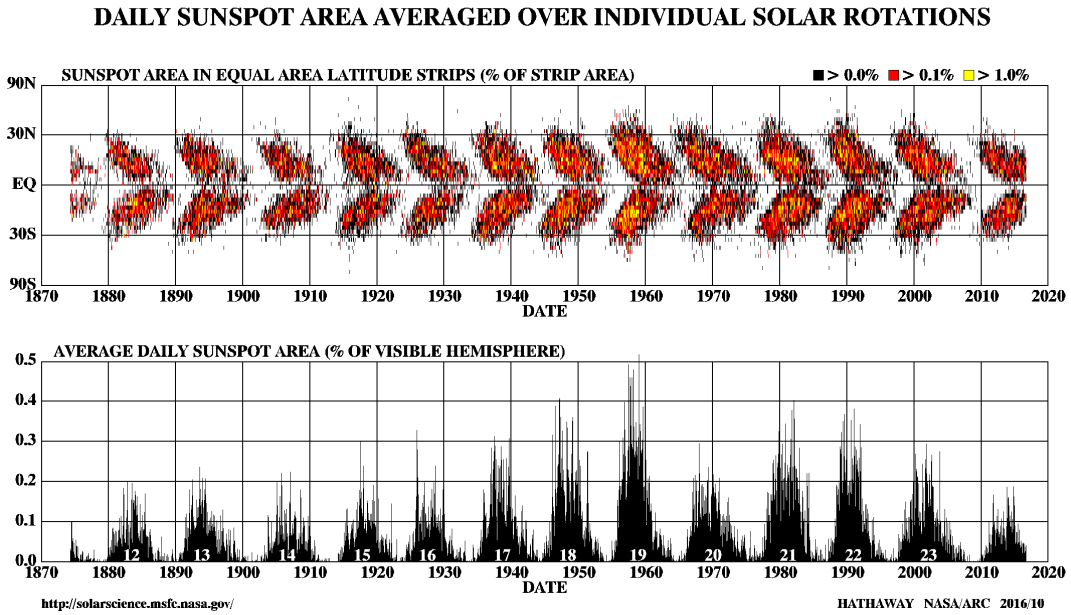

Figure 2.3: *The number of Sunspots and their corresponding latitudes (upper panel) for the Solar cycles since the 1870s. Due to the characteristic of the Sunspots' latitudes of the time within the Solar cycles the upper panel is usually referred to as a butterfly diagram. (Source:* `https://Solarscience.msfc.nasa.gov/images/bfly.gif` *)*

field polarity therefore takes two 11 year cycles. Thus Solar cycles are referred to as + and −, depending on whether the magnetic north pole is in alignment with the Heliographic one, with one A^+ and one A^- cycle forming a full 22 year cycle after with the original polarity is restored again. The polarity of the Solar magnetic field influences how charged particles experience drift effects in the Heliosphere. This will be discussed in following in Section 5.3 alongside the so-called Heliospheric current sheet (HCS).

During times of maximum Solar activity magnetic the probability of Solar energetic particle (SEP) events, such as coronal mass ejections (CMEs) and Solar flares increases. Fig. 2.2b illustrates this by showing a CME as detected by SOHO on December 23 1996. Solar flares thereby are most likely caused by magnetic reconnection of flux tubes and therefore locally associated with Sun spot pairs according to e.g. Kallenrode (2004) and reference therein. They often consist of multiple phenomena such as radio burst accompagning the release of Solar particles. Whether the often observed common appearance of Solar flares and CMEs is physically connected is still under debate. In contrast to Solar flares CMEs are caused by large scale magnetic clouds and release much higher amounts of Solar plasma into the Solar wind.

Since this thesis is limited to idealised (undisturbed) Solar minimum condition, a detailed discussion of both the Solar cycle as well as SEPs events is beyond the scope of this work. But as they appear - although not as regular as during Solar maxima - during Solar mininum conditions, they have to be addressed in order to be able to identify them as disturbances and exclude them from data accordingly. This is applied e.g. in Section 3.4.2 and Section 7.4 to data obtained by *Pioneer 10* as well as *SOHO*, and implicitly in the spectral data published by several groups as listed in Tab. 3.1.

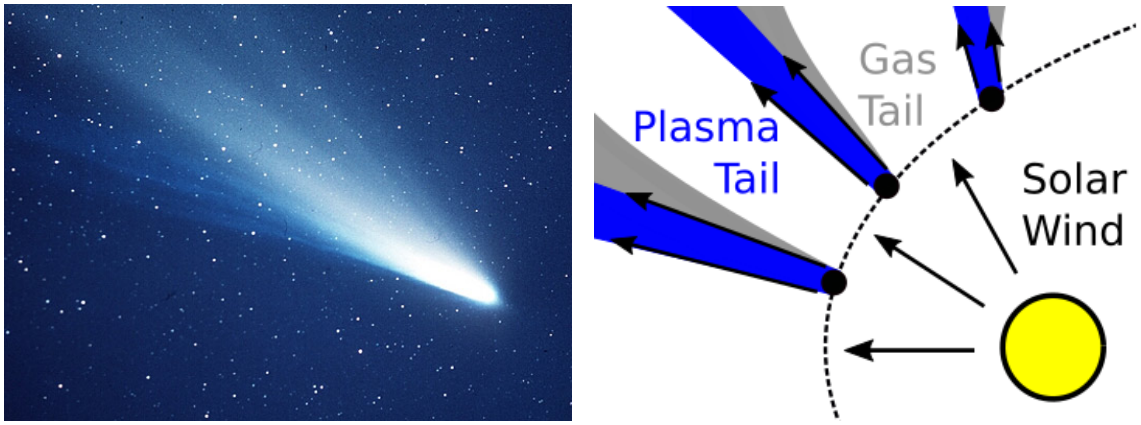

(a) [2] **(b)**

Figure 2.4: *Photograph and sketch of a comets two tails in the inner Heliosphere. As described by Biermann (1951) the radiation pressure is on capable to bend the gas tail (grey) away from the Sun whereas the radially outward direction of the plasma tail (blue) is caused by the interaction with the radially outward outflow of the Solar wind.*

2.2 The Solar Wind

The first prediction of the Solar wind by Biermann (1951) was a byproduct of investigating comet tails. As shown in Fig. 2.4a by the example of the famous Halley comet, there are two kinds of tails associated with a comet: a diffuse dust tail and a very pronounced plasma tail which points radially outward from the Sun at all times. The radiation pressure of the Sun's light is able to explain the behaviour of the dust tail, but not the behaviour of the ions within the plasma tail. As a consequence Biermann (1951) predicted the existence of what later became known as the Solar wind, a particle radiation originating in the Solar corona and moving radially outward. Figure 2.4b shows the qualitative idea. By calculating the momentum transfer it could be shown that the measured particle density at Earth is able to force the plasma tail to follow its direction.

The term Solar wind was coined subsequent to the work of Parker (1958) who together with Alfvén (1957) derived a theoretical model of the Heliospheric magnetic field (HMF). Under the assumption that the corona expanses radially outward into the interplanetary space Parker (1958) treated the Solar wind as fully ionised (as proven nowadays by *in situ* observations) and behaving like an ideal gas. Taking a constant outflow as given, it is possible to investigate the conditions to reach a static equilibrium. In order to do that, the barometric formula is applied to the Solar wind and via the radial dependence of the temperature, the pressure is calculated for $r \to \infty$. As the result, Parker (1958) could demonstrate that the pressure never vanishes and surpasses the pressure which is assumed for the local interstellar medium (LISM) today. As a consequence the concept of the steadily expanding corona was developed, defining the Heliosphere as the space being influenced by the Solar wind frozen into the HMF as discussed in detail in Section 2.4.

[2] Source: `https://www.jpl.nasa.gov/images/comet/halley-544-399.jpg`

2.2.1 Origin and Qualities

Shortly after the prediction of the Solar wind, Gringauz et al. (1960) as well as the *Mariner II* spacecraft were able to confirm the basic assumptions (see e.g. Neugebauer and Snyder, 1962) and measured radial velocities of about $400-700$ km/s corresponding to the outflow of plasma from the Sun. The Solar wind mainly consists of protons and electrons, with a notable population of helium isotopes. Its proton density is $n_P \approx 6$ cm^{-3} at Earth orbit (see e.g. Smith et al., 2001; Wang et al., 2007) with a temperature of $T_K \approx 10^5$ K. Subsequently the radial velocity of the Solar wind at Earth orbit makes it supersonic ($c_{SW} = \sqrt{2k_b T_{SW}/m_p} \approx 40$ km/s) and superalfvénic ($v_A = \sqrt{B^2/(\mu_B m_p n_p)} \approx 45$ km/s), which means that it is both faster than sound and plasma waves in the interplanetary medium (IPM). Even further the Solar wind speed at Earth is also supermagnetosonic ($v_{MS} = \sqrt{c_{SW}^2 + v_A^2} \approx 60$km/s).

The Solar wind originates from the Solar corona, the uppermost layer of the Solar atmosphere. Its composition consists mainly of hydrogen and helium ions with a density much lower than the underlying photosphere. However, the corona happens to be much hotter by more than two orders of magnitude. On this phenomenon referred to as coronal heating several theories exist, including magnetic reconnection or waves as the energy source, but it still happens to be a topic of research. An overview on both the acceleration theories as well as on the qualities of the Solar wind is given by e.g. Aschwanden (2004) and Meyer-Vernet (2007), amongst others.

As a theoretical concept, the so-called source surface was defined by Parker (1958) as the distance at which there are no further sources of coronal heat, it will be indicated in the following by its radial distance R_S. Although this definitions serves it's purpose for the means of deriving the HMF as discussed in Section 2.4.1, subsequent literature (see e.g. Schatten et al., 1969; Hoeksema and Scherrer, 1986; Wiengarten et al., 2013, amongst others) specified the source surface as the boundary inside which the magnetic field structure is dominated by the dynamics of the Solar corona whereas outside the source surface the magnetic field can be approximated by the idealised structure derived by Parker (1958).

As a consequence of the theory of the HMF by Parker (1958), the source surface is often also attributed as the origin of the Solar wind in theoretical approaches. Most generally the source surface serves as a proposed outer boundary of the Sun, since physically the Sun has no outer boundary as its atmosphere expands with the Solar wind and fills the Heliosphere as a whole. The corresponding theory of the Solar wind as well as the large scale structure of the Heliosphere as we know of it today, is discussed in the following.

2.2.2 Slow and Fast Solar Wind

The Solar wind is divided into two major populations, mainly categorisable by their velocity as slow and fast Solar wind as e.g. detailed in the overview by Schwenn (1990) or von Steiger et al. (1997). Fast and slow Solar wind are distinct in several ways, most prominent their source regions. Whereas the fast Solar wind originates from coronal holes around the Solar magnetic poles as discovered by Krieger et al. (1973), the slow Solar wind is assumed to

mostly originate from coronal regions close to the Heliomagnetic equator. Recent studies modelling the Sun magnetosphere however suggest a possibly more complex situation and raise the possibility that the slow Solar wind originates from the borders of the coronal holes, see e.g. Peleikis et al. (2017)and Kruse et al. (2020). As illustrated by *Ulysses* measurements in Fig 2.5 the picture becomes more complicated during times of high Solar activity as then coronal holes tend to expand way down into the ecliptic plane.

The slow Solar wind is named due to its slower radial speed ($200-400$ km/s in contrast to $400-800$ km/s) and has a density of ~ 8 cm^{-3}, roughly twice the density of the fast Solar wind. Especially during Solar minimum condition the slow Solar wind contains a significantly lower amount of helium ions (~ 2 %) than the fast Solar wind, which contains about 4 % helium ions. During times of high Solar activity the helium concentration of the slow and fast Solar wind appear to be the same on average.

Another important distinction is the fact that the slow Solar wind is highly turbulent variable and often contains structures of larger scale. Prominently to mention thereby are shocks and magnetic clouds. Fast Solar winds streams are often stable over several Solar rotations, a quality which consequences will be discussed in more detail in the following concerning so-called corotating interaction regions (CIRs) in Section 2.4.4. However, also the proton and electron temperature ($2 \cdot 10^5$ K and $1 \cdot 10^5$ K respectively) is higher than the proton temperature in the slow Solar wind of about $\sim 3 \cdot 10^4$ K.

2.2.3 The Third Dimension

The results of the *Ulysses* mission (see more details in Section 3.3) offered for the first time an *in situ* perspective on the source surface of the Sun and the Solar wind outside of the ecliptic. The data on the Solar magnetic field's radial component most notably failed to show any latitudinal gradient (see Balogh et al., 1995) and furthermore exposed differing magnetic fluxes on the northern and southern hemisphere. As discussed by e.g. Kallenrode (2004) this hints to the (empirical) concept of over-expansion and stress within the magnetic field, which can serve as a source of acceleration of the Solar wind.

The composition of the Solar wind likewise offered unexpected insights as it appeared to be more representative of the chromosphere than of the hotter corona as found by Geiss et al. (1995). Furthermore large-scale amplitude Alfvén waves were found to originate from acceleration region of the Solar wind. Due to the stable conditions outside the ecliptic they are less likely to decay than in the more turbulent regions around the heliomagnetic equator. Thus giving an explanation for the higher Solar wind speed around the Solar pole regions, according to Balogh et al. (1995) and the discussion by Kallenrode (2004).

The latitudinal dependence of the Solar wind speed as well as of the orientation of the HMF is shown in the two upper panels of Fig. 2.5. The left panel shows the results of the first latitude scan of *Ulysses* during Solar minimum conditions as indicated by the low Sun spot numbers given in the lower panel. Clearly visible are the latitude dependence of the Solar wind speed, with an abrupt change of the outflowing speed at $\sim \pm 40\,^\circ$. Furthermore the colour-coding reveals that the orientation of the HMF in the northern hemisphere is outward (red) whereas the HMF is oriented inward on the southern hemisphere.

As displayed in the upper right panel of Fig. 2.5, the two Solar wind populations and the inward and outward oriented magnetic field lines of the HMF are not likewise separated by latitude under Solar maximum conditions. This makes it particularly difficult for Solar maximum conditions to be expressed by analytical models. Therefore studies

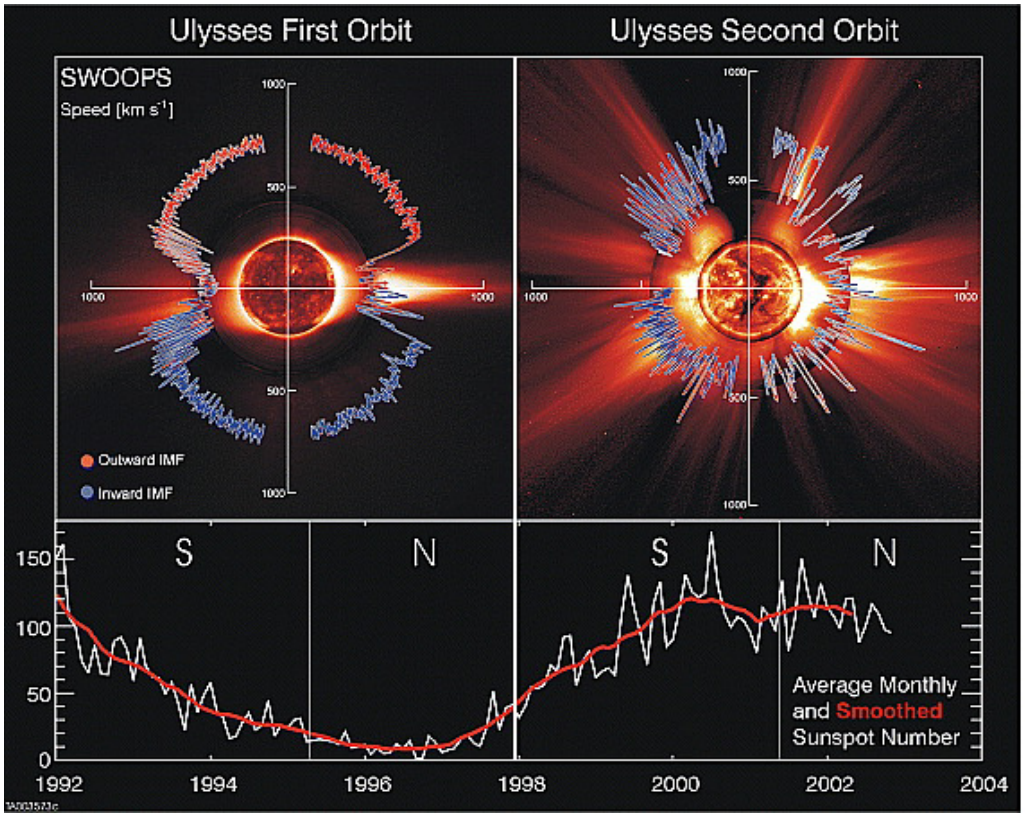

Figure 2.5: *The results of the first and second fast latitude scans according to McComas et al. (2003). The two upper panels show the latitudinal dependence of the Solar wind speed during Solar mininum (left) and Solar maximum (right) conditions. The inward and outward directions of the Solar magnetic field are colour coded in red (outward) and blue (inward). The two lower panels show the temporal evolution of the number of Sunspots, again split into one panel for the minimum and maximum.*

which attempt to simulate charged particle propagation as the present one, limit themselves to Solar minimum conditions. A notable exception being MHD based studies which incorporate Solar events or CIRs such as e.g. Wiengarten et al. (2014) and Kopp et al. (2017).

The different polarities of the HMF in the northern and southern hemispheres during Solar minimum conditions as displayed in the left upper panel of Fig. 2.5 and discussed in Section 2.1.1 causes the formation of the HCS which separates the Solar hemispheres due to their opposite magnetic polarities. Therefore at the source surface of the Solar corona, the HCS indicates the Solar magnetic equator, which is expanded into the IPM. Within the HMF the HCS forms a neutral layer which is often described by the metaphor of a waving skirt of a Ballerina (see e.g. Alfvén, 1977; Smith et al., 1978) due to the fact that the rotational and the magnetic axis of Sun are inclined.

For the propagation of charged particles the HCS is important as it causes a drift corresponding to the polarity of he HMF. Thus, the time profiles of charged particle counting rates appear to be different during positive and negative Solar cycles. Drifts will be discussed alongside the other physical processes determining charged particle transport in the Heliosphere in Chapter 5, particularly in Section 5.2.

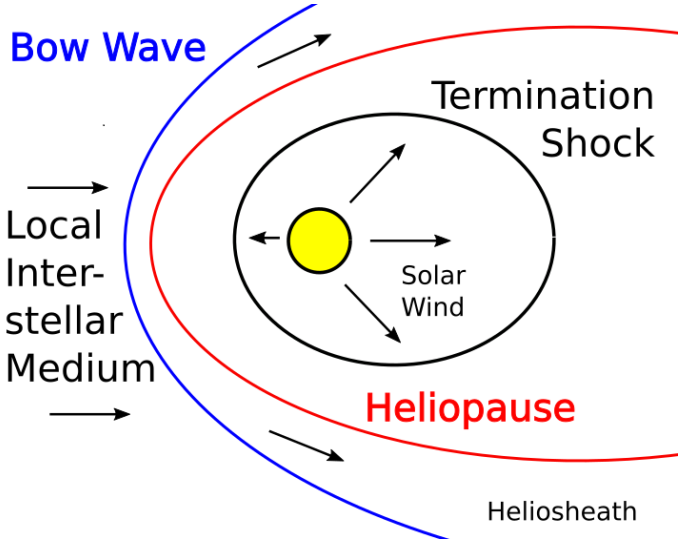

Figure 2.6: *Schmematic sketch of the main structural elements of the Heliosphere. Note that the geometry is both simplified as well as still under discussion as well as the inflow direction of the LISM*[3].

2.3 The Heliosphere

Most simply put, the Heliosphere can be defined as the spatial extent of the Sun's magnetic influence. Thereby its borders as sketched in Fig. 2.6 are determined by the interaction of the Solar wind expanding radially outward from the Sun and the counter pressure of the LISM. But not only is our understanding of the Heliosphere tied to the Solar wind, the fundamental concepts were derived in close dependence of each other. As discussed beforehand, the notion of Biermann (1951) that the (photonic) radiation pressure of the Sun can not explain the behaviour of th ionic tail, led Parker (1958) to the assumption that the Solar corona expanses radially into the interplanetary space. Thereby the Heliosphere can also be defined as the outer most layer of the Solar atmosphere. Taking a constant particle outflow as given Parker (1958) investigates the conditions to reach static equilibrium. As nowadays proven by *in-situ* observations the Solar wind is assumed to be fully ionised and treated as an ideal gas. Thus for the case of static equilibrium, it is possible to prove that the barometric equation leads to a non-vanishing finite pressure at the radial distance $R \to \infty$.

The radial distance at which the pressure of the Solar wind is in equilibrium with the in-flowing local interstellar medium (LISM) defines the outer border of the Heliosphere and is marked as the Heliopause in red in Fig. 2.6. As the plasma streams of the LISM and HMF can neither cross nor merge due to their frozen-in magnetic field, the LISM is therefore decelerated. Given a supersonic relative speed which is decelerated to subsonic, this would cause the formation of a bow shock, as indicated in blue. The labelling as more of a bow wave than a bow shock refers to McComas et al. (2012) and their interpretation of the observations of the Interstellar Boundary Explorer (IBEX). Assuming a more or less constant inflow direction of the LISM this region along with the Heliopause is believed to

[3]For more information how to indirectly estimate the inflow direction of the LISM via so-called pick-up ions see e.g. Drews et al. (2012)

be significantly stretched forming the so-called Heliotail, which is assumed to be of several hundreds of AU in length.

The inner counterpart to the bow wave is termination shock, at which the supersonic Solar wind is decelerated to a subsonic speed. It has been detected at $\sim$ 94 AU by (*Voyager 1*, see e.g. Stone et al., 2005) and at $\sim$ 84 by (*Voyager 2*, see e.g. Stone et al., 2008). After that both spacecraft stayed within the Heliosheath until they reached the Heliopause. Thereby the Heliosheath can be separated into an inner Heliosheath where the Solar wind and pick up ions are slowed down and heated (McComas et al., 2009) and an outer Heliosheath in which the LISM dominates but is disturbed by the influence of the Heliosphere - regardless if the bow shock exist as pointed out by e.g. Scherer et al. (2011). *Voyager 1* reached the LISM at 121.7 AU on August 25, 2012 (see e.g. Gurnett et al., 2013; Krimigis et al., 2013) and on November 5, 2018 at a radial distance of 119.0 AU (*Voyager 2*, see e.g. Stone et al., 2019). Thus making the two twin spacecraft the only man-made objects which are confirmed to have left the Heliosphere[4].

Within this thesis the Heliosphere will be modelled as a sphere with a radius of $R =$ 120 AU, based on the results on the two *Voyager* missions. Although a simplification this approach meets the requirements for modelling charged particle transport in the very inner Heliosphere (i.e. Earth and Jupiter are only at distances of 1 AU and 5.2 AU away from the Sun, respectively). A more detailed discussion will be given in Section 6.1 and 6.4.4.

2.4 The Heliospheric Magnetic Field

The HMF which fills the complete Heliosphere and thereby marks its borders, is formed by the constant outflow of the Solar wind. Despite it has be been shown to be strongly variable, the following Section will focus on the idealistic approach by Parker (1958) which assumes a constant Solar wind outflow both in speed and density and provides a model of an averaged HMF. The limitations of this approach will be discussed in Section 2.4.5 alongside the most prominent suggestions to expand this so-called Parker field accordingly. As the main advantage of the Parker field is the fact that it is easily applicable within modelling approaches such as the one presented by this thesis, the implications of both the HMF model by Parker (1958) as well as its limitations on transport theory will be addressed in Section 5.3.

2.4.1 The Parker Model

The most common model to estimate the HMF was derived by Parker (1958) based on the concept of the expanding corona within the same publication. A similar estimation directly based on the results of Biermann (1951) and his suggestion of a Solar Wind has been given by Alfvén (1957). As this so-called Parker field or Parker model is the estimation of the HMF utilised by this work (see the corresponding studies by Vogt et al., 2015, 2020, as well as Section 6.1 for the implementation) it will be discussed more carefully and detailed in the following.

[4] *Pioneer 10*, although on a similar trajectory, had to be abandoned in January 2003.

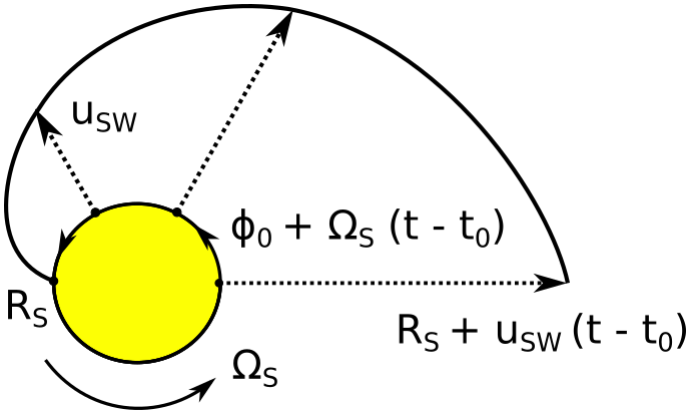

Figure 2.7: *The nominal structure of the HMF as introduced by Parker (1958). Thereby the dashed arrows indicate the radial outflow of the Solar wind particles from the soruce regions R_S whereas the solid line shows the nominal pathway of the resulting magnetic field line, the so-called Parker spiral.*

As the Parker model estimates the HMF analytically, four simplifying assumptions have to be made. Whether these assumptions are realistic and under which conditions deviations are negligible will be discussed at the end of the Section. Generally speaking Parker (1958) assumes an idealised Solar wind as well as an idealised rotational behaviour of the Sun:

- The Solar wind flows radially outward
- The Solar wind speed u_{SW} is constant on small time scales
- The Sun's angular speed Ω_S is constant
- The Sun's rotational axis is aligned with the axis of the Sun's magnetic dipole field

As illustrated by Fig. 2.7 the structure of the HMF follows directly from these assumptions. Therefore it is necessary to define an infinitesimal source region from which only one Solar wind ion is emitted simultaneously. In Fig. 2.7 this source region is indicated as a dot on the source surface at the radial distances R_S from the center of the Sun. The radial distance of the Solar wind ions thereby are given by the time $(t - t_0)$ since they left the source region (at the time t_0) and with respect to their radial speed (which is by definition the Solar wind speed u_{SW}). In mathematical terms this reads as follows:

$$r(t) = R_S + u_{SW}(t - t_0) \tag{2.1}$$

Figure 2.7 illustrates the motion of the Solar wind by three dotted radial arrows, indicating the distances covered by three different Solar wind ions emitted at three different times from the *same* source region. At the time $(t - t_0)$ as shown by the sketch this source region has moved from is position at the origin of the long dotted horizontal arrow at the time t_0 to the opposite site of the Sun. This motion of course is due to the rotation of the Sun itself with the angular speed Ω_S. If the source region was located at ϕ_0 by the time t_0 it therefore has changed it's position by the time $(t - t_0)$ to

$$\phi(t) = \phi_0 + \Omega_S(t - t_0). \tag{2.2}$$

The solid line shown in Fig. 2.7 connects the radial positions of the the different Solar wind ions emitted from the same rotating source region. In physical terms these Solar wind ions emanating from the same source form a Solar wind stream line $r(\phi)$ which mathematically

can be derived from a combination of Eqs. (2.1) and (2.2). The resulting Archimedian spiral is mostly referred to as a Parker spiral in this regard:

$$r(\phi) = R_S + \frac{u_{SW}}{\Omega_S}(\phi - \phi_0). \tag{2.3}$$

2.4.2 The Concept of Frozen-in Magnetic Field Lines

Due to the special conditions within the Heliosphere Parker spirals can be interpreted as frozen-in magnetic field lines. The term "frozen-in" basically indicates that the magnetic field lines of the HMF are attached to corresponding parcels of Solar wind ions and therefore have to follow the motion of the plasma. In order to make this phenomenon comprehensible, the theoretical background will be outline in the following, based on Kippenhahn and Möllenhoff (1975) and similar to the discussion presented in Vogt (2013). Concerning the theoretical framework of MHD this quality has important consequences. First, Ohm's law changes in regard that the contribution of the current density $\vec{j}$ vanishes or the electric conductivity σ within the Solar Wind plasma increases to infinity:

$$\frac{\vec{j}}{\sigma} = \vec{E} - \vec{v} \times \vec{B} = 0 \quad \text{for } \vec{j} \to 0 \text{ or } \sigma \to \infty. \tag{2.4}$$

Therefore, by this approach it is assumed that there are no permanent large scale electric fields within the Heliosphere. The only electric fields present within this approach are the ones caused by the motion of the plasma within the magnetic field. Therefore the electric field $\vec{E}$ within Faraday's law of induction can be expressed via the particle's speed $\vec{v}$ and the magnetic flux $\vec{B}$ as

$$\frac{\partial \vec{B}}{\partial t} = -\vec{\nabla} \times \vec{E} = \vec{\nabla} \times (\vec{v} \times \vec{B}), \tag{2.5}$$

indicating that the evolution of the magnetic field (partly) depends on the current state of the magnetic field itself. This becomes important if (as a gedanken experiment) one would insert a ring into the plasma and release this ring to follow the motion of the plasma with the speed $\vec{v}$. Due to it's motion within the time dt the ring will engulf a cylinder of the length $\vec{v}dt$. In order to change the magnetic flux Φ through the area A inside the ring there are only two possible causes:

- Temporal variation within the magnetic flux density itself crossing the area $d\vec{a}$ of the ring

$$\frac{d\Phi}{dt} = \int_A \frac{\partial \vec{B}}{\partial t} \cdot d\vec{a} \tag{2.6}$$

- Magnetic field lines cross the cladding of the cylinder C engulfed by the ring's motion

$$\frac{d\Phi}{dt} = \int_C \vec{B} \frac{d\vec{a}_C}{dt} \tag{2.7}$$

The differential $d\vec{a}_C$ denoting the area of the cylinder's cladding thereby is the cross product of the line element $d\vec{l}$ along the ring and the motion of an arbitrary point on the ring along the cladding $\vec{v}dt$. Combined with Stoke's law this allows to rewrite Eq. (2.7) as

$$\int_C \vec{B} \frac{d\vec{f}_C}{dt} = \oint_{U(A)} \vec{B} \cdot \vec{v} \times d\vec{l} = -\oint_{U(A)} \vec{v} \times \vec{B} \cdot d\vec{l} = -\int_A \vec{\nabla} \times (\vec{v} \times \vec{B}) \cdot d\vec{a} \tag{2.8}$$

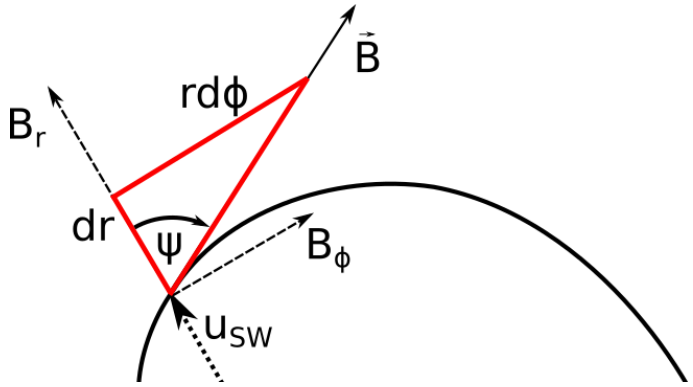

Figure 2.8: *The major properties of the Parker field. As introduced via Fig. 2.7, the solid line represents the nominal Parker spiral whereas the dashed arrow indicates the radial outflow of the Solar wind particles. The red triangle shows the definition of the Parker angle* Ψ *between the radial component of the HMF and the nominal direction of the HMF as given by the tangential of the Parker spiral.*

with $U(A)$ denoting the perimeter of the ring A for which the line integrals are defined. As a consequence the addition of Eqs. (2.6) and (2.8) in order to obtain the total possible change of the magnetic flux leads to

$$\frac{d\Phi}{dt} = \int_A \left(\frac{\partial \vec{B}}{\partial t} - \vec{\nabla} \times (\vec{v} \times \vec{B}) \right) \cdot d\vec{a} = 0, \tag{2.9}$$

proving that the magnetic flux Φ through an arbitrary area within the Solar wind plasma is not allowed to change. Within the image of a ring moving with the plasma this means, that magnetic field lines pointing through the area inside the ring at a given time will continue to do so at all times. The magnetic field lines are tied to the motion of the plasma.

Referring back to Parker (1958) and his concept of the expanding corona causing the Solar wind as outlined in Sec. 2.3, the structure of the HMF evolves as follows: Below the source surface the motion of the Solar wind ions follow the radially outward magnetic field lines of the expanding corona. Note that the Sun's magnetic field thereby rotates around the same axis as the Sun itself and with the same angular speed Ω_S as stated above. As the energy density of the magnetic field lowers with the radial distance, the Solar wind plasma propagates radially outward within a fixed frame of references as shown in Fig. 2.7. This happens at the so-called source surface as introduced in Section 2.2.1 a few Solar radii above the photosphere.For a more detailed discussion see e.g. Parker (1963) and Weber and Davis (1967), the theoretical framework first was presented by Alfvén (1942).

Since the Solar wind ions, which reach the source surface (and on the source surface a particular source region) from below, are attached to a common magnetic field line, the concept of the frozen-in magnetic field as argued above tells us that they continue to do so. Therefore the magnetic field lines beyond the source surface are bent into Parker spirals (see Eq. (2.3)) as they are attached to Solar wind ions which form a stream lines of that structure.

2.4.3 Properties of the Parker Field

Regarding the qualities of the HMF (which sometimes also is referred to as the Parker field) an important parameter is the so-called Parker angle $\psi(r)$ describing the (local) curvature

of the Parker spiral by the angle between the radial outflow of the Solar wind and the tangent of the spiral as shown in Fig. 2.8. As indicated by the red triangle the Parker angle can be derived via its tangens:

$$\tan\psi = -\frac{B_\phi}{B_r} = \frac{r d\phi}{dr} = \frac{r\omega_s}{u_{SW}} \tag{2.10}$$

via Eq. (2.3). Since charged particles propagate along magnetic field lines within plasma the Parker angle is an important parameter in order to mathematically describe charged particle transport. Its implementation within the simulation approach used for this thesis will be discussed in Section 6.1.1.

In order to completely derive an expression for the Parker field within a fixed spherical polar coordinate system the second Maxwell equation also known as Gauss law for magnetism $\vec{\nabla} \cdot \vec{B} = 0$ has to be solved

$$\frac{1}{r^2}\frac{\partial}{\partial r}(r^2 B_r) + \frac{1}{r}\frac{\partial}{\partial \phi} B_\phi = 0. \tag{2.11}$$

Due to the rotational symmetry the second term vanishes and Eq. (2.11) can be solved by integration. Combined with the expression for the Parker angle (Eq. (2.10)) the result leads to the complete equation to describe the HMF according to Parker (1958):

$$\begin{aligned} \vec{B}(r,\phi) &= B_r \cdot \vec{e}_r + B_\phi \cdot \vec{e}_\phi \\ &= B_0 \cdot \left(\frac{r_0}{r}\right)^2 \cdot \left(\vec{e}_r - \left(\frac{r\Omega_S}{u_{SW}}\right)\vec{e}_\phi\right), \end{aligned} \tag{2.12}$$

whereas r_0 and $B_0 = B(r_0)$ serve as normalization factors. As most spacecraft data on the Heliospheric magnetic flux density have been obtained at Earth orbit, Eq. (2.12) is commonly normalised to an averaged quiet time value at $r_0 = 1$ AU typically about $B_0 \approx 5$ nT in modelling approaches (see e.g. Jokipii, 2001; Ferreira et al., 2003; Caballero-Lopez et al., 2004a,b, amongst others) pertaining conditions during Solar minima.

2.4.4 Corotating Interaction Regions

The notion that geomagnetic storms could be correlated to the Solar rotation dates back as early as Maunder (1905). With *in situ* measurements of the relevant quantities becoming available in the 1960s they finally could be associated with recurring magnetic structures within the HMF, the so-called corotating interaction regions (CIRs)[5]. CIRs form if persistent coronal holes expand into low latitudes and therefore cause fast Solar wind to run into the slow Solar wind which usually originates from the photosphere at these latitudes. If they happened to be stable for more than one Solar rotation, they are more precisely referred to as interaction regions.

As sketched in Fig. 2.9 the fast Solar wind can not overtake the slow Solar wind ahead of it due to the fact that the frozen-in magnetic field lines (see Section 2.4.1) can not cross. Therefore, as indicated in grey, an area of high magnetic flux and particle density forms, which corotates with the source region on the Sun, the CIR. It is divided by a stream interface, indicated by the dashed line, which separates the slow from the fast Solar wind. Within the stream interface both the plasma density and temperature are increased up to a

[5]See e.g.Dessler and Fejer (1963) and Parker (1963)

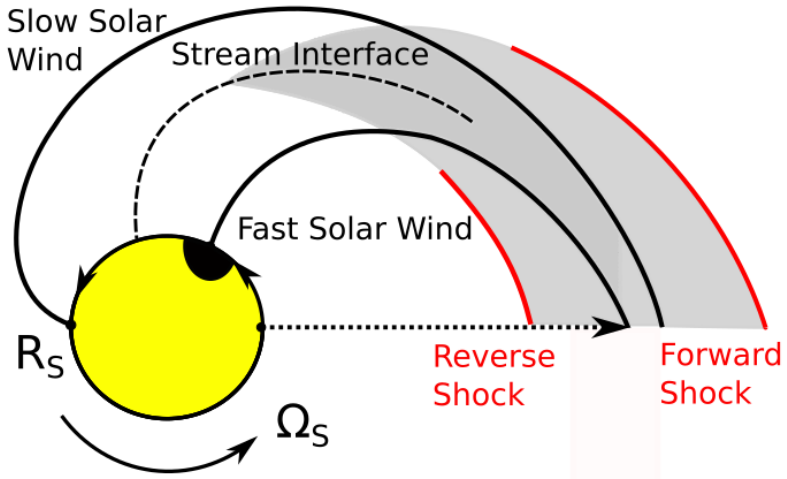

Figure 2.9: *Sketch of a typical CIR. The coronal hole as the source region of the fast Solar wind is indicated in black. The grey area shows the region of increased density where the reverse and forward shock (red) are formed.*

factor of 2 according to e.g. Burlaga (1974) and Wimmer-Schweingruber et al. (1997). The area in which the fast Solar wind catches up the slow one and therefore causes an increased particle and magnetic flux density is referred to as the compression region, whereas the subsequent area shows decreased particle and magnetic densities and is therefore often called the rarefaction region[6].

At a distance of about $\sim$ 2 AU (Gosling et al., 1976) the magnetosonic speed inside the compression region is decelerated below the difference of the fast and slow Solar wind speed as shown by Burlaga (1974). A recent study by Yu et al. (2017) and detailed in Yu (2018), however, indicates that shocks associated to CIRs may form as inward as the Earth orbit, based on measurements of charged particle spectra. The increasing pressure ultimately results in the formation of two shock fronts as indicated in red in Fig. 2.9, the inward directed one usually referred to as the reverse and the outward directed as the forward shock. At these shocks energetic particles are accelerated up to several MeVs as discussed by e.g. Mason et al. (1999). The geomagnetic storms as mentioned beforehand are subsequently easy to explain as a consequence of magnetic interactions between the CIR and the Earth magnetosphere whenever they cross each other.

2.4.5 Limitations of the Parker Field Approach

Although the predictions of the Parker model as discussed in Secs. 2.4.1 and 2.4.3 are on average in agreement with observations in the ecliptic according to e.g Klein et al. (1987), several observational based modification concerning higher latitudes were suggested by e.g. Jokipii and Kota (1989) and Smith and Bieber (1991) due to the known simplifications made by Parker (1958) in the first place. As shown by Raath et al. (2016) by means of an SDE-based model comparable to the one utilised within this thesis, the proposed modifications render the drift effects to be irrelevant over the Solar poles. The question how to address latitudinal dependences became urgent with the observations made by

[6] An attempt to include the rarefaction region effectively into an analytical model for CIRs is discussed by Vogt (2013)

Ulysses (see Section 3.3 for more details) because they revealed unexpected low cosmic ray intensities along the polar regions of the Sun (see e.g. Simpson et al., 1996; Heber et al., 1996) as well as recurring variations (see Kunow et al., 1995; Simpson et al., 1995; Zhang, 1997; Dunzlaff et al., 2008a, amongst others).

Most prominently these findings were addressed by the development of the so-called Fisk field Fisk (1996), which incorporated a motion of the magnetic foot-points based on the differential rotation of the photosphere as observed by Snodgrass (1983). Although the basic concept was validated through MHD simulations by Lionello et al. (2006), any Fisk-type behaviour of the HMF appeared to be difficult to detect in *Ulysses* data. The supposed effects appeared to be smaller than expected in modelling approaches, the only exception being the one by Sternal et al. (2011), which showed weak traces of Fisk-type behaviour by comparison of Lomb-scargle analyses' of both simulated and measured Jovian electron counting rates. In order to address the second problem, that the Fisk field can only be divergence free if a constant Solar wind speed is assumed, the so-called Schwadron-Parker field (Schwadron, 2002; Schwadron and McComas, 2003; Hitge and Burger, 2010) was developed, which basically is a hybrid version of both the Parker and Fisk field, governing the transition between both types of field by a transition function.

Since this thesis focuses on particle transport between the Jovian source and observational points which appear to be located in the ecliptic too, the latitudinal effects are neglected by the simulation setup as discussed in Section 6.1. The major limitation concerning the present study is the fact that the Parker field only describes a turbulence free long scale average of the HMF. Therefore these phenomena must be include otherwise into a any simulation setup which aims to realistically reproduce charged particle transport. These obstacles will be addressed in detail in Section 5.3, especially Secs. 5.3.1 and 5.3.2 in the context of deriving the parameters of the TPE according to Parker (1965). Effectively the simplification of the HMF approach are compensated by the more complex nature of the corresponding mean free path.

Chapter 3

Jovian Electrons

An overview on the planet Jupiter (Section 3.1) and its magnetosphere as a source of the electron population which dominates the low-MeV energy range in the inner Heliosphere (Section 3.2). The main spacecraft missions which obtained in situ data of Jovian electrons both at Earth orbit and during flybys are introduced in Section 3.3. The focus is set on the investigation of the Jovian electron source spectrum providing an expanded discussion based on the results presented previously by Vogt et al. (2018). This includes a re-evaluation of the previous suggestions for a Jovian source spectrum (Section 3.4.1) and of the data used for these means, especially the Pioneer 10 data (Section 3.4.2). The new source spectrum as introduced in Section 3.4.3 thereby incorporates the results obtained and discussed in this Chapter and is contextualised with regard to acceleration and transport theory. This discovery of a new and improved source spectrum completes the first part of this thesis which revisits the data basis and will be followed up by two Chapters outlining the scientific background for SDE modelling approaches (Chapter 4) and theoretical treatment of particle propagation in the inner Heliosphere (Chapter 5).

JUPITER as the largest planet in the Solar system has been a topic of astronomical (and astrological) thinking since the antiquity. The ancient Egyptians possibly identified Jupiter with their God of resurrection, Osiris[1], to whom the dead Pharaoh travelled after leaving the pyramid. The Babylonians identified the planet with Marduk[2] the head of their pantheon, an idea the Greeks and Romans adopted when they interpreted the planet as a representation of their most important God, Zeus and Jupiter, respectively.

The beginning of the scientific investigation of Jupiter can be attributed to the discovery of the four so-called Galilean moons of Jupiter. Discovered independently by Galileo Galilei and Simon Marius in 1610[3] they were named by Johannes Kepler and Marius as Io, Europa, Ganymede and Callisto. They were the first discovered bodies inside the Heliosphere which did neither orbit the Sun or the Earth and therefore could not be explained by he geocentric theory of Ptolemaios. Therefore the Galilean moons play an important role in the history of science as they proved the contemporary doctrine of the church as wrong and paved the way for the self-conception of science as being independent of religious and political influences. Furthermore the orbital motion of the Galilean moons later was utilised by Rømer (1676) in order to determine the speed of light.

The great red spot as visible in Fig. 3.1 first has been described within in the late 1600s but only continuously observed since the early 1800s. However due the almost identical positions there is the possibility that this anticyclonic storm already lasts for over 360 years.

[1] Lieven (2007)
[2] Jastrow Jr. (1911)
[3] Oudemans and Bosscha (1903)
[4] `https://www.nasa.gov/sites/default/files/thumbnails/image/jupapr3colour-jd-170304.png`

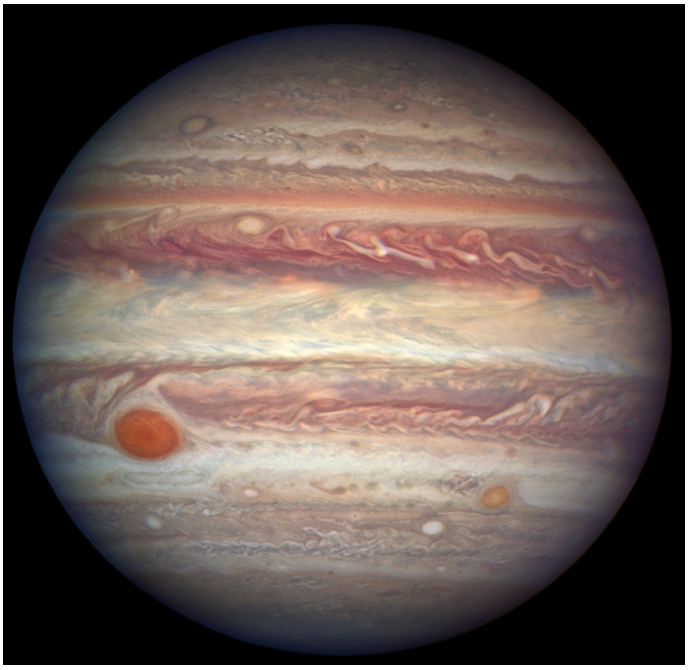

Figure 3.1: *Jupiter as seen by the Hubble space telescope*[4]*.The band-like structure of the Jovian atmosphere is clearly pronounced as well as the big red spot in the lower left quarter.*

3.1 The Planet Jupiter

Counting from inward to outward, Jupiter is the fifth planet of the Solar system, separated from the inner four terrestrial planets such as Mercury, Venus, Earth and Mars by the asteroid belt. Concerning both mass and radius Jupiter is the largest planet by far in the Heliosphere. With an equatorial radius of $R_{Jovian} = 71492 \pm 4$ km according to Seidelmann et al. (2007) it is 11 times larger than Earth, and more massive by a factor of 318 with a mass of estimably $m_{Jovian} = 1.89 \cdot 10^{27}$ kg.

Due to the elliptic nature of its Kepler orbit the radial distance of Jupiter to the Sun varies between $\sim$ 4.8 and 5.4 AU with an average distance of 5.2 AU. Jupiter's siderial period amounts to $T^{sid.}_{Jovian} = 4331.6$ days or $\sim$ 11.9 years, which leads to a synodical period of

$$\Omega^{syn.} = \Omega^{sid.}_{Earth} - \Omega^{sid.}_{Jovian} \rightarrow T^{syn.} = \left(\frac{1}{T^{sid.}_{Earth}} - \frac{1}{T^{sid.}_{Jovian}} \right)^{-1} \approx 399\text{days}. \tag{3.1}$$

As discussed in more detail in Section 3.2, this $\sim$ 13 month periodicity of the relative motion between Earth and Jupiter, can be found in MeV-electron counting rates which lead to the assumption that Jupiter's magnetosphere could be a dominant electron source (see McDonald et al., 1972).

The planet itself consists mainly of hydrogen and helium, with other gases like methane and ammonia being less than 13 %, making Jupiter the prototypical example of a gas giant. The noticeable coloured structures on Jupiter's surface as depicted by e.g. Fig. 3.1 are attributed to traces of sulfur and carbon. Generally it is assumed that Jupiter is structured in layers, with an outer hydrogen dominated atmosphere, followed by a much more helium rich envelope consisting of metallic hydrogen. The inner most core of the planet however

remains uncertain. Never the less it is generally agreed that the electrically conducting regions within Jupiter form a convection driven dynamo similar to the Sun,which causes both an internal magnetic field as well as Jupiter extra ordinary large magnetosphere.

3.1.1 The Jovian Magnetosphere

Both the structure as well as the origin of the Jovian magnetosphere is still an ongoing topic of research.Its investigation was one the major scientific goals of three spacecraft missions in recent years, namely *Galileo*, *Cassini* and *Juno*. Therefore it is beyond the scope of this work to discuss the physics of the Jovian magnetosphere in full detail.

The extent of the Jovian magnetosphere ranges between $40 - 100\ R_{Jovian}$ towards the Sun and to it sides with a magnetotail pointing radially away from the Sun as long as 7000 R_{Jovian}. This means that the Jovian magnetotail is able to reach the perihel of the Kronian orbit according to Khurana et al. (2004). The large-scale appearance of the Jovian magnetosphere is formed by the interaction of the Solar wind with planet's magnetic field. Encountering the Jovian magnetosphere the Solar wind is decelerated to subsonic speeds which results in a bow shock and a magnetosheath, similar to the effects described in context of the Heliophere as a whole as illustrated in Fig. 2.6. Likewise the IPM is separated from the Jovian magnetosphere by a magnetopause. How and whether particle can diffusive inward is still under debate and a candidate for the acceleration (as well as the source) of the Jovian electron population. Almost certain is the existent of a current sheet in the equatorial region, again similar to the HCS, caused by plasma streaming outwards from the Jovian surface and dragging magnetic field lines along.

Since the *Pioneer* and *Voyager* spacecraft missions encountered Jupiter and obtained *in situ* data, it is common to describe the substructure of the Jovian magnetosphere as divided into the inner, the middle and the outer magnetosphere as three distinct regions. The inner magnetosphere is notably current free and the source of the plasma inside the magnetosphere as a whole (see e.g. Garrett et al., 2005). Due to the strong tidal forces on Io which are still debated to be caused by the mass of Jupiter or resonance phenomena among the three inner satellites or a combination of both (see e.g. Yoder, 1979; Lainey et al., 2009), the moon is the most volcanic in the Solar system (McEwen et al., 2000) and was identified as the origin of most of the plasma in the inner magnetosphere (Broadfoot et al., 1981), emitting about 1 ton/s of mostly sulfur and oxygen. These emission after being ionised by electron impact or charge exchanged are carried radially outward from the planet and form he current sheet mentioned beforehand.

The middle magnetosphere can be identified with the region dominated by the presence of the current sheet. Similar to the HCS also the Jovian current sheet drags the magnetic field lines along and thereby causes the Jovian magnetic field to strongly deviate from the originally dipole-like field. This effect is enhanced as the rotational and the magnetic axis of Jupiter are tilted by $\sim 9.6°$. A more detailed discussion on the consequences of these phenomena can be found by e.g. Dunzlaff (2012).

The outer magnetosphere is mostly dominated by the interaction with the IPM, in particular the Solar wind and Solar events. Therefore the extension of the outer magnetosphere, especially towards the Sun, is highly variable depending on the condition within the HMF. Since it was shown by Pyle and Simpson (1977) (see the discussion in the next Section) that the Jovian source can be assumed as almost point-like in Heliospheric scales[5],

[5]The term point(-like) source refers back to simulations via the finite difference scheme method which usually operates on a grid. Thereby the Jovian source was included as as single grid point. See e.g. Sternal

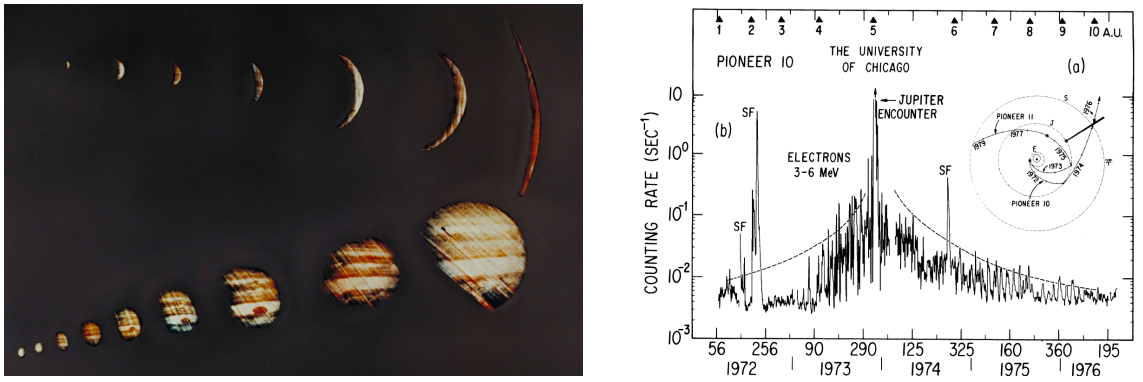

(a) **(b)**

Figure 3.2: *The Jovian flyby of Pioneer 10 confirmed the Jovian magnetosphere as the source of low-MeV electrons as well as the point-like nature of this source. Figure 3.2a thereby shows a combination of several photographs taken from on board the spacecraft during the approach after the flyby*[6]*. The corresponding electron counting rates are shown in Fig. 3.2b in the left panel as published by Pyle and Simpson (1977).*

the variations of the outer magnetosphere and of the extended magneto-tail in particular can be neglected within the scope of this thesis. Therefore a constant Jovian magnetosphere will be assumed for the simulation setup as detailed in Section 6.1, ranging 1.03° longitudinally and 0.28 AU radially.

3.2 The Jovian Source

The investigation of Jupiter as a source of low-energy electrons started when McDonald et al. (1972) found an accordance between Jupiter's synodical period (see Eq. (3.1)) and the characteristic $\sim$ 13 month periodicity of electron counting rates at Earth orbit. This hypothesis was confirmed by measurements of the spacecraft *Pioneer 10* and *Pioneer 11* during their Jupiter flybys in December 1973 and 1974, respectively, As Chenette et al. (1974) concluded it was possible to observe Jovian electrons throughout the inner Heliosphere in the low-MeV range. Only a few years later, the Jovian electrons population first was utilised as test particles for transport modelling by Conlon (1978). Subsequently the history of investigating the Jovian source is discussed as well as why the Jovian source can be assumed both continuous and point-like. As an important exception (which will become significant when revising previous spectral data in Section 3.4) an overview on so-called Jovian Jets as found by Ferrando et al. (1993) completes the Section.

(2010); Vogt (2013)

[6]Source: `https://Solarsystem.nasa.gov/resources/707/pioneer-10-at-jupiter`

3.2.1 Quiet-Time Electrons at 1 AU

The *Pioneer 10* Jovian flyby on December 4th, 1973, was the first time a man-made object reached Jupiter. The event is nicely illustrated by Fig. 3.2a as a montage of picture taken by the optical instrument of the spacecraft during the approach and on the spacecraft's way further out. In Fig. 3.2b, the counting rates for electrons in the energy range from $3 - 6$ Mev are shown as obtained by the Charged Particle Instrument (CPI) onboard *Pioneer 10* during the first years of the mission. The ▲ symbols on top thereby indicate the radial distance of the spacecraft. A sketch of the corresponding trajectory is shown in the upper right quarter. The figure shows how the flux increases during the flyby with a few exceptions identified as Solar flares. Pyle and Simpson (1977) concluded that the Jovian source can be considered as point-like in opposition to prior conjections that Jovian extended magneto-tail would be emitting electrons as well. This conclusion basically could be drawn because several CIRs passed in between Jupiter and the observing spacecraft but did not interfere with the magnetic connection between the spacecraft and the Jovian magneto-tail. Since the passing of these CIRs nevertheless caused significant decreases within the Jovian electron flux, the Jovian magneto-tail with its length over 1 AU outward could be excluded as a source. These findings were further supported by the measurements of *Pioneer 11* one year later and the approach of the two *Voyager* spacecraft in 1979.

Apart from this point-like nature, Pyle and Simpson (1977) confirmed that the Jovian source was continuous and constant based on the *in situ* measurements. These findings resonated with Earth orbit observations of low-MeV electron counting rates varying with Jupiter's synodic period (see Eq. (3.1)) as first described by McDonald et al. (1972). As the electron background seems to be periodically constant apart from times of Solar activity, already Teegarden et al. (1974) coined the term (Jovian) quiet-time electrons in an attempt to distinguish them from short term Jovian flux increases. The term became widely accepted and describes accurately the Jovian electron population this work is investigating. The irregularities Teegarden et al. (1974) and Pyle and Simpson (1977) detected in the Jovian electron counting rates later turned out to be the first hints to the existence of Jovian Jets as confirmed by Dunzlaff et al. (2009) and discussed in Section 3.2.2.

The most important quality of Jovian quiet-time electrons with respect to this work, is the fact that their flux at Earth orbit periodically de- and increases. This effect can be found in observational data of several decades as demonstrated by Kanekal et al. (2003) for the Solar cycles 22 and 23. Earth orbit data illustrating this effect are shown by Fig. 3.3 for several synodical periods during the 1990s (*IMP-8*) and the 2000s (*SOHO*). As mentioned above this periodical variation of Jovian electron fluxes at Earth orbit is caused by the relative motion of Jupiter and Earth as described by Eq. (3.1) and discussed in Section 3.1. The combination of the siderial movement of Earth and Jupiter lead to the above mentioned periodicity of ≈ 399 days or 13 months for both planets to share the same nominal Parker spiral. As discussed in Section 2.4.1 this means that both planets are magnetically connected and therefore charged particles are more likely to propagate between them. The more effective particle transport along the nominal Parker spirals leads to higher electron intensities a Earth orbit during times of good connection. The periodical variation is at its lowest point in case of opposition (blue area) when perpendicular diffusion becomes most significant. As discussed in Secs. 6.4.1 and 6.4.2, this will be utilised during this thesis in order to quantify the effectiveness of parallel and perpendicular transport, respectively. For a detailed account on charged particle transport in the HMF and the diffusive processes therein in particular, see Sections. 5.1 and 5.3.

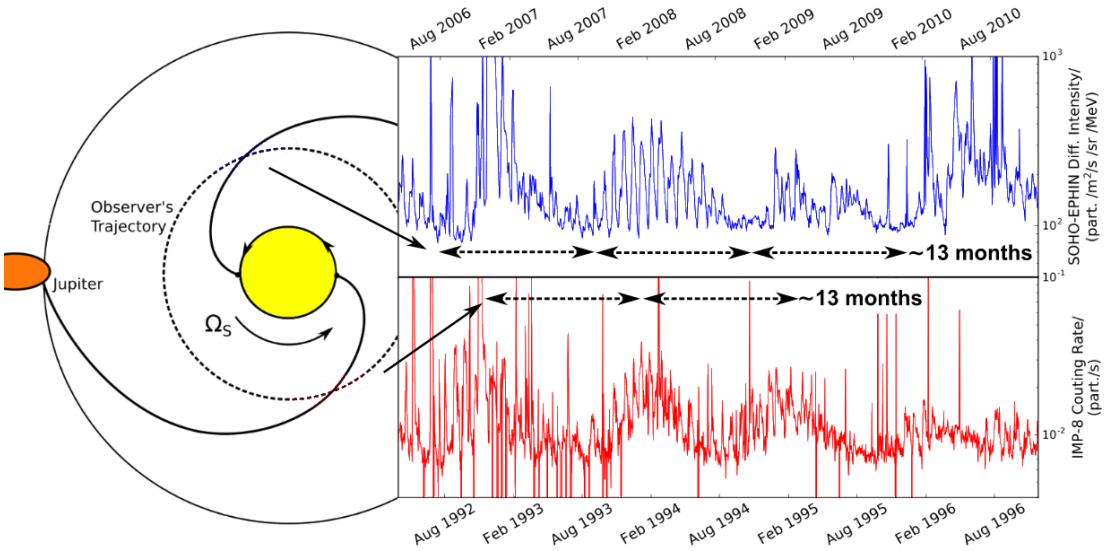

Figure 3.3: *The 13 months periodicity in electron data at Earth as seen by SOHO in blue (see Section 3.3 for details on the mission and the instrument) and IMP-8. The right panel shows a sketch of the magnetic geometry with a circular observer's orbit as dashed and two Parker spirals (solid) to indicate good and bad magnetic connection. The effects of the 13 months periodicity are indicated by three double-headed arrows indicating the periodicity of the minima (SOHO data, blue) and two double-headed arrows indicating the periodicity of the maxima utilising the IMP-8 data in red.*

Since Jupiter is the only validated decentral source which such a periodicity of a dominant particle population (for a discussion on the existence of a Kronian population see e.g. Lange and Fichtner (2008) whereas Palmaerts et al. (2016) and Roussos et al. (2016) discuss electron releases within the Kronian magnetosphere), Jovian electrons are often used as a test population in order to investigate charged particle propagation. The first approach to model Jovian electron propagation in order to derive more realistic values for transport parameters was undertaken by Conlon (1978) closely after the confirmation of the point-like nature of the Jovian source. Since then various models have been developed and applied in order to study Jovian electron propagation and its implications on various corresponding phenomena. Most of them are based on finite-difference schemes[7] and utilised for such different tasks such as determining latitudinal and radial transport parameters (see e.g. Ferreira et al., 2001a,b), to distinguish between the Galactic and Jovian component (see e.g. Fichtner et al., 2000), investigating the magnetic qualities of CIRs (see e.g. Kissmann et al., 2003, 2004) or the transport within high latitudes and its consequences on the understanding of the HMF (see e.g, Moeketsi et al., 2005; Lange et al., 2006; Sternal et al., 2011). The importance of CIRs with respect to Jovian electron related investigations of charged particle transport (and vice versa) has been prominently pointed out by Pyle and Simpson (1977), Conlon (1978),Kissmann et al. (2003) and Dunzlaff et al. (2008b), amongst others. Measurements of Jovian electron modulation by CIRs are discussed by e.g. Daibog et al. (2013) and Kühl et al. (2013b) concerning several aspects of transport theory. More recently SDE based transport models became more prominent and were successfully applied by (e.g. Strauss et al., 2011a,b; Vogt et al., 2018, amonst others)[8].

[7] A prominent example being the model based on the work of Blom and Verwer (1994, 1996) and discussed by e.g. Fichtner (2001).

[8] The model developed and discussed by Dunzlaff et al. (2015) which is utilised and expanded for this work will be discussed in more detail in Chapters 4 and 6.

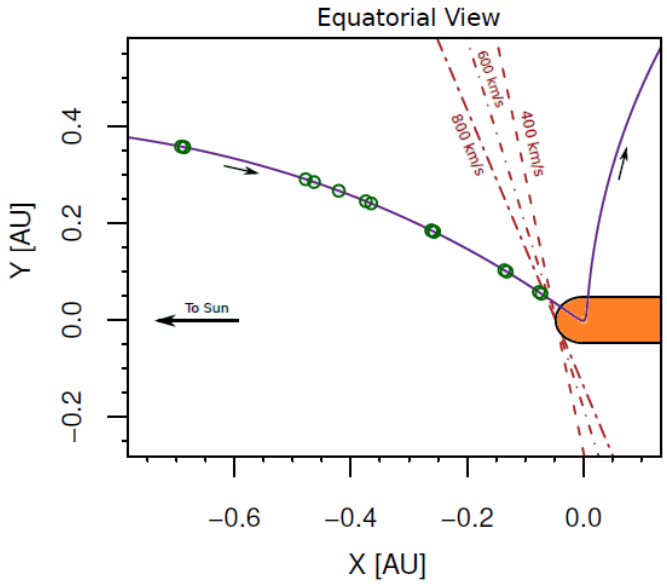

Figure 3.4: *The trajectory of Pioneer 10 during its Jovian flyby, taken from Dunzlaff (2012) and adapted to the colour coding used within this work. Whereas the orange area indicates the position of the Jovian magnetosphere, the green dots mark the position at which Pioneer 10 encountered a Jovian jet.*

Of the topics related to Jovian quiet-time electron investigations this work will revisit the discussion concerning the derivation of realistic transport parameters in Section 6.4 and Chapter 8. The influence of CIRs which are assumed to act like a diffusion barrier on Jovian electrons (see e.g. Kissmann et al., 2003, amongst others) will be discussed again in Section 7.4.2 in order to identify Jovian electron data which represent undisturbed propagation conditions. Therefore this work is related to most the topics connected to quiet-time Jovian electron investigations and aims to contribute to all of them.

3.2.2 Jovian Jets

Whereas the measurements cited above indicated a quasi isotropic Jovian electron population in the inner Heliosphere, Ferrando et al. (1993) reported that *Ulysses* observed 35 short-term events of high anisotropy. These so-called Jovian Jets show a strong (pitch-angle) anisotropy during some minutes up to several hours alongside with sharp in- and decreases of the particle flux aligned to the magnetic field lines. The second more distant flyby of *Ulysses* confirmed these findings (McKibben et al., 2007). As e.g. concluded by Dunzlaff (2012), several common characteristic qualities of Jovian were identified based on these studies:

- The local magnetic field during Jovian Jets is aligned with the spacecraft's viewing direction
- The time profiles of Jovian jets is characterised by sharp in- and decreases of the Jovian flux with respect to the quiet time background
- Jovian Jets show a significant anisotropy with respect to the magnetic field

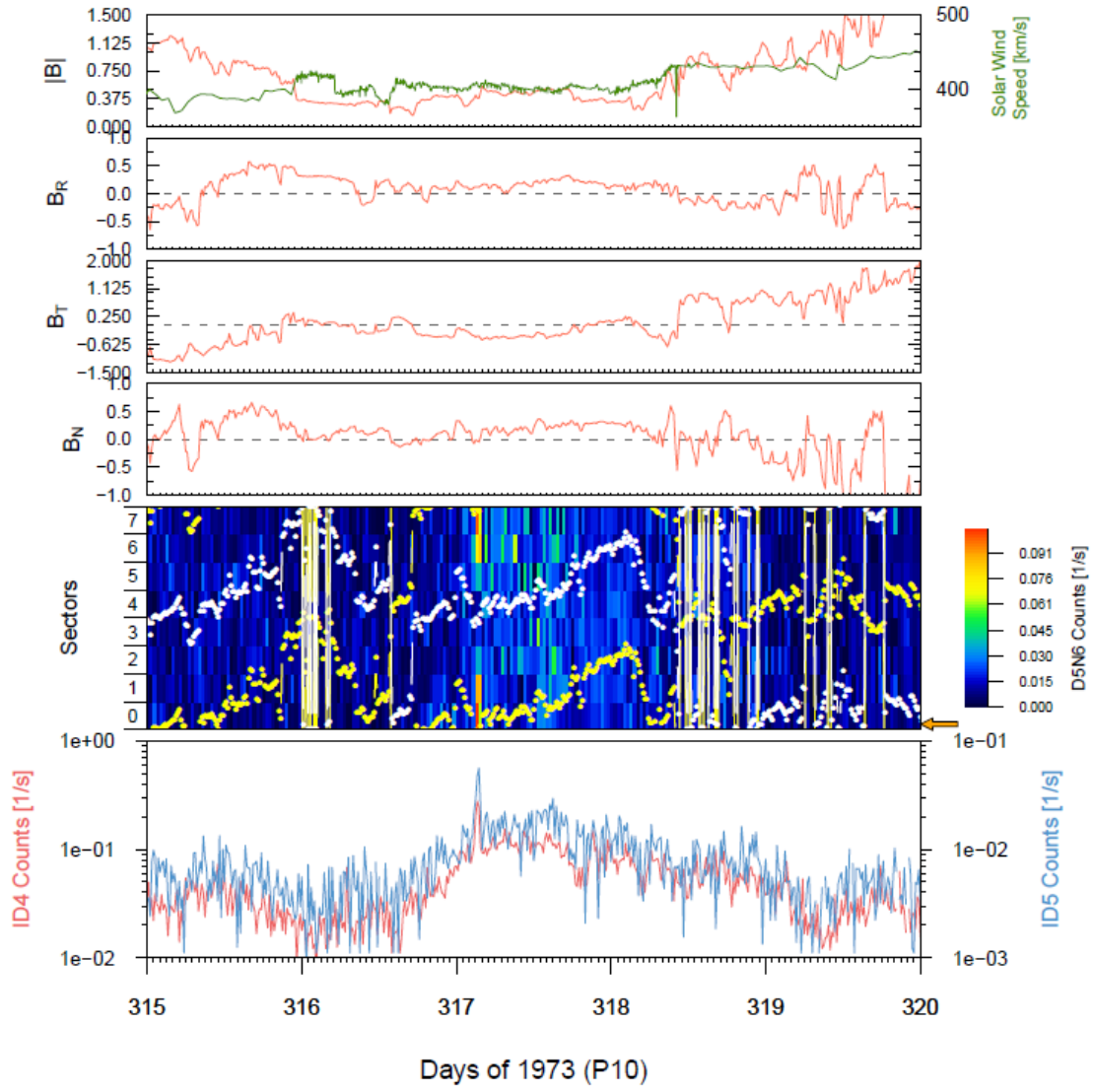

Figure 3.5: *A Jovian jet as observed by Pioneer 10 on 317/1973 according to Dunzlaff (2012). The four upper panels show the Solar wind speed (green) together with the magnetic flux as well as the three indiviudual components of the HMF. The fifth panel shows the intensities in eight individual sectors as a contour plot, together with the parallel (orange) and anti-parallel (white) orientation to the HMF. The direction towards jupiter is indicated by an orange arrow. The lowest panel shows the electron count rates and displays the sharp in- and decreases typical for a Jovian jet.*

- The magnetic field during a Jovian jet often deviates strong from the expected HMF as derived by Parker (1958) in order to connect the observational point to the Jovian source. See e.g. in Fig. 3.4 nominal line configuration in red in contrast to the observational points of Jovian jets (green).
- Flux and anisoptropy are not related to the distance to the Jovian source.

Furthermore Ferrando et al. (1993) noted that the 10 hours periodicity of Jupiter's rotation can be found during jets up to distances of 0.5 AU from the source. Another striking similarity with the Jovian electron population is that except for two events Jovian jets are not accompanied with a significant increase of proton or ion fluxes as shown by McKibben et al. (2007). These observations confirmed sufficiently the Jovian origin of the electron

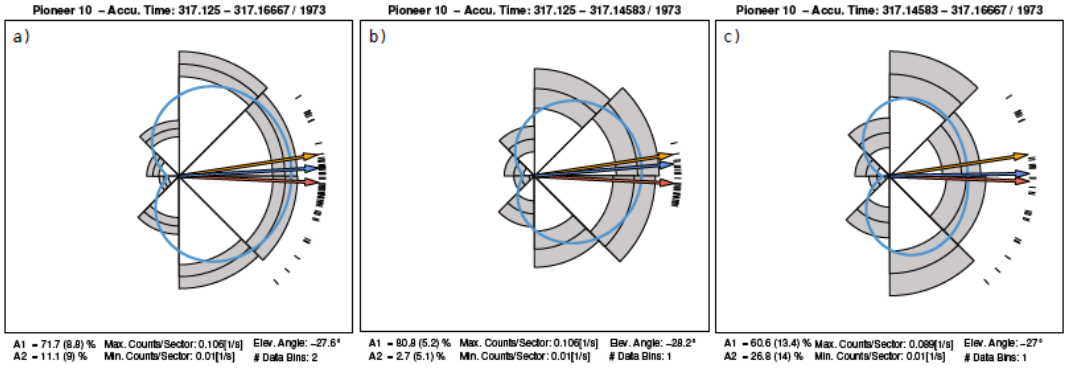

Figure 3.6: *Sector plots taken from Dunzlaff (2012), showing the same event as in Fig. 3.5. The three different panels show the temporal evolution of the event as a) shows the integrated particle counts of each sector for the whole event, whereas b) and c) show them for the first and second half, respectively. The arrows indicate the average direction toward Jupiter (orange), of the magnetic field (red) and of the anistropy (blue).*

beams and motivated the term Jovian jets.

Dunzlaff et al. (2009) identified the small time Jovian electron flux increases as reported by Chenette et al. (1974) to be Jovian jets as well. Subsequently 17 additional Jovian Jets during the *Pioneer 10* flyby were identified. The trajectory of *Pioneer 10* with the observational points of Jovian jets marked by green cycles is sketched in Figure 3.4. As they correspond to the spectral measurements by the *Pioneer 10* instrument CPI which themselves seem a bit increased with respect to the other data present in Fig. 3.7, these jets identified within *Pioneer 10*/CPI data are of most interest for this work. Therefore the qualities of Jovian jets will be illustrated in the following by *Pioneer 10*/CPI data. Due to a longer time time resolution of 15 minutes (compared to down to 2 minutes in case *Ulysses*/Kiel Electron Telescope (KET)) the Jovian jets identified within the *Pioneer 10*/CPI data are fewer and much longer in average.

The temporal evolution of the relevant *in situ* data is shown by Figures 3.5 and 3.6 for a Jovian jet identified on day 317 of 1973. In Fig. 3.4 the position of the encounter is marked by the second most right green dot. As shown in the four highest panels of Fig. 3.5, depicting the absolute value and the three spatial components of the magnetic field, alongside the Solar wind speed in green. Note that the magnetic field components are given in a radial-tangential-normal (RTN) coordinate system. Therefore the alignment to the viewing direction indicates a magnetic connection to the Jovian source as typically for Jovian jets. Furthermore the fluctuations of the magnetic field are decreased during the event. The colour-coded panel shows the particle counts in the eight sectors of the CPI/MT detector. As discussed e.g. by Chenette et al. (1974) and Dunzlaff (2012) with respect to the characteristics of Jovian jets, the sectorisation of of CPI/MT counting rates is possible because the spacecraft spins around an axis inclined by $\sim 46°$ to the viewing cone of the telescope. The bottom panel shows counting rates covering electrons with energy ranges of $2-7$ MeV and $6-28$ MeV, respectively. At day 317.1 a sharp increase is visible that last for about an hour and correlates to are high anisotropy as depicted in the sector panel. This event is accompanied by a smooth increase of the electron counting rates since day 316.

Figure 3.6 shows the corresponding sector plots, a) the accumulated counts over the whole time of the event, b) the first and c) the second half of the event. As discussed in detail by Dunzlaff (2012) Fig. 3.6 confirms a strong first order anisotropy of $\sim 72 \pm 9$ %

[8]For details on the instrumentation onboard *Pionner 10* used to obtain these data see Section 3.3.1

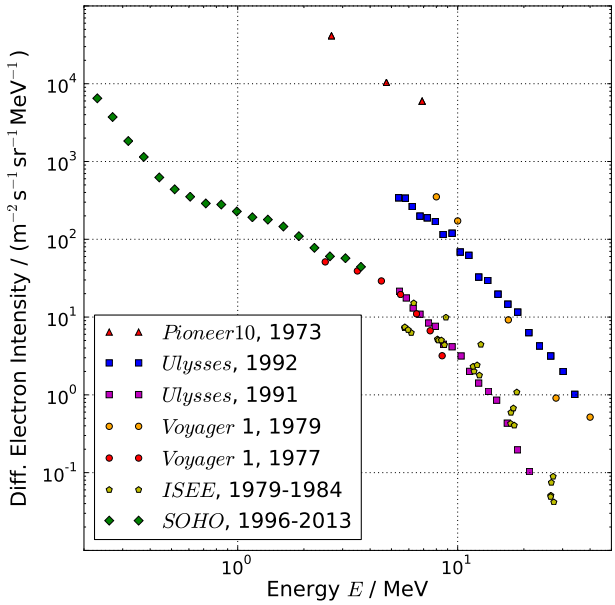

Figure 3.7: *Display of the different spectral measurements of low MeV electrons as listed in Tab. 3.1, both at the Jovian source (Pioneer 10,1973 and Ulysses,1992) and at Earth orbit. The intensity difference between the two flyby spectra is discussed and resolved in great detail in Section 3.4.2.*

during the event. Furthermore a correlation between the symmetry axis of the distribution (blue arrow), the magnetic field vector (red) and the direction towards Jupiter (orange). The temporal evolution between b) and c) is shown by Dunzlaff et al. (2015) to an effect of pitch-angle diffusion.

3.3 Measurements

The history of measuring Jovian electrons by spacecraft missions is basically the history of understanding the Jovian source by interpreting the results. Therefore the overview on the topic will be combined with a discussion of the spacecraft missions which contributed most to our understanding of Jovian electrons. Chronologically the most significant spacecraft missions are discussed with respect to their influence on this work. The spectral data obtained during these spacecraft missions is listed in Tab. 3.1 alongside the references to the corresponding publications. Prior to the discussion of these spacecraft missions and their measurements used within this work, it is necessary to introduce the most common detector principles.

Semiconductor Detectors are used in order to measure the kinetic energy of a particle, often build of Germanium (Ge) or Silicon (Si). When a charged particle penetrates a material it is able to ionise it via electron-hole pair production. Semiconductors thereby are the material of choice since they constitute a compromise between conductors in which valence electrons are unbound from the atomic cores as a Fermi

Table 3.1: *Overview of the electron spectra used in this thesis.*

Location	Spacecraft/Instrument	Source
Flyby	Pioneer 10/CPI	Teegarden et al. (1974)
	Ulyssses/KET	Heber et al. (2005)
	Voyager 1/TET	Nndanganeni and Potgieter (2018)
Earth orbit (well connected)	SOHO/EPHIN	Kühl et al. (2013a)
	Ulyssses/KET	Heber et al. (2005)
	ISEE 3/ICE	Moses (1987)
	Voyager 1/TET	Nndanganeni and Potgieter (2018)
Earth orbit (badly connected)	ISEE 3/ICE	Moses (1987)

gas and common isolators in which the electron-hole pairs would mostly vanish due to the irregularities of the target's structure. If the detector is kept under voltage the free electrons produced by the hitting particle are detected by the electrodes as a current pulse. Due to the quantified nature of the valence energy which is needed to lift an electron from the valence into the conduction band, the amount of electron-hole pairs being produced is proportional to the kinetic energy of the hitting particle. Therefore semiconductor detectors are often applied as calorimeters or used in combination with each other in order to estimate particle energies by the dE/dx method via the Bethe-Bloch formula as derived by Bethe (1930) and Bloch (1933): The finding that the energy loss of a particle in a solid is depending on its remaining kinetic energy, with the loss increasing with decreasing velocity, allows to estimate the particles total energies in case the particle is stopped within the detector. If a set of semiconductor detectors is used, the relation between the energy loss in the first detector and the total energy loss allows to discriminate between the different particle populations including electrons.

Cherenkov Detectors are based on the fact that relativistic particles can propagate through matter faster than the speed of light $c_n = c/n$ according to Čerenkov (1937). Thereby c is the vacuum speed of light, and n the refraction index of the medium. In this case, similar to the Mach cone, so-called Cherenkov light is emitted if the medium is a light transparent dielectric. The mechanism behind this phenomenon is the polarisation of the medium by the hitting particle. The light which is emitted in response is usually detected by a photo-multiplier. The response of a Cherenkov detector depends on the mass (indirectly by means of the kinetic energy i.e. velocity) of the hitting particle, therefore they are used in order to distinguish between electrons and protons or ions. Because only particles with $v > c_n$ can polarise the detector, the kinetic energy for electrons needed to cause a signal is much lower than for protons. In order to assure that this discrimination works for a far range of energies mostly aerogel and lead flouride are used as materials for Cherenkov detectors with refraction indices of $n = 1.05$ and $n = 1.8$, according to Gurav et al. (2010) and Malitson and Dodge (1969) respectively.

Scintillation Detectors are often used as an anti-coincidence as in the cases relevant to this thesis. They consist of a transparent crystal which fluoresces when it is hit by a particle. The light production is quantified as it takes places when free electrons produced by the hitting particle fall back into the valance band. Compared with other detector types, scintillation detectors have a much lower energy resolution but a much faster response and therefor qualify as anti-coincidences in order to shield

telescopes.

Unlike previous studies on Jovian electrons, this work estimates the Jovian source spectrum both in shape and strength based only on *in situ* measurements obtained during flybys. As shown and discussed by Vogt et al. (2018) and expanded in Sections. 3.4.2 and 3.4.3 the derivation of the source function will be based on flyby spectra whereas the Earth orbit data serves as a consistency check. Although three additional spacecraft visited the Jovian magnetosphere in recent years, the analysis by Vogt et al. (2018) could only rely to the spectral data obtained by *Pioneer 10* and *Ulysses*, since neither of *Galileo*, *Cassini* or *Juno* flyby spectra have been published up to now. However, considering the instrumentation onboard the spacecraft, the Jovian energy spectrum seems well covered, according to the literature on the Energetic Particle Detector (EPD) onboard *Galileo* (see e.g. Williams et al., 1992), the Low Energy Magnetosphere Measuring Systems (LEMMS) onboard *Cassini* (see e.g. Krimigis et al., 2004; Haggerty and Livi, 2004) as well as the Jupiter Energetic particle Detector Instrument (JEDI) onboard Juno as discussed by e.g. Mauk et al. (2013). As detailed in Section 3.4.3 especially in the low energy range of the Jovian spectrum, new possible spectral data would improve our understanding whereas the energy range above ~ 5 Mev is well covered.

The following discussion will therefor be limited to the spacecraft missions of which spectral measurements are published within the Jovian electron energy range. With an exception being the Voyager mission. The *Voyager 1* data as shown in Fig. 3.7 were made available by private communication through W. R. Webber and M. S. Potgieter but published by Nndanganeni and Potgieter (2018) after the derivation of the new source spectrum by Vogt et al. (2018). Therefore as handled by Vogt et al. (2018) and Vogt et al. (2020) the *Voyager 1* spectra will be used as collaborating evidence but not taken into account in that extent as the other electron spectra listed in Tab. 3.1.

3.3.1 Pioneer 10/11

As mentioned above the two *Pioneer* spacecraft were not only the first ones to reach Jupiter, but also to cross the Asteroid belt. Launched in March 1972 and April 1973, respectively, they were equipped to measure the HMF *in situ* as well as GCRs. Their trajectories went straight forward to Jupiter were *Pioneer 10* performed a swing-by maneuver in order to accelerate towards the outer Heliosphere whereas *Pioneer 11* performed a bounce back maneuver as indicated by Fig. 3.6 to reach Saturn in September 1979.

The **Charged Particle Instrument (CPI)** onboard the twin spacecraft is described by e.g Lentz et al. (1973), Chenette et al. (1974) as well as by McCarthy and O'Gallagher (1975). It is accompanied by several other energetic particle instruments such as the Cosmic Ray Telescope (CRT), the Geiger Tube Telescope (GTT) and the Trapped Radiation Detector (TRD). The CPI, also called Chicago instrument in the literature, consists of four individual instruments, the Main Telescope (MT), the Low Energy Telescope (LET), an Electron Current Detector (ECD) and a fission cell. The LET thereby consist in itself of two different telescopes the LET_1 and the LET_2.

Figure 3.8 shows the sketch of LET_2 by Trainor et al. (1974) as this telescope appears to be the most important one of the CPI instrument within this work. The LET_2 is designed to measure electrons in the energy range of 0.05 to 2.1 MeV being able to separate electrons and protons above 0.12 MeV. Protons are detectable between 0.2 and 21 MeV. These qualities are closely related to the structure of the telescope as it consists of very thin

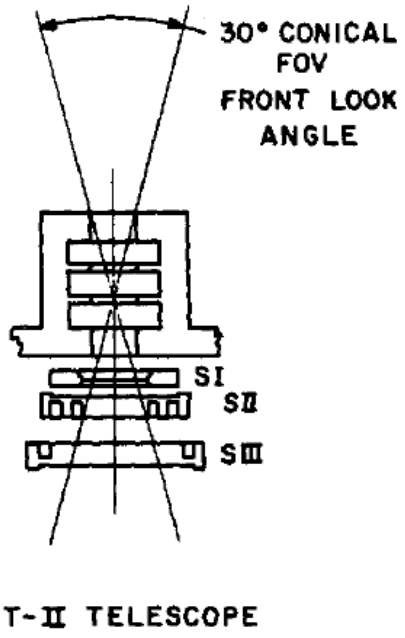

Figure 3.8: *Sketch of the LET_2 telescope onboard Pioneer 10/11 according to Trainor et al. (1974), which was used by Teegarden et al. (1974) to obtain the first Jovian electron spectra.*

detectors in order to resolve lower energies as detailed by Stilwell et al. (1975). According to Trainor et al. (1974), LET_2 it is surrounded by an aluminium and lead shield in order to stop electrons up to $\sim$ 25 and protons up to $\sim$ 140 MeV from entering the telescope outside the view cone. The three semiconductor detectors SI, SII and SIII are set up in the way that SI provides an electronic threshold. The energy loss of electrons will cause an energy deposition in SI below the threshold whereas protons would be above it.

Based on the measurements of LET_2 Teegarden et al. (1974) obtained the first spectra of the Jovian electron source, both inside and outside the Jovian magnetosphere. As discussed in Section 3.4.2 the spectrum outside the Jovian magnetosphere as depicted in Fig. 3.7 is based on measurements during a time of highly increased fluxes identified by Dunzlaff et al. (2009) as a so-called Jovian jet (see Section 3.2.2 for a detailed discussion) the implications of these findings are discussed by Vogt et al. (2018) and in an expanded version in Section 3.4.2.

3.3.2 Ulysses

The *Ulysses* spacecraft, launched October 6th, 1990, was the first mission to leave the ecliptic plane and investigate the third dimension of the inner Heliosphere *in situ*. Performing a swing-by maneuver to reach its orbit, *Ulysses* approached Jupiter on February 8 1992 up to 6.3 Jupiter radii. With the help of Jupiter's gravity the spacecraft was deflected

[9] `https://sci.esa.int/documents/33816/35255/1567218791004-THIRD_ORBIT_REV2007_BW_EXT-1280.jpg/6f9a6175-f89a-6493-c0b8-c944fd1e265a?version=1.0&t=1567218791841`

[10] `https://www.cosmos.esa.int/web/ulysses/instruments`

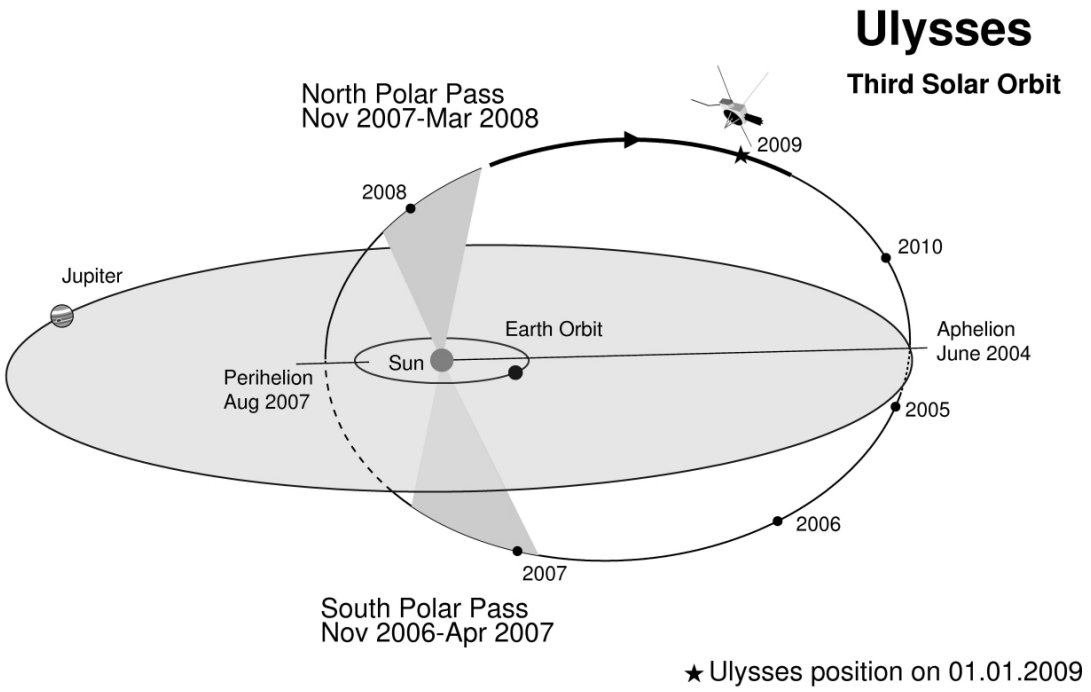

Figure 3.9: *Sketch of the trajectory of Ulysses during the spacecraft's third Solar orbit. As a reference to the ecliptic plane, the orbit of Jupiter is shown alongside the its encircled area in grey. The dark grey areas connected to the Sun's poles indicate the viewing direction of the spacecraft during its last fast latitude scans.*[9]

and turned southward to reach its final, highly Keplerian orbit with an inclination of about 80°. As indicated by Fig. 3.9 *Ulysses* approached Jupiter a second time in 2004 (up to a distance of 0.8 AU) while reaching its aphelion in its third Solar orbit. The mission ended on June 28 2009 after three Solar orbits and fast latitude scans (see Section 2.2.3) on the northern and southern Solar poles, respectively.

The **Kiel Electron Telescope (KET)** as described by e.g. Simpson et al. (1992) is part of the **COsmic-ray and Solar-Particle INvestigation** experiment which consisted of 6 individual charged particle telescopes. The COSPIN experiment is able to detect the energy, composition, intensity and anisotropy of nuclei, covering an energy range from ~ 0.5 MeV/nucleon to ~ 600 MeV/nucleon for H up to Ni. Regarding electrons COSPIN is covering an energy range from ~ 2.5 MeV to ~ 6000 MeV. Thereby the KET itself can detect electrons within an energy range of ~ 7 to ~ 500 MeV by means of a combination of different detector units as shown in Fig. 3.10.

The instruments consist of two semiconductor detectors referred to as D1 and D2 in Fig. 3.10 which work in combination with two Cherenkov detectors (C1 and C2) and three scintillation detectors as anti-coincidence. The measurement principle can be described as follows: The two semiconductors D1 and D2 at the entrance of the telescope obtain information of the energy loss via the dE/dx method. The first Cherenkov detector C1 placed between them separates electrons from protons and heavier nuclei, due to the fact that proton need much higher kinetic energies in order to produce Cherenkov light. The second Cherenkov detector C2 subsequently serves as a calorimeter as it reads out the total remaining energies of particles stopping there.

As discussed by e.g. Ferrando et al. (1996) and Heber (1997) and references therein

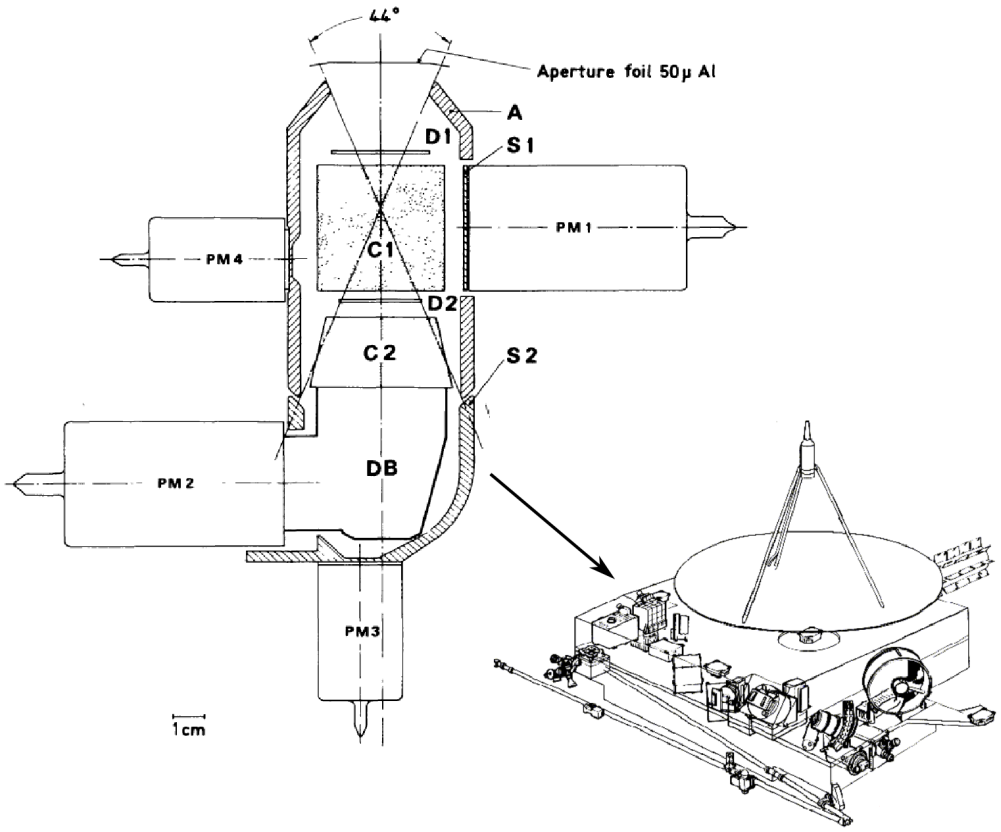

Figure 3.10: *Sketch of the KET according to Simpson et al. (1992) together with its place on the spacecraft*[10].

the different coincidence variants constitute of different energy channels. The minimum of the detectable energy range is define by the fact that in order to be counted, an electron has to penetrate D1, C1 and D2. In this case the electron either loses all its energy in the second semiconductor detector D2 or has too little kinetic energy left after passing it to trigger a signal in the second Cherenkov detector C2. Therefore electrons of these characteristics are assigned to the lowest ranging channel E4, which counts electrons with energies of $\sim$ 2.5 to 7 MeV. If as well the C2 is triggered the particle will be assigned to the E12 channel containing electrons of energies between $\sim$ 7 to 500 MeV. In the rare occurrence that also the anti-coincidence S2 is triggered, there is no possibility to determine the energy of the particle, and it will be counted within the E300 channel for electrons with energies $>$ 500 MeV. As mentioned above, protons of comparable energies would not be able to trigger neither of the Cherenkov detectors. These protons to only trigger D1 and D2 would be attributed to the P32 proton channel ranging between $\sim$ 5.4 to 23.1 MeV. The more complex identifications of α particles or protons with high enough energies to trigger C1 or C2 via energy thresholds is described by Sierks (1988) in large detail. Further information on KET's energies can be found in Heber (1997).

The energy deposits regarding the electron channels were discussed in detail by Heber et al. (2005). Therefore a GEANT 3 simulation (see Brun et al., 1987, for details) of the telescope was applied, alongside an analysis of the photon background. Subsequently the two electron spectra listed in Tab. 3.1 and shown in Fig. 3.7 were obtained together with a spectrum of a Jovian jet measure in August 1991.

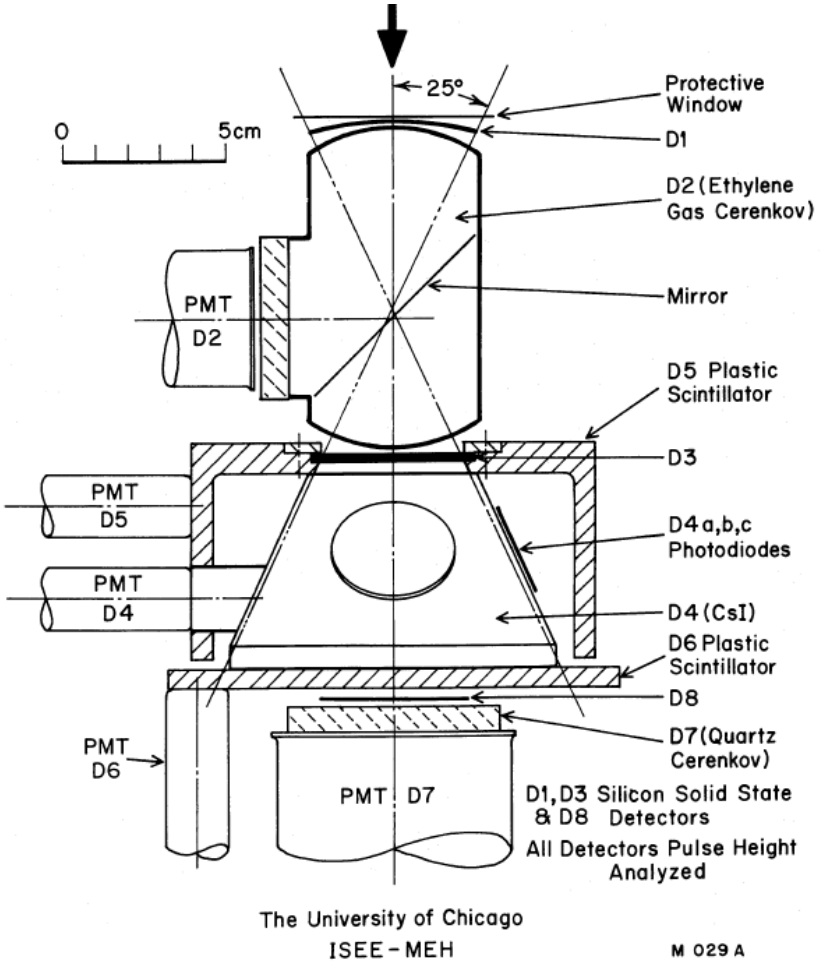

Figure 3.11: *Sketch of the particle detector onboard ISEE 3 according to Moses (1987). The bold arrow on top indicates the viewing direction of the instrument.*

3.3.3 ISEE 3

The **International Sun Earth Explorer (ISEE)** program consisted of three spacecraft ISEE 1-3, lauchend in 1977 and 1978 respectively. Whereas ISEE 1 and 2 had highly eliptical orbits around the Earth and finally vaporised in 1987, ISEE 3 instead was placed at the Lagrange point L_1 and was renamed after the mission ended in 1982. Subsequently the spacecraft sent was sent to the comets Giacobini-Zinner and Halley as **International Comet Explorer (ICE)**. Its systems are still operational and there was data transmission from ICE until September 16 2014.

Figure 3.11 shows a cross-Section sketch of the electron detector on board ISEE 3. As described by Meyer and Evenson (1978) and Moses (1987) electrons are identified by the telescope by a combination of conditions: The silicon detectors D1 and D3 have to detect a singly charged particle in coincidence, the ethylene gas Cherenkov detector D2 has to respond, the energy deposit of the particle in the plastic scintillator D3 has to be less than 100 KeV and furthermore the plastic scintillator D6 must not detect a signal as electrons within the detection of 3 to 50 MeV are supposed to stop in detector D4. The energy is estimated by combining the calculated energy loss in the detectors D1, D2 and D3 (and

Table 3.2: *Spectral data acquisition periods of ISEE 3 according to Moses (1987)*

Good Magn. Connection	Bad Magn. Connection
1978 November 4 to 1979 April 10	1979 April 10 to September 7
1979 September 7 to 1980 April 9	1980 April 9 to October 26
1980 October 26 to 1981 April 20	1981 April 20 to October 27
1981 October 27 to 1982 June 19	1982 June 19 to November 28
1982 November 28 to 1983 May 20	1983 May 20 to December 6
1983 December 6 to 1984 July 18	1984 July 18 to December 366

the associated material such as entrance window, etc) with the measured residual energy in the CsI calorimeter D4. Thereby five energy bins were defined for electrons: $2.3 - 5$ MeV, $3.5 - 6$ MeV, $6 - 10$ MeV, $10 - 15$ MeV and $15 - 20$ MeV. Combining these energy losses in D4 with the calculated energy loss in D1-D3, one obtains nominal incident energies for the five bins as $5, 7, 10, 15$ and 25 Mev, see Moses (1987).

The results contained twelve individual spectra of Jovian electron fluxes measured at Earth orbit, six each obtained during times of good and bad magnetic connection to the source, respectively. The intervals used to obtained the spectra are up to 200 days long in order to assure good statistics. Explicitly the periods of good magnetic connection were used to derive the Jovian spectra as shown in Fig. 3.7 and taken into account to obtain a measure for the parallel mean free path in Section 6.4.1 via Fig. 6.9 are detailed in Tab. 3.2.

Note that not the final data product published by Moses (1987) was used, but rather the raw data. As discussed by Vogt et al. (2018) the attempt to estimate the actual Jovian contribution by Moses (1987) was based on assumptions that are doubtful nowadays. The spectra were corrected both in intensity as in spectral shape in order to cancel out the influence of an else-wise dominant Solar component. These measures were taken based on a Monte Carlo simulation incorporating a strong influence of adiabatic deceleration (see Section 5.4 for more information). Due to the results of Fichtner et al. (2000) which were successfully applied in the meantime by e.g. Kissmann et al. (2004) and Sternal et al. (2011) this estimation as well as the results derived from it became dubious. Furthermore the final data product is in contradiction to the spectra obtained by Heber et al. (2005) as well as the *Voyager 1* spectra.

3.3.4 SOHO

The **Solar and Heliospheric Observatory (SOHO)** was launched December 2nd, 1995, and began its normal operations in May 1996 at an halo orbit around the Lagrange point L1. There it is able to investigate the Heliosphere near at Earth orbit (only 0.01 AU away from Earth) without disturbances by the Earth's magnetic field. Its major scientific goals range from investigating the outer layers of the Sun via remote sensing to Helioseismology and most important for this work, *in situ* observations of the Solar wind and the embedded HMF as well as the energetic particle environment.

The **Electron Proton Helium INstrument (EPHIN)** is one of the particle telescopes on board SOHO and part of the **Comprehensive SupraThermal and Energetic Particle analyser collaboration (COSTEP)**. The data obtained provide a electron

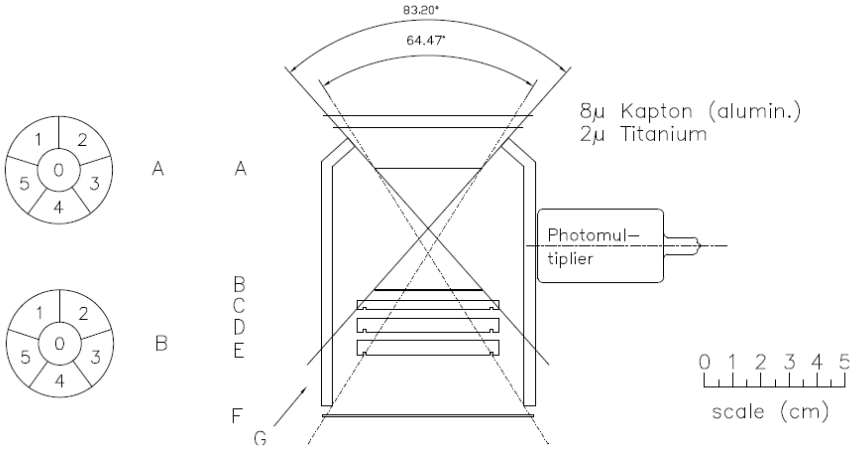

Figure 3.12: *Sketch of the EPHIN instrument onboard SOHO according to Müller-Mellin et al. (1995). On the right side the sectorisation of the detectors A and B are displayed which allows both a higher directional resolution as well as prevent the instrument from running into permanent dead time during times of high intensities as the sectors can be individually turned off.*

counting rates within up to four energy channels ranging over two Solar cycles. Schematically the instrument is shown in Fig. 3.12 via a sketch taken from Müller-Mellin et al. (1995). It consists of the semiconductor detectors A-F and a scintillation detector G which serves as an anti-coincidence. One of the main advantages of EPHIN is the fact the the detectors A and B are segmented in the way as shown by Fig. 3.12. By turning these segments on and off the geometry factor of EPHIN can be be varied e.g. to reduce the dead time in cases of high intensity influxes.

The particle identification itself is obtained via the $dE/dx - E$ method (Müller-Mellin et al., 1995)[11]. Thereby the energy loss in detector A is put in relation to the energy loss in the total of the detectors. Comparing the theoretical distributions with the measured ones then allows to differentiate the particle populations. This leads to the definition of four different electron channels. E150 contains electrons with energies between 0.25 to 0.7 MeV, E300 ranges between 0.67 and 3.0 MeV, followed by E1300 which covers 2.64 to 6.18 MeV and E1300 for energies between 4.8 and 10.4 MeV. Further details on how simulating the instrument allows for defining the energy channels are given by Kühl et al. (2013a) who applied their results to obtain the electron spectra listed in Tab. 3.1 and shown in Fig. 3.7. A more detailed discussion on the energy channels and how they are to interpret for simulation purposed will be given in Section 7.4.2.

3.4 The Source Spectrum

Since the first *in situ* confirmation of a Jovian electron population, several attempts were made in order to estimate the source spectrum. Therefore Section 3.4.1 will discuss these past approaches and outline how they are related to each other and to the spacecraft data

[11] Recently a new data product has been presented utilizing the so-called $dE/dx - dE/dx$ method. For details see Kühl and Heber (2019)

as listed in Tab. 3.1. Subsequently the re-evaluation of the flyby data, as presented by Vogt et al. (2018), will be discussed in Section 3.4.2 focusing on the *Pioneer 10* spectrum by Teegarden et al. (1974) which somehow deviates from the other flyby spectra as e.g. shown in Fig. 3.7. The new approach as introduced by Vogt et al. (2018) will be discussed in Section 3.4.3 in relation to the past approaches and the developments within the last years of electron transport modelling.

The Jovian electron source spectrum is of interest to several aspects of Heliospheric physics. Most obviously the source spectrum enables to quantitatively reconstruct the accelerations mechanisms within the Jovian magnetosphere. As mentioned beforehand in Section 3.1.1, the Jovian magnetosphere remains a topic of ongoing research, with three spacecraft (*Cassini*, *Galileo* and *Juno*) being sent to the Jovian magnetosphere to obtain *in situ* data in recent years. The Jovian source in that regard raises the question how electrons supposedly originating from the Solar wind (see e.g. Bolton et al., 1989) are accelerated to several MeV while diffusing inward into the Jovian magnetosphere. The mechanism proposed first by de Pater and Goertz (1990) is an acceleration process by conservation of the first and second adiabatic invariant. According to spacecraft data discussed by e.g. Fischer et al. (1996) and Bolton et al. (2002) also wave-particle interaction could contribute to the acceleration processes as shown by Horne et al. (2008).

The intensity difference between the spectrum inside the magnetosphere (as also measured within Jovian jets) and the flyby spectrum as mostly discussed in this thesis could provide information on the release mechanisms and therefore about the Jovian magnetosphere as well. Recently, Becker et al. (2017) reported that *Juno* observed large particle bursts at Jupiter's polar regions as well as MeV electrons in the inner radiation belt. Other measurements indicated the presence of open field lines (Clark et al., 2017; Zhang et al., 2017) whereas *Cassini* and *Galileo* data suggested that MeV electrons leak out ot the Jovian magnetosphere despite a closed field topology according to Krupp et al. (2002).

Apart from its relation to the physics of the Jovian magnetosphere, the Jovian source spectrum is important to charged particle transport modelling, as it determines the source strength of a significant test particle population as discussed in Section 3.2.1. Apart from the qualitative notion that the Jovian source spectrum serves as a calibration, this work will investigate the dependence of simulation results on its boundary conditions (i.e. the Jovian source spectrum in this particular case) further in Chapter 6 after introducing the necessary theoretical concepts, both physical and mathematical.

3.4.1 Past Approaches

The first approach in order to quantify the strength of the Jovian source, was made by Teegarden et al. (1974) as soon as Jupiter was confirmed to be the origin of the quiet-time electron population within the inner Heliosphere. Due to the limitation of *Pioneer 10* CPI and especially LET_2 which covers the low energy range of Jovian electrons (see Trainor et al., 1974; Teegarden et al., 1974, for more details) a statistical reasonable evaluation of electron spectra is only possible during times of increased fluxes. Based on measurements obtained during the Jovian approach on 11 May 1973, Teegarden et al. (1974) concluded that the Jovian source spectrum has the form of a power law in terms of kinetic energy with an exponent of about ≈ -1.5 given by

$$j(E) \propto \left(\frac{E}{E_0}\right)^{-1.5} \tag{3.2}$$

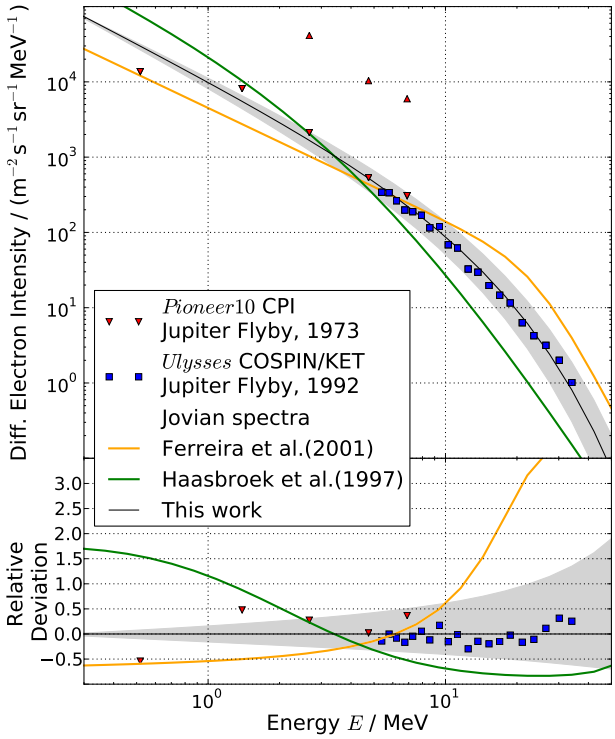

Figure 3.13: *Combined plot of the flyby data utilised by Vogt et al. (2018) in order to derive a new source spectrum alongside with the approaches by Haasbroek et al. (1997) green and Ferreira et al. (2001a) in orange as well as the approach developed within this thesis and discussed in Section 3.4.3.*

and normalised to $E_0 = 1$ MeV. Due to the exceptional conditions under which the spectral data were obtained, the approach to determine a Jovian source spectrum was constrained to the shape and did not quantify the strength. Therefore most subsequent approaches derived source spectra based on Earth orbit data and assumed the original strength at Jupiter according to then state of the art propagation models. In order to cover the steepening of the spectrum observed at higher energies, Baker and van Allen (1976) expanded the approach given by Eq. (3.2) by a second power law as

$$j(E) \propto \left(\frac{E}{E_0}\right)^{-1.5} \left(1 + \frac{E}{E_b}\right)^{-n} \tag{3.3}$$

and quantified the additional parameter as $4 \leq n \leq 6$ and 10 MeV $\leq E_b \leq$ 35 MeV, respectively. These two basic qualitative approaches were elaborated when more and more data (mostly obtained at Earth orbit) became available. For the following decades a series of attempts were made in order to quantify the parameters which were left unspecified in Eqs. (3.2) and (3.3). The first one was based on the initial approach by Teegarden et al. (1974). Additionally taking into account data of *IMP 8* and *Mariner 10* as well as the results from the first modelling code for Jovian electrons by Conlon (1978), quantitative analyses performed by by Chenette (1980) and Eraker (1982) concluded that the source function could be approximated as a point source with a source spectrum following $QE^{-\gamma}$ and suggested it quantitatively as

$$j(E) = \frac{3 \cdot 10^{25}}{\text{s MeV}} \left(\frac{E}{E_0}\right)^{-1.7}, \tag{3.4}$$

with $E_0 = 1$ MeV and in units of particles per seconds and energy. In order to determine whether the Jovian source varies with time, Lopate (1991) investigated the evolution of the spectral index throughout the whole mission of *Pioneer 10* up to 1991. This work confirmed that the Jovian source was both continuous and constant as the ratio between the 27 day averages of $2 - 7$ MeV and $7 - 17$ MeV electrons appeared to be quite stable and showed only minor fluctuations and a slight decrease during the Solar minimum period around 1987. As pointed out by Lopate (1991), the significance of this is questionable concerning the Jovian source since the spacecraft was already at a radial distance of ≈ 40 AU when the spectral shape began to vary. Subsequently it became justifiable to combine spectral measurements to investigate the shape and strength of the Jovian source even though they cover different time periods.

Thus, Haasbroek et al. (1997), additionally to *Pioneer 10* and *IMP 8* data, took observations by *Pioneer 8/9* and *ISEE 3* into account. Their suggestion was based on approach by Baker and van Allen (1976) given by Eq. (3.3),

$$j(E) = c \left(\frac{E}{E_0} \right)^{-1.5} \left(1 + \frac{E}{5\ E_0} \right)^{-3.5} \tag{3.5}$$

in units of electrons $\mathrm{m^{-2}\ s^{-1}\ sr^{-1}\ MeV^{-1}}$ and again using $E_0 = 1$ MeV as a normalization factor. The strength of the source indicated by the factor c is only implicitly given by referring to corresponding measurements obtained by *Pioneer 10* and *ISEE 3* as presented by Teegarden et al. (1974) and Moses (1987), respectively. Revisiting these data, a value of $c \approx 4 \cdot 10^4\ \mathrm{m^{-2}\ s^{-1}\ sr^{-1}\ MeV^{-1}}$ as used for the plot in Fig. 3.13 (orange) shows the smallest deviations.

An expanded, more sophisticated version of the two power law approach by Baker and van Allen (1976) and Haasbroek et al. (1997), respectively, was obtained by Ferreira et al. (2001a) who fitted their source function to the flyby data of *Pioneer 10* and the estimate by Moses (1987) to reconstruct the source spectrum by estimating the influence of particle transport on the spectral data measured by *ISEE 3*. As a result they combined the well established power law governing the behaviour at lower energies (see Eqs. (3.2, 3.3 and 3.5))

$$j(E)_{1.5} = 5 \cdot 10^3 \left(\frac{E}{E_0} \right)^{-1.5} \tag{3.6}$$

with a second power law added to cover the spectral shape at higher energies which appears to be much harder than suggested by Haasbroek et al. (1997) but matches the upper limit for the second exponent n in Eq. (3.3) according to Baker and van Allen (1976):

$$j(E)_{6.0} = 10^9 \left(\frac{E}{E_0} \right)^{-6.0}, \tag{3.7}$$

normalised to $E_0 = 1$ GeV. Both power laws as given by Eqns. 3.6 and 3.7 are combined to one spectral function as

$$j(E)_{Jovian} = \frac{1.5}{\mathrm{m^2 s\ sr\ MeV}} \left(\frac{c_k \cdot j_{1.5} \cdot d_k \cdot j_{6.0}}{c_k \cdot j_{1.5} + d_k \cdot j_{6.0}} \right) \tag{3.8}$$

with the fitting parameter $c_k = 0.6$ and $d_k = 5.0$. As pointed out by Vogt et al. (2018) the availability of both more *in situ* data as well as increasing computational power to re-analyse previous results, made it necessary to determine whether the Jovian source function given by Eq. (3.8) was still in best agreement with the available data. This question became especially urgent with the first *in situ* measurements of the local interstellar medium (LISM) after *Voyager 1* passed the Heliopause at the end of August 2012 (see Section 2.3). In order to investigate charged particle transport and understand the modulation

of the in-flowing Galactic cosmic ray (GCR), the spectrum of the LISM, local interstellar spectrum (LIS), is of equal significance as the Jovian source spectrum. Although GCR lack the decentral point-like origin, the long distance between the Heliopause and observations at Earth orbit amplifies the influence of transport effects. Therefore comparing the shape and strength of the LIS to the equivalent qualities of the corresponding particle spectrum at Earth is a common method within charged particle transport modelling. As the inner Heliosphere is dominated by the Jovian electron population in the low MeV range, the question how to distinguish between Galactic and Jovian electrons is of obvious importance.

Several attempts to establish an *in situ* electron LIS by (Potgieter and Nndanganeni, 2013; Bisschoff and Potgieter, 2014; Potgieter et al., 2015; Potgieter and Vos, 2017) based on *Voyager 1* data obtained beyond the Heliopause put into question whether the Jovian source spectrum described the Jovian electron flux in the low-MeV range correctly. This issue has been discussed in detail by Nndanganeni and Potgieter (2016). In the mean time also two additional flyby spectra became available, corresponding to the swing-by of *Ulysses* on 8. February 1992 and *Voyager 1* which already passed Jupiter on 5. March 1978. Although both spectra obtained by *Ulysses* KET data (Heber et al., 2005) and measurements by *Voyager 1* BSe instrument (published by Nndanganeni and Potgieter, 2018, but previously made available to the author by private communication) are in agreement to each other, they deviate from all previous suggestions how the Jovian source would behave in the energy range they cover as shown in Fig. 3.13. Therefore Vogt et al. (2018) made the decision to re-evaluate the available spacecraft data as listed in Tab. 3.1 and eventually present a new approach to estimate the Jovian source spectrum based exclusively on flyby data.

3.4.2 Revisiting Flyby Data

In order to avoid the uncertainties connected to previous estimations of the source spectrum (such as the incorporation of transport effect into the Earth orbit spectrum as tried by Moses (1987) and implicitly by the studies based on this work) the decision was made to focus entirely on flyby data and only utilise the spectra obtained at Earth orbit as also listed in Tab. 3.1 in order to assure consistency. On the downside this decision limited the available data to the spectra published by Teegarden et al. (1974) and Heber et al. (2005) based on the measurements of *Pioneer 10*/LET and *Ulysses*/KET, respectively. The additional flyby spectrum obtained by *Voyager 1*/TET as listed in Tab. 3.1 was known to the authors but not yet published and could therefore not be utilised. Nevertheless, by the notion that it supports the *Ulysses*/KET data by Heber et al. (2005) as shown in Fig. 3.15, the *Voyager 1*/TET spectrum hinted to revisit the *Pioneer 10*/CPI data as they deviated strongly, suggesting Jovian fluxes in the low-MeV and keV range much higher than the other available data. Since they have been used in order to derive some of the past approaches discussed in Section 3.4.1 they are given by the upright red triangles in Fig. 3.13, accompanied by their re-normalised values indicated by downright triangles as also used in Fig. 3.15. Although the original *Pioneer 10*/CPI spectrum is too intensive to agree with the ones obtained by *Voyager 1*/TET and *Ulysses*/KET its shape seems to agree with the expected behaviour.

As discussed by Vogt et al. (2018) the *Pioneer 10*/CPI spectrum was obtained during a day of unusual high fluxes, 11 May 1973, according to Teegarden et al. (1974). Due to statistical measures this spectrum was the only one derived from the flyby. A second

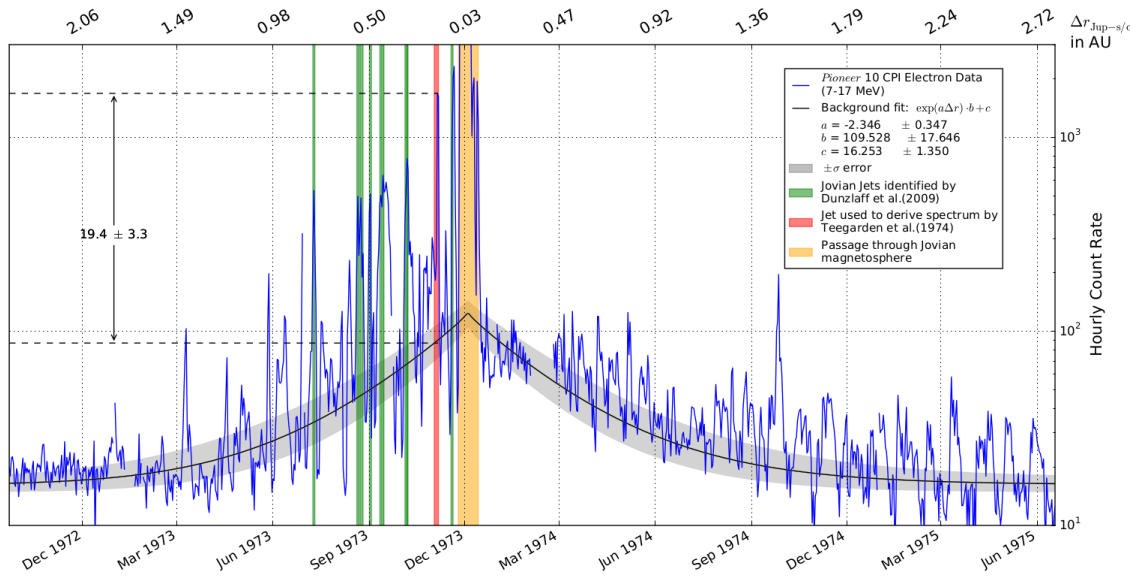

Figure 3.14: *Pioneer 10's CPI counting rates of the 7-17 MeV electron channel (blue) according to Vogt et al. (2018). They are displayed together with the result of an exponential background fit (black with a gray shaded region showing a 1 σ uncertainty). In order to estimate the increase of the electron flux in the Jovian jet used to determine the Pioneer spectrum by Teegarden et al. (1974) (shaded in red) all other jets identified by Dunzlaff et al. (2009) (green) were also excluded from the background, along with the fluxes obtained inside the Jovian magnetosphere (orange).*

spectrum published by Teegarden et al. (1974) is based on measurements inside the Jovian magnetosphere. The explanation for the unexpected high intensities of the *Pioneer 10*/CPI spectrum appears to be the occurrence of a Jovian jet as discussed in Section 3.2.2. The comparison with the list of Jovian jets detected by *Pioneer 10*/CPI according to Dunzlaff et al. (2009) showed that the event used to obtain the spectrum matched the criteria of a Jovian jet. As Jovian jets are known for their increased intensity but similar shape with respect to the quiet time population (see e.g. Heber et al., 2005), this offers the possibility to estimate the quite time intensities, if the relative increase due to the Jovian jet can be determined.

The approach is illustrated by Fig. 3.14. As discussed by Vogt et al. (2018), it shows the daily *Pioneer 10*/CPI electron flux taken from `ftp://spdf.gsfc.nasa.gov/pub/data/pioneer/pioneer10/particle/cpi/ip_1day_ascii/p10cpi.h24` in blue, combined with an exponential background fit in black, surrounded by a gray shaded region which indicates the 1 σ uncertainty. Marked in green are the Jovian Jets identified by Dunzlaff et al. (2009) and in orange the passage through the Jovian magnetosphere. The red shaded area marks the day on which the data used to obtain the spectrum was measured. Comparing the background fit to the intensities measured during the Jovian Jet on 11 May 1973, as indicated by the two horizontal dashed lined on the left side of the figure, one obtains an estimated increase of intensity by a factor around 19.4 ± 3.3.

Figure 3.13 shows the effect of re-calibration on the *Pioneer 10*/CPI spectrum. Whereas the upward triangles indicate the original intensities as published by Teegarden et al. (1974) the downward triangles show them decreased to the background intensity estimated via the method illustrated by Fig. 3.14. As especially shown in the MeV-range where the spectral ranges of the *Pioneer 10*/CPI and *Ulysses*/KET data overlap, the intensity-decreased spectrum is in good agreement. Furthermore the shape of the combined spectral data of *Pioneer 10*/CPI and *Ulysses*/KET agrees with the general shape within the low

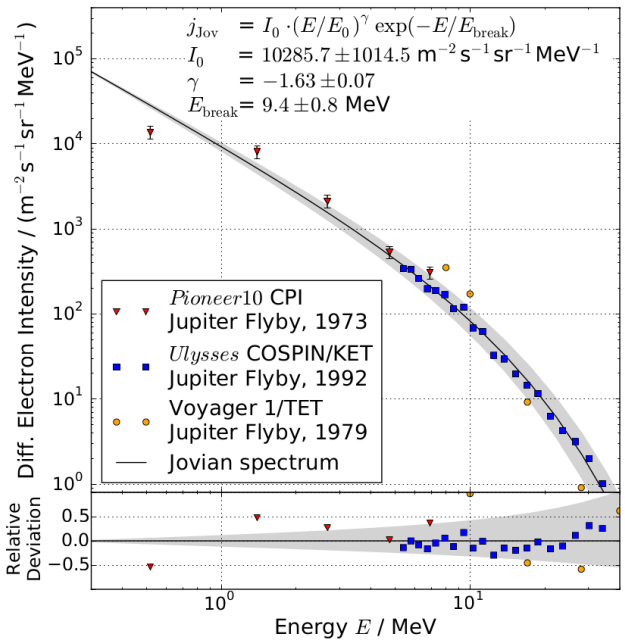

Figure 3.15: *The Jovian source spectrum (black) as introduced and discussed by Vogt et al. (2018, 2020). The Pioneer 10 and Ulysses flyby data were utilised in order to derive and fit the spectral shape whereas the Voyager data were not available yet in order to include them by Vogt et al. (2018). Subsequently within the investigations as presented by Vogt et al. (2020) it could be shown that the addition of Voyager data does not change the source spectrum significantly.*

MeV- and keV-range as indicated by the *SOHO*/EPHIN measurements shown in Fig. 3.7. However both the uncertainties connected to the re-calibration of the *Pioneer 10*/CPI data as well as the behaviour of the *SOHO*/EPHIN data in the keV range, which still is not perfectly understood (Kühl, private communications) have to be kept in mind. Therefore, as it will be addressed in more detail discussing the new suggestion for the source spectrum, the keV range of the Jovian electron population remains a topic of research.

3.4.3 The New Source Function

As already mentioned above and discussed by Vogt et al. (2018) the decision was made not only to derive a new Jovian source spectrum but to limit the data base to flyby spectra. Thereby we aimed to minimise the influence of transport effects (or more precisely: efforts to compensate them) on our estimation. Additionally we tried to be consistent with the known physics of particle acceleration theory (see e.g. the discussion of diffusive shock acceleration by Prinsloo et al., 2017) which suggest a single power-law-shaped spectrum and therefore questions the two power law approach as utilised for Eqns. 3.3, 3.5 and 3.8 by (Baker and van Allen, 1976; Haasbroek et al., 1997; Ferreira et al., 2001a) unless a second acceleration process can be offered. Since the combined general shape of the measured spectra indicates a deviation from a purely power-law-like shape due to a hardening towards higher energies, a combination of the initial approach by Teegarden et al. (1974) and an

exponential cutoff was chosen:

$$j(E)_{jov} \propto \left(\frac{E}{E_0}\right)^{\gamma} e^{-E/E_{break}}. \tag{3.9}$$

again normalised to the energy $E_0 = 1$ MeV. The spectral shape of a power law with an exponential cutoff corresponds to the suggestions of acceleration and particle transport theory as a power law would be the expected shape according to acceleration theory, whereas resonance scattering within magnetic field perturbations (as can be assumed within the Jovian magnetosphere) is supposed to result in an exponential cutoff as suggested by Eq. (3.9). For more details see e.g. Schlickeiser (1985) or Fisk and Gloeckler (2014) who argue for this particular spectral shape along with an exponent of $\gamma \approx -1.5$ being the common spectrum for particles accelerated anywhere within the Heliosphere.

This approach was fitted via the least-square method as implemented in the `scipy 0.9.0` library of `python 2.7.3` to the *Pioneer 10* CPI and *Ulysses* KET spectra. The result is given in Fig. 3.15 together with the fitted spacecraft data (as well as the *Voyager 1*/TET data which appear to be in agreement with the fit) and the uncertainties (grey area). The $\pm\sigma$ surrounding was calculated equivalent to the one given in Fig. 3.14 and shows that the fit reproduces the shape of the *Ulysses*/KET spectrum and also for energies in the MeV range the shape of the *Pioneer 10*/CPI spectrum. The *Voyager 1*/TET data despite being know by private communications could not be used by Vogt et al. (2018) in order to fit the spectrum. First, the *Ulysses*/KET spectrum is more in agreement with other measurements, especially at Earth orbit (see Fig. 3.7 in Section 3.2.1) but also with the re-normalised *Pioneer 10*/CPI spectrum. Second, although the *Voyager 1*/TET data (if considered alone) suggest a slightly softer shape for larger energies, taking them into the account for the fit does not influence the result beyond the margin of error. Therefore, taking the theoretical considerations as outlined above into account, too, the new spectral source function

$$j_{jov}(E) = \frac{1.029 \cdot 10^4}{\mathrm{m^2 s\ sr\ MeV}} \left(\frac{E}{E_0}\right)^{-1.63} e^{-E/E_b} \tag{3.10}$$

as suggested by Vogt et al. (2018, 2020) and utilised within this work is an improvement with regard to prior approaches and turns out to give a realistic estimation of both intensity and shape of the Jovian source within the low-MeV energy range. Thereby, again $E_0 = 1$ MeV whereas the break is determined by $E_b = 9.4$ MeV.

The improvement is emphasised by comparison with the previous estimations discussed above. As shown in Fig. 3.13 the value of the exponent $\gamma = -1.63$ fits in between the suggestions given by Eqns. 3.2 (Teegarden et al., 1974), 3.3 (Baker and van Allen, 1976), 3.5 (Haasbroek et al., 1997) and 3.8 (Ferreira et al., 2001a) as $\gamma = -1.5$ on the one side and the estimation of $\gamma = -1.7$ as proposed by Eraker (1982) and given by Eqn.3.4. Thereby it is important to note that the suggestion of an harder value of $\gamma = -1.5$ is almost entirely accompanied (Teegarden et al. (1974) covering mostly the high-keV range being the only exception) with the suggestion that a second power law would soften the source spectrum within the 10 MeV range. Significantly the only suggestion of a higher value of $\gamma = -1.7$ is corresponding to the single power law approach by Eraker (1982). The suggestion made by Vogt et al. (2018) and given in Eq. (3.10) therefore reflects the more general assumption made by choosing a single power law shape with an exponential cutoff to soften the spectrum at higher energies. As the comparison with the low-MeV data shows via Fig. 3.13 the exponential cutoff fits the shape of the measurements better and especially over a much broader range of energies.

With regard to the second power laws suggested by Haasbroek et al. (1997) (shown in green) and Ferreira et al. (2001a) (orange) the parameter $E_b = 9.4$ MeV as introduced by Vogt et al. (2018) (black) becomes significant as it governs at which energy the softening

of the spectrum begins. The source function proposed by Ferreira et al. (2001a) underestimates the softening in the regard that the spectral break sets in at a relatively high energy of about ≈ 30 MeV as shown in Fig. 3.13. Consequently the second power law proposed by Ferreira et al. (2001a) (see Eq. (3.7)) has to be very steep (with an exponent of -6.0) in order to produce a realistic relations between Jovian and GCR electrons. As mentioned above exactly this problem as discussed in further detail by Nndanganeni and Potgieter (2018) motivated to question the accuracy of the approach in the first place. In contrast the approach by Haasbroek et al. (1997) with an even smoother transition between the harder and softer range of the spectrum has to suggest this transition at much lower energies around 1 Mev. As Fig. 3.13 demonstrates this also has an effect on the assumptions of the source strength. In the high-keV range, Ferreira et al. (2001a) therefore estimates much lower intensities than Haasbroek et al. (1997) and although both suggestions in agreement with some of the wide spread spectral data points of the *Pioneer 10*/CPI spectrum, the suggestion by Vogt et al. (2018) serves as an average covering the likely general behaviour in that energy range.

Chapter 4

Stochastic Differential Equations

An Introduction to the mathematical treatment of diffusive processes. Beginning with the history of investigating Brownian motion (Section 4.1), this Chapter will introduce the theory of stochastic integrals (Section 4.2), derive the generalised Fokker-Planck equation (FPE) (Section 4.3) and discuss how to solve the corresponding stochastic differential equations numerically (Section 4.4). These mathematical basics combined with the overview on charged particle propagation theory given by the following Chapter 5 will combined become the background to interpret the results of the stochastic differential equation (SDE) based modelling approach as presented in Chapter 6 and 7.

The discovery of diffusion was a milestone in the history of science. During the Age of Enlightenment the perfect formalism of Newtonian physics supported the view that the world could be fully described by deterministic mathematical equations. Famously the French philosopher Julian Offray de La Mettrie coined the term man machine and promoted a completely mechanistic understanding of nature and life. When Robert Brown observed the irregular motion of pollen in water under a microscope in 1827, this discovery proved that stochastic phenomena existed even within physics and raised the question whether even non predictable processes exist for real: a question (preliminary) answered against the favour of determinism by Born (1926) and the subsequent Copenhagen interpretation of quantum mechanics.

Brown's observations are explained by irregular collisions of the pollen with water molecules (which are according to basic thermodynamics in motion themselves) causing the pollen to change their direction of motion. The average distances between two of such collusion is commonly referred to as the mean free path, a term that will be discussed in detail within Section 5.3. These sequences of undisturbed motion constitute a random walk through the medium which first was mathematically described by Einstein (1905) by means of a so-called Fokker-Planck equation (see Eq. (4.1) in Section 4.1 and especially Section 4.3 for more details). A different approach was used by Langevin (1908) applying Newton's second law of motion and deriving a stochastic equivalent to it now generalised as Langevin equation.

Not least due to this well established mathematical theory (which will be discussed in more detail in the following Sections) most approaches to stochastic or seemingly stochastic phenomena treat them as a modified version of Brownian motion. Apart from the physical ambiguity of generalizing a vast range of different physical processes as diffusion which itself is a generalisation of Brownian motion, the relative mathematical simplicity comes with

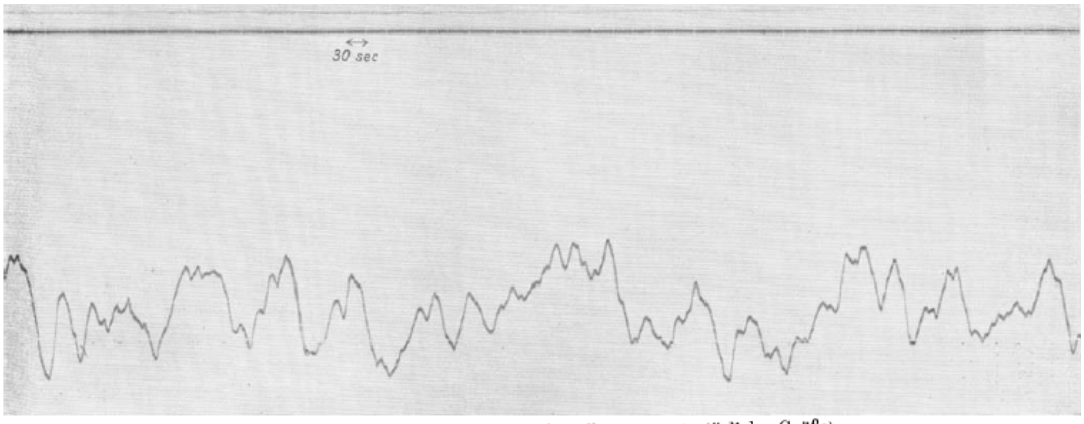

Registrieraufnahme der Brownschen Bewegung (natürliche Größe).
Direktionskraft $2{,}66 \cdot 10^{-9}$ abs. Einh. Trägheitsmoment $6{,}1 \cdot 10^{-6}$ abs. Einh. Abstand Spiegel–Kamera: 86,5 cm.
Zeitmarke: 30 sec $dx = 2$ mm. b) $4 \cdot 10^{-3}$ mm Hg. Temperatur 10° C

Figure 4.1: *An experimental two dimensional visualisation of Brownian motion, taken from Kappler (1931).*

the cost that the both the coefficients describing the physical processes are complicated to derive (see Chapter 5) as well as that the results of a diffusion approach depend heavily on the accuracy of the boundary conditions. This aspect will be discussed in detail in Section 6.3.1 and again in Section 7.2 with respect to the calculation of residence times.

4.1 The Physics of Brownian Motion

The stochastic motion Brown discovered in 1827 has been named Brownian after him and serves as a model for most stochastic processes in physics. Figure 4.1 shows an early experimental visualisation of Brownian motion in two dimensions. The subsequent Sections focused on the mathematical treatment of diffusive processes will discuss the origin of this implementation and the implication of treating diffusive processes as variation of Brownian motion. Therefore first the historical development will be outlined both in order to explain the origin of the terminology as well as to introduce the underlying mathematical concepts on a basic level.

4.1.1 Einstein's Solution

As mentioned above it was Einstein (1905) who initially gave a consistent mathematical theory of diffusive processes. Based on the idea of particles being suspended in a fluid (one may think of ink in water, e.g.) he was able to show that Brownian motion could be expressed by Fourier's heat equation

$$\frac{\partial f}{\partial t} = \kappa \frac{\partial^2 f}{\partial x^2} \tag{4.1}$$

and interpreted by what today is called a random walk governed by the diffusion coefficient κ. On the assumption that all suspended particles move independently from each other and (if we assume the motion as step-wise in time) independently from prior steps, it is possible to define a probability of motion $P(\Delta)$ with $[\Delta, \Delta+d\Delta]$ being the random step size in space within the time dt and $P(\Delta) = P(-\Delta)$. This approach is footed in Boltzmann's transport equation for collusion processes as it takes up the idea of investigating the evolution of the probability distribution $f(x,t)$ rather than the motion of the particles itself. The other similarity lies within the concept of what diffusion is according to this approach: a consequence of the interaction between the diffusing particles and the irregular motion of the molecules within the medium, which in the test case of Brownian motion would be collisions with the water molecules.

The probability density $f(x,t)$ within Eq. (4.1) is defined as the possibility that a particle is located inside the interval $[x, x+dx]$ at the time t. Its temporal evolution relates to the probability of movement $P(\Delta)$ as

$$f(x, t+dt)dx = dx \int_{-\infty}^{\infty} f(x+\Delta)P(\Delta)d\Delta. \tag{4.2}$$

By means of series expansion Einstein (1905) is able to show, that Eqn. 4.1 is a direct consequence of the assumptions. Thereby the right side of Eq. (4.2), precisely $f(x+\Delta, t)$ is expanded by potences of Δ below the integral as Δ can be assumed to be very small

$$f + \frac{\partial f}{\partial t} \cdot dt = f \cdot \int_{-\infty}^{\infty} P(\Delta)d\Delta + \frac{\partial f}{\partial x} \cdot \int_{-\infty}^{\infty} \Delta P(\Delta)d\Delta + \frac{\partial^2 f}{\partial x^2} \cdot \int_{-\infty}^{\infty} \frac{\Delta^2}{2} P(\Delta)d\Delta + ... \tag{4.3}$$

Due to the normalisation and the symmetry of $P(\Delta)$ the first two terms on the right side vanish together with the first term on he left. Eq. (4.3) becomes

$$\frac{\partial f}{\partial t} = \frac{1}{dt} \cdot \frac{\partial^2 f}{\partial x^2} \cdot \int_{-\infty}^{\infty} \frac{\Delta^2}{2} P(\Delta)d\Delta \tag{4.4}$$

which is equivalent to Eq. (4.1). Thereby the integral over the probabilities of movements $P(\Delta)$ is merged into the diffusion coefficient κ. The diffusion coefficient is thereby derived by Einstein (1905) by applying a dynamical equilibrium of particles diffusing through a volume $v = V/n$ with V being the complete volume and n the number of particles

$$\frac{vF}{6\pi\mu r} - \kappa \frac{\partial v}{\partial x} = 0, \tag{4.5}$$

with F being the force on the particle, μ the viscosity and r the radius of the particle. Combined with the ideal gas law Einstein (1905) solves Eq. (4.5) and gets

$$\kappa = \frac{RT}{N} \frac{1}{6\pi\mu r}. \tag{4.6}$$

Based on the notion that each diffusing particle can be interpreted as independent from each other as well as from their previous motion (or steps), Eq. (4.2) constitutes a random walk as visualised by Fig. 4.1: Since the particles are not interacting, each can be looked upon as being at the center of its individual coordinate system $x = 0$ at the time $t = 0$ and Eq. (4.2) therefore describes the step size - most accurate the probability that a particle took a step within the time dt so that it can be found within x and $x + dx$.

The accordingly simplified problem can be solved analytically for a constant diffusion coefficient κ. Applying the random walk interpretation of the probability density distribution f in Eq. (4.2) to Eq. (4.1) Einstein (1905) obtains :

$$f(x, t, x_0) = \frac{1}{\sqrt{4\pi\kappa t}} e^{-(x-x_0)^2/4\kappa t}. \tag{4.7}$$

The probability density distribution of the random walk steps therefore mirrors a Gaussian distribution with the variance $\sigma = \sqrt{2\kappa t}$. As Eq. (4.7) describes the probability density distribution of a (differential) step wise motion according to the assumptions, the variance can be interpreted as the mean square displacement (MSD) of the particles per time step dt:

$$\langle (x(t) - x_0)^2 \rangle = \langle (\Delta x)^2 \rangle = 2\kappa t. \tag{4.8}$$

In diffusion theory (see e.g. Metzler and Klafter, 2000, for an overview) the dependence of the MSD on time is an important measure to describe the "randomness" of the diffusive process. Generalised as $\langle (\Delta x)^2 \rangle \propto t^\alpha$ a value of $\alpha = 1$ as in the case discussed in here (see Eq. (4.8)), indicates that the diffusion satisfies the Markov-property and therefore is "memoryless" i. e. that the individual steps do not depend on the prior positions or past steps at all. This of course was one of the assumptions. Divergent cases are called anomalous diffusion with $\alpha < 1$ describing so-called subdiffusion and $\langle (\Delta x)^\beta \rangle \propto t$ with $1 < \beta < 2$ superdiffusion, respectively. The possibility of a superposition of different diffusion regimes is shown and discussed by Kopp and Shchekinov (2014). The transition to linear dynamics is given by $\alpha = 1$ and $\beta = 2$ for which the diffusion vanishes as the displacement becomes proportional to time with the speed being the proportional factor as given by the well known $x(t) = v(t) \cdot t$.

4.1.2 Langevin's Solution: Stochastic Differential Equations

Alternatively Langevin (1908) applied Newton's second law on the stochastic motion of only one representative particle. As this approach results in an equation equivalent to the one derived by Einstein (1905) but solvable via integration over time, equations of this sort are often referred to as Langevin equations in physics.

Equivalent to the approach of Einstein (1905), the original Langevin equation was derived for an ensemble of particles. In contrast to the very general approach to derive a differential equation of diffusion from basic principles, Langevin (1908) starts with Stokes' law describing the frictional force on a particle at x as:

$$m\frac{d^2x}{dt^2} = -6\pi\mu r\frac{dx}{dt} + \eta \tag{4.9}$$

with μ being the viscosity of the liquid and r the radius of the suspended particles. In order to include the stochastic forces causing the diffusion, the additional term $\eta(t)$ is defined as Gaussian distributed around zero. This term which was first introduced by Langevin (1908) can be interpreted as a stochastic differential and is nowadays often represented by the differential of the Wiener process dW_t as discussed in Section 4.2.2. Equations of these type are so-called Langevin equations a special case of SDEs [1]. To solve Eq. (4.9), it is multiplied by x leading to

$$mx\frac{d^2x}{dt^2} - = -6\pi\mu r x\frac{dx}{dt} + x\eta \tag{4.10}$$

[1] Historically SDEs are a generalised form of Langevin equations and were developed following the heuristic approach by Langevin (1908). For context see e. g. the historical introduction by Lemons and Gythiel (1997). An overview on the history of the mathematical developement of SDE theory is given by Föllmer (2006).

in terms of energy. Applying that

$$\begin{aligned} \frac{dx^2}{dt} &= 2x\frac{dx}{dt} \\ \frac{d^2x^2}{dt^2} &= 2\left(x\frac{d^2x}{dt^2} + \left(\frac{dx}{dt}\right)^2\right) \end{aligned} \tag{4.11}$$

Eq. (4.10) can be rewritten as

$$\frac{m}{2}\frac{d^2x^2}{dt^2} - m\left(\frac{dx}{dt}\right)^2 = -3\pi\mu r\frac{dx^2}{dt} + \eta x. \tag{4.12}$$

In thermal equilibrium, we can deduce the energy for the stochastic motion cause by the force η from the ideal gas model. For an ensemble of N_A particles with N_A being the Avogadro constant, the average kinetic energy is assumed as:

$$\frac{1}{2}m\bar{v}^2 = \frac{RT}{2N_A} \tag{4.13}$$

with T denoting the temperature, R being the ideal gas constant and $\bar{v}$ the average speed caused by η. Since the average value of ηx is more or less equal to zero since the stochastic force η is assumed to be Gaussian distributed, combining Eq. (4.13) with Eq. (4.12), Langevin (1908) finally obtains:

$$\frac{m}{2}\frac{d^2x^2}{dt^2} + 3\pi\mu r\frac{dx^2}{dt} = \frac{RT}{N_A}. \tag{4.14}$$

Solved for $z = dx^2/dt$ the expression above has a solution of the same form as Eq. (4.1) with a value for the diffusion coefficient of

$$\kappa = \frac{RT}{N_A}\frac{1}{6\pi\mu r}, \tag{4.15}$$

a solution previously also found by Einstein (1905) by solving an equation describing the probability density f instead of the motion of an individual (but representative) particle. This illustrates how two differently heuristic approaches to physically describe the same phenomenon (Brownian motion) turned out to be seemingly mathematical equivalent. As Lemons and Gythiel (1997) point out, an unusual mathematical object were forced into existence in the process such as the stochastic differential ηx introducing Gaussian white noise into differentiation and integration theory. The cautious heuristic handling of stochastic forces by Langevin (1908) was set to inspire the new mathematical field of stochastic analysis which generalised the approach and proved it's qualities. The subsequent Section will therefore provide an introduction on the mathematical approach to diffusion in order to make the conditions transparent under which stochastic processes within particle propagation theory can be described.

4.2 The Mathematical Description of Diffusion

As outlined above the development of stochastic analysis was fundamentally driven by the aim to mathematically describe Brownian motion. The existence of a parallel terminology in physics still reflects the fact that an initial, heuristic understanding of stochastic

processes emerged within theoretical physics and then was adapted and systematised by mathematics later on. In order to make the following more accessible, this overview will gradually introduce the concepts necessary for the subsequent Sections loosely based on this historic development rather than in a mathematical fashion. As a result the classic logical top-bottom structure often applied within mathematics is only used to introduce the basic concepts.

4.2.1 The Ito Process

Mathematically stochastic processes like Brownian motion and it's adopted variants are generalised as Ito processes as introduced by Ito (1944). The differential form often referred to as the Ito stochastic differential equation (SDE) is given by

$$dX_t = a(X_t)dt + b(X_t)dW_t, \tag{4.16}$$

is heuristically already introduced above by Eq. (4.9) and following. Thereby the process $X = \{X_t, t \geq 0\}$ itself consists of two deterministic functions $a, b : \mathbb{R} \to \mathbb{R}$, covering the convective and diffusive processes, respectively. The stochastic nature within this formalism is implicated by the second differential, dW, which denotes a Wiener process $W\{W_t, t \geq 0\}$. This bears a problem if the Ito SDE is transformed into it's integral form

$$X_t = X_0 + \int_0^t a_t dt + \int_0^t b_t dW_t, \tag{4.17}$$

with $X_0 = x_0$ indicating the initial value. Only the first integral governing the convective processes $a_t = a(X_t)$ can be defined as the common (Lebesgue or Riemann) integral, whereas the second integral for the diffusive processes $b_t = b(X_t)$ can not. In order to understand how Ito (1944) was able to find a solution the subsequent Section has to examine the qualities of Wiener processes a bit further.

4.2.2 The Wiener Process

The Wiener process was introduced by Norbert Wiener in 1923 as a mathematical description of Brownian motion. Based on the previous work of Bachelier (1900)[2] and Einstein (1905) the Wiener process introduced the random-walk approach correctly into probability theory and served as the basis for the subsequent developments. Most simply put, the Wiener process thereby represents a normalised mathematical model for Brownian motion. The standard Wiener process utilised within this thesis is a Gaussian process, which increments are independent from each other, resulting in the following qualities:

$$W(0) = 0 \text{ with probability } 1, \quad E(W(t)) = 0, \quad \mathrm{Var}(W(t) - W(s)) = t - s \tag{4.18}$$

with $E(W(t)) = 0$ indicating the expectation value and $\mathrm{Var}(W(t) - W(s))$ for all times $0 \leq s \leq t$. Equivalent to the solution of Einstein (1905) given by Eq. (4.7), the more general analytical solution of the Wiener process is given by

$$f(s, x; t, y) = \frac{1}{\sqrt{2\pi(t-s)}} \exp\left(-\frac{(y-x)^2}{2(t-s)}\right) \tag{4.19}$$

[2] See Bachelier et al. (2011) for an English translation and commentary

according to Kloeden and Platen (2011) with y denoting the spatial position at the time t and x the spatial position at the time s. The normalization of the Wiener process thereby can be illustrated by dividing the unit interval $[0, 1]$ into N subintervals of equal length $\Delta t = 1/N$ and therefore defining the resulting random walk steps S, depending on the corresponding time steps t_n numbered by $0 \leq n \leq N$) as

$$S_n(t) = (\zeta_1 + \zeta_2 + ...\zeta_n)\sqrt{\Delta t}, \quad \text{with } S_n(t) = S(t_n) \tag{4.20}$$

with $\zeta_1, \zeta_2...\zeta_n$ being Gaussian distributed random variables. Taking the time increment into account via its square root $\sqrt{\Delta t}$ reflects the the normalization of the Variance $\mathrm{Var}(W(1)) = 1$ as following Eq. (4.18) as a direct consequence. For a detailed discussion of the further mathematical properties of Wiener processes see e. g. Kloeden and Platen (2011), which also have provided the basics for this overview.

Applying the limes $N = 1/\Delta t \to \infty$ to Eq. (4.20) as the representation of a Wiener process conclusively leads to the definition of the differential dW_t as it appears in Eq. (4.16):

$$dW_t = \zeta\sqrt{dt}. \tag{4.21}$$

As mentioned above, the issue how to integrate such a stochastic differential constituted a problem. Although the trajectories of Wiener processes (or their integrands respectively) are continuous their integral is not defined within common integration theory because their variance is not finite for $t \to \infty$.

4.2.3 The Concept of Stochastic Analysis

Although a deeper analysis of the mathematical details is way beyond the scope of this work, it is possible to qualitatively outline how Ito (1944) was able to avoid the problem of an infinite variance. As already discussed above in Section 4.1 the dependence of the MSD within Brownian motion and the Wiener process, respectively, indicates that the process is "memoryless". This means that the state of a system governed by such process at the time t does not depend on its previous behaviour at a time $t_0 < t$. The previous state thereby is indicated by the initial value X_0 as shown by the notation of the integral SDE given by Eq. (4.17) . Therefore it can be concluded that the variance of the trajectories of the Wiener process is finite as is the integration time t. In mathematical terms: The Riemann sums according to integration theory are martingales under these conditions as the Wiener process itself[3].

As a consequence Ito (1944) applied the concept of adaptive integrands. The basic principle is already indicated by the presence of the intial value X_0 in Eq. (4.17). As explained by e.g. Schachermayer and Teichmann (2007), amongst others, the solution was to not define the integral $\int \xi dW_t(\omega)$ path-wise for each stochastic element ω and each integrand $(\xi)_{t\geq 0}$ individually, but globally for the whole probability space Ω. As mentioned above, the Brownian motion which herein is represented by the Wiener process $(W_{t_0})_{0\leq t_0\leq t}$ is memoryless and therefore does not depend on previous states as does the integrand ξ_t neither. This limits the possible variance leading to the conclusion that the Riemann sums have the same martingale qualities as the Brownian motion itself. The solution therefore

[3]Martingales are define as stochastic processes with conditional expectation values, which can be considered fair, i.e. the expectation value for each subprocess is zero $\forall k \in \mathbb{N} : E(X_k) = 0$ In case of the Wiener process the process is symmetrical around zero and the conditional value is the initial value. Therefore the Wiener process is an adaptive martingale.

could be simply put as follows: Instead of solving the integral SDE according to Eq. (4.17) for $t \to \infty$ for one global integrand ξ_t, the integrands are defined to evolve according to the temporal evolution of the integral. Thus the integrand ξ_n is valid for the differential time interval dt_n only (corresponding to the steps n of the random walk defined by Eq. (4.20)) and then adapts accordingly. Instead of solving $\int \xi dW_t(\omega)$ for the whole integration time t, it is solved step-wise. As Ito (1944) could prove, the adaptive integrands ξ_n thereby could be of infinite variance as long as they only depend on the Wiener process $dW_t(\omega)$ until $t = t_n$.

Another strategy was applied by Doeblin (1940)[4] who focused on the differential SDE Eq. (4.16). By means of temporal transformation, he could reduce general diffusion processes to the case of Brownian motion which herein is represented by the Wiener process $X_t = W_t$ and derived a stochastic version of the chain rule, nowadays usually referred to as the Ito-Doeblin Lemma (see e.g. Kloeden and Platen, 2011)

$$dY_t = \left(\frac{\partial U}{\partial t}(t, X_t) + \frac{1}{2} b^2(X_t) \frac{\partial^2 U}{\partial x^2}(t, X_t) \right) dt + \frac{\partial U}{\partial x}(t, X_t) dX_t \tag{4.22}$$

for $Y_t(\omega) = U(t, X_t(\omega))$ being a stochastic process with continuous second order partial derivatives. In the case of U being linear (i.e. no stochastic motion and therefore no diffusion) the second order derivative $\partial^2 U / \partial x^2 = 0$ would reduce Eq. (4.22) to the usual chain rule.

4.3 Fokker Planck Equations

Whereas the heuristic approach of Langevin (1908) lead to the development of stochastic analysis within mathematics, the approach of Einstein (1905) and his probability density equation was subsequently generalised as Fokker-Planck type equations (due to the studies of Fokker, 1914; Planck, 1917) and sometimes are referred to as Kolmogorov equations in mathematics. As already mentioned above, the idea to favor the evolution of a representative sample over tracing the behaviour of a large number of individual (and mostly coupled) particles originates in thermodynamics, most prominent in its statistical description associated to the works of Ludwig Boltzmann. Heuristically used in Section 4.1.1 this concept is generalised in the following. Thereby the phase space density f is defined as the probability that a particle is present in a given part of the phase space. The integration over the whole phase therefore leads to the normalization

$$\int_{-\infty}^{\infty} \int_{-\infty}^{\infty} f(\vec{x}, \vec{v}, t) d^3x d^3v = 1 \tag{4.23}$$

whereas the velocity coordinate(s) are often substituted by the momentum $\vec{p}$ or the energy E in order to reduce the number of variables as done within the approach used here. As indicated by Eq. (4.23) the normalization of the probability density to unity demands the result to be transformed in order to represent a physical quantity such as a counting rate or a differential intensity. This problem, associated to the interpretation of the mathematical results itself, will be discussed in Secs. 6.2 and 6.3.1 and leads to the new approach to estimate the residence times in Section 7.2.

[4] See (e.g. Lindvall, 1991; Bru and Yor, 2002) for more information on Doeblin and how his contribution was discovered in the year 2000, 60 years after his suicide during WW II.

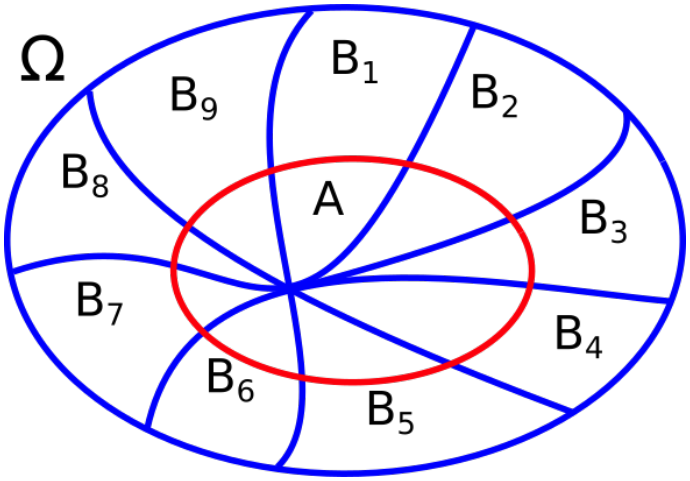

Figure 4.2: *Topology qf the deterministic (A) and stochastic (B_i) parameter Within a FPE, after Gardiner (2009)*

4.3.1 Derivation

As shown by e.g. Chandrasekhar (1943) and Gardiner (2009) the general FPE can be derived from the Chapmann-Kolmogorov equation by means of Taylor expansion. In the following this will be outlined applying the nomenclature by Kloeden and Platen (2011). In order to derive this relation, first consider the integral formulation of the Chapman-Kolmogorov equation usually referred to as

$$f(s,x;t,y) = \int f(s,x;\tau,z)f(\tau,z;t,y)dz \tag{4.24}$$

in a different notation derived from the approach by Einstein (1905) who expressed stochastic processes with respect to their transition probability $\Phi(y-\Delta y, \Delta y)$ describing the probability to transit from $(y-\Delta y)$ to y:

$$f(y,t) = \int f(y-\Delta y, t-\Delta t)\Phi(y-\Delta y,\Delta y)d(\Delta y). \tag{4.25}$$

Both expressions Eq. (4.24) and 4.25 describe the transition from $(s,x) = (t-\Delta t, y-\Delta y)$ to (t,y) via a Markov type process. Whereas Eq. (4.24) expresses this via a third step in between denoted as (τ,z) the latter notation by Eq. (4.25) explicitly takes into account that only the last position influences the state of a random walk as discussed above in Section 4.1 via Eq. (4.2). The random walk steps in space and time are thereby defined as $\Delta y = y - x$ and $\Delta t = t - s$. Under the assumption that y is continuous and only small steps take place (in other words: Φ is small for large values of Δy) the Taylor expansion of Eq. (4.25) reads as

$$\begin{aligned} f(y,t) \approx \int f(y,t)\Phi(y,\Delta y) - \Delta t\frac{\partial}{\partial t}f(y,t)\Phi(y,\Delta y) - \Delta y_i\frac{\partial}{\partial y_i}f(y,t)\Phi(y,\Delta y) \\ + \frac{1}{2}\Delta y_i\Delta y_j\frac{\partial^2}{\partial y_i\partial y_j}f(y,t)\Phi(y,\Delta y)d(\Delta y), \end{aligned} \tag{4.26}$$

utilising the Einstein summation convention. Since $f(y,t)$ does not depend on the integrand $d(\Delta y)$, the integration of Eq. (4.26) simplifies the expression significantly. With the

normalization that $\int \Phi(y, \Delta y) d(\Delta y) = 1$ we obtain utilizing the sum convention

$$\frac{\partial p}{\partial t} = -\frac{\partial}{\partial y_i} a_i p + \frac{1}{2} \frac{\partial^2}{\partial y_i \partial y_j} b_{ij} p \tag{4.27}$$

as the most general form of a FPE, also referred to as the diffusion equation. The parameter a_i and b_{ij} thereby are defined as:

$$\begin{aligned} a_i &= \frac{1}{\Delta t} \int \Delta y_i \Phi d(\Delta y) \\ b_{ij} &= \frac{1}{\Delta t} \int \Delta y_i \Delta y_j \Phi d(\Delta y). \end{aligned} \tag{4.28}$$

with a topology as sketched by Fig. 4.2, demonstrating why the first term depending on a_i is referred to as the linear and the second term as the stochastic one. For the case of a one dimensional space as utilised within this Chapter, the parameters given via Eq. (4.28) reduce to

$$\begin{aligned} a(s, x) &= \lim_{t \to s} \frac{1}{t - s} \int (y - x) f(s, x; t, y) dy \\ b^2(s, x) &= \lim_{t \to s} \frac{1}{t - s} \int (y - x)^2 f(s, x; t, y) dy. \end{aligned} \tag{4.29}$$

according to Kloeden and Platen (2011), utilizing the same parameter definitions as the discussion of the Wiener process in Section 4.2. With respect to its origin in physics FPEs whose parameters satisfy these conditions are called diffusion equations. Thereby $\Delta t = t - s$ and $\Delta y = y - x$. The transitions probability Φ between $f(y, t)$ and $f(s, x)$ is transformed back, too, reversing the nomenclature change between Eqns. 4.24 and 4.25, applied in order to make the Taylor expansion more comprehensible. The quantity $a(s, x)$ in that regard is referred to as the linear (i.e. drift) term whereas $b(s, x)$ denotes the diffusion coefficient at the time s and the position x and therefore governs the stochastic processes.

4.4 Numerical Implementation

Having discussed the concept of the probability density function and the Wiener process and derived by that means the general Fokker Planck equation from fundamental stochastics, the subsequent Section will focus on how to apply the SDE method in order to solve Fokker Planck type equations. Therefore, the possibility of time-backward and time-forward integration will be discussed and derived. This possibility to choose the direction of time depending on the scientific goal is one of the advantages of SDE modelling in regard to finite-difference schemes. As noted by Kopp et al. (2012) second order finite-difference schemes as demanded by the TPE become unstable for negative time steps if applied to parabolic differential equations. Finally the Euler-Maruyama-scheme of solving a set of SDEs will be presented alongside a discussion how this results into a random walk through the phase-space.

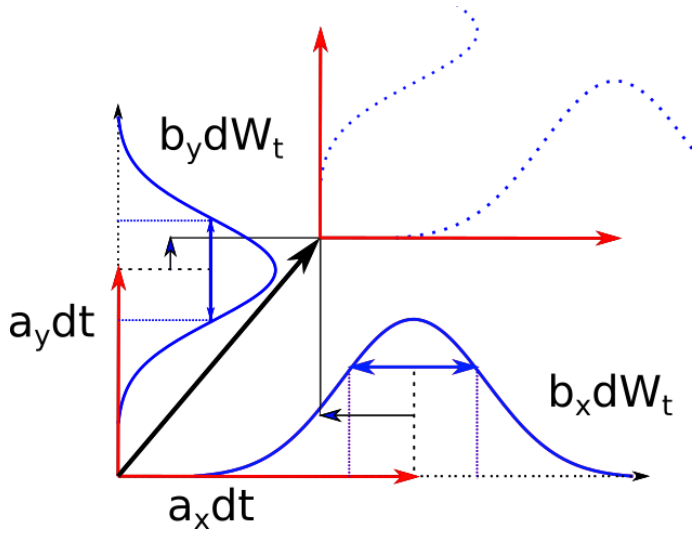

Figure 4.3: *Visualisation of the random walk as performed by a SDE modelling approach. The colour coding follows the same convention as used in Fig. 4.2. The deterministic parts of the random walk step are indicated in red whereas the possible stochastic parts of the step are indicated by the blue Gaussians. The resulting step is shown by its two dimensional vector representation in black.*

4.4.1 Time-Forward and Time-Backward Integration

Taking into account the transition density of the Wiener process given by by Eq. (4.19), the solution is a smooth function depending on two temporal variables $t > s$. Therefore the choice of the initial variable allows for a time-forward and time-backward treatment of corresponding processes. The evaluation of the partial derivatives of Eq. (4.19) lead to the respective differential equations for the transition probabilities p

$$\frac{\partial p}{\partial t} - \frac{1}{2}\frac{\partial^2 p}{\partial y^2} = 0, \quad (s, x) \text{ fixed}, \tag{4.30}$$

for the time-forward and

$$\frac{\partial p}{\partial s} + \frac{1}{2}\frac{\partial^2 p}{\partial x^2} = 0, \quad (t, y) \text{ fixed}, \tag{4.31}$$

for the time-backward case. With that regard it is possible to identify Eq. (4.27) as the time-forward equation which reduces to Eq. (4.30) in case of a standard Wiener process without a drift component. Equivalently the time-backward variant which is referred to as the Kolmogorov backward equation can be derived as detailed by e.g. Kloeden and Platen (2011). Note that due to the inverse direction, the differential operator in the time-backward case is the adjoint one to the time-forward case as pointed out by Kopp et al. (2012). Therefore, written in one dimension the Kolmogorov time-backward equation reads as

$$\frac{\partial f}{\partial s} + a(s, x)\frac{\partial f}{\partial x} + \frac{1}{2}b^2(s, x)\frac{\partial^2 f}{\partial x^2} = 0, \quad (t, y) \text{ fixed} \tag{4.32}$$

in contrast to the Kolmogorov time-forward equation which is the common FPE:

$$\frac{\partial f}{\partial t} + \frac{\partial}{\partial y}\{\tilde{a}(t, y)f\} - \frac{1}{2}\frac{\partial^2}{\partial y^2}\{\tilde{b}^2(t, y)f\} = 0, \quad (s, x) \text{ fixed}. \tag{4.33}$$

Note the convention to refer to the time-marching coordinate as s for the backward and as the usual t for the time-forward case. Likewise the spatial coordinates are given by x for the backward and y for the time-forward case: A convention implicitly introduced by the definition of the Wiener process and its solution via Eqs. (4.18) and (4.19). As pointed out by e.g. Strauss and Effenberger (2017) the main difference between the time-backward and time-forward equations is the explicit vs. implicit formulation of the coefficients, both for drift and diffusion. Furthermore in most cases $a \neq \tilde{a}$ and $b^2 \neq \tilde{b}^2$, a relation discussed in depth by Kopp et al. (2012) and Bobik et al. (2016). The quantity b or b_{ij} in the higher dimensional case (see Eq. (4.27) for reference) is sometimes called the volatility matrix in mathematical texts to distinguish it from the diffusion matrix or tensor given by

$$C_{ij}(x_i, s) = (b_{ij}(x_i, s) \cdot b_{ji}(x_i, s)) \quad \text{or } C = BB^T, \tag{4.34}$$

according to Strauss and Effenberger (2017). As a consequence the corresponding SDE formulation

$$dx_i = a_i(x_i, s)ds + \sum_j b_{ij}(x_i, s)dW_i(s) \tag{4.35}$$

as already introduced in detail above (see Eq. (4.16) in Section 4.2) can be easily derived from the FPEs given by Eqs. (4.32) and (4.33). Thereby b_{ij} is given by the square root of C_{ij}. Although possibly not easy to obtain for higher dimensions, it is always possible as pointed out by e.g. Strauss and Effenberger (2017) as C_{ij} is a positive finite tensor (Gardiner, 2009) and usually symmetric as shown by Kopp et al. (2012). Furthermore the n-dimensional probability density function (PDF) can be thereby transformed to a set of $n-1$ two-dimensional SDEs which would be more easily solve-able. A detailed overview on how this has been applied for the present study will be given in Section 6.1.1.

4.4.2 The Euler-Maruyama-Scheme

In order to apply the time-backward integration approach to solve the TPE the Euler-Maruyama scheme is used by this thesis. This method as developed by Maruyama (1955) is generally assumed to be the most simple one to solve a set of SDEs. As we aim for an effective solver which is able to exploit the qualities of parallelised computing on GPUs (see Dunzlaff et al., 2015) this turns out to be a great advantage due to the limited computing capacities. Essentially the Euler-Maruyama scheme is a time stochastic process which utilises a finite time increment Δs in order to solve Eq. (4.16) iteratively.

As we aim for simplicity and efficiently the time increment Δs is implemented as constant. The question how to choose the right value for Δs in order to avoid influence on the simulation results will be discussed subsequently in Section 6.4. Therefore we can define the iterative scheme

$$X_{n+1} = X_n + a(X_n)ds + b(X_n)\Delta W_n \tag{4.36}$$

via assuming

$$X_n = X(s_n) \tag{4.37}$$

as the solution after $n = 0, 1, 2...N-1$ iterations at the time

$$s_n = n \cdot \Delta s + s_0. \tag{4.38}$$

The time interval of simulation (or as referred to subsequently: the simulation time) thereby is discretised as given by Eq. (4.38) for $s \in [s_0, T_N]$. The notion of the Wiener process as present in Eq. (4.36) is follows equivalently as

$$\Delta W_n = W(s_{n+1}) - W(s_n). \tag{4.39}$$

As discussed by Dunzlaff et al. (2015) the stochastic features of the Wiener process are implemented as

$$\Delta W_n = \eta_n \sqrt{\Delta s} \quad \text{with} \quad \eta_n \in N(0,1) \tag{4.40}$$

following the definition given by Eq. (4.18) with $N(0,1)$ as a random number drawn from a standard Gaussian distribution, i.e. with a mean of zero and unit variance. How the iterative steps as defined by Eq. (4.36) form the resulting phase-space trajectories is illustrated by Fig. 4.3. Reduced to the x and y spatial components the bold arrow indicates the step of the random walk. In each dimension (which correspond to the individual SDEs) the change in position is consists of a convective step (colour coded in red) and a diffusive step (blue) as indicated by convective $a(X_n)dt$ and diffusive term $b(X_n)\Delta W_n$ in Eq. (4.36). As the red arrows along the axis of the coordinate system illustrate, the convective steps can be given with a defined length. This is possible because both the differential dt refers to a defined quantity Δs as well as the coefficients $a_{x/y}$. Two Gaussian distributions given in blue indicate the diffusive terms governed by means of two Wiener processes dW_t and scaled by the coefficients $b_{X/y}$. The double-headed arrows in blue illustrate the variance of the resulting distribution whereas the realised stochastic part of the random walk step is given by a black arrow. This leads on the x-axis to a reduced and on the y-axis to an increased step size. The resulting positions form the vector parallelogram which constitutes the resulting step in the 2D phase-space as indicated by the bold arrow. The hinted coordinate system at the head thereby of the step vector indicates the iterative nature of the random walk. This recursive scheme is be repeated until a spatial or timely boundary t_{end} is reached. For a detailed discussion on handling boundary condition see e. g. Strauss and Effenberger (2017) and Section 6.3. Overviews concerning the choice of the time increment Δs and the time boundary T_{end} will follow in Section 6.4 of this thesis.

4.4.3 Interpretation

Whereas Fig. 4.3 illustrates the particular steps of the random walk, the convergence of the resulting phase-space trajectories as well as of the method itself yet has to be discussed.According to Kloeden and Platen (2011) it is usual to differentiate between path-wise convergence and approximations of functionals of the Ito process, in case of the TPE the probability density function and the differential intensity derived thereafter. Therefore as discussed in further detail in Secs. 6.2, only the whole ensemble of phase space trajectories as represented by the path-wise solutions contains meaningful physical information but not the path-wise solutions individually.

Chapter 5

Charged Particle Transport

An introduction to the main concepts of charged particle transport theory as they are of importance to this thesis. After a general overview on charged particle motion in magnetic fields (Section 5.1) and a discussion on drift effects (Section 5.2), a focus will be set on outlining how mean free paths to describe the diffusive motion (Section 5.3) can be derived from turbulence theory concerning the fluctuations within the HMF. Equally detailed the concept of adiabatic energy changes will be discussed and a sketch of their theoretical derivation will be given in Section 5.4, as they will become crucial to interpret the results of this thesis later on. The Chapter finishes with the derivation of the transport equation (Section 5.5) and the discussion of its qualities and limitations. These physical basics combined with the overview on SDEs given by the previous Chapter 4 will combined become the background to interpret the results of the modelling approach as presented in Chapter 6 and 7.

THE history of charged particle transport research regarding what today is called Heliospherical and extraterrestrical physics can be traced back to Birkeland (1908), who first explained the aurora borealis as being caused by the interaction of charged particles with the Earths magnetic field. The fact that the inflow of charged particles, the so-called Galactic cosmic rays (GCRs) into both the Earth's atmosphere and magnetosphere, respectively, originated not from the surface of the Earth but from space was subsequently discovered by Hess (1912).

With the beginning of the space era and the first *in situ* measurements the behaviour of charged particles in and further outside the Earths magnetosphere gained renewed energy, a major discovery being the radiation belts by van Allen and Frank (1959) due to the *Explorer 1* and *Explorer 3* missions. Utilizing the first *in situ* measurement of the Solar wind plasma and the HMF, Parker (1965) proposed a transport equation (TPE) describing isotropic charged particle populations within the Heliosphere under stable conditions.

Since this work focuses on a modelling approach utilizing this TPE according to Parker (1965), the following Sections will be limited to the physical processes incorporated into this specific approach. Subsequently the derivation of the TPE itself will be discussed (see Section 5.5) as well as a detailed review the assumptions made by Parker (1965). The closing Section will give an overview on the restrictions of the TPE and briefly point out alternative formulations of charged particle transport.

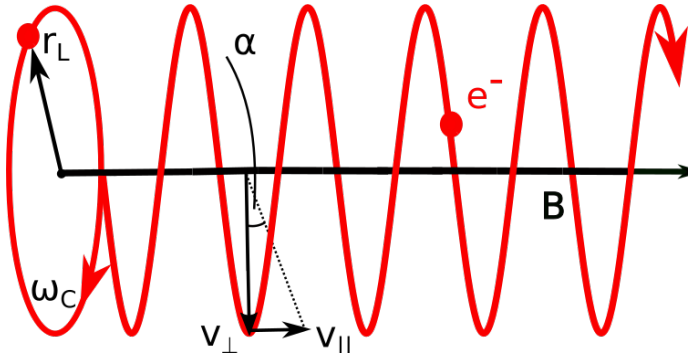

Figure 5.1: *Sketch on how charged particles behaviour is determined by the magnetic field due to the Lorentz force. On the left side see the gyration with the Larmour radius r_L around the guiding center at the radius's footpoint. With a velocity component $v_{\parallel}$ parallel to the magnetic field present, the angle between this component and the direction perpendicular to the field (given here by the component $v_{\perp}$) is defined as the pitch angle α.*

5.1 General Considerations

The most peculiar quality of the interplanetary space concerning the understanding of particle propagation is the very low density of particles (i.e. the Solar wind as the most abundant population shows $\approx 6/\mathrm{cm}^3$ near Earth). As a consequence the interaction between charged particles and the HMF becomes the determining factor since particle collisions can be expected to be negligible. In the idealised model case of the Parker field as described in Section 2.4.1 the magnetic field is not affected by the energy density of the moving particles nor by turbulence in itself and the particle propagation can be entirely explained by gyration around the magnetic field lines governed by the Lorentz force $\vec{F}_L$. The Lorentz force is derived from Newton second law of motion $d\vec{F} = d\vec{p}/dt$ and reads as

$$\vec{F}_L = m\frac{d\vec{v}}{dt} = q(\vec{E} + \vec{v} \times \vec{B}) \tag{5.1}$$

for non-relativistic particles with the charged particle's mass m, the particle's velocity $\vec{v}$, the particle's charge p, the electric field $\vec{E}$ and the magnetic field $\vec{B}$. In a pure magnetic field, the electric Field component would equal zero. Applying this to a homogeneous magnetic field B_z orientated along the z-axis $\vec{B}_z = B_z\vec{e}_z$ as shown in Fig. 5.1 the free spatial components read

$$\begin{aligned} m\frac{dv_x}{dt} &= qBv_y \\ m\frac{dv_y}{dt} &= -qBv_x \end{aligned} \tag{5.2}$$

and can be separated in order to solve them as

$$\begin{aligned} \frac{d^2v_x}{dt^2} &= \frac{qB}{m}\frac{dv_y}{dt} = -\left(\frac{qB}{m}\right)^2 v_x \\ \frac{d^2v_y}{dt^2} &= -\frac{qB}{m}\frac{dv_x}{dt} = -\left(\frac{qB}{m}\right)^2 v_y. \end{aligned} \tag{5.3}$$

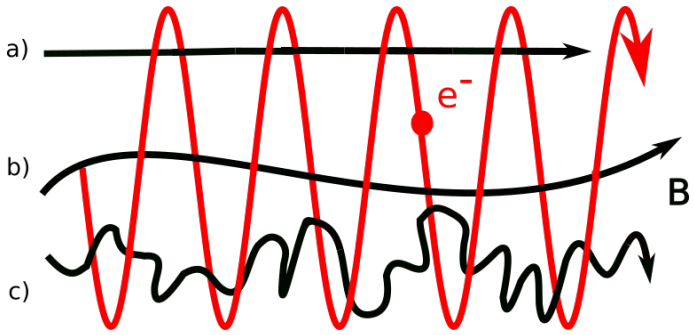

Figure 5.2: *Schematic visualisation of the different intensities of possible fluctuations of the HMF. a) shows the ideal stable conditions, whereas b) shows regular fluctuations which can be covered by an average field approach. c) finally covers the case within the Heliosphere which leads to the necessity to incorporate a diffusion based transport model.*

As discussed by e.g. Kallenrode (2004) Eqs. (5.3) can be solved by using the approach to solve an harmonic oscillator $v_i = v_{0,i}e^{i\omega t}$ with an cyclotron frequency of

$$\omega_C = \frac{|q|B}{m}. \tag{5.4}$$

Therefore the spatial components of the trajectory as well as the components of the particle velocity are given as

$$\begin{aligned} x(t) &= \pm r_L \sin(\omega_c t + \phi_x) \quad \rightarrow \quad v_x(t) = \pm r_L \omega_C \cos(\omega_c t + \phi_x) \\ y(t) &= -r_L \cos(\omega_c t + \phi_y) \quad \rightarrow \quad v_y(t) = r_L \omega_C \sin(\omega_c t + \phi_y) \end{aligned} \tag{5.5}$$

and the particle velocity perpendicular to the magnetic field becomes

$$v_\perp = \sqrt{v_x^2 + v_y^2} = r_L \omega_C. \tag{5.6}$$

Therefore it is possible to now derive the radius of the gyration shown on the left in Fig. 5.1, the so-called Larmor radius, as

$$r_L = \frac{v_\perp}{\omega_c} = \frac{m v_\perp}{|q|B}. \tag{5.7}$$

A different way to express the Larmor radius is via the rigidity P as

$$r_L = \frac{P}{B} \tag{5.8}$$

with the rigidity being the ratio between the perpendicular momentum and the charge

$$P = \frac{p_\perp}{|q|}. \tag{5.9}$$

If the initial velocity of the particle has a component parallel to the magnetic field, the gyration performs a helical trajectory around the magnetic field line as it is sketched in Fig. 5.1. The radius of the spiral being reciprocally dependent on the (possibly) changing magnetic field. The relation between the velocity component parallel and perpendicular to the magnetic field relates to the so-called pitch angle α as

$$\frac{v_\perp}{v_\parallel} = \tan\alpha. \tag{5.10}$$

and offers third possibility to estimate the Larmor radius by means of the pitch angle cosine

$$\mu = \cos\alpha \tag{5.11}$$

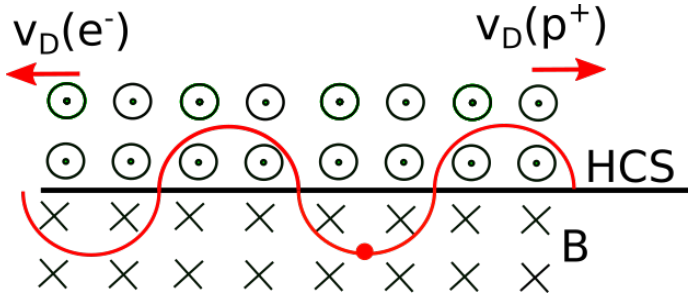

Figure 5.3: *Sketch of the HMF along the Heliospheric current sheet (HCS). $\vec{v}_D$ indicate the direction of the resulting drift for electrons e^- and protons p^+ along the gyrating trajectory in red. The different directions are caused by the opposing charge-signs of p in front of the vector product in Eq. (5.1).*

as derived by e.g. Longair (1992)

$$r_L = \frac{m|\vec{v}|\sqrt{1-\mu^2}}{|q|B}. \tag{5.12}$$

Figure 5.1 shows the relations between quantities. Thereby the center of the Larmor radius is often referred to the guiding center of the particle. This concept is especially useful to describe how to handle the irregularities in the HMF as its fluctuations make it necessary to expand the simplistic approach to handle charged particle propagation above. As exemplified in Fig. 5.2 the fluctuations of magnetic fields can be roughly divided into three cases according to e.g. Kallenrode (2004)

a) The magnetic field only varies very weakly or not at all in scales of the of gyrations. Therefore the the guiding center approach can be applied. An example for such magnetic fields are the Earth's radiation belts due to the field's magnitude.

b) The variation of the magnetic field is significant and not irregular. Therefore the particle propagation can be described by integration of the equation of motion.

c) The fluctuations are irregular and significant in scales of the gyration. The particle motion can not the described by an average magnetic field but has to include the influence of scattering by the field's fluctuations.

The third case is the one applicable to the HMF. Since the scattering by the fields fluctuations is a stochastic process, charged particle propagation in the HMF can only be described via ensembles of particles. The scattering itself is often estimated as diffusion-like process with several parameters derived from Heliospheric plasma physics in order to restrain the approach.

5.2 Drift

The physical mechanism of the neutral sheet drift as discussed by e.g. Kallenrode (2004) is shown in Fig. 5.3. Due to the changing polarity of the HMF, the gyration around the magnetic field lines is reversed in case the particle crosses the HCS. This effect is notably

important for the modulation of GCRs[1]. As argued by Ferreira (2002) drift effects can be neglected for electrons below $\sim$ 10 MeV. Although more recent studies on Galactic electrons include drift effects (see e.g. Potgieter and Nndanganeni, 2013), this notion holds true for electrons of Jovian origin even for higher energies, since diffusion and convection dominate the transport process on the relative small distances between the Jovian source and possible observers in the inner Heliosphere. Therefore in agreement with Dunzlaff et al. (2015) drift effects are neglected within this thesis.

5.3 Diffusion

Whereas the mathematical treatment of diffusion has been introduced and discussed in Chapter 4 this Section aims to show how these concept can be and are applied to the stochastic processes within charged particle transport. As mentioned above the particle density within the Heliosphere is very low, thus the probability of particle on particle or Coulomb scattering is almost zero. Instead, particles are scattered due to interaction with the fluctuations of the HMF. Nevertheless the concept of the mean free path λ, introduced implicitly by means of the step size of the random walk in Section 4.2.2 is the relevant concept to describe the diffusive process. As discussed in Section 4.1, the concept of diffusion is derived from Brownian motion which originally describes the erratic motion of small biological particles like pollen on a water surface due to its interaction with colliding water molecules. The approach to define the diffusive processes governing charged particle transport is quite similar: The step size of the random walk is governed by the particles' mean free paths λ which are defined by the mean distance they would propagate between two scattering incidents. A more detailed discussion on how to define the mean free path is given in the following Sec, 5.3.1.

The diffusive processes within charged particle transport are to described by the concept of the mean free path particularly because the effect of charged particle diffusion is limited to the individual particles themselves rather than influencing the IPM[2]. A contrasting example would be the dissolution of one fluid into another as used by Einstein (1905) to illustrate how to derive a concept of diffusion based on the diffusion coefficient (see Section 4.1.1). In this case the main effect is not the propagation of individual particles but the increasing intermingling of the two fluids.

Whereas heuristic approaches to mean free paths lead to simulation setups capable of providing reliable results, the theoretic derivation still is an ongoing topic of research. The turbulence within the Heliospheric magnetic field interacts with the particles due to their electric charge, leading to separate mean free paths parallel ($\lambda_{\parallel}$) and perpendicular ($\lambda_{\perp}$) to the nominal field lines. Furthermore as discussed above in Section 5.1 the conditions within the HMF are mostly unique and can not the reproduced by laboratory experiments, most prominent the extreme low magnetic flux and particle density. Therefore in the following first a brief introduction to scatter theories is given before outlining the major concepts of turbulence within the HMF. Finally some recent estimation of the electron mean free paths are discussed.

[1] For a review on drift effects see e.g. Potgieter (2008)

[2] For a more in depth discussion see e.g. Kallenrode (2004)

5.3.1 Kinetic and Scatter Theory

The most basic equation of motion in kinetic theory is the Boltzmann equation which is a direct consequence of continuity in the velocity phase space. Assuming the acceleration $\vec{a}$ being independent from the velocity $\vec{v}$ the Boltzmann equation is given by

$$\frac{\partial f}{\partial t} + \vec{v} \cdot \nabla f + \frac{\vec{F}}{m} \cdot \frac{\partial f}{\partial \vec{v}} = \left(\frac{\partial f}{\partial t} \right)_{collision} . \tag{5.13}$$

In case of a collisionless motion, the right term is zero and the solution is an Maxwell distribution. If the Lorentz force as defined by Eq. (5.1) is inserted into the Boltzmann equation, it is called the Vlasov equation (Vlasov, 1968) and Eq. (5.13) subsequently reads as

$$\frac{\partial f}{\partial t} + \vec{v} \cdot \nabla f + \frac{q}{m} \left(\vec{E} + \vec{v} \times \vec{B} \right) \cdot \frac{\partial f}{\partial \vec{v}} = 0 \tag{5.14}$$

and forms the fundamental equation of motion in a phase space dominated by electromagnetic forces. In order to understand how Eq. (5.14) is related to scatter theory one has to include the quasi linear theory (QLT) by Jokipii (1966) which estimates the variations within the HMF and their influence on charged particles. Particularly, the QLT only considers wave-particle interactions of the first order. Since all higher terms of disturbance are assumed to be weak, the QLT can only describe interaction of low turbulence. Therefore the QLT explains the scattering of particles in magnetic field fluctuations by means of changes in the particles pitch-angle as discussed by e.g. Dröge (2003). An assumption that would cause particles with large Larmor radii only respond to large fluctuations and vice versa. As discussed by e.g. Kallenrode (2004) this means, that the waves within the HMF generated by the particle population interact with it in a self regulatory manner: The effect these waves have onto the particle population lead to a behaviour which reduces the generation of new waves. Including these first order terms of disturbance into the Vlasov equation as given by Eq. (5.14) leads to a reformulation which includes a collision term of the nature as given by the Boltzmann equation in Eq. (5.13):

$$\frac{\partial f_0}{\partial t} + \vec{v} \cdot \nabla f_0 + \frac{q}{m} \vec{v} \times \vec{B_0} \cdot \frac{\partial F_0}{\partial \vec{v}} = -\frac{q}{m} \left\langle (\vec{E_1} + \vec{v} \times \vec{b}) \cdot \frac{\partial f_1}{\partial \vec{v}} \right\rangle . \tag{5.15}$$

As transparent in Eq. (5.15) the right hand term consists of the non-vanishing disturbance terms ($\vec{E_1}$ and $\vec{b}$, respectively) caused by the turbulence within the HMF. This is mathematically consistent with the notion above, that the turbulent nature of the HMF causes the stochastic (diffusive) processes of charged particle transport. Within this framework it is important to note that the approach assumes that the fluctuations are separable from the average behaviour of the HMF. In contrast to the approach of the Boltzmann equation which describes particle-particle interaction within kinetic theory, Eq. (5.15) describes interactions between particles and the variations of the electric and magnetic fields $\vec{E_1}$ and $\vec{b}$, respectively, which can be interpreted as wave-particle interactions. Therefore it is necessary to discuss the nature of these interactions in more detail. As discussed by Dunzlaff (2012) explicitly likewise for Jovian electrons, these wave-particle interactions are interactions in the pitch-angle space. This diffusion in the pitch-angle space can be related to spatial diffusion as shown by Jokipii (1966),Earl (1974) and Bieber et al. (1994) and discussed in detail by e.g. Shalchi (2009) via

$$\kappa_{\parallel} = \frac{v^2}{8} \int_{-1}^{1} d\mu \frac{(1-\mu^2)^2}{D_{\mu\mu}} \tag{5.16}$$

with $D_{\mu\mu}$ being the pitch-angle diffusion coefficient[3]. The result refers to Eq. (5.10) and (5.11) in the way that small changes in the pitch-angle (cosine) $d\mu$ are mirrored by changes in the particles speed with respect to the guiding v center given by $dv = d\mu v$. This is most effective in resonance with the waves of the HMF leading to so-called resonance scattering as introduced by Hasselmann and Wibberenz (1968). The interpretation of spatial diffusion as a consequence of pitch-angle diffusion also demands a closer look on the definition of the mean free path. Borrowed from kinetic gas theory the mean free path is derived via Fick's law of diffusion to be related to the diffusion coefficient as

$$\kappa_{\parallel} = \frac{1}{3} v \lambda_{\parallel}. \tag{5.17}$$

As the mean free path being the distance between two scattering events makes no sense in the way it is defined in kinetic gas theory, the equivalent in cosmic ray physics is defined as the mean distance until wave-particle interactions changed the pitch-angle by 90°. In order to understand the significance of these diffusive processes, one has to look at the first temporal derivative of the analytical solution of the diffusion equation as given by Eq. (4.7) in Section 4.1.1. By inserting the definition of κ via the mean free path λ into the analytical solution for the residence time (see the derivation in detail in Section 7.1.1 and Parker (1965)) the residence times within a sphere of the radius R appears to be

$$\langle \tau \rangle = \frac{R^2}{6\kappa} = \frac{R}{2\lambda_{\parallel}} \cdot \frac{R}{v}. \tag{5.18}$$

As pointed out by Wibberenz (1973) the second term R/v represents the time needed to cover R propagating straightly inward. Therefore the first term $R/2\lambda_{\parallel}$ marks the influence of the diffusive processes on the efficiency of the transport and can be interpreted as a measure for the amount of mean free paths within the distance R. In contrast to the diffusion parallel to the HMF, the diffusive processes perpendicular to the nominal field lines are more complicated and still under debate. Though generally, the displacement of particles perpendicular to the average background field $\vec{B}_0$ is attributed to a combination of the following effects according to Bieber et al. (2004): field line random walk, back scattering from parallel diffusion and cross field line transfer of particles. Whereas in the first two cases the guiding center still moves along the magnetic field lines and the perpendicular displacement is an effect of the turbulent nature of the HMF, in the third case the guiding center is thought to move perpendicular to another field line due to local inhomogeneties.

Due to the diffusive processes discussed above the pitch-angle distribution tends to become less anisotropic under normal propagation conditions. Therefor in interplanetary space the pitch-angles can be assumed as being uniformly distributed according to Schlickeiser (1989). In this case, the theoretical treatment of charged particle diffusion can be simplified, an approach implicitly used within this thesis as a simulation code based on the TPE by Parker (1965) is applied which does not consider transport effects depending on the particles pitch angles. As shown by Parker (1965) (see Section 5.5 for the derivation) theoretically and demonstrated for the case of Jovian electrons by Fichtner et al. (2000), Ferreira et al. (2001a), Kissmann et al. (2003), Zhang et al. (2007) ,Sternal et al. (2011) and ,Strauss et al. (2011a), amongst others, this approach towards diffusion as an abstract scattering process governed solely by the mean free path as utilised to derive Fokker-Planck type equations (see Section 4.3) can be successfully applied to describe charged particle transport[4]. A more detailed discussion on how interpret the results are given in Section 6.2 in the context of the simulation setup applied by this study.

[3]For a treatment of pitch-angle dependent transport of Jovian electrons see the already referenced detailed discussion by Dunzlaff (2012).

[4]Also momentum diffusion is not considered within this framework. But momentum changes are implicitly incorporated by adiabatic energy changes as discussed in Section 5.4

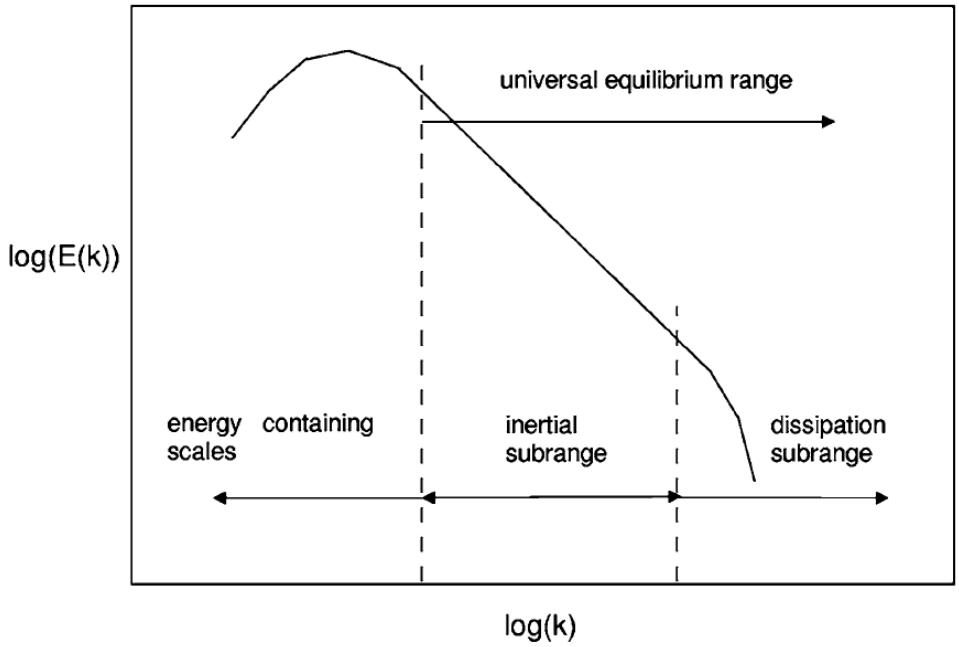

Figure 5.4: *The turbulence spectrum of the HMF according to Petrosyan et al. (2010).*

5.3.2 Remarks on Turbulence

As turbulence within the HMF causes the diffusive processes dominating charged particle transport in the interplanetary space, the following Sections aims to introduce the basic concepts of turbulence theory. The idea to split the HMF into an average background field according to the theory of Parker (1958) as discussed in Section 2.4.1 and an additional turbulent component was already briefly introduced beforehand. In the most abstract and simply way, this approach can be formalised as:

$$\vec{B} = \vec{B}_0 + \vec{b} \tag{5.19}$$

with $\langle \vec{B} \rangle = \vec{B}_0$ and therefore the turbulent component as $\langle \vec{b} \rangle = \vec{0}$. In the context of charged particle propagation of course the correlation of this fluctuation between different points in phase space is the important quantity in order to estimate the significance of the turbulence. The correlation thereby is given as

$$R_{ij}(\vec{r}) = \langle b_i(\vec{x}) b_j(\vec{x} + \vec{r}) \rangle \tag{5.20}$$

with $\partial R_{ij}/\partial x_i = 0$ due to $\vec{B}$ being divergence free as $\nabla \cdot \vec{B} = 0$. Based on these considerations Batchelor (1982) defines a homogeneous spectral tensor

$$S_{ij}(\vec{k}) = \left(\delta_{ij} - \frac{k_i k_j}{k^2} \right) S(\vec{k}) \tag{5.21}$$

with δ_{ij} being the Kronecker symbol and the angular wave number $k = 2\pi/\lambda$. The angular wave number thereby is a consequence of the way the spectral tensor is obtained via the Fourier transformation of the correlation function as

$$S_{ij}(\vec{k}) = \frac{1}{(2\pi)^3} \int d^3 r R_{ij}(\vec{r}) \exp(-i\vec{k} \cdot \vec{r}). \tag{5.22}$$

In order to quantify the fluctuations of the HMF, the inverse Fourier transformation of Eq. (5.22) leads to

$$R_{ij}(\vec{k}) = \int d\vec{k} S_{ij}(\vec{r}) \exp(i\vec{k} \cdot \vec{r}) \tag{5.23}$$

according to e.g. Engelbrecht (2012) due to $\vec{B}$ being divergence free and the corresponding qualities of R_{ij} as discussed above with respect to Eq. (5.20). Via this expression it is now possible to define the strength of the turbulent fluctuations as

$$\int_{-\infty}^{\infty} d^3k S_{ij}(k) = \langle b^2 \rangle = \delta B^2. \tag{5.24}$$

As shown in Fig. 5.4 the power spectrum of the turbulence as derived by its modal spectral density $S_{ij}(\vec{k})$ herein can be divided into three subranges depending on the angular wave number k and resembling the processes driving the turbulence. Thereby the lowest range represents scales at which energy is added to the spectrum (Petrosyan et al., 2010) and provide it to derive the turbulent eddies and the turbulent cascade (Goldstein et al., 1995) according to e.g. the discussion by Engelbrecht (2012). Beyond what could be called a turnover scale there is the universal equilibrium range (Kolmogorov, 1941), in which the eddies are both isotropic as well as in statistical equilibrium with each other as discussed by e.g. Batchelor (1982) and Engelbrecht (2012) and reference therein. The inertial subrange is named due to the energy transfer by inertial forces between the fluctuations (Batchelor, 1982), whereas the turbulence in the dissipation range breaks down and the contained energy starts to heat the background plasma (see e.g. Smith et al., 1990; Goldstein et al., 1995). According to Kolmogorov (1941) the spectral index in the inertial range is expected to be $-5/3$ whereas the exact value for the dissipation range is still under debate as well as the scale at which the transition between inertial and dissipation range happens. Commonly the spectral index is assume to be -3 or steeper from MHD theory (Engelbrecht, 2012) due to the condition of a divergence-free magnetic field according to Smith et al. (1990) and Bieber et al. (1994), amongst others.

Turbulence Models

In a right-handed coordinate system with the z-axis oriented along B_0, the power spectra and $\vec{k}$ can be divided in terms of wave numbers which are parallel (k_z) and perpendicular (k_x, k_y) to the background HMF, B_0. According to Engelbrecht (2012) the impetus was given by the findings of Shebalin et al. (1983) that initially isotropic states turned into anistropic ones. Expanding the thesis into full 3D Oughton et al. (1994) found this effect to be connected to the transformation of excitations into modes which wave vectors appeared to be perpendicular to the nominal magnetic field. This kind of turbulence is called 2D turbulence and the fluctuations are assumed to be functions of the perpendicular or transverse coordinates (x, y) leading to an expression for the turbulent HMF as

$$\begin{aligned} \vec{B} &= \vec{B}_0 + \vec{b}(x, y) \\ &= B_0 \cdot \vec{e}_z + b_x \cdot (x, y)\vec{e}_x + b_y(x, y) \cdot \vec{e}_y. \end{aligned} \tag{5.25}$$

In contrast to the 2D turbulence, the slab turbulence as proposed by Jokipii (1966) is based on the assumption that the fluctuations are a function of the z coordinate along the nominal field lines and can be therefore defined as

$$\vec{B} = B_0 \cdot \vec{e}_z + b_x(z) \cdot \vec{e}_x + b_y(z) \cdot \vec{e}_y. \tag{5.26}$$

As the fluctuations propagate along the magnetic field, slab turbulence can be used to describe Alfvén type fluctuation in the Solar wind according to e.g. Goldstein et al. (1995).

Whereas it is beyond the scope of this work to discuss the details of these concepts, it is important to note that for 2D turbulence as given by Eq. (5.25) as well as for slab turbulence (Eq. (5.26)) 3D spectra can be derived with corresponding correlation lengths $\lambda_{c,2D/slab}$. Combined these two approaches form a model to cover fluctuations depending on all three spatial coordinates as

$$\vec{b}(x,y,z) = \vec{b}_{slab}(z) + \vec{b}_{2D}(x,y) \tag{5.27}$$

and therefore

$$\delta B^2 = \delta B^2_{slab} + \delta B^2_{2D}. \tag{5.28}$$

which is estimated as a total variance of $\delta B^2 \approx 12$ nT^2 according to Smith et al. (2006b). Usually a ratio of 80 : 20 is assumed between the 2D and the slab component, although recent studies such as Zhao et al. (2018) show that a ration of 60 : 40 match the observations slightly better and are theoretical possible as well. An overview on how to estimate this ratio and the uncertainties accompanied by it is given by Oughton et al. (2015).

Dynamical Turbulence

In order to consider time-dependent effects within the correlation function (see Eq. (5.20)) Bieber and Matthaeus (1991) and Bieber et al. (1994) suggested an additional factor in order to modify the correlation function accordingly. Conceptual this leads to an expression of the form

$$S_{ij}(\vec{k},t) = S_{ij}(\vec{k})\Gamma(\vec{k},t) \tag{5.29}$$

with $\Gamma(\vec{k},t)$ being the time dependent modification factor, known as the dynamical modification function. In a first attempt Bieber and Matthaeus (1991) proposed what became the so-called damping model of dynamical turbulence as

$$\Gamma(\vec{k},t) = \exp(-\alpha|\vec{k}|V_A t) \tag{5.30}$$

with V_A being the Alfvén speed and $\alpha \in [0,1]$ a scaling factor corresponding to the strength of the dynamical effects. The abstraction of the model allows for several interpretations, for example to identify the exponential decay as equivalent to the Kolmogorov decay as argued by Bieber et al. (1994). The proposition of a Gaussian type correlation function, also by Bieber et al. (1994), is known as the random sweeping model of dynamical turbulence:

$$\Gamma(\vec{k},t) = \exp(-\alpha^2\vec{k}^2V_A^2t^2). \tag{5.31}$$

Both suggestions to cover the time dependence of turbulence in the HMF have been applied to various scattering theories to derive mean free paths, see e.g. Bieber et al. (1994), Teufel and Schlickeiser (2002, 2003) and Shalchi (2009) and lead to simulation approaches such as by Engelbrecht and Burger (2010). Therefore the focus of the next Section will be the derivation of parallel and perpendicular mean free paths from these theoretical considerations.

5.3.3 Parallel and Perpendicular Mean Free Paths

The consensus range suggested by Palmer (1982) as indicated by the grey area in Fig. 5.5 is most commonly regarded as the reference for any attempt to derive a mean free path at Earth orbit. It is based on several different studies which estimated the mean free paths of electrons and protons by fitting intensity and anisotropy profiles to measurements as wells

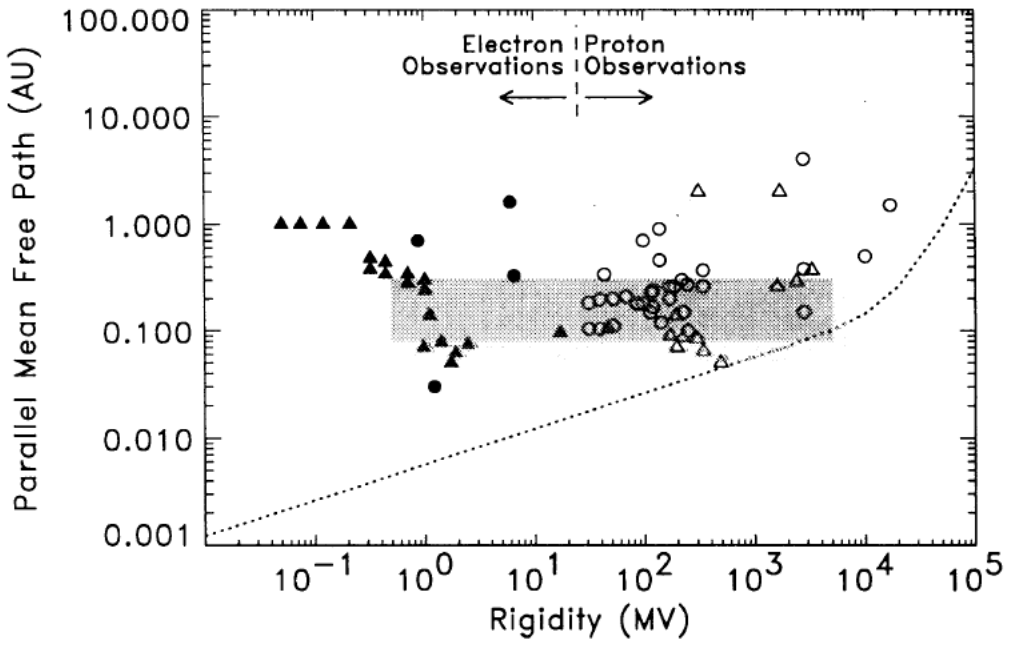

t

Figure 5.5: *The Palmer consensus range (grey area, see Palmer, 1982) alongside data obtained from electron and proton observations as published by Bieber et al. (1994). The dotted line indicates the prediction by the slab QLT approach according to Jokipii (1966).*

as to numerical simulations. The results still serve their purpose up until day, although they are mostly calculated by utilizing Solar energetic particles and neglecting the possible influence of perpendicular diffusion (see Kelly et al., 2012). More recent studies which incorporate perpendicular diffusion are e.g. Dalla et al. (2003), Zhang et al. (2007) and Dröge et al. (2010).

In comparison with the prediction of the QLT by Jokipii (1966) the results of Palmer (1982) show a contradicting low energy dependence as also indicated by Fig. 5.5 which shows as the dotted line the theoretical rigidity dependence of the mean free path according to slab linear theory. The results of Dröge (2000) too, as shown in Fig. 5.6, indicate as well that the rigidity dependence within the low MeV range is rather low and diverges significantly from the slab QLT predictions as again shown by the dotted line.

As these examples show, the theoretical treatment of diffusion and the derivation of mean free paths in particular still holds a lot of difficulties and is an ongoing topic of research. A most general approach based on the results of Jokipii (1966) amongst others as given by Eq. (5.16) was derived by Teufel and Schlickeiser (2003). Applying a slab omnidirectional turbulence power spectrum in order to calculate the pitch-angle diffusion tensor $D_{\mu\mu}$, the subsequent expression for the random sweeping (RS, see Eq. (5.31)) and damping turbulence (DT, see Eq. (5.30)) read as

$$\lambda_{\parallel}(RS) = \frac{B_0^2}{\delta B_{slab}^2} \frac{3s}{\sqrt{\pi}(s-1)} \frac{R^2}{k_{min} b} K_{RS} \tag{5.32}$$

and

$$\lambda_{\parallel}(DT) = \frac{B_0^2}{\delta B_{slab}^2} \frac{3s}{(s-1)} \frac{R^2}{k_{min} a} K_{DT}, \tag{5.33}$$

respectively, with the random sweeping and damping turbulence parameters K_{RS} and K_{DT}. Thereby s represents the spectral index of the inertial range whereas the influence of the spectral index p of the dissipation range is implicitly included in the parameters K_{RS}

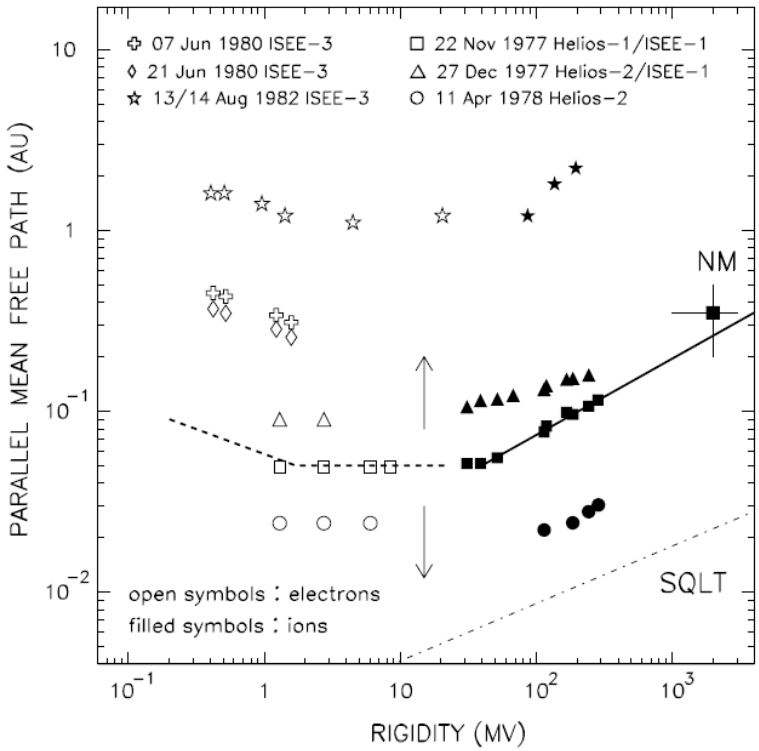

Figure 5.6: *Measurements and theoretical suggestions for the parallel mean free path according to Dröge (2000). The measurements were obtained through several Solar energetic particle events as indicated, the upper line features he power law dependences to the data whereas the dotted line shows the prediction according to a pure slab QLT approach.*

and K_{DT}. As an additional condition, Teufel and Schlickeiser (2003) found that $p > 2$ and $1 < s < 2$. With k_{min} and k_d giving the onsets of the inertial and dissipation range, respectively, further parameter are defined for reasons of clarity and comprehensibility as

$$\begin{aligned} a &= \frac{v}{\alpha V_A} \\ b &= a/2 \\ R &= R_L k_{min} \\ Q &= R_L k_d. \end{aligned} \tag{5.34}$$

Determining the parameter K_{RS} and K_{DT}, respectively, is a topic of ongoing research. An extended overview, also on possible solutions, is given by Shalchi (2009) and Dosch et al. (2009) and the references therein, as well as by Engelbrecht (2012). A suggestion for the parallel electron mean free path would be the following expression derived by Engelbrecht and Burger (2010) based on the random sweeping approach

$$\begin{aligned} \lambda_\parallel = &\frac{3s}{\sqrt{\pi}(s-1)} \frac{R^2}{k_{min} b} \left(\frac{B_0}{\delta B_{slab}} \right)^2 \\ &\left[\frac{b}{4\sqrt{\pi}} + \left(\frac{1}{\Gamma(p/2)} + \frac{1}{\sqrt{\pi}(p-2)} \right) \frac{b^{p-1}}{Q^{p-s} R^s} + \frac{2}{\sqrt{\pi}(2-s)(4-s)} \frac{b}{R^s} \right]. \end{aligned} \tag{5.35}$$

A possible corresponding perpendicular mean free path is given by Engelbrecht (2017) as

$$\lambda_\perp = \left[\alpha_\perp^2 \sqrt{3\pi} \frac{s-1}{2s} \frac{\Gamma(s/2+1)}{\Gamma(s/2+1/2)} \lambda_{2D} \frac{\delta B_{2D}^2}{B_0^2} \right]^{2/3} \lambda_\parallel^{1/3} \tag{5.36}$$

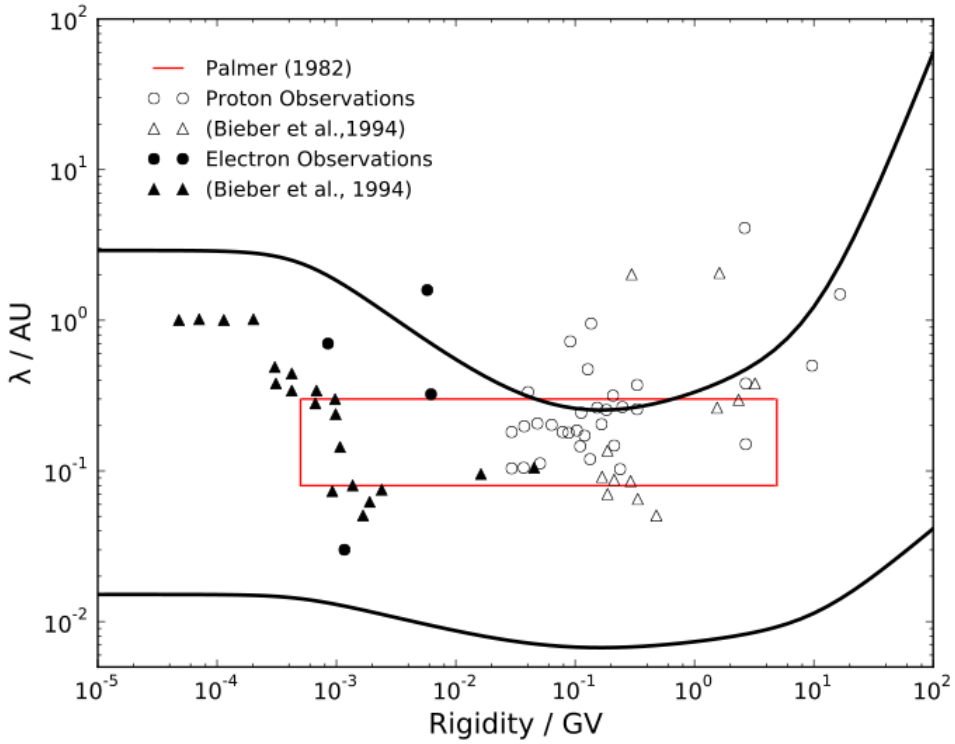

Figure 5.7: *The suggestion for the electron parallel and perpendicular mean free according to Engelbrecht and Burger (2010) and Engelbrecht (2017) as given by Eqs. (5.35) and (5.36). The red square indicates the consensus range according to Palmer (1982) whereas the data is taken from Bieber et al. (1994) as shown in Fig. 5.5.*

Figure 5.7 shows the two suggestion for the parallel and perpendicular mean free path as given by Eqs. (5.35) and 5.36 at a radial distance of $r = 1$ AU. For the magnetic field a mean value of $B_0 = 5$ nT was assumed alongside with the turbulence parameters included being $p = 2.6$ (Smith et al., 2006a), $\alpha = 1$ and $s = 5/3$ as suggested by Kolmogorov (1941). Following a simplified version of the approach by Leamon et al. (1998) it was assumed that $k_d = 2\pi/u_{SW} b B_0 q/m$ with the parameter $b = 3.19$ according to according to Leamon et al. (2000). The onset of the inertial range was chosen as $k_{min} = 1/\lambda_{slab}$. According to observations made at Earth orbit discussed by Dasso et al. (2005); Weygand et al. (2009, 2011) the slab correlations length thereby is assumed as $\lambda_{slab} = 2.55(\pm 0.76)\lambda_{2D}$ and the 2D correlation length as $\lambda_{2D} = 0.0074(\pm 0.0007)$ AU.

5.4 Adiabatic Energy Changes

The importance of understanding the role of adiabatic energy changes for this work can not be overstated. In the following they will play a key role in order to transform the simulation results into physical meaningful differential intensities (see Section 6.3) or to derive new and improved estimates for the residence times both numerical (Section 7.2) and analytical (Section 7.3.3). Therefore the following paragraphs will detail how the expansion of the

Solar wind and the outwardly decrease of the HMF cause adiabatic changes of the particles' kinetic energies. The account will be based on the study by Webb and Gleeson (1979) and their detailed mathematical derivation the phenomenon as first suggested by Parker (1965). Thereby two mechanisms will be explored, first the betatron deceleration process due to the changing HMF and the therefore induced electric field and second the inverse Fermi effect causing the particles to loose energy due to scattering within the expanding Solar wind.

5.4.1 Betatron Deceleration

In order to understand betatron deceleration it is suitable to assume a particle moving along a field line at $\vec{r}_0$. With the Solar wind velocity at $\vec{r}_0$ being $\vec{u}_{SW}(\vec{r}_0) = \vec{u}_0$ the law of induction suggest an electric field due to irregularities in the Solar wind velocity as

$$\vec{E} = -(\vec{u}_{SW} - \vec{u}_0) \times \vec{B}. \tag{5.37}$$

Taking the gyration along the field line into account as explained in Section 5.1 and sketched in Fig. 5.1 the circular orbit has a radius of $\rho = p \sin\alpha/(|q|B)$ perpendicular to the magnetic field line. Thereby p denotes the particle's momentum, α the pitch angle and $|q|$ the absolute value of the charge. Since $\vec{E}$ is perpendicular to the magnetic field $\vec{B}$ according to Eq. (5.37) the work per particle and orbit is

$$\Delta T = q \int_C \vec{E} \cdot d\vec{s} \tag{5.38}$$

with the path of integration being a circle whose normal vector $\vec{n}$ is right handed related to the circulation around $\vec{B}$ according to Webb and Gleeson (1979). Explicitly $\vec{n}$ is parallel or anti-parallel to $\vec{B}$ based on the particle's charged and can be calculated as

$$\vec{n} = \frac{-q\vec{B}}{|q|B}. \tag{5.39}$$

Applying Eqs. (5.38) and (5.39), Stoke's theorem shows that

$$\Delta T = q \int_\sigma (\nabla \times \vec{E}) \cdot \vec{n} dA \tag{5.40}$$

with A being the area of the circle. As Eqs. (5.37) and 5.39 trace back the parameters of Eq. (5.40) to the magnetic field $\vec{B}$, Eq. (5.40) can be solved as follows. The expression inside the brackets becomes

$$\begin{aligned} \nabla \times \vec{E} =& - \nabla \times [(\vec{u}_{SW} - \vec{u}_0) \times \vec{B}] \\ =& (\vec{u}_{SW} - \vec{u}_0) \cdot \nabla \vec{B} + \vec{B} \nabla \cdot (\vec{u}_{SW} - \vec{u}_0) \\ & - (\vec{u}_{SW} - \vec{u}_0) \nabla \cdot \vec{B} - (\vec{B} \cdot \nabla)(\vec{u}_{SW} - \vec{u}_0) \\ =& \vec{B}(\nabla \cdot \vec{u}_{SW}) - (\vec{B} \cdot \nabla)\vec{u}_{SW}. \end{aligned} \tag{5.41}$$

Since $\nabla \cdot \vec{B} = 0$ and $\vec{u}_0$ =const in the frame of reference and assuming $\vec{u}_{SW} - \vec{u}_0 \to \vec{0}$, applying Eq. (5.41) along with the definition of $\vec{n}$ by Eq. (5.39) to Eq. (5.40) becomes

$$\Delta T = -|q|\pi\rho^2 \frac{\vec{B}}{B} \cdot \{\vec{B}(\nabla \cdot \vec{u}_{SW}) - (\vec{B} \cdot \nabla)\vec{u}_{SW}\}. \tag{5.42}$$

In order to combine the results with the momentum change due to the inverse Fermi effect, the change of energy ΔT has to be transformed into a momentum change. Thereby ΔT is related to the momentum change Δp as $\Delta p = \Delta T dT/dp = \Delta T/v$ with v being the particle speed. The gyrofrequency connected to v as $\omega = v/r$ is given by $\omega/(2\pi) = |q|B/(2\pi m)$. Considering furthermore an amount of $4\pi p^2 F_0 dp$ particles in $(p, p+dp)$ with F_0 being the zeroth moment of the momentum distribution function.[5] Thus the average momentum change rate due to betatron deceleration reads as

$$\begin{aligned}\left\langle \frac{p}{t} \right\rangle_b &= \int_0^\pi \frac{\omega}{2\pi} \Delta p (2\pi^2 p F_0) \sin\alpha d\alpha / (4\pi p^2 F_0) \\ &= -\frac{p}{4} \left[\nabla \cdot \vec{u}_{SW} - \frac{\vec{B}}{B}\frac{\vec{B}}{B} : \nabla \vec{u}_{SW} \right] \int_0^\pi \sin^3\alpha d\alpha \\ &= -\frac{p}{3} \left[\nabla \cdot \vec{u}_{SW} - \frac{\vec{B}}{B}\frac{\vec{B}}{B} : \nabla \vec{u}_{SW} \right]\end{aligned} \tag{5.43}$$

according to Webb and Gleeson (1979). The result consists of the adiabatic rate $-p\nabla\vec{u}_{SW}/3$ and a second term based on the scalar product[6] between $\vec{B}\vec{B}$ and $\nabla\vec{u}_{SW}$ which later cancels out with the results of the inverse Fermi effect.

In order to understand betatron deceleration physically it is important to note that although the expansion leads to a decrease of the magnetic field strength in the observer's rest frame with increasing radial distance to the Sun, in the particle's rest frame the magnetic field strength does not change. This is reflected in the derivation from Eq. (5.41) to Eq. (5.42) when it is assumed that $\nabla\vec{B} = 0$ in the frame of reference. As the particle's energy has to be conserved independent from the the rest frame the following happens. The invariance of the magnetic moment $\mu = mv_\perp^2/2|B|$ leads to an decreasing perpendicular particle speed $v_\perp$ if $|B|$ decreases with radial distance. In order to conserve the kinetic energy in the particle's rest frame therefore the parallel speed has to increase. As the particle gyrates along the magnetic field lines as discussed above in Section 5.3 this leads to a change of the pitch angle α. The integration of the pitch angle space as apply in Eq. (5.43) therefore leads to a momentum (or energy) change in the observers rest frame due the energy conservation in the particle's frame.

5.4.2 Inverse Fermi Effect

According to Webb and Gleeson (1979) the effect of the expanding Solar wind can best be understood by focusing on the outer parts of the Heliosphere. This due to the fact that the Parker spiral are bent to almost circular in that region. Fig. 5.8 shows a particle gyrating along such a nominal Parker field line in the outer Heliosphere between two scattering centers P and Q. In the viewing frame of a resting observer these scattering centers move away from each other with v_{SC} due to the expansion of the Solar wind. Assuming that the particle is scattered back elastically one can transform between the scattering center's and the observer's rest frame by a simple Galilei transformation.

$$v \rightarrow v' = v + v_{SC} \tag{5.44}$$

[5] As F_0 cancels out in the following the interested reader may look up the explicit derivation of it in Webb and Gleeson (1979).

[6] Thereby the expression of the form $\vec{A} : \vec{B}$ denotes the scalar or Frobenius product of two matrices. It is defined as $\vec{A} : \vec{B} = \langle \vec{A}\vec{B} \rangle_F = \sum_{i=1}^m \sum_{j=1}^n a_{ij} b_{ji}$

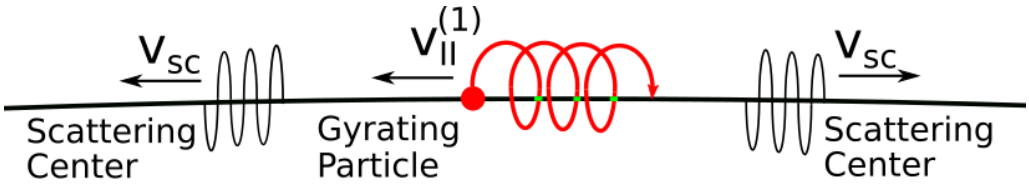

Figure 5.8: *Sketch of the principle of the inverse Fermi effect. In contrast to the classical Fermi effect with increasing radial distance to the Sun also the distance between the scattering centers Q and P increases due to the expansion of the HMF. Thus the scattered particles experiences the inverse effect and loses energy based on the radial distance and the expansion rate according to the Solar wind speed as given by Eq. (5.50).*

Thus, relative to an observer at r_0 the momentum change at Q and P is given by

$$\begin{aligned}(\Delta p)_Q &= -p\left[\frac{2[v_{SC}(Q)-v(r_0)]}{v}\cdot\frac{\vec{B}}{B}\cos\alpha + O\left(\frac{|v_{SC}(Q)-v(r_0)|^2}{c^2}\right)\right]\\ (\Delta p)_P &= p\left[\frac{2[v_{SC}(P)-v(r_0)]}{v}\cdot\frac{\vec{B}}{B}\cos\alpha + O\left(\frac{|v_{SC}(P)-v(r_0)|^2}{c^2}\right)\right]\end{aligned} \tag{5.45}$$

with α as the pitch angle and the second terms O indicate higher loss terms in case of non elastic scattering. Assuming λ as the mean free path the average time to scatter both at Q and P is given by

$$\langle t_{QP}\rangle = \frac{2\lambda}{v|\cos\alpha|} \tag{5.46}$$

Combining both Eqs. (5.45) and (5.46) one obtains a momentum change for a particle being reflected between Q and P per time unit as

$$\begin{aligned}\frac{\Delta p}{\Delta t} =& \frac{2\lambda}{v|\cos\alpha|}[(\Delta p)_Q + (\Delta p)_P]\\ =& \frac{2\lambda}{v|\cos\alpha|}p\left[\frac{2[v_{SC}(P)-v_{SC}(Q)]}{v}\cdot\frac{\vec{B}}{B}\cos\alpha + O\left(\frac{|v_{SC}(P)-v_{SC}(Q)|^2}{c^2}\right)\right]\end{aligned} \tag{5.47}$$

Applying that the distance between P and Q is given by $\lambda\vec{B}/B$, Eq. (5.47) can be rewritten to

$$\frac{\Delta p}{\Delta t} = \frac{-p\cos^2\alpha}{\lambda}\left[\lambda\frac{\vec{B}}{B}\cdot\frac{\partial}{\partial\vec{r}}\left(\vec{u}_{SW}\cdot\frac{\vec{B}}{B}\right)\right] = -p\cos^2\alpha\cdot\frac{\vec{B}}{B}\frac{\vec{B}}{B} : \nabla\cdot\vec{u}_{SW} \tag{5.48}$$

Averaging over the pitch angle α in polar coordinates finally leads to an expression comparable to the one for the betatron deceleration (see Eq. (5.43)) as

$$\left\langle\frac{dp}{dt}\right\rangle_{if} = -p\frac{\vec{B}}{B}\frac{\vec{B}}{B} : \nabla\vec{u}_{SW}\frac{\int_0^\pi\cos^2\alpha\sin\alpha d\alpha}{\int_0^\pi\sin\alpha d\alpha} = -\frac{p}{3}\frac{\vec{B}}{B}\frac{\vec{B}}{B} : \nabla\cdot\vec{u}_{SW}. \tag{5.49}$$

As Webb and Gleeson (1979) note the inverse Fermi effect is expected to be dominant within the inner Heliosphere. In the simplified approach that the Solar wind speed is radially outward (as implemented in the simulation setup used herein) Eq. (5.49) reduces to

$$\left\langle\frac{dp}{dt}\right\rangle_{if} = -\frac{p}{3}\cos^2\psi\frac{u_{SW}}{r} \tag{5.50}$$

which decreases with radial distance due to the Parker angle ψ as defined in Eq. (2.10). As a consequence in the outer Heliosphere only the first term of the betatron deceleration (as given by Eq. (5.43)) is of significance.

5.4.3 Total Momentum Change

As already hinted above, combining Eqs. (5.43) and 5.49 cancels out the terms depending on the magnetic fields direction and reduces the total momentum change to the adiabatic rate

$$\left\langle \frac{dp}{dt} \right\rangle = \left\langle \frac{dp}{dt} \right\rangle_b + \left\langle \frac{dp}{dt} \right\rangle_{if} = -\frac{p}{3} \nabla \cdot \vec{u}_{SW}. \tag{5.51}$$

A heuristic derivation of this term can be found in Parker (1965) who included it as the adiabatic energy change term in the TPE. This will be discussed in the following Section 5.5. Converted into terms of energy E Eq. (5.51) reads as

$$\frac{dE}{dt} = -\frac{1}{3} E \cdot \nabla \cdot \vec{u}_{SW}. \tag{5.52}$$

Assuming the Solar wind as constant as well as radially outward the divergence in Eq. (5.52) can be solved as $\nabla \vec{u}_{SW} = 2u_{SW}/r$ and therefore leads to the well known expression of

$$\frac{dE}{dt} = -\frac{2}{3} E \frac{u_{SW}}{r}. \tag{5.53}$$

5.5 Parker's Transport Equation

Based on the formal discussion of the FPE by Chandrasekhar (1943) as discussed in Section 4.3.1, Parker (1965) suggested a transport equation, covering drift effects, diffusion, adiabatic energy changes as well as the convection of particles with the Solar wind. Proceeding from the guiding center approach (see Section 5.1) the diffusion is assumed to be describable by a Markov process, i.e. a random walk approach as discussed in Section 4.2.2 and used to derive the FPE. Parker (1965) therefore applied the classical approach of the probability distribution as introduced by Einstein (1905) and discussed in Section 4.1.1.

The diffusion tensor thereby is defined as $-\kappa \nabla f(r,t)$ in the frame of reference of the scattering irregularities. As these irregularities in the HMF move outward with the Solar wind speed u_{SW}, an additional convective particle flux of $u_{SW} f(r,t)$ has to be considered. In order to obtain the accumulation at a certain point, however, as argued by Parker (1965), the divergence is needed. This yields to the expression

$$\frac{\partial f}{\partial t} = \vec{\nabla} \cdot (\hat{\kappa} \cdot \vec{\nabla} f) - \vec{u}_{SW} \cdot \vec{\nabla} f \tag{5.54}$$

which is identifiable as a FPE describing the temporal and spatial evolution of the particle distribution f. Based on heuristic considerations due to the radial expansion of the HMF, Parker (1965) suggested an additional term covering the adiabatic cooling of the particle, causing a decline in momentum. Although both seemingly plausible as well as successful applied, it took over a decade until a correct theoretical derivation was provided by Webb and Gleeson (1979) as it is outlined in Section 5.4. Incorporating also a second additional term S for external sources, the complete TPE by Parker (1965) as applied also within this thesis reads as

$$\frac{\partial f}{\partial t} = S + \vec{\nabla} \cdot (\hat{\kappa} \cdot \vec{\nabla} f) - \vec{u}_{SW} \cdot \vec{\nabla} f + \frac{1}{3} (\vec{\nabla} \cdot \vec{u}_{SW}) P \frac{\partial f}{\partial P}, \tag{5.55}$$

with $\vec{u}_{SW}$ as the Solar wind speed and P being the particles rigidity.

5.5.1 Limitations

The TPE by Parker (1965) has been successfully applied to calculate and model charged particle transport up until today. A simplified analytical version by Gleeson and Axford (1968) known as the force field solution was applied to approximate the modulation of GCRs as well as Eq. (5.55) has been used for several numerical simulation approaches to model GCR and Jovian electrons propagation. However, the approach by Parker (1965) bears several limitation which have to considered in order to assure the reliability of the results, not least the fact that the TPE is not analytically solvable. The consequences for this thesis and the interpretation of the results are one focus of the following Chapter.

As discussed above, the TPE by Parker (1965) as well as the approach to estimate the HMF providing the guiding magnetic field lines (Parker, 1958) neglect the small scale structure and turbulences of the HMF and their influence on the particles and incorporates them into the diffusion tensor. Therefore, the accuracy of the results depend on how accurate the diffusion tensor $\hat{\kappa}$ and the corresponding estimations of the parallel and perpendicular mean free paths $\lambda_{\parallel}$ and $\lambda_{\perp}$ incorporate these effects. Furthermore the underlying approach to categorise the stochastic motion of charged particles as diffusion, basically assumes a Brownian motion as discussed in Section 4.1 and 4.2, which is modified by diffusion tensor and the corresponding parameters and theories in order to emulate the actual physical behaviour. Referring to the discussion in Section 5.3.1 one has to bear in mind, that also the assumption to identify the average distance until wave-particle interactions change the pitch angle by 90° as a mean free path between to scattering points is a rather drastic simplification.

Therefore the TPE by Parker (1965) is only applicable if one can assume an isotropic pitch-angle distribution within the particle distribution in question. Most prominently Eq. (5.55) is not able to describe the behaviour of SEP events accordingly or the highly anisotropic Jovian jets. In order to describe these phenomena the pitch-angle has to be included as a relevant transport parameter. An alternative to the TPE by Parker (1965) which covers this so-called focused transport was established by Roelof (1969).

Chapter 6

Particle Propagation Modelling

Expanding the discussion given by Vogt et al. (2020), this Chapter presents the results of the extensive parameter studies on Jovian electron transport performed during the course of this study. After introducing the simulation setup (Section 6.1.1) and the implementation of the transport parameters (Section 6.1.2) as they were discussed in the previous Chapter 5, a focus it set on the interpretation of the mathematical results (Section 6.2) and how they are transformed into physical meaningful quantities via the boundary conditions of the simulation setup in Secs. 6.3.1 and 6.3.2. This discussion is accompanied by a parameter study investigating the dependence of the resulting differential intensities on energy and different values for the parallel (Section 6.4.1) and perpendicular mean free path (Section 6.4.2). A comparison with in situ data is shown and will lead to the suggestion of new values to estimate the electron mean free paths realistically in Section 6.4.3. A subsequent parameter study based on these results discusses the influence of the radial extent of the simulation setup (Section 6.4.4) as well as the influence of the time increment (Section 6.4.5) and whether the Heliospheric magnetic field can be assumed as static during the simulation or has to be considered as corotating with time as shown in Section 6.4.6.

Since the SDE numerical scheme was introduced to astroparticle physics around two decades ago (see e.g. Zhang, 1999) the method became increasingly popular and common within the scientific community due to various reasons. As Strauss and Effenberger (2017) point out in their review there are five major advantages of the SDE method in comparison to prior approaches such as the finite difference scheme:

- The SDE numerical scheme is unconditionally stable in contrast to e.g. finite difference schemes. Although this fact does not ensure the numerical accuracy of the results, the investigated parameter space is independent from limitations of the numerical method.
- The SDE method is able to handle large gradients much better than e.g. finite different schemes, limited in its accuracy only by the choice of the time step. However, since large gradients would cause the spatial step size to increase it is necessary to note, that adaptive of very short time steps should be chosen to investigate the influence of such phenomena on charged particle transport.
- Instead of calculating solutions on a specific pre-defined grid, the SDE numerical scheme provided solutions on a number of discrete phase-space positions, which in their temporal succession can be interpreted as phase-space trajectories. Thereby SDE numerical scheme avoid unnecessary calculations which save computational memory and increase the performance. As a consequence, calculations in higher dimension come with much less costs as by utilizing other numerical approaches. An exception of cause is any scientific goal which demands a global solution of the TPE.
- As the individual solutions are completely independent from each other, calculation can be performed on different computational environments and combined afterwards.

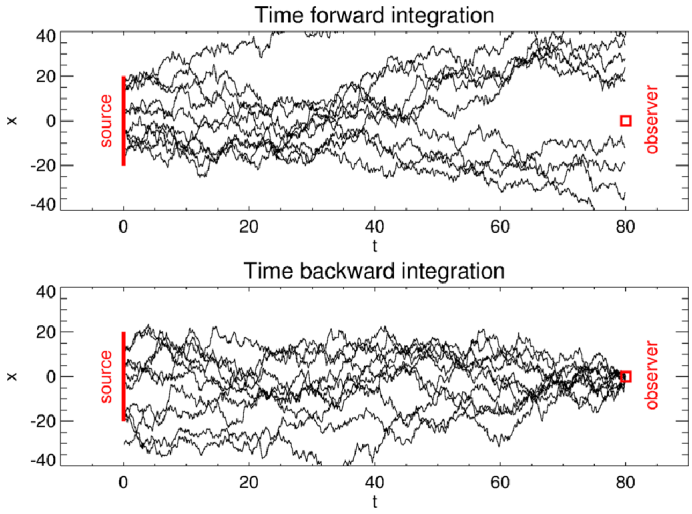

Figure 6.1: *Illustration by Strauss and Effenberger (2017) of the efficiency of the time-forward and time-backward simulation approach, respectively. Shown are the results from a one dimensional scenario, the integration was performed by an SDE solver comparable to the one used for this thesis.*

This is often implemented by using parallel computational environments such as GPUs - an approach carried out by Dunzlaff et al. (2015) and also utilised for this work.

- More physical processes can be visualised by SDE based solutions of transport modelling. As the temporal succession of solution constitute phase-space trajectories, not only the resulting differential intensities at an observational point but also the transport itself is open to numerical investigation.

Especially, a consequence of the last point, how to interpret phase-space trajectories based on SDE numerical solutions, will be a major question in the subsequent work. Therefore the following Chapter will discuss in detail the interpretation of phase-space trajectories and how they relate to the so-called pseudo-particle interpretation. This will be based on the detailed analysis of both the Wiener process and its significance in the mathematical treatment of diffusion in Chapter 4 as well as on the discussion of the TPE and its parameter dependence in the previous Chapter 5. Furthermore the importance of boundary conditions will be examined and therein the new source spectrum for Jovian electron as developed by Vogt et al. (2018) and discussed in Section 3.2.

6.1 The Simulation Setup

The main advantage of writing a SDE solver in CUDA and running it on GPUs its speed as the massive parallel architecture of GPUs. Therefore codes which aim to solve parallelised tasks such as the random walks within the SDE approach benefit greatly from an implementation on GPUs. On the other hand the limited storage space demands a limitation of variables and therefore a simplification of the modelling approach. As pointed out by Dunzlaff et al. (2015) the framework used for this thesis shows a performance increase of a factor of ≈ 50 in comparison to equivalent modelling approaches running on CPU clusters.

As many SDE based numerical schemes in astroparticle physics, the framework established by Dunzlaff et al. (2015) and utilised herein follows the time-backward integration approach. Figure 6.1 taken from Strauss and Effenberger (2017) demonstrates for a one dimensional test case the benefits of the time-backward integration approach. Due to the fact that the aim of most parameter studies concerning charged particle transport is the validation of the result via comparison with spacecraft data, simulation results should provide a reasonable high statistic a certain observational points. Both panels of Fig. 6.1 show the simulation setup from a physical point of view: At $t = 0$ the red vertical red line indicates a source region whereas the observer is located at $t = 80$ by a red square. Since we are only interest in the solutions of the probability density equation (PDE) at this certain point, the time-forward solutions as shown in the upper panel would have to simulate much more phase-space trajectories in comparison to achieve the same statistics as the time-backward approach. Because all trajectories which do not pass through the observational point can not contribute to the differential intensity at the observational point, they appear to be unnecessarily solved. In order to avoid wasting computational resources, it is therefore suitable to implement the time-backward approach as shown in the lower panel of Fig. 6.1. In contrast to the time-forward approach in the upper panel the integration starts at the observational point. By starting at the point where one wants the solution the only limiting factor whether the trajectories would contribute is whether they reach a boundary which serves as a possible source. As illustrated by Fig. 6.1 this approach is often more efficient, mostly due to the fact that possible source regions are usually much more widespread than the observational points in question as it is in our case. Therefore, in order to simulate differential intensities with a certain observational energy, the time-backward approach produces less trajectories which do not meet the aims of the simulation (i.e. due to the diverging exit positions as discussed below) than the time-forward approach. The case of Jovian electrons, however, can be considered as a kind of "stalemate" due to the fact that the source region in question is only $\approx 1^\circ$ in longitude as is the Jovian magnetosphere. Whereas this is in reality of course much bigger than a the aperture of a charged particle counter, due to statistical limitations is is questionable whether longitudinal scales significantly smaller can be meaningfully resolved. Regard the simulation of GCR electrons, however, as discussed in Section 7.3.2 the time-backward approach shows its advantages.

The setup realised for this thesis is sketched in Fig. 6.2. Shown is a trajectory of observational points following the Earth orbit and colour coded four phase-space trajectories. These four phase-space trajectories exemplify the four different boundaries of the time-backward integration as discussed in more detail in Section 6.3 regarding the mathematical implementation:

- The Sun located at the center of the spherical simulation setup (yellow)
- The Jovian magnetosphere at $r_{Jov} = 5.11 - 5.39$ AU and $\phi_{Jov} = (90 \pm 1.03)^\circ$ (orange)
- The Heliopause at a radial distance of $R = 120$ AU (blue)
- The termination of the integration due to a predefined maximal integration time (green). These trajectories can be discarded due to their unrealistic energy gains corresponding to the long integration time. For a more detailed discussion see Section 6.4.5.

As discussed in detail in Chapter 4 and Section 4.4 in particular, the time-backward approach not only traces the pseudo-particles trajectories back from the observer (the initial point in the time-backward setup) to the source, but also inverts the adiabatic energy changes as introduced in Section 5.4. Instead of decreasing the pseudo-particles energies corresponding to their radial position, the energy E_i associated with each phase-space

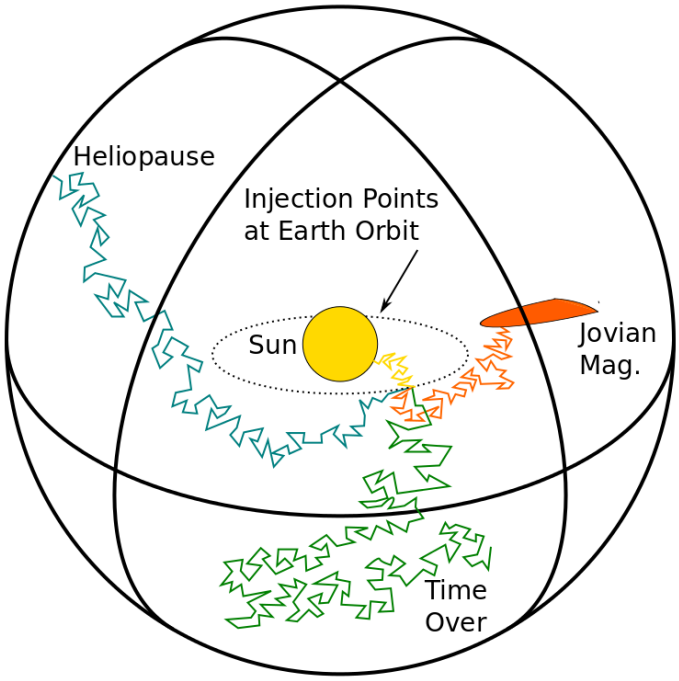

Figure 6.2: *Schematic sketch of the model setup as presented byVogt et al. (2020). Note that the proportions are out of scaled due to illustrative purposes.*

trajectory and the pseudo-particles it represents increases after each step as given by Eq. (5.52). Therefore each phase-space trajectory is assigned to three variables in order to calculate the physical quantities corresponding to the results of the SDEs:

Exit Position: indicates the boundary hit by the phase-space trajectory to terminate the simulation, e.g. the Jovian magnetosphere

Exit Energy: the sum of the adiabatic energy changes (increases in the time-backward frame), E_i^{exit} can be physically interpreted as the energy E_i^{source} that the corresponding pseudo-particles were released with

Exit Time: the sum over the time increments Δs corresponding to the trajectory. The exit time is related to the number of steps performed by the random walk n_i as $s_i^{exit} = n_i \cdot \Delta s$.

By means of simplicity a spherical setup is chosen for the model Heliosphere. As this thesis exclusively deals with charged particle transport within the inner Heliosphere (explicitly between the Jovian source at roughly 5 AU and spacecraft missions mostly located at Earth orbit) this deviation from the physical shape of the Heliosphere is negligible. However, as discussed in Section 6.4.4 the radial extend of the model Heliosphere R shows a significant influence on the resulting differential energies and therefore has to be carefully chosen as shown by Vogt et al. (2015) and applied by e.g. Kopp et al. (2017). Furthermore the simulation setup uses a coordinate system corotating with Jupiter. As described above the Jovian source is defined at a static longitude $\phi_{Jov} = (90 \pm 1.03)^\circ$ at all times. Therefore any trajectory has to be transformed into a coordinate system relative to the Jovian motion. The geometry of the HMF as discussed in Section 2.4 thereby is implicitly included in the diffusion tensor $\hat{\kappa}$ as described in the following. This setup is well established for Jovian electron simulations and tested successfully by e.g. (Strauss et al., 2011a).

Figure 6.3 shows this approach in a top view, alongside simulation results for Jovian electrons with an initial (or observational) energy of $E^{init} = 6$ MeV. The nominal Parker

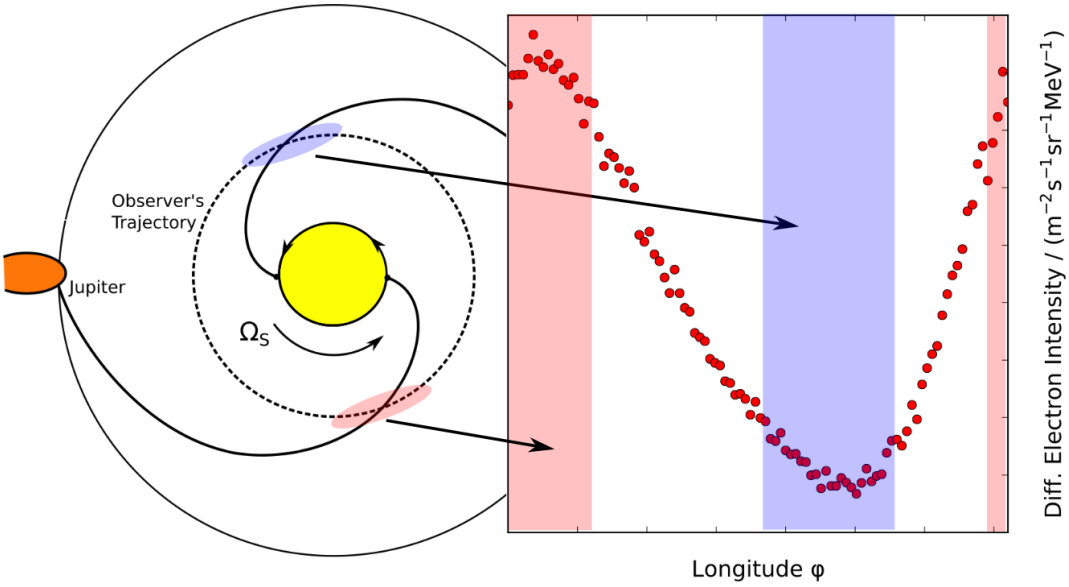

Figure 6.3: *Influence of the connectivity between the Jovian magnetosphere (orange) and the observer's trajectory (dashed circle). Whereas the left panel shows the (magnetic) geometry as a top view sketch the right panel shows the corresponding simulation results for an initial (or observational) energy of $E^{init} = 6$ MeV. The shaded areas indicate good (red) and bad (blue) magnetic connection. Whereas Jovian electron are able to reach the observer by propagation along the Parker spiral (parallel diffusion) in order to reach the badly connected observational point, perpendicular diffusion has to dominate the propagation process.*

spirals as introduced in Section 2.4.1 are sketched for good (red) and bad (blue) magnetic connections to representative points on the observer's trajectory (dashed circle). The simulation results in the right panel show the characteristic variation due to the changing connectivity with longitude which is detectable as a 13 month synodical periodicity in Earth orbit low-MeV electron data as discussed in Section 3.2 and shown in Fig. 3.3. As indicated by the sketched nominal Parker spirals in case of good connection Jovian electrons are able to reach the observational point by means of more effective parallel diffusion along the magnetic field lines whereas in case of bad connection the propagation has to be dominated by perpendicular diffusion. The deviating effectiveness of parallel and perpendicular diffusion subsequently are reflected in the variation of the differential intensities depending on the magnetic connection to the source. This correlation will be utilised in Secs. 6.4.1 and 6.4.2 in order to estimate the parallel and perpendicular mean free paths $\lambda_{\parallel}(1\text{ AU})$ and $\lambda_{\perp}(1\text{ AU})$. The skewness of the differential intensity variation will be discussed in Section 6.4.6 by means of Fig. 6.15.

6.1.1 Numerical Implementation

In order to investigate the parameter dependences of charged particle modelling the TPE by Parker (1965) is solved via its SDE representation in a time-backward numerical scheme. Therefore the equivalent set of SDEs for the TPE as given by Eq. (5.55) has to be found. As discussed in Chapter 4 the Kolmogorov time-backward equation as given by Eq. (4.32) and its corresponding SDE formulation Eq. (4.35) are equivalent as they describe the same differential equation. To highlight the fact that a set of multiple SDEs has to be derived, here the Kolmogorov time-backward equation is given explicitly as

$$-\frac{\partial f}{\partial s} = \sum_i \left(A_i \frac{\partial f}{\partial x_i} \right) + \frac{1}{2} \sum_{i,j} \left(C_{ij} \frac{\partial^2 f}{\partial x_i x_j} \right) \tag{6.1}$$

with $C_{ij} = (B \cdot B^T)_{ij}$ describing the diffusive processes according to Eq. (4.34). The backward time variable s thereby can be defined as related to the normal time t via

$$t = T_{end} - s \tag{6.2}$$

via a final time T_{end} for $s \geq 0$. As shown by e.g. Strauss et al. (2011a) the time backward integration of Eq. (6.1) from the initial time defined as $s = 0,\ t = T_{end}$ to the present time $s = T_{end},\ t = 0$ leads to

$$\frac{\partial f}{\partial t} = \sum_i \left(A_i \frac{\partial f}{\partial x_i} \right) + \frac{1}{2} \sum_{i,j} \left(C_{ij} \frac{\partial^2 f}{\partial x_i x_j} \right) \tag{6.3}$$

with $\partial t = -\partial s$. Eq. (6.3) thereby contains both time-backward phase-space coordinates and a time forward time coordinate (Kloeden and Platen, 2011). Furthermore this variant of the Kolmogorov time backward equation allows to rewrite the TPE as given by Eq. (5.55) accordingly. Therefore the diffusion tensor which is assumed to be aligned to the magnetic field as

$$\hat{\kappa} = \begin{pmatrix} \kappa_{\parallel} & 0 & 0 \\ 0 & \kappa_{\perp r} & 0 \\ 0 & 0 & \kappa_{\perp \theta} \end{pmatrix}, \tag{6.4}$$

has to be transformed into the geometry of a Parker-like HMF:

$$\hat{\kappa} = \begin{pmatrix} \kappa_{\parallel} & 0 & 0 \\ 0 & \kappa_{\perp r} & 0 \\ 0 & 0 & \kappa_{\perp \theta} \end{pmatrix} \quad \longrightarrow \quad \hat{\kappa}_{\text{sphere}} = \begin{pmatrix} \kappa_{rr} & \kappa_{r\theta} & \kappa_{r\phi} \\ \kappa_{\theta r} & \kappa_{\theta\theta} & \kappa_{\theta\phi} \\ \kappa_{\phi r} & \kappa_{\phi\theta} & \kappa_{\phi\phi} \end{pmatrix}. \tag{6.5}$$

Figure 6.4 visualises this transformation. The Parker angle Ψ as introduced by Eq. (2.10) in Section 2.4 therey describes the deviation of the tangent $\vec{B}(r)$ of the HMF from the radial outflow whereas the angle ζ indicates the deviation from the ecliptic plane, defined as

$$\tan\psi = -\frac{B_\phi}{\sqrt{B_r^2 + B_\theta^2}} \quad \text{and} \quad \tan\zeta = \frac{B_\theta}{B_r}, \tag{6.6}$$

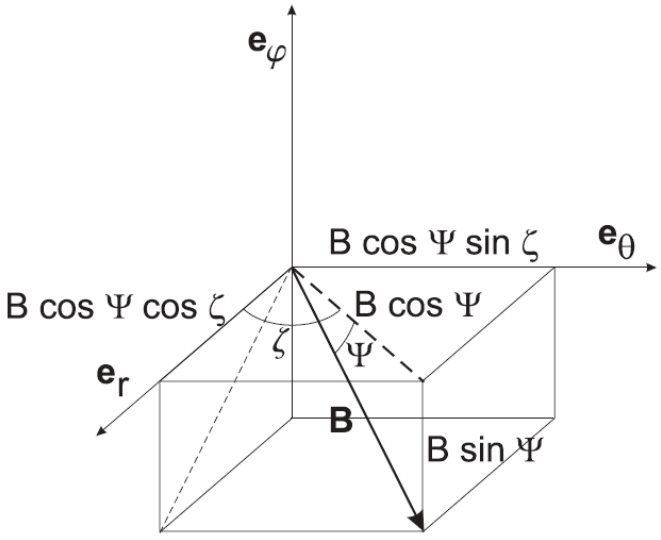

Figure 6.4: *Geometrical transformation of the diffusion tensor $\hat{\kappa}$ aligned to the HMF as given by Eqs. (6.7) and (6.8) according to Burger et al. (2000)*

respectively. As shown in detail by Burger et al. (2000) and indicated in Figure 6.4 by means of annotation this leads to the general transformation terms

$$\begin{aligned}
\kappa_{rr} &= \kappa_{\perp\theta}\sin^2\zeta + \cos^2\zeta(\kappa_{\parallel}\cos^2\psi + \kappa_{\perp r}\sin^2\psi)\\
\kappa_{r\theta} &= \sin\zeta\cos\zeta(\kappa_{\parallel}\cos^2\psi + \kappa_{\perp r}\sin^2\psi - \kappa_{\perp\theta})\\
\kappa_{r\phi} &= -(\kappa_{\parallel} - \kappa_{\perp r})\sin\psi\cos\psi\cos\zeta\\
\kappa_{\theta r} &= \sin\zeta\cos\zeta(\kappa_{\parallel}\cos^2\psi + \kappa_{\perp r}\sin^2\psi - \kappa_{\perp\theta})\\
\kappa_{\theta\theta} &= \kappa_{\perp\theta}\cos^2\zeta + \sin^2\zeta(\kappa_{\parallel}\cos^2\psi + \kappa_{\perp r}\sin^2\psi)\\
\kappa_{\theta\phi} &= -(\kappa_{\parallel} - \kappa_{\perp r})\sin\psi\cos\psi\sin\zeta\\
\kappa_{\phi r} &= -(\kappa_{\parallel} - \kappa_{\perp r})\sin\psi\cos\psi\cos\zeta\\
\kappa_{\phi\theta} &= -(\kappa_{\parallel} - \kappa_{\perp r})\sin\psi\cos\psi\sin\zeta\\
\kappa_{\phi\phi} &= \kappa_{\parallel}\sin^2\psi + \kappa_{\perp r}\cos^2\psi.
\end{aligned} \tag{6.7}$$

As in case of this thesis the transformation is performed as a rotation around the $\vec{e}_\theta$ axis (Burger et al., 2008), the corresponding angle is given by $\zeta = 0$ and as a consequence the transformed diffusion tensor becomes diagonal and $\kappa_{\theta r} = \kappa_{r\theta} = \kappa_{\phi\theta} = \kappa_{\theta\phi} = 0$[1]. The set of transformed diffusion coefficients subsequently simplifies to

$$\begin{aligned}
\kappa_{rr} &= \kappa_{\parallel}\cos^2\psi + \kappa_{\perp r}\sin^2\psi\\
\kappa_{r\phi/\phi r} &= -(\kappa_{\parallel} - \kappa_{\perp r})\sin\psi\cos\psi\\
\kappa_{\theta\theta} &= \kappa_{\perp\theta}\\
\kappa_{\phi\phi} &= \kappa_{\parallel}\sin^2\psi + \kappa_{\perp r}\cos^2\psi.
\end{aligned} \tag{6.8}$$

With this transition it now is possible to explicitly formulate Eq. (6.3) in relation to the TPE by Parker (1965) as given by Eq. (5.55). Taking the transformed diffusion tensor into

[1] A generalised expression for non axis-symmetrical perpendicular diffusion is given by Effenberger et al. (2012)

account, the TPE reads in spherical spatial coordinates and terms of energy as

$$\begin{aligned}\frac{\partial f}{\partial t} =& \left[\frac{1}{r^2}\frac{\partial}{\partial r}(r^2\kappa_{rr}) + \frac{1}{r^2\sin\theta}\frac{\partial\kappa_{\phi r}}{\partial\phi} - u_{SW}\right]\frac{\partial f}{\partial r} \\ &+ \left[\frac{1}{r^2\sin\theta}\frac{\partial}{\partial\theta}(\kappa_{\theta\theta}\sin\theta)\right]\frac{\partial f}{\partial\theta} \\ &+ \left[\frac{1}{r^2\sin\theta}\frac{\partial}{\partial r}(r\kappa_{r\phi}) + \frac{1}{r^2\sin^2\theta}\frac{\partial\kappa_{\phi\phi}}{\partial\phi}\right]\frac{\partial f}{\partial\phi} \\ &+ \kappa_{rr}\frac{\partial^2 f}{\partial r^2} + \frac{\kappa_{\theta\theta}}{r^2}\frac{\partial^2 f}{\partial\theta^2} + \frac{\kappa\phi\phi}{r^2\sin^2\theta}\frac{\partial^2 f}{\partial\phi^2} + \frac{2\kappa_{r\phi}}{r\sin\theta}\frac{\partial^2 f}{\partial r\partial\phi} \\ &+ \frac{1}{3r^2}\frac{\partial}{\partial r}(r^2 u_{SW})\frac{\partial}{\partial E}(\Gamma E f) \\ &\text{with}\quad \Gamma = \frac{E+2E_0}{E+E_0}.\end{aligned} \tag{6.9}$$

according to e.g. Strauss et al. (2011a). Thereby Γ which is $\Gamma = 1$ for highly relativistic and $\Gamma = 2$ for non-relativistic particles appears as a consequence of transforming the adiabatic momentum changes to relativistic energies as pointed out by Parker (1966). Thereby E_0 denotes the rest energy of the particle. Rearranged and written in terms of Eq. (6.3) it becomes transparent, how to construct the corresponding set of SDEs

$$\begin{aligned}\frac{\partial f}{\partial t} =& a_r\frac{\partial f}{\partial r} + a_\theta\frac{\partial f}{\partial\theta} + a_\phi\frac{\partial f}{\partial\phi} + a_E\frac{\partial f}{\partial E} \\ &+ C_{rr}\frac{\partial^2 f}{\partial r^2} + C_{\theta\theta}\frac{\partial^2 f}{\partial\theta^2} + C_{\phi\phi}\frac{\partial^2 f}{\partial\phi^2} + C_{r\phi}\frac{\partial^2 f}{\partial r\partial\phi},\end{aligned} \tag{6.10}$$

Whereas the elements of the convection vector $\vec{a}$ can be identified by comparing Eq. (6.9) and (6.10) as

$$\begin{aligned}a_r &= \frac{1}{r^2}\frac{\partial}{\partial r}(r^2\kappa_{rr}) + \frac{1}{r\sin\theta}\frac{\partial\kappa_{\phi r}}{\partial\phi} - u_{SW} \\ a_\theta &= \frac{1}{r^2\sin\theta}\frac{\partial}{\partial\theta}(\kappa_{\theta\theta}\sin\theta) \\ a_\phi &= \frac{1}{r^2\sin\theta}\frac{\partial}{\partial r}(r\kappa_{r\phi}) + \frac{1}{r^2\sin^2\theta}\frac{\partial\kappa_{\phi\phi}}{\partial\phi} \\ a_E &= \frac{1}{3r^2}\frac{\partial}{\partial r}(r^2 u_{SW})\Gamma E.\end{aligned} \tag{6.11}$$

according to e.g. Strauss et al. (2011a), in contrast the elements of volatility matrix b connect to the elements of the diffusion tensor $C_{ij} = (B\cdot B^T)_{ij}$ as discussed in Section 4.4 in a way that is not that intuitive to obtain. Kopp et al. (2012) discuss in great detail several possibilities to find square roots of the diffusion tensor by means of permutations. As shown by Strauss et al. (2011a) applying these findings leads to two possible solutions for the volatility matrix which are mathematical equivalent and provide the identical results (Gardiner, 2009) and are given by

$$b^{\pm} = \pm\sqrt{2}\begin{pmatrix}\sqrt{\kappa_{rr} - \frac{\kappa_{\phi r}^2}{\kappa_{\phi\phi}}} & 0 & \frac{\kappa_{\phi r}}{\sqrt{\kappa_{\phi\phi}}} \\ 0 & \frac{\sqrt{\kappa_{\phi\phi}}}{r} & 0 \\ 0 & 0 & \frac{\sqrt{\kappa_{\phi\phi}}}{r\sin\theta}\end{pmatrix}. \tag{6.12}$$

As no second order energy effects are taken into account, Eq. (6.12) only contains spatial elements as pointed out by Strauss et al. (2011a). In following the b^+ variant of Eq. (6.12)

will be used. Combining the parameters found by Eqs. (6.11) and (6.12) with the derivation of the corresponding set of SDEs in Section 4.4 resulting in Eq. (4.35) one obtains the set of SDEs as derived by Strauss et al. (2011a) and implemented in the framework by Dunzlaff et al. (2015). The set of SDEs as used for this work therefore are given by

$$\begin{aligned}
dr &= \left[\frac{1}{r^2}\frac{\partial}{\partial r}(r^2\kappa_{rr}) + \frac{1}{r\sin\theta}\frac{\partial\kappa_{r\phi}}{\partial\phi} - u_{SW}\right]ds \\
&\quad + \sqrt{2\kappa_{rr} - \frac{2\kappa_{r\phi}^2}{\kappa_{\phi\phi}}}d\omega_r + \frac{\sqrt{2\kappa_{r\phi}}}{\kappa_{\phi\phi}}d\omega_\phi \\
d\theta &= \left[\frac{1}{r^2\sin\theta}\frac{\partial}{\partial\theta}(\sin\theta\kappa_{\theta\theta})\right]ds + \frac{\sqrt{2\kappa_{\theta\theta}}}{r}d\omega_\theta \\
d\phi &= \left[\frac{1}{r^2\sin^2\theta}\frac{\partial\kappa_{\phi\phi}}{\partial\phi} + \frac{1}{r^2\sin\theta}\frac{\partial}{\partial r}(r\kappa_{r\phi})\right]ds + \frac{\sqrt{2\kappa_{\phi\phi}}}{r\sin\theta}d\omega_\phi \\
dE &= \left[\frac{1}{3r^2}\frac{\partial}{\partial r}(r^2u_{SW})\Gamma E\right]ds.
\end{aligned} \tag{6.13}$$

In case of a radial constant Solar wind speed $du_{SW}/dr = 0$ the energy equation simplifies to

$$dE = \left[\frac{2}{3r}u_{SW}\Gamma E\right]ds \tag{6.14}$$

corresponding to the term for the adiabatic energy changes (see Eq. (5.53)) derived in Section 5.4.

6.1.2 Transport Parameters

As already pointed out in the introduction to this Chapter, the simulation setup used for this work is optimised regarding efficiency in order to perform large parameter studies. Therefore the modelling approach uses a simplified parameter approach, optimised for electron propagation in the low-MeV range. First of all, all drift effects are neglected as they appeared to be insignificant within the energy range in question. As a consequence the drift velocity usually referred to as $\vec{v}_d$ is omitted from the derivation of the SDEs as given by Eq. (6.13). This assumption is based both on previous modelling studies by e.g. Potgieter (1996), Burger et al. (2000) and Ferreira and Potgieter (2002) (amongst others) and theoretical investigations such as the studies by e.g. Bieber et al. (1994) and Engelbrecht and Burger (2010). Furthermore the Solar wind speed $\vec{u}_{SW}$ is assumed to be globally constant and radially outward at all times, a simplified estimation based on observations by e.g. Kojima et al. (1992) and Gazis et al. (1994). These assumptions mirror ideal conditions as present during Solar minima as discussed in Section 2.1.1, disregarding phenomena such as CIRs and CMEs, which have to be excluded from corresponding spacecraft data in order to assure comparability with the simulation results. For a detailed discussion see Section 7.4.2, in which these considerations are applied. In continuation of the approach by Strauss et al. (2011a) as implemented by Dunzlaff et al. (2015) this work derives the diffusion coefficients as they appear in Eq. (6.4) in terms of the mean free path as discussed in Section 5.3. The radial dependence of the mean free path thereby is given in relation to the length of the mean free path at Earth orbit $\lambda_0 = \lambda(r_0)$ with $r_0 = 1.0$ AU:

$$\lambda_\parallel(r) = \frac{\lambda_0}{2}\left(1 + \frac{r}{r_0}\right), \tag{6.15}$$

As shown and discussed based on propagation and turbulence theory in Section 5.3.3, it is reasonable to assume the electron mean free path as not rigidity dependent in the energy range in question. In Section 6.4.1 this estimation will be shown as successfully tested in order to reproduce the Jovian source spectrum as measured at Earth orbit. The parallel diffusion coefficient $\kappa_{\parallel}$ is scaled by the parallel mean free path $\lambda_{\parallel}$ by means of the particle speed ν:

$$\kappa_{\parallel}(r) = \frac{\nu}{3}\lambda_{\parallel}(r). \tag{6.16}$$

Because electrons in the high-keV to low-MeV range propagate more or less with the speed of light, it is assumed that $\nu = c$. The perpendicular diffusion coefficients as they are defined in Eq. (6.4) are set as $\kappa_{\perp} = \kappa_{\perp r} = \kappa_{\perp\theta}$. The resulting perpendicular diffusion coefficient $\kappa_{\perp}$ is assumed as being proportional to the parallel one by the proportional factor χ such that

$$\kappa_{\perp}(r) = \chi\kappa_{\parallel}(r). \tag{6.17}$$

As already pointed out by Vogt et al. (2020) this is basically an *ad hoc* approach to modelling diffusion parameters. Nevertheless the results represent the radial dependence of the quasi-linear theory electron diffusion coefficient as developed and used by e.g. Burger et al. (2000), Ferreira et al. (2001a), Strauss et al. (2011a, 2013) and Engelbrecht and Burger (2015) in the inner Heliosphere. Although the behaviour of the parallel mean free path appears to be more complex as indicated by e.g. Shalchi (2009), Engelbrecht and Burger (2015) and Gammon and Shalchi (2017)(amongst others) the approach as given by Eq. (6.17) serves the purpose of the limited cases investigated herein. A more detailed discussion about the dependences and reliability of this approach to the parallel and perpendicular mean free path will be given in Secs. 6.4.1, 6.4.2 and 6.4.3, respectively. How a more up to date approach to implement the dependences of the mean the free path can be utilised in order to apply this simulation setup to turbulence research will be outlined in Chapter 8, regarding future works.

6.2 The Interpretation of Phase Space Trajectories

As discussed in Chapter 4 and Secs. 4.2 and 4.4 in particular, the solutions of the SDE modelling approach provide a set of phase-space trajectories due to the random-walk like nature of the Wiener process. Again, these phase-space trajectories themselves consist each of a chain of point-like solutions of the TPE both in position space and time and form the phase-space trajectory by means of their timely succession. Due to the nature of this solution-method one has to sample over a multitude of phase-space trajectories in order to approximate the global solution of the PDF $f(\vec{r}, t)$ as defined by the differential equation form of the TPE. This notion of course raises the question how the individual phase-space trajectories of point-like solutions are related to the global solution. And how they have to be sampled on order to obtain such an approximated global solution.

Therefore we have to consider first how to interpret a point-like value of a probability density. If we define N_i as the number of steps the random walk performed in order to constitute a phase-space trajectory i, then r_n with $0 \leq n \leq N$ is the spatial point the random walk reached after n steps. The value of the PDF in that point $f(r_n, t_n)$ would provide the probability to find the particle there. In contrast the point-like solutions of the set of SDEs are equally probable in a mathematical sense. In order to bring them to

accordance with a global solution, therefore a large amount of phase-space trajectories have to be simulated and subsequently normalised. Else-wise the solution would be depending on the number of phase-space trajectories, on the number which hit the respective boundary and indirectly on the total number of phase-space trajectories which are simulated, too. In mathematical terms, the solutions describe the point-like the evolution of a probability density function which has to meet the definition given by Eq. (4.23) that its integral over the whole phase space has to be unity. This is often illustrated by the perception that different amounts of so-called pseudo-particles are assigned to the different trajectories based on their physical significance (see e.g. Kopp et al., 2012; Strauss et al., 2011a) and for a roundup of the discussion herein, Vogt et al. (2020). The term pseudo-particle however demands an explanation itself.

As the TPE by Parker (1965) describes particle propagation by means of a PDF, the SDE representation of the TPE can not describe the motion of physical particles. Rather the phase space trajectories represent the evolution of the particle density distribution f point-like through the Heliosphere. Considering the assumptions made for the TPE by Parker (1965) as discussed in Section 5.5 these phase space density elements can be interpreted as isotropic and gyrotropic i.e. that there is no significant anisotropy in the pitch-angle space either. This leads to the concept that phase space trajectories are representing the evolution of an ensemble of pseudo-particles which is averaged over both the pitch angle and the gyrophase. But since the TPE describes the evolution of a distribution function, the impression that the results of its SDE restatement would also cover particle motion is caused by the method of solution and not rectified within the equations themselves. Taking up the interpretation of the local solutions as representing an ensemble of pseudo-particles with certain common qualities, the phase-space trajectories appear to be more accurately interpreted as a physically guided but random search for these particles position. Within this picture the spatial evolution decides where to look next for the value of the distribution function and the particle ensemble, respectively. Therefore, this gedanken experiment leads to the conclusion that the individual solutions which form the space-space trajectories can not represent the motion of physical particles, because the definition of the ensembles of pseudo-particles which evolution is described by their corresponding phase-space trajectories, exhibits a reverse causality. The motion of a consistent ensemble of pseudo-particles does not define the phase-space trajectory, but the common phase-space trajectory defines the associated ensemble of pseudo-particles.

While the random walk which subsequently form the phase-space trajectories aims to be determined by the same physical processes as the particle motion itself, its implementation differs as the probability density is calculated for point-wise and not globally. Mathematically this is reflected by the fact that two variants of convergence are to be distinguished for SDE simulations in order to evaluate the accuracy of the solutions: functional and path-wise convergence as detailed by e.g. Kloeden and Platen (2011). As the original TPE does not describe the motion of individual particles but the evolution of the particle ensemble throughout the whole Heliosphere, as discussed above, its SDE representation consequently can only achieve functional convergence too. This is, in mathematical terms the interpretation derived from physical considerations in the paragraph above.

How to handle the consequences of the discrepancy between the mathematical and physical probability of the phase-space trajectories, is one of the major question determining the following Chapters and Sections of this work. Therefore it is important to restate in this context that despite the fact that a sufficient ensemble of phase-space trajectories can be interpreted physically, the particular phase-space trajectories are not to be mistaken for representing the actual motion of physical particles. As pointed out by Vogt et al. (2020) a phase-space trajectory should bear the same physical significance regardless which physical quantity corresponding to it is investigated. Due to these considerations this work prefers

a different terminologies and avoids the pseudo-particle interpretation. Instead this work restricts itself to assign a physical significance (or more accessible: a weight with respect to the resulting differential intensity) to individual phase-space trajectories which bear themselves no physical meaning despite being mathematically correctly derived solutions of the FPE. Therefor to distinguish these weighted and unweighted trajectories also the terms physical vs. mathematical solution will be used. How the physical significance of the individual phase-space trajectories is determined will be discussed in the following Section.

6.3 The Calculation of Differential Intensities

Applying the considerations made above in the previous Section 6.2 to the mathematical framework of the SDE modelling approach raises the question, how the individual phase-space trajectories are mathematically linked to the resulting differential intensity and what the distributions of the exit energies of these phase-space trajectories tell about the method itself. Linked to this question of course is the one how the concept of diffusion itself (as represented by the solutions of the SDE approach) is related to the physical processes within the Heliosphere and whether the application of boundary conditions within the SDE approach illustrates this relationship.

6.3.1 Boundary Conditions

According to Strauss and Effenberger (2017) the (physical) solution at any point within the phase space can be obtained by solving the convolution of the Green's function $G(x,t)$ of the PDE (see e.g. Webb and Gleeson, 1977) with the boundary conditions $f_b(x,t)$

$$f(x,T) = \int_0^T \int_x G(x',t) f_b(x',t) dx' dt \tag{6.18}$$

at any point x and any final time T. Within this relation as pointed out by e.g. Pei et al. (2010) (amongst others) the Green's function $G(x,t)$ is normalised as

$$\int_0^\infty \int_{-\infty}^\infty G(x',t) f_b(x',t) dx' dt = 1. \tag{6.19}$$

As discussed by Strauss and Effenberger (2017) the boundary condition $f_b(x,t)$ for both the spatial boundaries and the temporal boundary at $t = T$ can be most generally given by

$$f_b(x,t) = g(t)\delta(x + x_{b,+}) + h(t)\delta(x - x_{b,-}) + k(x)\delta(t), \tag{6.20}$$

with $x_{b,+/-}$ denoting the spatial boundaries and $g(t)$ being the left and $h(t)$ the right boundary conditions. Due to the qualities of the δ function the normalization as defined by Eq. (6.19) still applies. In the case of this thesis however, the last term with $k(x)$ representing the initial boundary conditions can be omitted. This is due to the fact that by means of the time-backward integration not only Jovian source but also the spatial boundary of the Heliopause as the source of the GCR population become spatial boundary

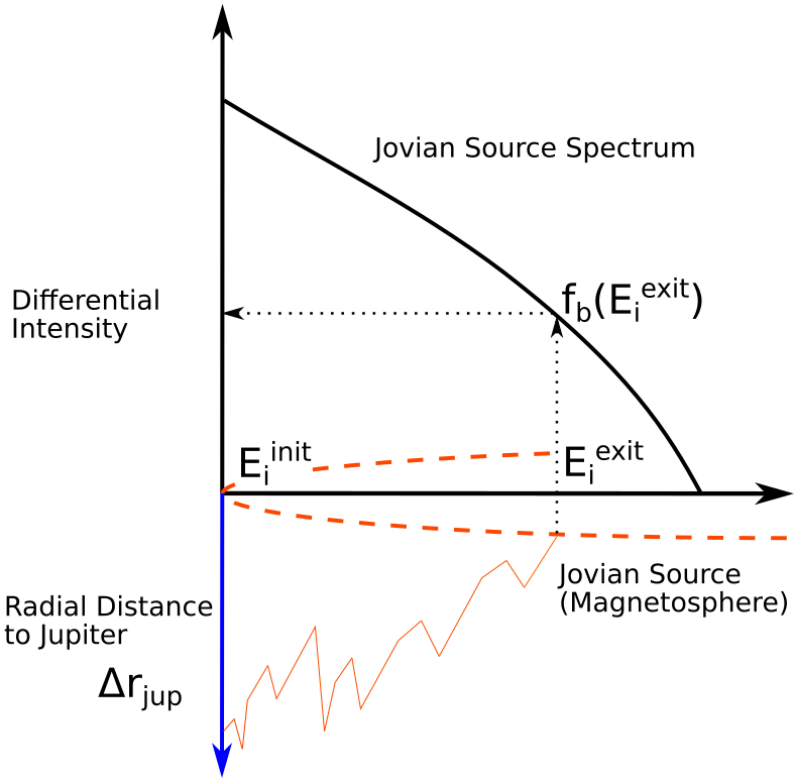

Figure 6.5: *Visualisation of how the (Jovian) source spectrum determines the resulting differential intensity. The sketch thereby is to be read from bottom to top. The pseudo-particle is injected with an initial energy E_i^{init} at a certain distance to the (Jovian) source. As given by Eq. (6.14) only the radial distance does influence the adiabatic energy gain in case of a constant Solar wind speed. When the pseudo-particle's phase-space trajectory hits the source with the exit energy E_i^{exit} it is convoluted with the source spectrum as the boundary condition. Subsequently the differential intensity is calculated as $\sum_i f_b(E_i^{exit})$. The dashed representation of the Jovian magnetosphere thereby only serves and illustrative purpose.*

conditions instead of initial conditions. Therefore the different exit positions as discussed in Section 6.1 are implemented as different spatial boundary conditions. As noted by Strauss and Effenberger (2017) the Green's function appears to be invariant to the transformation from forward time t to backward time $s = T - t$:

$$G(x, t = 0) = G(x, s = T). \tag{6.21}$$

As pointed out by Strauss and Effenberger (2017) Eq. (6.18) can be rewritten under these assumptions as

$$f(x_0, t_0) = \int_0^{t_0} \int_{x \in \Omega_b} f_b(x, t) \rho(x, t) d\Omega dt \tag{6.22}$$

with $\rho(x, t)$ representing the conditional probability density (i.e. the point-wise solution where the phase-space trajectory hits the boundary) and $f(x_0, t_0)$ the resulting phase space density at the observational point (x_0, t_0). The boundary of the integration domain is given by Ω_b representing the corresponding source region in more physical terms. Eq. (6.22) can be simplified even further, if only steady state solution of the TPE are considered which means that $t \to \infty \Rightarrow \rho(x, t) :\to \rho(x)$. Due to the nature of both the Wiener process and the solution method, respectively, each random walk step of the phase-space trajectory can be interpreted in this case to constitute a steady state solution independent from the

temporal dimension. Therefore only considering the steady state case enables to reduce Eq. (6.22) to

$$f(x_0) = \int_{x\in\Omega_b} f_b(x)\rho(x)d\Omega. \tag{6.23}$$

Because the boundary conditions are in this case the source function of the Jovian source (see Eq. 3.9) in Section 3.2) or the LIS, it follows that the boundary values only depend on the momentum or energy assigned to the corresponding phase-space trajectory. Therefore only integration over the energy space has to be performed, i.e. $d\Omega :\rightarrow dE$ and Eq. (6.23) can be transformed to

$$f(x_0) = \int_{E^{init}}^{\infty} f_b(E)\rho(E)dE\Big|_{x\in\Omega_b} \tag{6.24}$$

which is (as pointed out by Strauss and Effenberger, 2017) a convolution of the boundary condition with the probability distribution. The most general method to apply the boundary conditions as given by Eq. (6.24) would be to solve the set of SDE in order to calculate $\rho(x)$. The numerically easier approach as also utilised in this work calculates for each phase-space trajectory an individually weighted value of $f_i(x_0)$. The normalization to the correct magnitude is subsequently performed at the end of the integration process. Mathematically, reaching a boundary for a single phase-space trajectory with $E_i = E_i^{exit}$ can be expressed as

$$\rho_i(x) = \delta(E_i - E_i^{exit})\big|_{x\in\Omega_b} \tag{6.25}$$

as follows from the normalization condition Eq. (6.19) equivalently to the definition of the general boundary condition by Eq. (6.20). As a direct consequence of Eq. (6.25), the convolution given by Eq. (6.24) reduces for individual phase-space trajectories to

$$f_i(x_0) = f_b(E_i^{exit}). \tag{6.26}$$

The result can be described as an individual weighting factor determining how much the phase-space trajectory contributes to the differential intensity and therefore also defining its physical significance. In Fig. 6.5 the relation as described by Eq. (6.26) is visualised. Below the x-axis representing the energy E_i the negative y-axis indicates the radial distance of the phase-space element to Jupiter. In orange the trajectory through the energy space is sketched until the Jovian magnetosphere is crossed where $E_i = E_i^{exit}$. Above the x-axis the Jovian source spectrum is given as differential intensity over energy. By dotted arrows the convolution with the boundary is sketched as as performed by applying Eq. (6.26). This provides a differential intensity for each trajectory depending on the exit energy E_i^{exit}. As each phase-space trajectory is basically a series of δ injections normalised to one (see e.g. Parker, 1965, and the discussion of probability density peaks therein) the obtained differential intensities for the complete set of N phase-space trajectories subsequently have to be normalised as

$$f(x_0) = \frac{1}{N}\sum_{i=1}^{N} f_b(E_i^{exit}). \tag{6.27}$$

In the following the significance of applying Eq. (6.27) will by examined. Thereby we will compare the distribution of the phase-space trajectories with the fractions of the resulting Differential intensities as attributed to them by Eq. (6.27). Understanding the genesis of the simulation results subsequently provides the possibility to judge more reliable how to apply them in order to investigate the (parameter) dependences of charged particle transport and the physics therein. These tasks will be picked up in the following Section 6.4 and expanded in the remaining Chapters to the question of how to estimate residence times and a realistic measure of mean free paths as well as the turbulence physics underlying them.

6.3.2 The Significance of Weighting with the Source

In order to illustrate how the individual phase-space trajectories relate to the resulting differential intensities, Fig. 6.6 shows the normalised histogram of the number of phase space trajectories for three different representative initial energies E^{init}. In total simulations were carried out for thirty initial energies spaced logarithmically between $E^{init}_{min} = 0.0003$ GeV and $E^{init}_{max} = 0.1$ GeV over the whole energy range of the Jovian source spectrum for two observational points a $r^{init} = 1$ AU. A complete overview of the results for all thirty different initial energies will be given by Fig. 6.7 and discussed later on in this Section. In order to display the dependence on the magnetic connection as illustrated before in Fig 6.3 the point of best and worst magnetic connectivity was chosen (i.e. the points of maximal and minimal Jovian fluxes). For the parallel mean free path according to Eq. (6.15) a value of $\lambda_0 = 0.15$ was chosen alongside $\chi = 0.0125$ following the definition by Eq. (6.17). The Heliospheric boundary was set at $R = 120$ AU and the Solar wind speed at the constant value of $u_{SW} = 400$ km/s, which is a standard value for the slow Solar wind speed as discussed in Section 2.2. As the time increment $\Delta s = 0.0001$ in program units was utilised, which corresponds to $\Delta s \approx 0.0004$ days≈ 0.62 min and a maximum integration time of $T_{end} = 800$ in program units, corresponding to $\sum \Delta s \approx 300$ days. For a more detailed discussion on these parameters and how they are derived to be the most realistic and reliable parameter set in order to simulate Jovian electron transport via the SDE approach see Section 6.4 and the corresponding subsections as well as Tab. 6.1.

A total of #50000 trajectories are integrated for each simulation seen in Fig. 6.6 in order to obtain a statistical significant and reliable amount of trajectories exiting at the Jovian source boundary. Therefore the histograms displayed in Fig. 6.6 are binned according to the exit energies E^{exit}_i at the Jovian source boundary. This means that the phase-space trajectories with exit energies in the range of $E^{exit}_i \in [E^{init}, 20E^{init}]$ are sorted into 100 logarithmically spaced bins. In red the phase-space trajectories are shown (binned as N_i/N) whereas the blue histograms show the same phase space trajectories weighted by the Jovian source boundary, illustrating their fractional impact on the differential intensity according to Eq. (6.27). Both distributions are normalised to unity. Whereas the red histogram show the results of the random walk based on the probabilities as defined by the Wiener process (see Eq. (4.18) and the subsequent discussion in Secs. 4.2 and 4.4) the blue histograms show how these results are weighted according to their physical probability (see the discussion in Section 6.2) as visualised by Fig. 6.5. Regarding the pseudo-particle interpretation one can say that the phase-space trajectory within the blue histogram are weighted according to the amount of pseudo-particle they represent. Contrary the red bins refer to just the evolution of the phase-space density elements without considering the boundary conditions.

In order to cover the influence of the magnetic connection on the simulation results, the left panels of Fig. 6.6 show the energy distribution of the phase-space trajectories in case of optimal connection between observer and the source whereas the right panels show the opposite case. Whereas the point of optimal connectivity can be obtained by calculating the relative position of the observer and Jupiter if they are connected by the same Parker spiral (see e.g. Section 2.4.1) the point of opposition or worst magnetic connection was set to be the minimum of the longitudinal dependent intensity distribution as shown e.g. by Fig. 6.3.

Most significantly Fig. 6.6 shows by comparison of the red and blue histograms that only a very limited fraction of phase-space trajectories contribute to the results. Looking at the

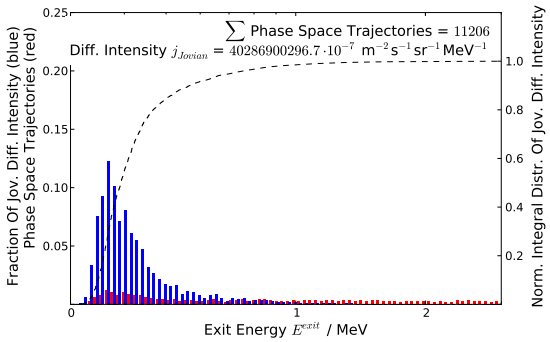

(a)

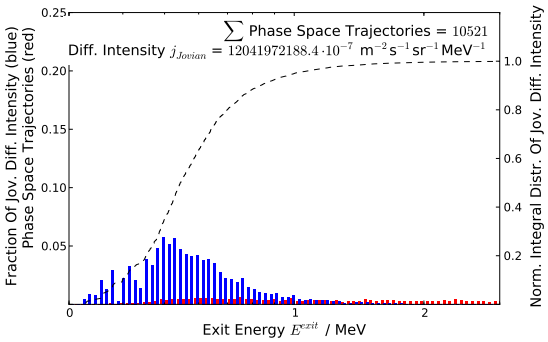

(b)

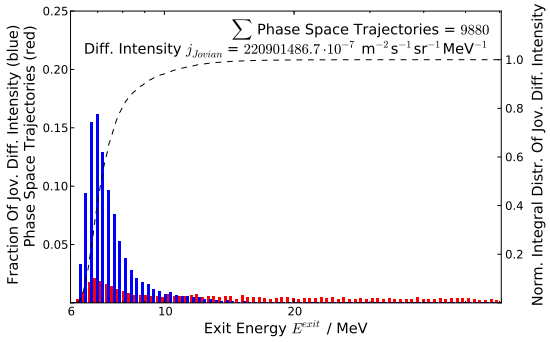

(c)

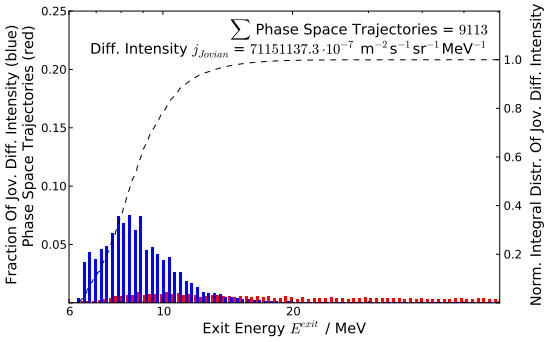

(d)

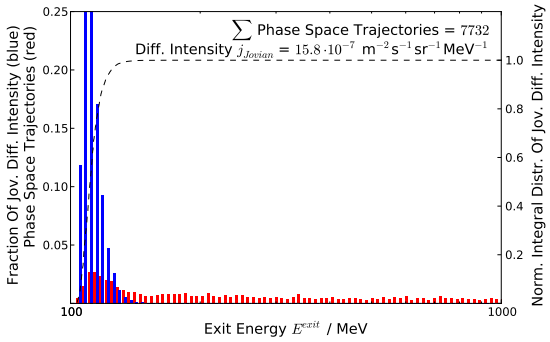

(e)

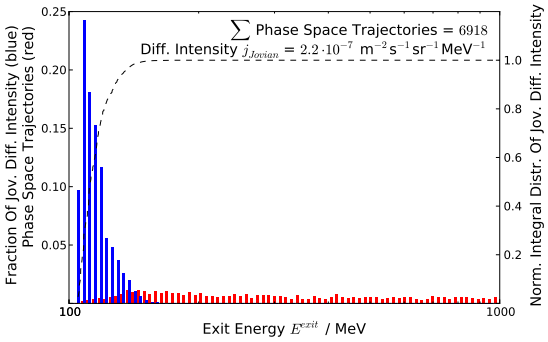

(f)

Figure 6.6: *Binned distribution of exit energies E_i^{exit} (red) and their corresponding significance to the resulting differential intensities (blue). The left panels Figs. 6.6a, 6.6c and 6.6e show the case of good connection in contrast to case of bad connection on the right panels. The dashed lines show the integral distribution of the fractional differential intensities, visualising the convergence with increasing exit energies. The upper most panels Figs. 6.6a and 6.6b show the distributions for an initial energy of $E_i^{init} = 0.3$ MeV, whereas the two middle panels Fig. 6.6c and 6.6d as already published by Vogt et al. (2020) show the case of $E_i^{init} = 6$ MeV. The distributions within Fig. 6.6e and 6.6f show an initial energy of $E_i^{init} = 100$ MeV. In order to show the energy dependent effects of weighing the phase-space trajectories with the source spectrum, all panels show the range of $[E_i^{init}, 10 \cdot E_i^{init}]$ on the energy axis.*

both upper most panels with an initial energy of $E^{init} = 0.3$ MeV the range of exit energies relevant for the resulting differential intensity is narrowed to $\sim 2E^{init}$ for good (Fig. 6.6a) and $\sim 3E^{init}$ for bad magnetic connection as shown in Fig. 6.6b. In order to illustrate this effect further and more comprehensible the dashed black lines in the panels of Fig. 6.6 show the normalised integral distribution of the differential intensity which indicates to what amount the phase-space trajectories with lower or equal exit energies contribute to the result (right hand axis). As one would expect the integral distribution are much steeper in case of good connection as given by Figs. 6.6a, 6.6c and 6.6e in contrast to Figs. 6.6b, 6.6d and 6.6f. This of course is due to the fact that parallel diffusion dominates the particle propagation in case of good connection and therefore leads to a much more efficient particle transport reflected in less energy gain (in our time backward simulation, i.e. less energy loss for Jovian electrons propagating to 1 AU). The comparison of Fig. 6.6a with Fig. 6.6c which shows the corresponding distributions for an initial energy of $E^{init} = 6$ MeV and Fig. 6.6e for $E^{init} = 100$ MeV further supports that explanation. The energy dependence (as further detailed by means of Fig 6.7) shows that with increasing particle energy the exit energy range of interest narrows in units of the corresponding initial energy. This reference quantity is justified by the fact that the energy gain (as displayed by the bins) is defined as depending on the present kinetic energy of the particle (see Eq. (5.52)). This relation and not that much the absolute range of energy in MeV indicates, how strong weighting the exit energies by the Jovian source boundary cancels out longer trajectories (presumably) dominated by perpendicular transport as physically insignificant. Although this of course is an effect of the softening of the spectrum towards higher energies (i.e. a simulation effect) it also reflects the physical reality: Electron which are detected with relatively low energies (the initial energies E^{init} within the time-backward frame) could have escaped the source with any higher release energy (which would be the exit energy E^{exit} within the simulation setup). But for electrons which are detected with high energies the range of possible release energies narrows as reflected by the lower panels of Fig. 6.6 simply due to the exponential cutoff within the source spectrum. Or in other words: Only electrons which propagated very effectively between the source and the observer can be detected at high energies.

Comparing the cases of good and bad magnetic connection, another (simulation) effect emerges. Whereas the maxima of the red and blue histogram distributions are more or less aligned in case of good connection they are not in the opposite case. Figure 6.7 shows the effect of changing magnetic connection by looking at the differences between the distributions. In the upper most panel Fig. 6.7a shows the distributions of phase-space trajectories for good magnetic connections as given by the red histogram in Fig. 6.6a, 6.6c and 6.6e but as a contour plot covering the whole energy range. The corresponding distributions of the contributions to the resulting differential intensities as shown in the blue histograms are shown by Fig. 6.7b. A comparison between these upper most panels displays that there is an intensity gap within the phase-space trajectory distributions in Fig. 6.7a indicated by the thin blue area diagonal through the figure. As Fig. 6.7b suggest, only phase-space trajectories located below this intensity gap contribute significantly to the differential intensity in case of good connection. This notion leads to the assumption that the trajectory population below the intensity gap represents the pseudo-particles which propagation is mostly governed by parallel diffusion along the nominal magnetic field field lines. The uniform distribution of phase-space trajectories above the intensity sink however suggest that they constitute a kind of 'diffusive background' which exists independently from the propagation conditions and does not contribute to the resulting differential intensity due to the high exit energies corresponding to them.

The two middle panels Fig. 6.7c and Fig. 6.7d displaying the distributions in case of bad magnetic connections support this further. The comparison between the distributions

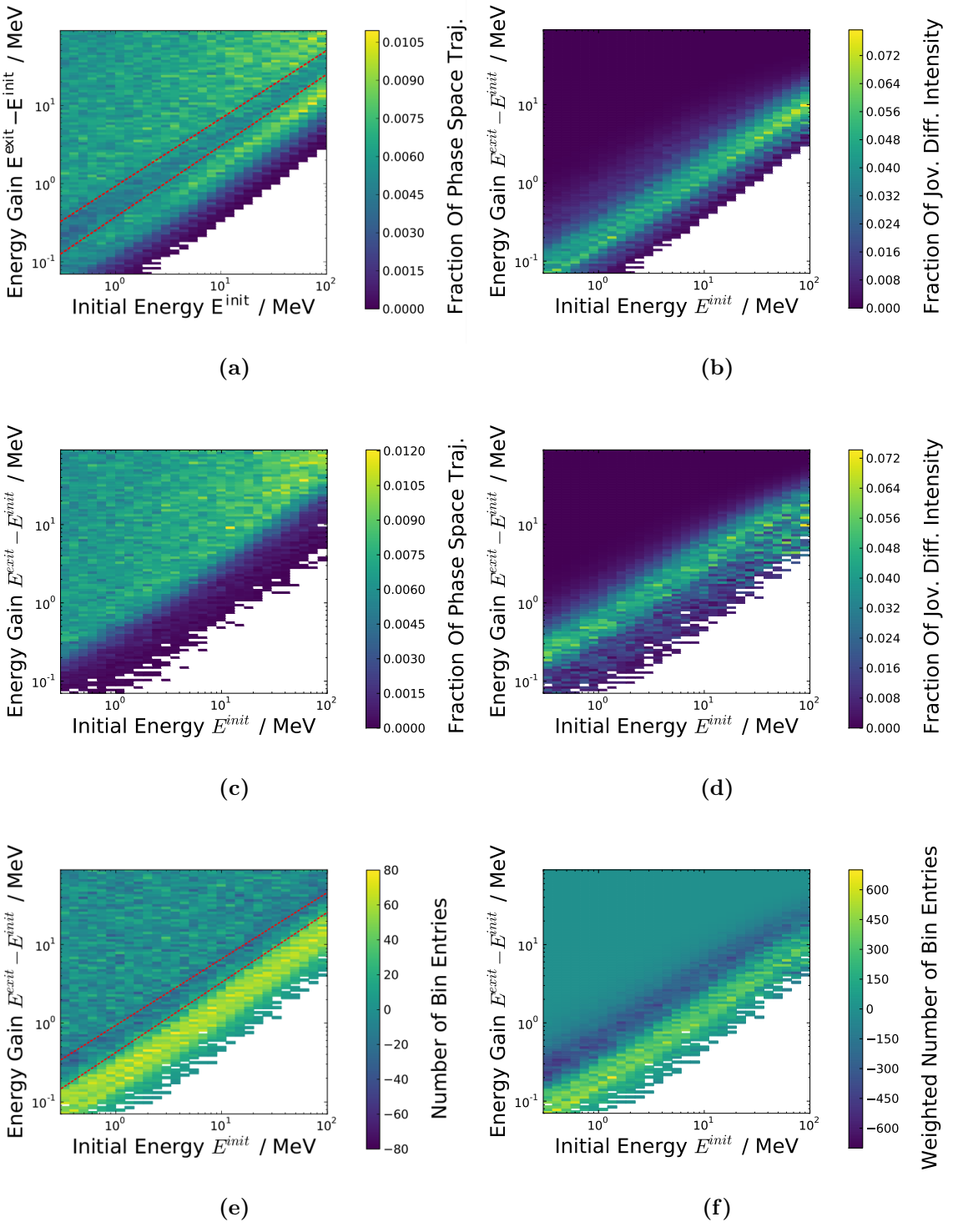

Figure 6.7: *Binned distributions of exit energies E_i^{init} over the whole energy range dominated by Jovian electron. Whereas the right panels show them weighted by their contribution according to Eq. (6.27), the left side displays the unweighted results of the simulation. The upper most panels Figs. 6.7a and 6.7b show the case of good magnetic connection to the source, whereas Figs. 6.7c and 6.7d show the case of bad magnetic connection. The differences between those distributions are depicted by the two lower panels Figs. 6.7e and 6.7f*

of the phase-space trajectories shows that in case of bad connection almost no phase-space trajectories are present in the area below the intensity gap present in Fig. 6.7a. The additional assumption that the remaining distribution shows a diffusive background population is proven by Fig. 6.7e which shows the difference between the phase-space trajectory distributions for good and bad connections. As expected the diffusive background is almost cancelled out proving that its constant regardless of magnetic connection. The fact that almost only the parallel diffusion dominated population is left in Fig. 6.7e indicates the following situation: If every phase-space trajectory is treated as equally significant, the diffusive background as shown in Fig. 6.7c dominates the distribution and therefore phase-space trajectories would dominate the resulting differential intensities which are governed by the perpendicular diffusion coefficients regardless of the magnetic connection between the observer and the Jovian source. As the comparison with the distribution of the fractional contribution to the differential intensities in Fig. 6.7d show, the distribution of phase-space trajectories as present in the diffusive background disagrees strongly with the physical solution. Furthermore the presence of the 13 month periodicity in the Jovian electron counting rates shows that the results of Jovian electron transport modelling have to depend significantly on the magnetic connection to the Jovian source.

As a consequence the convolution given by Eq. (6.27) and illustrated by Fig. 6.5 which weights the phase-space trajectories according to their physical significance, appears to be especially important in order to estimate the influence of perpendicular diffusion. Because even in case of good connection more phase-space trajectories cross the Jovian boundary after perpendicular diffusion dominated propagation as also discussed by Vogt et al. (2020), handling this diffusive background according to its physical significance is the key challenge in order to interpret the these results correctly. As shown in Chapter 7 this notion is crucial in order to understand the problems which appeared in previous attempts to estimate the residence times of charged particles within the Heliosphere, both numerical and analytical. As the difference of the flux distribution for good and bad connections given by Fig. 6.7f show, only a small band-like population of phase-space trajectories behaves according to the changing magnetic connection. Due to the fact that the convolution in order to assume the significance of the individual phase-space trajectories correctly depends on the energy change during the transport, the physical interpretation of diffusion appears to be linked to the adiabatic energy changes as introduced in Section 5.4. This relation will be discussed in appropriate detail in Secs. 7.2 and 7.3.3 as part of the derivation of new estimates for the residence time based on the considerations made herein.

6.4 Parameter Dependences

As argued above, the main advantage of using a simplified modelling approach based on a code written in CUDA is the performance increase. Thus, the code by Dunzlaff et al. (2015) as it is utilised herein, offers the possibility of extended parameter studies. Therefore in the following the dependences of the physical parameter such as the mean free path $\lambda_{\parallel}(1\ \mathrm{AU})$, the relation to the perpendicular mean free path χ as well as the radial size of the model Heliosphere R will be investigated and compared the available Jovian electron data. Furthermore also the two computational parameter T_{end} determining the maximum simulation time i.e. the maximum run time of the code as well as the size of the time increment determining the temporal step size of the random walk will be investigated. The resulting values as they appear to provide the most realistic results are

Table 6.1: *The computational and physical parameters used for the code (when not stated otherwise).*

Computational Parameters	
# Trajectories	50000
Δt	0.0001/$\sim$ 0.62 min
T_{End}	800/$\sim$ 300 days
Physical Parameters	
R	120 AU
u_{SW}	400 km/s
$\lambda_{\parallel}$(1 AU)	0.125 AU
$\chi = \lambda_{\perp}/\lambda_{\parallel}$	0.0125
E^{init}	6 MeV

listed in Tab. 6.1. The complete study is presented in the way that these parameter values are utilised in all simulations shown herein, unless stated otherwise. In order to cover energy dependent effects, the whole energy range of the Jovian source spectrum as shown by e.g. Fig. 3.10 will be included into the simulations. An example being Figs.6.6 and 6.7 in the previous Section 6.3.2.

6.4.1 The Parallel Mean Free Path

Whereas Fig. 6.7 shows the distribution of the phase space trajectories (left side) as well as of their weighted contribution (right side) regarding different initial energies E^0 within the energy range of Jovian electrons, Fig. 6.8 illustrates them regarding different parallel mean free paths $\lambda_{\parallel}$ normalised to their value at 1 AU, and radial dependent as defined in Eq. (6.15). The two panels show the phase-space trajectory distributions and weighted contributions in case of good magnetic connection between the source and the observer. Thereby due to the effect described above the influence of perpendicular diffusion related processes on the results is supposed to be small. The simulations were performed by utilizing a Solar wind speed of $u_{SW} = 400$ km/s, an outer boundary at $R = 120$ AU and values for the time increment and maximal integration time of $\Delta t = 0.0001$ and $T_{end} = 800$ in progamme units. Whereas the value for λ_0 was varied the value for the relation to the perpendicular mean free path was assumed to be $\chi = 0.01$. Due to Jupiter's decentral position within the HMF, Jovian electrons are an ideal test population in order to perform such an investigation. Picking up the discussion in Secs. 3.2.1 and 3.2 on the Jovian source, the changing magnetic connection offers the possibility to investigate cases in which the particle transport between the source and the observer is almost entirely dominated by parallel and perpendicular diffusion, respectively, due to the fact that the phase-space trajectories else-wise would miss Jupiter. The fact that Vogt et al. (under rev.) could show via Fig. 6.7 that in case of good connection a population of trajectories determines resulting differential intensity which disappears entirely in case of bad connection, further strengthens the argument that it is possible to investigate the parallel and perpendicular mean free path almost independently from each other. Therefore the chosen value of $\chi = 0.01$ determining the perpendicular mean free path can be assumed to be a negligible influence on the results in case of good magnetic connection, especially as it is shown to be within the range of error determined for this value in the subsequent Section 6.4.2.

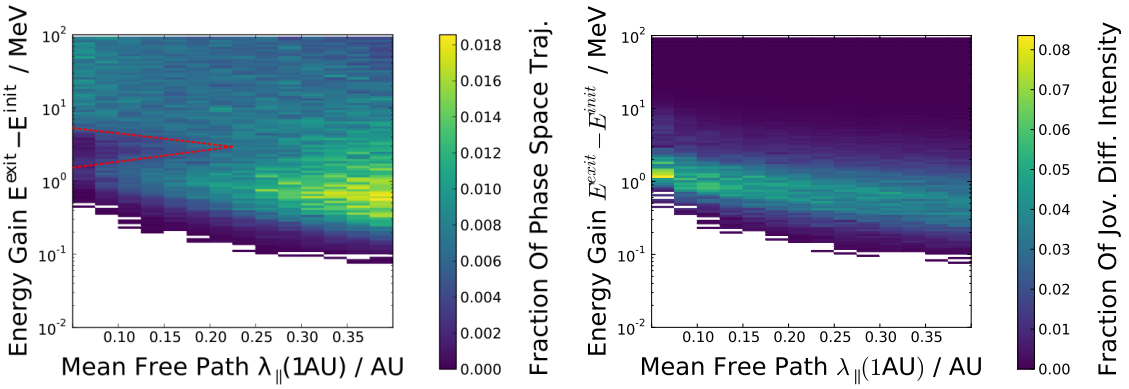

(a) **(b)**

Figure 6.8: *Simulation results for a varied parallel mean free path* $\lambda_{\parallel}(1\ AU)$*, utilizing an initial energy of* $E_i^{init} = 6\ MeV$ *and a relation to the perpendencular mean free path fo* $\chi = 0.01$.

For small values of $\lambda_{\parallel}$ Fig. 6.8a again shows the intensity sink already discussed above in relation to Fig. 6.7a. Towards higher values not only this sink smears out but also the distribution concentrates more since larger mean free paths reduce the scattering per distance and therefore in case of this simulation setup also the steps of the random walk. Since the step size increases it becomes possible to reach a possible exit position with fewer steps, especially when good connected to the Jovian source as it is the case for Fig. 6.8. This is also reflected by the decreasing minimum exit energy gains as larger mean free paths or step size reduce the adiabatic energy changes, simply by reducing the propagation time as it will be discussed in more detail in Section 7.2. Comparing Fig. 6.8b to 6.8a shows the equivalent findings already pointed out with regard to Figs. 6.7a and 6.7b. Furthermore note that with increasing $\lambda_{\parallel}$ the distribution of the weighted contribution gets broader, again due to the increasing step size leading to a wider range of trajectories reaching the Jovian boundary.As Figs. 6.6, 6.7 and 6.8 show, the range of exit energies for which the corresponding phase-space trajectories contribute significantly to the resulting differential intensity is relatively small and does not cover more of half of an order of magnitude in case of good connection. This allows to neglect a possible energy dependence of the mean free path (see e.g. Section 5.3.3 and the discussion therein, as well as the Palmer consensus range) in order to utilise the simulation setup in combination with the Jovian spectra at Earth to investigate possible and realistic values for the parallel mean free path.

As shown in Fig. 6.9 the resulting differential intensities were subsequently compared to the spacecraft data at Earth orbit. The upper panel of Fig. 6.9 as previously published by Vogt et al. (2020) shows the available Jovian spacecraft data at Earth orbit as listed in Tab. 3.1 for times of good connection. The black dashed line represents the fit of the spectral shape as given by Eq. (3.9) to the Earth orbit data. This is done in order to have a measure to define the relative deviation as stated by Vogt et al. (2020). The relative deviation is shown in the middle panel of Fig. 6.9, the simulated spectra at Earth given by the same colour coding corresponding to different values of λ_0 as in the upper panel. The deviations amplifies what is visible in the upper panel as well, a great scale energy dependence, which indicates smaller values of the parallel mean free path in the keV range and for energies above $\approx$ 20 MeV as shown in the lower panel. In order to cover the uncertainties the grey area in the middle panel covers the range of relative deviation of ± 0.5, resulting in in an energy dependence of the best fitting input parameter for λ_0 as given by the lower panel. Since the uncertainties provided by the data were too small to

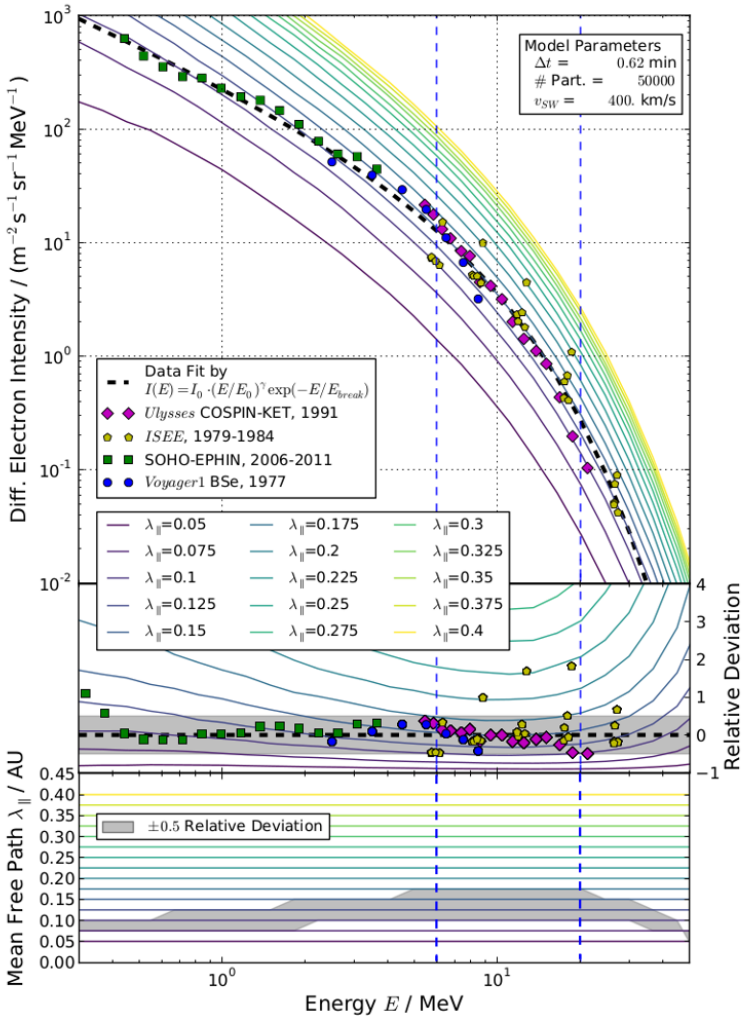

Figure 6.9: *The influence of different values for $\lambda_{\parallel}(1\ AU)$ on the simulated Jovian electron spectrum at Earth orbit in case of good magnetic connection. The top panel shows the simulation results alongside the Earth orbit data as listed in Tab. 3.1 and a data fit indicated by the bolt dashed line. This date fit is utilised in the second panel to show the relative deviation of both the data and the modelling results. A area of ±0.5 relative deviation is given in shaded grey for illustration purposes. The bottom panel subsequently displays this shaded area with respect to the values of the mean free path $\lambda_{\parallel}(1\ AU)$ on the y-axis. The low-MeV range previously published and discussed by Vogt et al. (2020) is indicated by the two dashed blue lines.*

be significant this ad-hoc method was chosen. A re-examination of the spacecraft data to estimate reasonable values for error-bars would have been clearly beyond the scope and temporal resources of this thesis.

The lower panel shows the range of values used for the parameter study in a very straight forward way. The investigated range of $\lambda_0 = \lambda_{\parallel}(1\ \text{Au}) = [0.05, 0.4]$ AU in steps of 0.05 AU thereby is in agreement with the suggestions by Palmer (1982) and Bieber et al. (1994) as well as with studies such as e.g. Strauss et al. (2011b) and Vogt et al. (2018) which successfully implemented values in the investigated range to model Jovian electron transport. In grey the area of ±0.5 relative deviation from the middle panel is

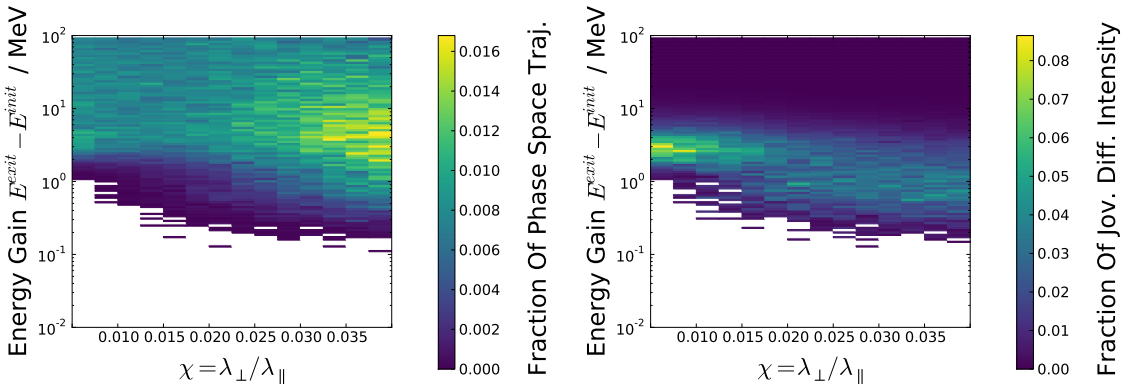

(a) **(b)**

Figure 6.10: *Simulation results for varying values of of* $\chi = \lambda_\perp / \lambda_\parallel$ *utilizing a for the parallel mean free path* $\lambda_\parallel(1\ AU) = 0.125\ AU$ *and likewise Fig. 6.8 for an initial energy of* $E_i^{init} = 6\ MeV$.

transformed into this display and shows a energy dependence of λ_0. The low-MeV range between the two dashed horizontal lines has already been discussed by Vogt et al. (2020). The plateau in that energy range suggest values for the parallel mean free path in the range of $\lambda_0 = [0.1, 0.175]$. Because all of these possible values are in agreement with previous studies it is reasonable to compare the corresponding results for χ and therefore the perpendicular diffusion coefficients in order to determine the most realistic combination. Another influence would be that if only the low-MeV range is about to be investigated a higher value for λ_0 would fit best. For investigations of a more broader energy range of course lower values λ_0 appear to be more realistic according to the lower panel of Fig. 6.9

6.4.2 The Perpendicular Mean Free Path

Having established a well defined range of values covering realistic approaches to the parallel mean free path in Section 6.4.1, it seems reasonable to first investigate the dependence of a varying value of χ as define by Eq. (6.17) equivalently. Again for the corresponding simulations a set of standard variable was applied such as a Solar wind speed of $u_{SW} = 400$ km/s, an outer boundary of $R = 120$ AU and the time increment and maximum integration time of $\Delta t = 0.0001$ and $T_{end} = 800$ in program units, respectively. Two values for the parallel mean free path that appear most realistic according to the results shown in Fig. 6.9 were applied, $\lambda_{0\parallel} = 0.125$ AU and $\lambda_{0\parallel} = 0.15$ AU. The first one being a realistic compromise to cover the whole energy range as shown in Figs. 6.9 and 6.8 whereas he latter seems to be the better fit if only the low MeV range is ought to be investigated.

Taking a look at the results, is striking how similar Fig. 6.10 is to the two lower panels of Fig. 6.8. As noted beforehand for varying values of energy (Fig. 6.7) and λ_0 (Fig. 6.8), Fig 6.10 shows that only a limited range of exit energies contributes significantly to the resulting differential intensities. Although the corresponding distributions broaden for higher values of χ the range of energy gains for which the phase-space trajectories contribute significantly is limited to the order of magnitude of the initial energies. A very prominent feature that deserves to be addressed in Fig. 6.10 is the fact that for increasing values of χ, the minima of the energy gains of the phase-space trajectories decrease. This is

due to the same effect as described to increasing values of λ_0 above. Due to the increasing values of χ the perpendicular diffusion becomes more effective (i.e. the perpendicular step size increases) and therefore is becomes possible to reach a possible exit position faster. This statistically also leads to less adiabatic energy changes (i.e. gains within this simulation setup) as later discussed in more detail in Section 7.3.1.

Similar to Fig. 6.9, Fig. 6.11 shows the differential intensities calculated via the distributions shown in Fig. 6.10b with respected to spacecraft data at Earth in case of opposition to the Jovian source. As described by Vogt et al. (2018) the upper panel of Fig. 6.11 shows these data as listed in Tab. 3.1 together with a fit of the source spectrum' shape similar to what is shown in the upper panel of Fig. 6.9. The second and the third panel of Fig. 6.11 show the relative deviation of the simulation results for different values of χ in the range of $\chi = [0.005, 0.04]$ in steps of 0.0025. Of the four possible values of λ_0 to choose according to Fig. 6.9 two are displayed in Fig. 6.11, namely $\lambda_0 = 0.125$ and $\lambda_0 = 0.15$. The results for the two other possible values considerable for the parallel mean free path ($\lambda_0 = 0.1$ and $\lambda_0 = 0.175$) are not shown, since they were not utilised for further parameter studies, neither for the results presented by Vogt et al. (2020) nor for this thesis as discussed in the next Section.

6.4.3 A Realistic Fit of the Diffusion Coefficients

Because the perpendicular mean free path is defined as proportional to λ_0 via the factor χ (see Eqns. 6.16 and 6.17), both values behave reciprocally. These kind of degenerate simulation results with a several parameter sets which meet the requirement of providing realistic simulation results have been reported regularly e.g. by Savopulos and Quenby (1997, 1998) and are discussed specifically dealing with Jovian electron modelling by Strauss et al. (2013). Due to this effect $\lambda_0 = 0.1$ demands values of $\chi \geq 0.02$ to be in a realistic range whereas a value of of $\lambda_0 = 0.175$ would suggest $\chi \leq 0.0075$ within the low MeV range. Although these parameter values are in agreement with the proposed range according to e.g. Palmer (1982), Bieber et al. (1994) and Dröge et al. (2016), values of $\lambda_0 = [0.125, 0.15]$ and the corresponding ranges of values for χ are more in agreement with previous transport models for both Jovian and Galactic electrons by e.g. Ferreira et al. (2001a), Strauss et al. (2011a,b), Engelbrecht and Burger (2013) and Nndanganeni and Potgieter (2018), which have successfully tested such values in the inner Heliosphere.

Therefore, as stated by Vogt et al. (2020), taking the best fit χ into account, a value of $\chi = 0.0125$ seems to be justifiable within the margin of error for both $\lambda_{\parallel} = 0.125$ AU and $\lambda_{\parallel} = 0.15$ AU. However, the value suggested for χ via Fig. 6.11 appears to be outside of the range defined by Palmer (1982), who finds that $0.02 \leq \chi \leq 0.08$. But compared to more recent numerical modulations studies as cited above, a value of $\chi = 0.0125$ is in agreement with the parameter setups successfully tested on Jovian electron transport. Concerning the energy dependence of both values, Vogt et al. (2020) chose the higher value for the parallel mean free path as $\lambda_{\parallel} = 0.15$ AU as only the energy range marked by the two dashed lines in Figs. 6.9 and 6.11 was investigated. In order to simulate the whole energy range of the Jovian source spectrum, however, Fig. 6.9 suggest the smaller value of $\lambda_{\parallel} = 0.125$ AU. A comparison of the corresponding panels of Fig. 6.11 shows that the value of $\chi = 0.0125$ is supported by both choice of $\lambda_{\parallel}$. In the keV range especially χ becomes obscure, due to an energy dependence also slightly visible in Fig. 6.9 for the parallel mean free path. There it is possible due to the intensity dip in the keV range of the SOHO data. Whether this behaviour reflects real physical effects or the qualities of the detector is still under debate

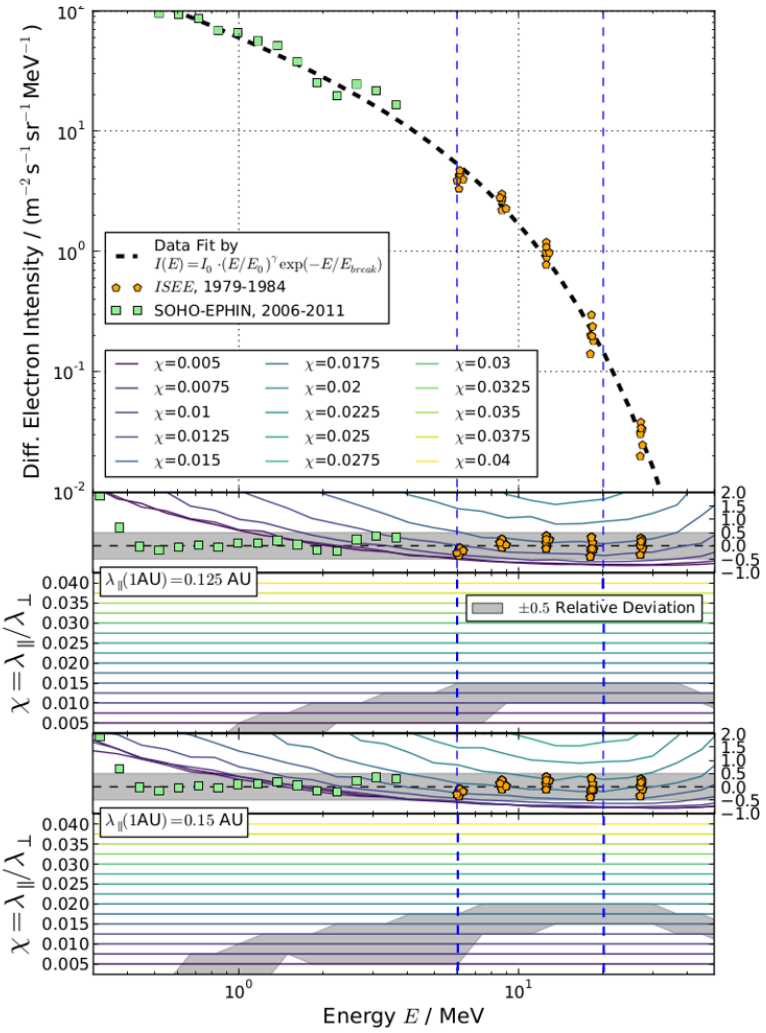

Figure 6.11: *The influence of different values for χ on the Jovian electron spectrum at Earth orbit in case of bad magnetic connection. Similar to Fig. 6.9 the top panel shows the corresponding spectral data as listed in Tab. 3.1 alongside a data fit indicated by the bolt dashed line. The second and fourth panels show the relative deviation for the different values of χ with respect to two different possible values for the parallel mean free path $\lambda_{\parallel}(1\ AU) = 0.125\ AU$ and $\lambda_{\parallel}(1\ AU) = 0.15\ AU$. The third and fifth panel show these shaded grey areas with respect to χ on the y-axis similar to the bottom panel of Fig. 6.9. Again the low-Mev range previously published by Vogt et al. (2020) is indicated by two dashed blue line.*

as already discussed in Vogt et al. (2015). Nevertheless, as pointed out above, it appears to be useful to include this broad energy range in order to point out energy dependent effects of the simulation setup which otherwise could have been lost. Due to these considerations choosing $\lambda_{\parallel} = 0.15$ AU and $\chi = 0.125$ as listed in Tab. 6.1 appears to be the most realistic fit regarding the purpose of this work.

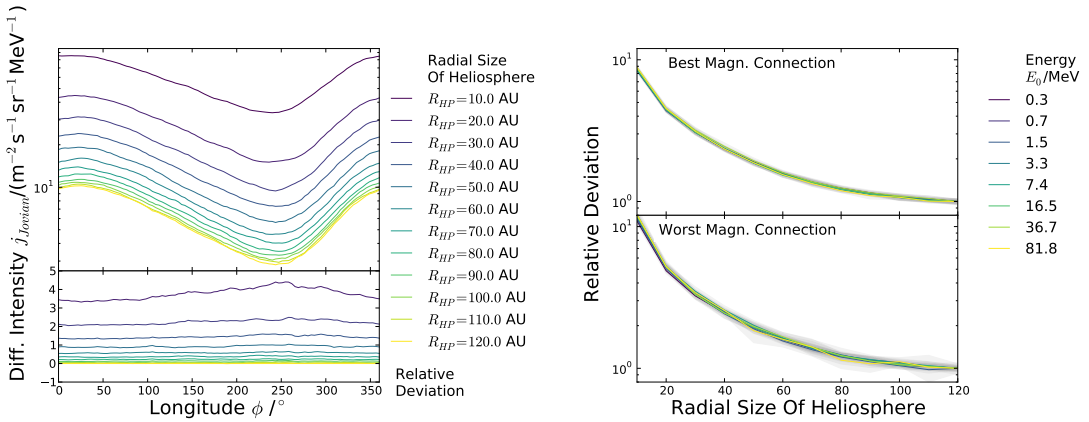

(a) **(b)**

Figure 6.12: *The influence of radial extend of the model Heliosphere R on the simulation results. The left panel shows the modelling results over the whole range of longitude at Earth orbit with the left bottom panel showing the relative deviation from the results with the maximal chosen radial extent. The right panels shows the relative deviations with respect to the size of R on the x-axis for the case of good (top) and bad (bottom) magnetic connection. The grey shaded area thereby denotes the standard deviation of the 27 day running mean.*

6.4.4 The Radial Extent of the Model Heliosphere

The possible significance of the size of the model Heliosphere R for the simulation results is indicated by the discussion in Section 6.3.1. First indications which are investigated more detailed in here are already presented by Vogt et al. (2015). As shown e.g. by means of Figs. 6.6 and 6.7 phase-space trajectories corresponding to exit energies half an order of magnitude larger than the initial energies determine the resulting differential intensities significantly. This especially is highlighted by the behaviour of the integral distributions shown as dashed lines in Fig. 6.6. Although as argued above in Secs. 6.4.1 and 6.4.2, this range is small with respect to the (theoretically assumed) energy (or rigidity) dependence of the electron mean free path and therefore allows to approximate the behaviour by an energy independent approach such as the one presented by Eq. (6.15) and used by this thesis, this does not necessarily mean that this relatively small energy range only corresponds to phase space trajectories contained within the inner most part of the model Heliosphere. Regarding the left panels of Fig. 6.7 showing the distribution of the phase-space trajectories this notion is supported by the fact that even in case of good magnetic connection to the Jovian source, the population of phase-space trajectories, which can be attributed to parallel transport and therefore to more or less direct trajectories between the observer and Jupiter, only corresponds to the lower part of the exit energy range significantly for the resulting differential intensities.

Figure 6.12 shows that indeed the model Heliosphere has to be extended towards $R \approx 120$ AU in order to provide reliable results. The simulations were performed by utilising the parameter set as listed in Tab. 6.1, most importantly $\lambda_{\parallel}(1\text{ AU}) = 0.125$ AU and $\chi = 0.0125$ as determined in Section 6.4.3. The two panels of Fig. 6.12a show the influence of different values of R on the differential intensity of Jovian electrons over the whole range of longitudes. As explicitly shown by the relative deviations to the results obtained

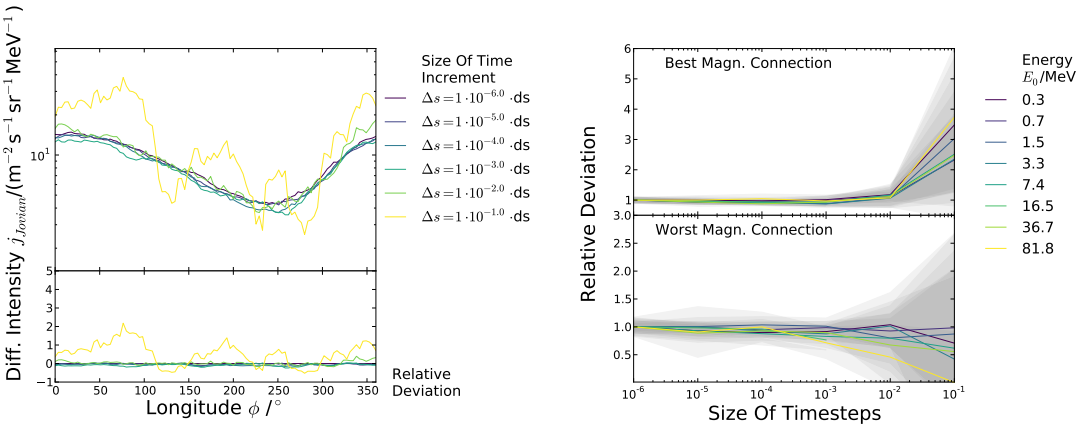

(a) **(b)**

Figure 6.13: *The influence of the time increment Δs on the simulation results. The left panels shows modelling results over the whole range of longitudes at Earth orbit with the left bottom panel showing the relative deviations from the results with the smallest increment. The right panels shows the relative deviations with respect to the size of Δs on the x-axis for the case of good (top) and bad (bottom) magnetic connection. The grey shaded area thereby denotes the standard deviation of the 27 day running mean due to the Solar rotation period.*

by utilising $R = 120$ AU in the bottom panel, these results deviate up to a factor of nearly twelve, if only the inner Heliosphere is considered for the simulation. The comparison with Fig. 6.12b confirms the slightly greater deviations in case of bad connectivity and the asymptotic convergence of the results for the differential intensity.

As already indicated by the discussion above this can be understood by more carefully interpretation of the relations shown in Fig. 6.6 and 6.7. Because the adiabatic energy gain (in a time-backward approach) is directly linked to the radial position, as discussed e.g. by means of Fig. 6.5, a small value for R effectively means that phase-space trajectories with high exit energies are more likely to reach the outer boundary and are therefore flagged with the Galactic instead of the Jovian exit position as discussed in Section 6.1. As shown by the contrast between the red and blue distribution in Fig. 6.6, the contribution of the phase-space trajectories decreases with higher exit energies, therefore the asymptotic behaviour of the relative deviations with increasing values for R. Figure 6.12b shows, that the convergence is exponential in log-space both for good and bad magnetic connection. For both cases the relative deviation becomes highly asymptotic for $R \geq 100$ AU indicating that a value of $R = 120$ AU sufficiently assures that the simulated differential intensities are not influence by the chosen size of the model Heliosphere.

6.4.5 The Influence of the Time Increment

Another technical parameter which demands to be carefully chosen is the size of the time increment Δs. It has the most obvious influence on the simulation results as Vogt et al. (2020) stated due to its association with the Wiener process and, hence, with the mathematical representation of diffusion. On more conceptual level this is due to the fact that the simulation setup has to approximate a time continuous process by a time discrete one. On the question how to choose the time increment in order to resolve the influence of small scale structures or disturbances see e.g. Strauss and Effenberger (2017), whereas

this Section explores the influence of the time resolution provided by the different sizes of the time increments on the results for modelling idealised Solar mininum conditions.

The simulation in order to determine which values of Δs and T_{end}, respectively, lead to an asymptotic convergence, were performed by utilizing $\lambda_0 = 0.125$ AU and $\chi = 0.125$ AU. According to the results of Secs. 6.4.1 and 6.4.2 these two values most reliable cover the whole range of energy realistically. Furthermore an outer boundary at R was utilised as well as a Solar wind speed of $u_{SW} = 400$ km/s to represent ideal Solar minmum conditions.

As shown by Fig. 6.13 there is a high sensitivity to the magnetic connection. This influence is expected as the choice of the time increment possibly influences both the adiabatic energy changes and the duration of the random walk. Since the trajectories in cases of bad connectivity are dominated by perpendicular diffusion and are much longer by average (see e.g. Fig. 6.7 and the accompanying discussion) the effects due to the choice of the time increment are likely to be cancelled out by the number of timesteps as noted by Vogt et al. (2020). However, since the trajectories in case of good connection are mostly dominated by parallel diffusion and therefore governed by the geometry of the underlying HMF, the possible deviation due to the choice of a larger time increment have a more significant impact. As shown in Fig. 6.13a over the whole range of longitudes these deviation causes a significant variability in the results for the differential intensities if a large time increment is chosen. This is due to the fact that smaller time increments cause more time steps and therefore more random number chosen, which limits the individual influence of each random number pick and each random walk step.

Explicitly these deviation are shown relatively to the results for the smallest tested time increment ($\Delta s = 10^{-6}$ in programme units) in the lower panel of Fig. 6.13a and separated to the cases of good and bad connection in the two panels of Fig. 6.13b. Comparing the deviations in case good and bad magnetic connections for the same energies and sizes of the time increments as shown by Fig. 6.13b, the first appear to be larger by a factor of two and more. The energy dependence, on the other hand, seems to be more prominent in case of good connection. Therefore it seems necessary to look for a value of conversion with respect to the deviation in case of good connection and chose a tendentiously smaller value. Based on the results presented in Fig. 6.13 a value of $\Delta s = 10^{-3}$ in programme units is suggested by Vogt et al. (2020) which corresponds to about 0.004 days as a compromise between reasonable reliability and the need to keep the total simulation times short.

The convergence in case of changing maximal simulation times as shown by Fig. 6.14 on the other hand appears to be more gradual. Thereby the smaller maximal simulation times limits the population of trajectories exiting at a certain source (i.e. the Jovian magnetosphere) to trajectories low simulation times and therefore small adiabatic energy changes. As the differential intensity according to Eq. (6.27) is calculated by the convolution of the phase-space trajectories with the source via the exit energies divided by the number of corresponding trajectories, further limiting the population to short phase-space trajectories with a relatively high impact increases the resulting differential intensities as illustrated by Fig. 6.14. As shown by the lower panel of Fig. 6.14a which shows the relative deviations to the results for the largest maximum simulation times tested (1000 in programme units) over the whole range of longitudes, this effect is more or less independent from the magnetic connection. The comparison with Fig. 6.14b proves this assumption with the constraint that the uncertainties are significantly larger in case of bad connection. Since Fig. 6.14b shows the relative deviation normalised to the value with the the $T_{end} = 10000$ in program units, two panels show the convergence of the simulation results with respect to the time increment in case of both good and bad magnetic connection to the source. Thereby the slightly asymptotic behaviour is reflected in the amount of phase-space trajectories which decrease from ≥ 3900 and ≥ 3240 for $T_{end} = 100$ and $T_{end} = 200$ in programme units, respectively, to nearly a fifth for $T_{end} = 10000$ in programme units, specifically ≈ 800

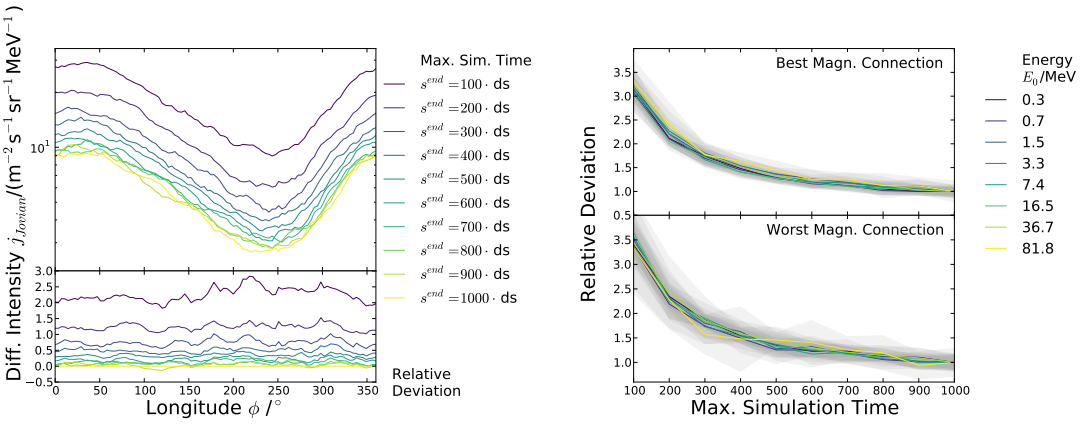

(a) **(b)**

Figure 6.14: *The influence of the maximum simulation time T_{end} on the simulation results. The left panel shows the modelling results over the whole range of longitude at Earth orbit with the left bottom panel showing the relative deviation from the results with the longest chosen maximum simulation time. The right panels shows the relative deviations with respect to the size of T_{end} on the x-axis for the case of good (top) and bad (bottom) magnetic connection. The grey shaded area thereby denotes the standard deviation of the 27 day running mean.*

abandoned phase-space trajectories.

Vogt et al. (2020) therefore suggest a required maximum simulation time of required duration of about 700 to 800 programme units in order to avoid deviations of more than 20%. This corresponds to a total time of simulation of $\sum \Delta s \geq 3000$ days. As Vogt et al. (2020) further note, the numerical step sizes of the pseudo-particles are ultimately dependent on the choice of the energy transport parameters which influences the diffusive step size. Thus there is a slight energy dependence on the optimal size of the time increment which has to be considered if a similar simulation setup is to applied to cases which suggest strongly deviating physical transport parameters.

6.4.6 Differences Between a Corotational and a Static Approach

A question of direct physical significance is whether it is necessary to consider the corotation of the Jovian source during the transport. As discussed by Vogt et al. (2020), to keep the setup mathematically as simple as possible, the code according to Dunzlaff et al. (2015) is designed in a way that both the positions of the Sun and the Jovian source are kept fixed. This means that the position of the observer as the starting point of the time-backward phase space trajectories has to be included in a coordinate system that is defined relative to the position of Jupiter. Thereby this relative position of Jupiter can be kept static during the random walk as originally implemented by Dunzlaff et al. (2015) and utilised by previous attempts to model Jovian electron transport such as Strauss et al. (2011a,b) or consider the relative motion of Jupiter and more precisely, its effect on the magnetic connection to the Jovian source. As stated by Vogt et al. (under rev.) two different motions determine the magnetic connection between Jupiter and a possible observer:

1. The synodic period, in case of Earth the characteristic ≈ 13 months first discussed by McDonald et al. (1972).

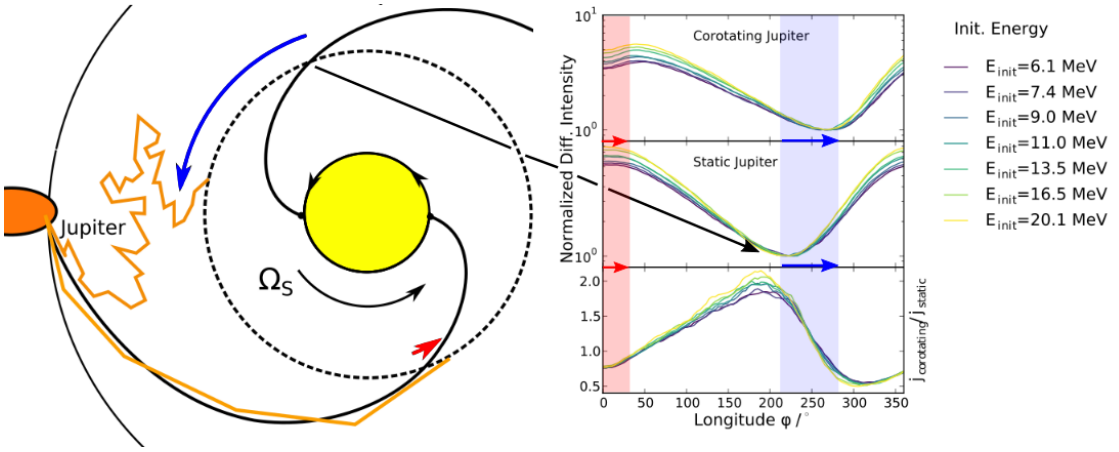

Figure 6.15: *Differential intensities of Jovian electrons for different initial energies E^{init}. The simulation results are taken from Vogt et al. (2020). The top panel shows the longitudinal variation due to varying connection for a corotating Jovian source, while the middle panel shows the case of a static Jupiter. The bottom panel shows the ratio of the results of the two approaches. A version of this Figure containing the whole range of energies in order to discuss the energy dependence of his effect is given by Fig. 7.9a in Section7.4.1.*

2. The corotation of the HMF due to the Sun's rotational period of $\Omega_S \approx 27$ days

The slow orbital motion of Jupiter which causes the synodic period thereby can be neglected with respect to the corotatoin of the HMF which causes a longitudinal shift about 13 times larger. In order to consider this effect an additional longitudinal advection velocity given by

$$V_\phi = \Omega_{Sun} \cdot r \tag{6.28}$$

is added to the third SDE within Eq. (6.13) which governs the evolution of the longitudinal coordinate.

The corresponding differential intensities are shown by Fig. 6.15 for different initial energies and as a function of longitude. As discussed by Vogt et al. (2020), simulations were performed for both a corotating coordinate system (top panel) and for the case of a static Jupiter (second panel). The significance of the corotation is illustrated by the bottom panel, which shows the ratio of the two scenarios. It is obvious that the corotation of the Jovian source has been neglected mistakenly. Causing deviation up to a factor of two and a significant shift in longitude both for the angle of best and worst connectivity, the seemingly slow orbital motion of Jupiter has to be considered as one of the greatest sources of possible uncertainties due to its interaction with the magnetic connection of the HMF. A detailed discussion of this effect including how to quantitatively estimate it will be given in Section 7.4.1. Furthermore the energy dependence of the longitudinal shift detectable in Fig. 6.15 will be investigated therein in order to compare both simulation results as well as analytical estimates to spacecraft data.

As concluded by Vogt et al. (2020), the corotation of the Jovian source has to be considered as an important effect and should be incorporated into numerical models. Due to this fact all simulations presented within this thesis and in the corresponding papers have been performed with a corotating Jovian source. The physical significance of including the corotation of Jupiter will be further amplified later in Section 7.4 where it is shown that it can be used in order to validate the existence of corresponding effects as the corotation effect can be seen in spacecraft data, too, as discussed in Section 7.4.1 in great detail. The significance of this effect therefore hints that the Jovian residence times should range within a few days, which appear to be not the case by applying the previously available

methods of estimation as will be discussed in the next Chapter.

Chapter 7

Residence Times

Based partly on Vogt et al. (2020) and Vogt et al. (under rev.) this Chapter presents a new approach to estimate residence times. First the previous attempts to estimate them both analytically (Section 7.1.1 and numerically (Section 7.1.2) will be discussed and a estimation to calculate residence times motivated by the inconsistencies found in this discussion. The new estimation then will be derived self consistently with the derivation of the differential intensities in Chapter 6 by convoluting the simulation results with the boundary condition (Section 7.2.1), in this the Jovian source spectrum according to Chapter 3. Subsequently an equivalent parameter study to the one discussed in Section 6.3.2 will by evaluated regarding the residence times in Section 7.2.2 with a focus set on the relation between the adiabatic energy changes within the simulation and the simulation times as investigated in Section 7.3.1. The subsequent discussion how these finding reflect the relation between the analytical and numerical estimations to calculate residence times (Section 7.3.2) then lead to the developed of an new and improved analytical estimation (Section 7.3.3) which avoids the inconsistencies of the the previous attempts and is self consistent with the new numerical one, both regarding the mathematical derivation and the results. The Chapter finishes by comparing spacecraft data with the results of the simulation setup developed by this thesis utilising the effects of the corotating HMF as discussed in Section 6.4.6. As shown in Section 7.4.2 the data meets the expectations due to the effects of the Jovian residence times according to this thesis and therefore confirms that the results presented herein reflect a realistic behaviour.

In recent years the prediction of space weather became an increasingly important topic within the field of Heliospheric physics. The raising awareness about the vulnerability of satellite based communication systems to CME encounters as well as about the possible effects of SEP events on electronic infrastructure at he Earth's surface, gained interest in whether and how it is possible to estimate both their trajectory and arrival time. Prediction models have been published by e.g. Gopalswamy et al. (2001) and Vršnak et al. (2013), a most recent approach is the European HESPERIA REleASE project (see e.g. Núñez et al., 2018), a real time prediction tool based on a framework by Posner (2007).

It is apparent that in order to predict arrival times reliably, a more than heuristic understanding of residence times is necessary. Suggestion on how to analytically estimate the residence times of charged particles date back to Parker (1965, 1966) another prominent example being the suggestion presented by O'Gallagher (1975). More recently, suggestions based on numerical simulation by means of SDE approaches have been published on both GCR and Jovian electron residence times by e.g. Florinski and Pogorelov (2009) and Strauss et al. (2011b). Despite SEP events are being preferably described by focused transport models based on pitch-angle sensitive equations like the one suggested by Roelof (1969), the isotropic test cases of GCRs and Jovian electrons are able to provide insights to the relation between diffusive transport models in general and the corresponding residence times of the particles. A recent example for the role of residence times in order to reconstruct the magnetic structures associated to a SEP event is e.g. Dresing et al. (2016).

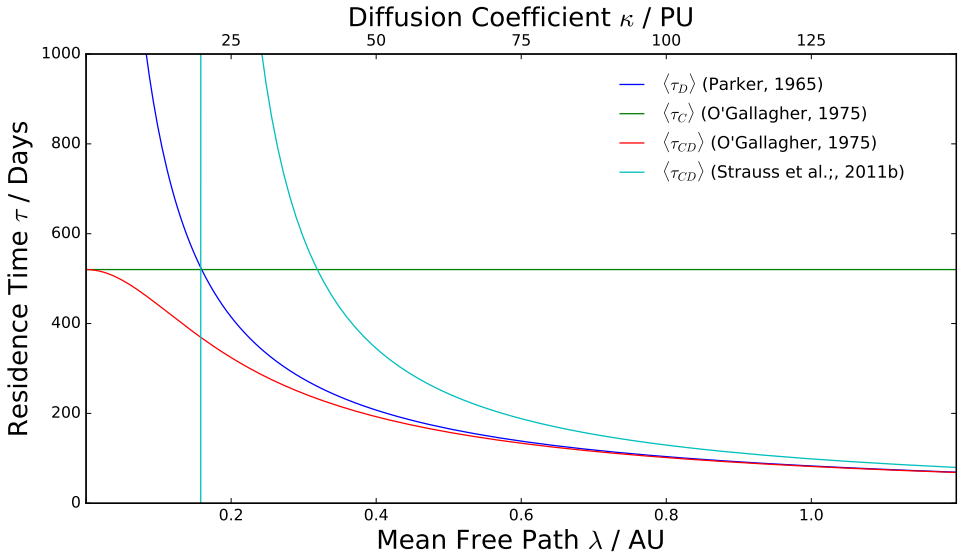

Figure 7.1: *Analytical estimates for residence times of GCRs. Thereby the one according to Parker (1965) shown in blue provides a limit in case of only diffusive transport processes occur (τ_D), whereas the the estimation by O'Gallagher (1975) given in green the equivalent limit for convection (τ_C). The two suggestion to combine these results by O'Gallagher (1975) (red) and Strauss et al. (2011b) are discussed with respect to their derivation in Section 7.1.1.*

7.1 Past Approaches

Although the attempts to estimate residence times of charged particles date back to Parker (1965), their number - both analytically and numerical - is actually very limited. The following Sections therefore provide a detailed overview on the noteworthy suggestions that have been made. The limited cases in which actually numerical values for he residence times were obtained via the SDE approach, also results using GCRs are being discussed. Since Strauss et al. (2011b) utilised the same numerical approach to model both GCR protons and electrons as well as Jovian electrons, this work will serve as a benchmark to make the results for the different population comparable.

7.1.1 Analytical Estimations

As a special case, derived from the diffusive term of the TPE as given by Eq. (5.55), Parker (1965) introduced a probability wave approach to estimate the propagation times of Cosmic Rays isotropically penetrating the Heliosphere. The Fokker-Planck equation describing the evolution of the probability $f(r,t)$ to find a particle after the time t at the radial distance r from the Sun,

$$\frac{\partial f(r,t)}{\partial t} = \frac{1}{r^2}\frac{\partial}{\partial r}\left(r^2 \kappa \frac{\partial f(r,t)}{\partial r}\right) \tag{7.1}$$

is, in contrast to Eq. (5.55), in 1D. The only process governing the evolution of $f(r,t)$ in this simplified version of the TPE is diffusion, defined by the 1D diffusion coefficient κ as a global average over the parallel and perpendicular diffusive processes. As the approach holds diffusion as the dominant process, in order to simplify the TPE to the form of Eq. (7.1), the radial Solar wind speed is set to $V_{SW} = 0$ km/s and therefore the convective term $-V_{SW}\partial f(r,t)/\partial r$ as well as drift effects are neglected.

The initial condition the approach additionally requires is an empty Heliosphere at the injection time $t = 0$. Assuming a penetration length h (as Parker (1965) puts the first mean free path by which the particle enters the Heliosphere) of $h \ll R$, with R being the radial distance of injection, the general solution simplifies to

$$f(r,t) \approx \frac{h}{2R^3 r} \sum_{n=1}^{\infty} (-1)^{n-1} n \sin\left(\frac{n\pi r}{R}\right) \exp\left(-\frac{n^2\pi^2\kappa t}{R}\right), \tag{7.2}$$

leading to an expectation value of

$$\langle \tau_D \rangle = \frac{\int_{t=0}^{\infty} f(r_0,t) t dt}{\int_{t=0}^{\infty} f(r_0,t) dt} = \frac{R^2}{\pi^2\kappa} \sum_{n=1}^{\infty} \frac{1}{n^2} \rightarrow \frac{R^2}{6\kappa}. \tag{7.3}$$

at the center of the heliosphere r_0, a result which is referred to as the diffusion limit $\langle \tau_D \rangle$ of the mean propagation time by O'Gallagher (1975). In order to include the influence of convection into the estimation of the mean propagation time, O'Gallagher (1975) introduces an approach to obtain the convection limit $\langle \tau_C \rangle$ as a complementary measure to the diffusion limit $\langle \tau_D \rangle$. Therefore the assumption is made that $\kappa \ll r u_{SW}$ in contrast to the approach leading Parker (1965) to obtain Eq. (7.1) and thereby the diffusion limit Eq. (7.3). Considering the radial form of of the TPE as given by Eq. (5.55),

$$\frac{\partial f}{\partial t} = \kappa \frac{\partial^2 f}{\partial r^2} + \left(\frac{2\kappa}{r} - u_{SW}\right) \frac{\partial f}{\partial r} - \frac{u_{SW}}{r} f, \tag{7.4}$$

the terms $(2\kappa r)(\partial f/\partial r)$ and $u_{SW} f/r$ are small compared with $u_{SW}\partial f/\partial r$ und this assumption. As an result Eq. (7.4) can be rewritten into a much more simplified version which takes the form

$$\frac{\partial f}{\partial t} \approx \kappa \frac{\partial^2 f}{\partial r^2} - u_{SW} \frac{\partial f}{\partial r}. \tag{7.5}$$

As the the derivation of a convection limit $\langle \tau_C \rangle$ is only valid if the diffusive processes do not dominate the particle propagation, the further condition can be made that

$$\frac{1}{f} \left| \frac{\partial f}{\partial t} \right| \ll \frac{1}{\tau_D} \tag{7.6}$$

and the gradient can be approximated by a stationary value of $\partial f/\partial r = u_{SW} f/\kappa$. Under these assumptions O'Gallagher (1975) finds a measure of the convection limit $\langle \tau_C \rangle$ as

$$\langle \tau_C \rangle = \frac{R - r}{V_{SW}} \approx \frac{R}{V_{SW}}, \tag{7.7}$$

equivalently to the diffusion limit $\langle \tau_D \rangle$ given by Eq. (7.3) as obtained by Parker (1965). The diffusion limit $\langle \tau_D \rangle$ and the convection limit $\langle \tau_C \rangle$ given by Eqs. (7.3) and (7.7), respectively, both assume a case in which only one of the two transport processes contributes significantly to the particles motion. In order to combine these two estimation one has to consider how diffusion and convection interact with each other. On account of that it is beneficial to consider the motion of a particle's scattering center. The diffusion limit $\langle \tau_D \rangle$ given by Eq. (7.3) provides a solution for the average time this scattering center needs to propagate

from as distance of $r = R$ to $r = 0$ if its behaviour is solely influenced by diffusion. According to Strauss et al. (2011b) the average velocity of such a scattering center than can be assumed as

$$\langle \vec{v}_D \rangle = -\frac{6\kappa}{R}\vec{e}_r \tag{7.8}$$

with $\vec{e}_r$ being the radial unity vector of the spherical coordinate system and the negative sign denoting the inward motion opposed to the orientation of $\vec{e}_r$. Convection with the Solar wind on the other follows the outward orientation of the Solar wind speed and therefore expands Eq. (7.8) as

$$\langle \vec{v}_{CD} \rangle = V_{SW}\vec{e}_r - \frac{6\kappa}{R}\vec{e}_r \tag{7.9}$$

For a covered distance of $-R\vec{e}_r$ this estimation of the average velocity $\langle \vec{v}_{CD} \rangle$ leads Strauss et al. (2011b) to obtain an average residence time of

$$\langle \tau_{CD} \rangle = \frac{R^2}{6\kappa - V_{SW}R}. \tag{7.10}$$

Considering the result for the convection limit $\langle \tau_C \rangle$ given Eq. (7.7), this expression can be rewritten in terms of

$$\langle \tau \rangle = \left[\frac{1}{\langle \tau_D \rangle} - \frac{1}{\langle \tau_C \rangle} \right]^{-1}. \tag{7.11}$$

Applying this method Strauss et al. (2011b) calculates values of $\langle \tau \rangle \approx 80$ days using a radial extent of $R = 100$ AU for the Heliosphere, a Solar wind speed of $u_{SW} = 400$ km/s and a diffusion coefficient $\kappa = 6 \cdot 10^{22}$ cm^2/s. Compared with the simulation setup used for this work as discussed in Section 6.1 (see especially Eqs. (6.15) to (6.17)) this value is equivalent to a global value of $\lambda_\parallel = \lambda_\perp = 0.8$ AU. As it will be discussed in more detail in Section 7.3.2, this result for the average GCR residence times will be proven to be in agreement with the results of the simulation setup used in this thesis.

Figure 7.1 shows the four approaches to analytically estimate the residence time with respect to the mean free path and diffusion coefficient, respectively. In solid blue the approach for the diffusion dominated case is shown as given by Eq. (7.3) as described by Parker (1965). In contrast the convection dominated case (solid green) as given by Eq. (7.7) is constant for regardless of the length of the mean free path. Whereas the combination of both as derived by Strauss et al. (2011b) and given by Eq. (7.10) is well discussed, the prior estimate to consider both transport mechanism in one estimate by O'Gallagher (1975) (solid red) needs a short addendum.

Essentially, O'Gallagher (1975) aims to derive an expectation value for $\langle \tau \rangle$ equivalent as done by Parker (1965) via Eq. (7.3) but for a general case which includes both the convection limit $\langle \tau_C \rangle$ as given by Eq. (7.7) as well as the diffusion limit $\langle \tau_D \rangle$. In order to do so, a general behaviour of the expectation value as following

$$P(t) = \int_0^\infty t^{-n/2} e^{\beta/t - \gamma/t} dt \tag{7.12}$$

is assumed with n being an integer and β and γ coefficients depending on the Heliospheric radius R, the Solar wind speed u_{SW} and the diffusion coefficient κ, respectively. If K is a generalised Bessel function of imaginary argument, Eq. (7.12) subsequently converges to

$$\int_0^\infty t^{v-1} e^{\beta/t - \gamma/t} dt = 2 \left(\frac{\beta}{\gamma} \right)^{v/2} K(2(\beta\gamma)^{1/2}) \tag{7.13}$$

according to O'Gallagher (1975). The coefficients $v = 1/2$, $\beta = R^2/4\kappa$ and $\gamma = u_{SW}^2/4\kappa$ are determined by inserting Eq. (7.13) into the equation for the expectation value, assuming

the time dependent solution of the TPE as simplified given by Eq. (7.5) in the form of

$$P(r, u_{SW}, \kappa, t) = \frac{r}{\sqrt{4\pi\kappa}} t^{-3/2} \exp\left(-\frac{(u_{SW}t + r)^2}{4\kappa t} - \frac{\kappa t}{r^2}\right). \tag{7.14}$$

The difference between the analytical solution of Parker (1965) given by Eq. (7.2) and Eq. (7.14) is that the simplified TPE given by Eq. (7.5) as solved by O'Gallagher (1975) still contains the convective term. It can be shown that this approach leads to a general solution of τ as

$$\tau = \frac{R^2/\kappa}{u_{SW}^2/\kappa + 4\kappa/R^2}. \tag{7.15}$$

Based on this result, it is possible to derive the results for the convection $\langle\tau_C\rangle$ and diffusion limit $\langle\tau_D\rangle$, respectively as done above and given by Eqs. (7.7) and (7.3). In case of $u_{SW} = 0$ Eq. (7.15) simplifies to

$$\langle\tau_D\rangle = \frac{R^2}{2\kappa} \tag{7.16}$$

which can be specified as according the derivation by Parker (1965). Equivalently the solution in case of $\kappa = 0$ Eq. (7.15) simplifies after some rearrangements to

$$\langle\tau_C\rangle = \frac{R}{u_{SW}} \tag{7.17}$$

leads to the well known convection limit as given by Eq. (7.7). But regarding the general solution outlined by Eq. (7.15) which contains both case limits, the approach by O'Gallagher (1975) bears a neglected difficulty. The relation between the radial direction of the convection in regard to the investigated direction of the diffusive propagation is not addressed. Compared to the result by Strauss et al. (2011b) as given by Eq. (7.11) the approach by O'Gallagher (1975) combines the diffusion and convection limits by inverse addition instead of calculating the inverse difference.

As already pointed out by Strauss et al. (2011b) the estimate by O'Gallagher (1975) behaves non-physically for small values of λ and κ, respectively. In order to make Fig. 7.1 comparable to previous publications which mostly plotted $\langle\tau\rangle$ with respect to the diffusion coefficient κ, a corresponding scale is given on the top x-axis in program units of $PU = 6 \cdot 10^{22}$ cm^2/s. The vertical dashed line (cyan) indicates the value of λ and κ below which the convection starts to dominate over diffusion. It indicates a singularity as the inversed term inside the brackets in Eq. (7.11) becomes zero in this case. As briefly introduced above the other straight but horizontal line in green indicates the residence time $\langle\tau_C\rangle$ corresponding to an electron propagating outward to the Heliopause at R via convection. Based on these two straight lines it is possible to make the analytical estimations for $\langle\tau\rangle$ very easily comprehensible. As derived above the convection limit $\langle\tau_C\rangle$ only depends on the size of the Heliosphere indicated by R and the Solar wind speed u_{SW}. As the convection with the Solar wind is directed outward it works against the inward diffusion of particles. Hence the singularity where the diffusion limit $\langle\tau_D\rangle$ and the convection limit cross. In case of $\langle\tau_C\rangle < \langle\tau_D\rangle$ particles can not diffuse inward due to the outward convection being dominant.

Based on these considerations the notion of Strauss et al. (2011b) that the red line representing the estimation by O'Gallagher (1975) behaves non-physical becomes transparent. As the red line shows in comparison to the diffusion limit in blue, the combined estimation would decrease as convection becomes more dominant. This results in the combined estimation being equal to the convection limit in case of no diffusion if $\kappa = 0$ PU. Of course this behaviour is only possible if one assumed that diffusion and convection work together and not against each other. Therefore, as Strauss et al. (2011b) notice, the estimation by O'Gallagher (1975) is non-physical for the case of particle diffusing inward against the

convective forces but rather describes the behaviour of particles picked up by the Solar wind and carried outward with it. Thus explaining the deviation from the result of Strauss et al. (2011b) as O'Gallagher (1975) implicitly assumed a positive Solar wind speed with regard to the diffusive propagation whereas the case of particles diffusing inward against the direction of the Solar wind requires the Solar wind speed to be treated as negative.

7.1.2 Numerical Estimations

The major advantage of SDE modelling with respect to residence times is the structure of the solution, i.e. the fact that we calculate phase-space trajectories. If the phase space incorporates the temporal dimension a duration is assigned to each phase-space trajectory by the combination of the time increment ds and the number of steps performed n_i by the individual phase-space trajectories. Because the Euler-Maruyama scheme as implemented for this thesis (see Section 4.4 for details) utilises a well defined constant time increment, the durations τ_i corresponding to the phase space trajectories are easy to obtain. Most generally τ is given by the difference

$$\tau_i = |s_i^{exit} - s_i^0| \tag{7.18}$$

between the exit time s_i^{exit} as introduced in Section 6.1 and s_i^0 which often is simply the start time of the simulation and therefore set to be $s_i^0 = s_i^{init} = 0$. Under the assumption discussed above Eq. (7.18) therefore can be rewritten as

$$\tau_i = s_i^{exit} = n_i \cdot ds. \tag{7.19}$$

Despite often being labelled as propagation or residence time (see e.g. Florinski and Pogorelov, 2009; Strauss et al., 2013; Dunzlaff et al., 2015, amongst others), it has been pointed out by Vogt et al. (2020) that τ_i should better be referred to as the trajectory duration. By means of this distinction it is made transparent that τ_i is foremost a technical or mathematical quantity, respectively. In order to calculate a the physical quantity describing the residence times traditionally the expectation value of the time

$$\tau = \frac{\int f(x,t)t dt}{\int f(x,t) dt} \tag{7.20}$$

is utilised. But in case of the SDE approach this method is difficult to apply straight forward. Lacking a global solution for the probability density as demanded in order calculate τ via Eq. (7.20), τ has been calculated by previous studies somehow parallel to the approach to calculate the differential intensity as discussed in Section 6.3. Instead of calculating a global value of τ the expectation value is calculated for each phase space trajectory and averaged thereafter. Limited to individual trajectories the probability density $\rho(x_i^{exit})$ at the exit point x_i^{exit} thereby can be defined equivalent to Eq. (6.25). Applied to Eq. (7.20) the integrand of the denominator becomes one in case of s_i^{exit} and zero otherwise. As a consequence Eq. (7.20) reduces to

$$\tau_i = \frac{\int \rho(x_i^{exit}) s_i^{exit} ds}{\int \rho(x_i^{exit}) ds} = \frac{\sum_i^N s_i^{exit}}{\sum_i^N 1} = \frac{1}{N} \sum_i^N s_i^{exit}. \tag{7.21}$$

The seemingly equivalence of Eq. (7.21) to Eq. (6.27) (which describes the process of weighting the trajectories with the boundary condition in order to obtain the differential

Table 7.1: *Overview on the numerical estimations to calculate residence times. In brackets the radial distance at which the mean free paths are normalised is given, else-wise the mean free paths are normalised at* 1 *AU.*

τ/days	Population	$\lambda_\parallel, \lambda_\perp$/AU	R/AU	Source
		Galactic Cosmic Rays		
~ 300	H^+/100 MeV	$3, 0.03$ (10 AU)	100	Florinski and Pogorelov (2009)
~ 70	H^+/1 GeV	$6, 0.06$ (10 AU)	100	Florinski and Pogorelov (2009)
$\sim 50/150$	H^+/100 MeV	$0.2, 0.004$	100	Strauss et al. (2011b)
$\sim 15/70$	H^+/1 GeV	$0.2, 0.004$	100	Strauss et al. (2011b)
~ 430	e^-/10 MeV	$0.2, 0.004$	100	Strauss et al. (2011b)
~ 250	e^-/100 MeV	$0.2, 0.004$	100	Strauss et al. (2011b)
~ 180	e^-/6 MeV	$0.125, 0.0016$	120	this work, Section 7.3.2
		Jovian Electrons		
~ 6.3	e^-/6 MeV	$1, 0.01$ (global)	6	Strauss et al. (2013)
$\sim 6/11$	e^-/6 MeV	$0.125, 0.0016$	120	this work, Section 7.2.1

intensities) motivated to apply this method to obtain a measure of residence times for GCRs and Jovian electrons, respectively. In the following the main previous studies will shortly be discussed before analysing the problems concerning both their results as well as the derivation of the residence times as discussed above.

7.1.3 Previous Studies

Previous attemps to estimate the residence times of charged particles numerically by the means discussed above are given by Tab. 7.1. In order to make the results of these studies somewhat comparable the particle population, along with the estimated energies, mean free paths and Heliospheric radii are listed and discussed. Pioneering Florinski and Pogorelov (2009) modelled the GCR inflow into the Heliosphere and its residence times in different regions until it eventually reaches the Earth orbit . As the focus of their study is to determine radial gradients and diffusion coefficients by means of simulation of GCR modulation, the focus of Florinski and Pogorelov (2009) is not on the residence times. But the modelling approach as well as the discussion suggests that they are derived via the temporal expectation values as given by Eq. (7.21). Only the most inner region of the simulation setup, referred to as the Solar Wind by Florinski and Pogorelov (2009) as it is dominated by the radial outflow of the Solar Wind as described by Parker (1958) is comparable to the study presented herein. The simulation setup of Florinski and Pogorelov (2009) is difficult to handle in particular since the observational point is located at $r = 30$ and the Solar Wind dominated region is not centered around the Sun but shifted by the inflow direction of the LISM around 20 AU. Therefore Tab. 7.1 list the radius of ~ 100 AU as the radius of the sphere of the Solar Wind dominated region and not as the Solar centered radius. Compared to the approach used by this thesis as discussed qualitatively in Section 6.1.1 and quantitatively in Section 6.4.1 and 6.4.2 the values of $\lambda_\parallel$ and $\lambda_\perp$ are higher by a factor of $2-3$ from what is expected for electrons at $r = 10$ AU. This of course makes it difficult to compare the results as listed in Tab. 7.1 to the results by e.g. Strauss et al. (2011b).

The approach by Strauss et al. (2011b) explicitly is derived to estimate the residence times of Jovian electrons but also applied to GCR protons and electrons, thus making it

comparable to the approach by Florinski and Pogorelov (2009). In order to derive the residence times, Strauss et al. (2011b) bin the individual durations τ_i (see Eq. (7.18)) corresponding to the individual phase-space trajectories in a normalised histogram and weight them as

$$\langle \tau \rangle = \sum_{l=1}^{M} \tau_l \rho_l, \tag{7.22}$$

with M referring to the number of bins and ρ_l denoting the probability to find τ_l in the corresponding bin. Thereby this probability is defined by $\rho_l = N_l/N$ with N as the total number of trajectories and N_l as the number of trajectories with durations τ_l in the bin. As a consequence of these definitions the probabilities weighting τ_l in Eq. (7.22) are normalised to unity. Another quality of this method pointed out by Strauss et al. (2011b) is the fact that is it possible to distinguish between the maximum and the average of the distribution quite easily, defining a most likely residence time τ_{max} in contrast to the expectation value given by the average $\langle \tau \rangle$.

Tab. 7.1 shows a selection of results in order to be able to compare them both to the results of Florinski and Pogorelov (2009) and to the results obtained by this thesis. The first thing to highlight is the fact that two values are given for the Galactic proton residence times by Strauss et al. (2011b) due to the influence of drifts in A positive and negative Solar cycles, respectively. As the drift in A positive Solar cycles support the propagation of protons inward, the corresponding residence times are significantly lower in comparison. Therefore it seems reasonable to only discuss the comparability of the result regarding the A negative cycle. Since Strauss et al. (2011b) used the same approach to estimate the radial dependence of the mean free paths as this thesis (see Eq. (6.15)) it is easily possible to calculate the values of $\lambda_{\parallel/\perp}$ at 10 AU and compare them. As it turns out they appear to almost equal to the values used by Florinski and Pogorelov (2009) for the 100 MeV protons, $\lambda_{\parallel}$ being slightly smaller and $\lambda_{\perp}$ being slightly larger. Due to the differing radial dependences (the increase of the mean free paths with the radial distance applied by Florinski and Pogorelov (2009) is flatter) and the additional contribution of drifts, it is reasonable for the estimated residence times by Strauss et al. (2011b) to be much lower. However, compared to the approach developed by this work and discussed in the subsequent Section 7.2, the GCR electron residence times appear to be almost twice as long, although simulated by applying larger values for $\lambda_{\parallel}$ and χ. Also compared to the Jovian electron residence times by Strauss et al. (2011b) for which the drift effects are irrelevant due to their insignificance on small radial distances compared to diffusion and convection, the proton residence times by Florinski and Pogorelov (2009) appear to reasonable within the limitations of both simulation setups. Therefor this benchmark indicates that - although the setup used for this work does not incorporate drift effects - also the GCR electron residence times as listed in Tab. 7.1 deviate due to the different approach to estimate the residence times and not due to the different modelling approach considering additional drifts.

Strauss et al. (2013) who cover Jovian electron instead of GCR protons and electrons, applied significantly larger values for the parallel and perpendicular mean free path using $\lambda_{\parallel} = 1$ AU and $\chi = 0.01$. In order to find a measure for Jovian electron residence times within data, quiet-time increasess (QTIs) as first reported by McDonald et al. (1972) were taken into account. These phenomena are transients released from the Sun which first increase and decrease the quiet-time electron flux from Jupiter if they are located between the source and the observer. A prominent example being CIRs which act as diffusion barriers as shown by the modelling by Kissmann et al. (2004) and Vogt (2013). As pointed out by Strauss et al. (2013) two effects take place that allow to estimate the Jovian residence time: first a decrease in the flux measured at Earth orbit due to the diffusion barrier and secondly an increase of electron flux due to the interaction of the

transient with the Jovian magnetosphere, causing an increased outflow of Jovian electrons. The propagation parameter therefore could be set in order to meet the residence times estimated with respect to the data.

In contrast to the results of Florinski and Pogorelov (2009) and Strauss et al. (2011b) who applied models both quantitatively and qualitatively for the mean free paths in order to find an estimation of the residence times, Strauss et al. (2013) applied a measured value of the Jovian residence time in order to get an estimation for the mean free path. The fact that the values for the electron mean free path differ by almost an order of magnitude, demands a more further discussion on the physical inconsistencies within these results and possible measures to avoid them. As a consequence, these consideration will lead to the derivation of new estimations for the residence time, both numerically (Section 7.2.1) and analytically as well given in Section 7.3.3. As shown in Tab. 7.1, this approach is able to give an estimation for the Jovian residence time in agreement with the results of Strauss et al. (2013) but in contrast by applying values of $\lambda_{\parallel}$ and χ within the range used by comparable modelling studies.

7.1.4 Physical Inconsistencies

A dependence of the numerical results on the simulation setup can be identified in the results by Florinski and Pogorelov (2009) who noticed that charged particles observed at $r = 95$ AU were attributed to residence times one third higher than the residence times derived for particles observed at $r = 30$ AU. As this is a clearly unphysical result, Tab. 7.1 as well as the discussion in Section 7.1.3 only takes the residence times of particles observed at $r = 30$ AU as the innermost observational point into account. The reason for this behaviour is most likely explained by the method of time-backward SDE simulation itself. If all phase-space trajectory are treated equally likely, a observational point at $r = 95$ AU adds an additional population of trajectories, namely trajectories of pseudo-particles which either propagate inward, pass the Sun and reach the outer boundary on the opposite side, or turn back and then follow the trajectory of a pseudo-particle which directly propagated outward from the injection point. Since these possibilities are mathematically more likely than they are physically as already discussed in Secs. 6.2 and 6.3, they mathematically increase the residence times for observational points more out in the Heliosphere, although physically particles entering the Heliosphere reach these observational points physically at lot sooner.

The comparison with the results of Strauss et al. (2011b) shows another problem: how long these residence times are, both in comparison to the electrons residence times estimated by Strauss et al. (2011b) and with respect to physical considerations. As already discussed above, the proton residence times by Florinski and Pogorelov (2009) and Strauss et al. (2011b) differ due to the inclusion of drift effects and the radial dependences of the mean free paths applied. But since the proton and electron residence times estimated by Strauss et al. (2011b) are based on the same modelling approach the electron results can be used to evaluate the comparability of the results as indicated above. As argued by Vogt et al. (2020), one would expect to find significantly shorter residence times for relativistic particles, since the result for e.g. 10 MeV electrons suggest that the average radial distance covered per day is less than a forth of 1 AU or in other terms, the length of the parallel mean free path at Earth orbit.

This problem gets even more highlighted when discussing the results of Strauss et al. (2013). Tab. 7.1 shows that the values for mean free paths are unrealistically high compared

to the results of this thesis presented in Section 6.4.1 and 6.4.2 and the discussion of the literature therein, including previous studies of the same authors as Strauss et al. (2011a,b) which aimed to model not the residence times but the differential intensities of Jovian and GCR electrons. Furthermore, as mentioned above, the effect of the Jovian corotation as discussed in Section 6.4.6 strongly suggest a connection between the significance of this effect, Jovian residence times in the range of a few days (and not weeks or months) and the values of the mean free paths. Thus, despite the limitation of comparing proton and electron residence times of different modelling approaches, the numerical estimations so far show an inconsistency in the way that either the mean free paths or the residence times appear to be unrealistically high, if Eq. (7.21) or Eq. (7.22) are applied. As already argued by Vogt et al. (2020) this is due to the fact, that these approaches assign equal probability to each individual phase-space trajectory in contrast to the calculation of the differential intensity. Following the discussion in Section 6.2, the individual trajectory durations τ_i have to be weighted as well, according the physical significance of the corresponding phase-space trajectories. If the phase-space trajectories are interpreted as an ensemble of pseudo-particles propagation through the phase space, the problem can be formulated as follows: The same physical significance (or amount of pseudo-particles) has to be assigned to a phase-phase trajectory regardless of whether the differential intensity or the residence time is calculated. As shown here based on Vogt et al. (2020) this is not the case for the methods applied above, thus the inconsistency of the results listed in Tab. 7.1.

7.2 A Self Consistent Approach

As discussed e.g. in Section 6.2 and shown by Vogt et al. (2020, under rev.) SDE based modelling schemes are physically interpreted by assigning each individual solution (phase-space trajectory) a physical significance by applying boundary conditions as a weight. The effect on the individual contribution of the phase-space trajectories is shown by e.g. Figs. 6.6 and 6.7. The following Section will establish an approach to weight the exit times of the phase-space trajectories in the same way they are considered to calculate the resulting differential intensity. It already has been mentioned by Tab. 7.1 and in the discussion above that the new approach not only is self consistently derived but also delivers estimates for the residence in a reasonable range of values.

7.2.1 Derivation

According to Vogt et al. (2020) and discussed in more detail in Secs. 7.1.3 and 7.1.4, in order to estimate the residence times equivalently to the differential intensities as given by Eq. (6.27), the weighting by the boundary conditions has to be incorporated into the calculation of the expectation value by Eq. (7.20). As shown by Vogt et al. (2020) this can be done by a redefinition of the probability density ρ as

$$\rho(x_i^{exit}, t) = \frac{f(x_i^{exit}, t)}{f_0(x)}. \tag{7.23}$$

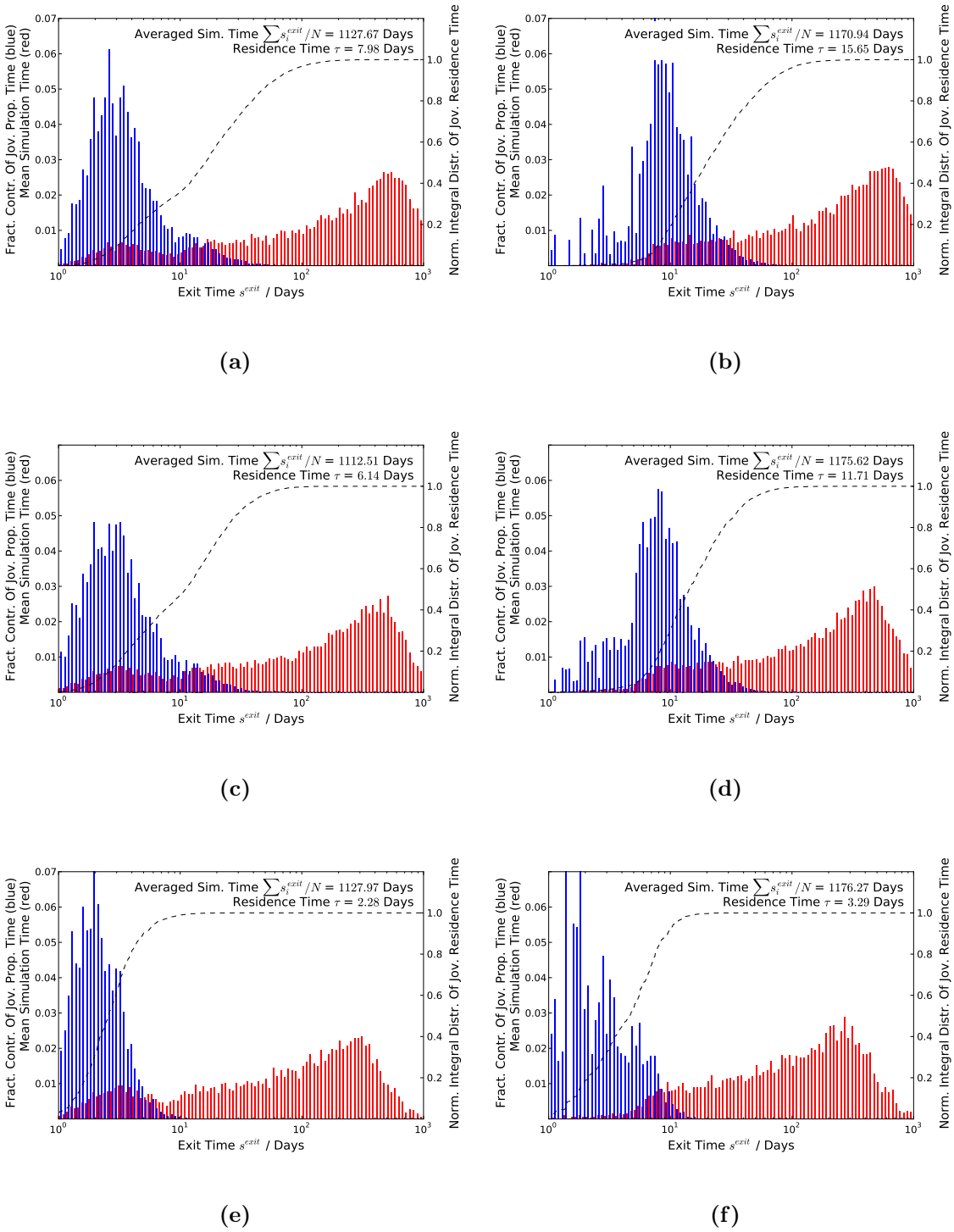

Figure 7.2: *Binned distributions of simulation times (red) and their corresponding contribution to the residence times according to Eq. (7.25). Equivalent to Fig. 6.6 the right panels show the case of and the left panels the case of bad magnetic connection to the Jovian source. The upper most panel thereby show the distribution for initial energies $E^{init} = 0.3$ MeV, the panels in the middle for $E^{init} = 6$ MeV, whereas the lower panels illustrate the case for relative high initial energies of $E^{init} = 100$ MeV. The dashed line represents the integral distribution of the residence times with respect to the exit times, similar as shown in Fig. 6.6 for the differential intensities.*

This redefined probability density incorporates the boundary conditions within the numerator (see Eq. (6.26) in Section 6.3) in contrast to the approach given by Eq. (7.21). Normalised by the global phase-space density

$$f_0(x) = \int f(x^{exit}, t)dt \tag{7.24}$$

in the position space equivalent to the which later cancels out in the calculation. Eq. (7.23) essentially describes the probability density not isolated at one point but in relation to the (approximated) global solution. Therefore the redefined ρ given by Eq. (7.23) serves as an equivalent weighting as applied to the differential intensity in Eq. (6.27). Thus assigning the same weight to each phase-space trajectory in order to calculate the resulting differential intensity as well as to calculate the residence times. In the frame of attributing pseudo-particles to the evolution of the phase-space density elements: The phase-space trajectories represent the same amount of pseudo-particles regardless which physical quantity (differential intensity or residence time) is derived from them. Applying this to Eq. (7.20) cancels out the global phase-space density as incorporated by Eq. (7.24) and if transformed from position space to energy space subsequently leads to the expression

$$\tau(r^0, E^0) = \frac{\sum_{i=1}^{N} s(E_i^{exit}) \cdot f(E_i^{exit})}{\sum_{i=1}^{N} f(E_i^{exit})}, \tag{7.25}$$

for individual phase-phase trajectories. Assigning the same physical significance to the individual phase-space trajectories in order to calculate the residence time as for calculating the differential intensity appears to be even more important to the distribution of exit times as shown by Fig. 7.2. For the simulation the same parameter set was used as listed in Tab. 6.1, most significantly $\lambda_{\parallel} = 0.125$ AU and $\chi = 0.0125$ as estimates for the parallel and its relation to the perpendicular mean free path. Equivalent to Fig. 6.6 in Section 6.3 the unweighted distribution of exit energies E^{exit} is shown in red accompanied by the fractional contribution to the (Jovian) residence time in blue i.e. the distribution of exit times weighted by Eq. (7.25). The left panels of Fig. 7.2 represent the case of good magnetic connection to the Jovian source and show that the maximum of the blue distribution is in agreement with the maximum of the red one similar to the situation as notice for the differential intensity in Fig. 6.6. But for the residence times the weighted contribution to the residence times is only in agreement with the minor second maximum of the distribution of the exit times. This holds to be true for small initial energy such as $E^{init} = 0.3$ MeV as shown by Fig. 7.2a, for $E^{init} = 6$ Mev (Fig. 7.2c) and for a large initial energy as $E^{init} = 100$ MeV as shown by Fig. 7.2e. As discussed in more detail by means of Fig. 7.3 an increase of the initial energy just narrows the distributions a bit to smaller exit times but does not change the overall interdependence.

Most significant is the discrepancy between the binned results for the residence times obtained by applying Eq. (7.25) according to the findings of Vogt et al. (2020) and the average simulation times. The integral distribution of the blue histogram given by dashed lines in Fig. 7.2 shows that the ranges of convergence is almost a magnitude lower than the maxima of the distributions of the exit times. Normalised to the value of the residence times (equivalent to the presentation in Fig. 6.6) the integral distributions thereby show, that trajectories with higher exit times are almost negligible according to the approach derived by this thesis. This of course explains the disparity between the values of the averaged simulation times and the new estimations for τ. The red histograms thereby suggest values about ~ 1000 days for the average simulations times with very limited variation between cases of good and bad connection as shown in the right panels of Fig. 7.2. For a radial distance of ~ 4 AU between the Jovian source and the observer these values seem unrealistically high, especially the lack of dependence on the magnetic connection. This is

due to the fact that again the influence of the magnetic connectivity is limited to a small trajectory population of small exit times which in case of good connection constitutes a second minor maximum. The comparison between the left and the right panels of Fig. 7.2 shows this relation quite clearly. Equivalent to the observation made by means of Fig. 6.7, also Fig. 7.2 shows a large diffusive background population which dominates the calculation of the average simulation times and therefore almost hides the influence of the magnetic connection. This effect will be discussed subsequently based on Fig. 7.3 in more detail. A possible application of this finding in order to improve the analytical estimations of diffusive transport (in case of this thesis but not generally limited to the residence times) will be introduced and tested in Section 7.3.3.

The comparison between the values of the averaged simulation times and the residence times quantifies this notion. The new approach developed within this work suggest values of $\tau \sim 8$ days (see Fig. 7.2a for $E^{init} = 0.3$ MeV), $\tau \sim 6$ days (see Fig. 7.2c for $E^{init} = 6$ MeV) and only $\tau \sim 2$ days for high energies such as $E^{init} = 100$ MeV as shown by Fig. 7.2e in case of good connection. As shown for the equivalent energies by Figs. 7.2b, 7.2d and 7.2f the residence times increase in case of bad connection by a factor of $\sim 1.5 - 2$. Calculated with the realistic parameters as derived in Section 6.4 and listed in Tab- 6.1 these values are in agreement with the quantitative estimate by Strauss et al. (2013) as discussed above in Section 7.1. But in contrast to Strauss et al. (2013) the new method calculates realistic values for the residence times even for small (and more realistic) values of $\lambda_{\parallel/\perp}$ whereas Strauss et al. (2013) had to utilised much larger values for the mean free path deemed as unrealistic not only by our findings as presented by Vogt et al. (2020) but also by prior studies on the electron mean free path such as e.g. Palmer (1982), Bieber et al. (1994) and Tautz and Shalchi (2013) and modelling approaches by e.g. Potgieter and Ferreira (2002), Dröge (2005) and Strauss et al. (2011a). Therefore this thesis accomplished to harmonise the concurring modelling results for the Jovian electron mean free path based on comparison with spacecraft measurements of the electron differential intensity and estimates of the residence times, respectively.

7.2.2 Parameter Dependences

Similar to Fig. 6.7 in Section 6.3.2, also Fig. 7.3 shows the intensity sink (marked in red) over the whole range of initial energies in case of good connection to the Jovian source. Similar to the discussion on the energy dependence of the differential intensities the right side shows the distributions of the phase-space trajectories binned by their corresponding exit times. The top panel thereby represents the case of good magnetic connection to the source, the panel in the middle the case of bad connection and the bottom panel the difference between the distributions. The right side shows the equivalent plots for the distributions of the corresponding contributions to the resulting residence times. As already discussed in Section 6.3.2, also Fig. 7.3e shows that the difference between the phase-space trajectory distributions for good and bad magnetic connection to the source is limited to the population below the intensity sink as indicated in red in Fig. 7.3a. The fact that the distribution apart from this area appear to be almost equal further strengthens the assumption made for the differential intensities that the case of bad connection displays the population of trajectories which would reach the source independently from the magnetic connection. This notion is also supported by the fact that in the range of this populations the difference between the distribution for magnetic connection (Fig. 7.3a) and bad magnetic connection (Fig. 7.3c) as shown in Fig. 7.3e are negligible. As also shown in Fig. 7.3f

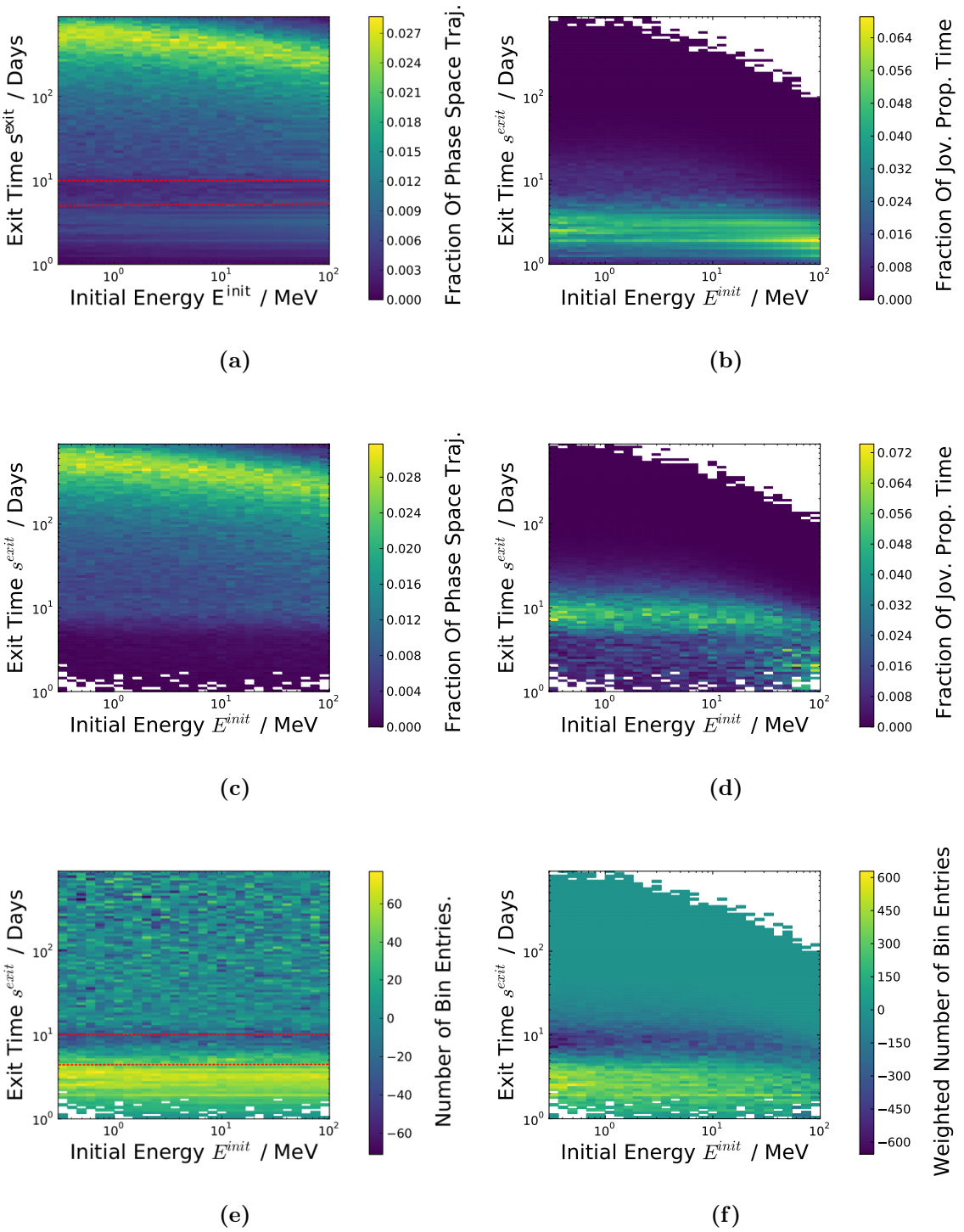

Figure 7.3: *Binned distributions of exit times s_i^{exit} over the whole energy range dominated by Jovian electrons according to the spectrum shown e.g. in Fig 3.15. Whereas the right panels show them weighted by their contribution according to Eq. (7.25), the left side displays the unweighted results of the simulation. Equivalent to Fig. 6.7 the top panels show the case of good and the middle panels show the case of bad magnetic connection to the Jovian source. The bottom panels show the differences between the distributions above. Also similar to Fig. 6.7 the intensity sink separating the population of phase-space trajectories which are dominated by parallel transport is marked in red.*

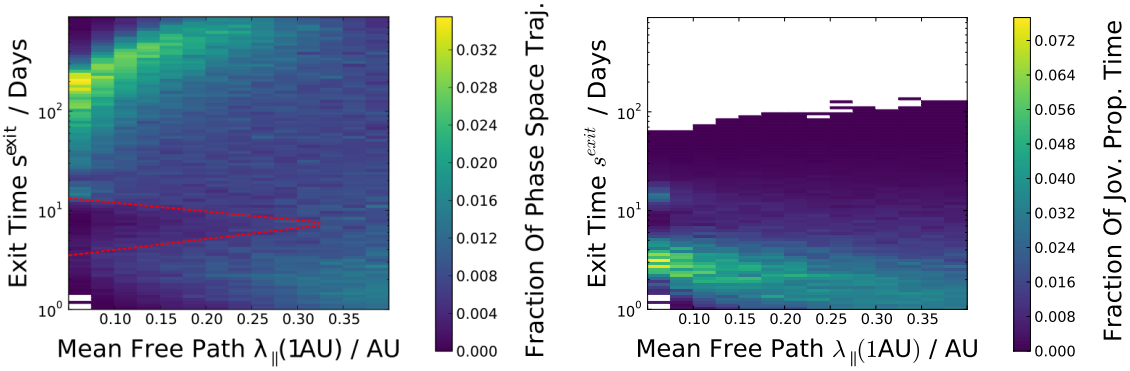

(a) **(b)**

Figure 7.4: *Binned distribution of exit times s_i^{exit} for simulations performed for different values of $\lambda_\parallel$ (see the range investigated in Figures 6.8 and 6.9) and an initial energy of $E_i^{init} = 6$ MeV. Similar to Fig. 6.8 discussing the differential intensity, the left panel which shows the unweighted simulation times displays the intensity sink (red) as fading out towards larger values of $\lambda_\parallel$. This behaviour is reflected by broadening of the distribution of the weighted contributions in the right panel. Since $\lambda_\parallel$ most dominantly influences the particle propagation during times of good magnetic connection, only this case is shown.*

displaying the differences of the weighted number of bin entries in case of good magnetic connection an additional population of phase-space trajectories with short durations is present.

In case of an observer getting closer to the point of good magnetic connection, the population of phase-trajectories does not entirely change but additional, shorter phase-space trajectories connect the observer and the source. These additional phase-space trajectories, which are more dominated by parallel than perpendicular diffusion, are displayed in Fig. 7.3e. Also the distributions of the corresponding contributions to the residence times as shown by the right panels of Fig. 7.3 reflect this. Although it seems that the maxima of the distributions for good (Fig. 7.3b) and bad magnetic connection (Fig. 7.3d) are just at different values on the y-axis denoting the exit times, the difference shown by Fig. 7.3f reveals the same relation between the distributions for good and bad connection as discussed for the phase-space trajectories by means of Fig. 7.3e.

Equally significant is the influence of different values for the parallel mean free path $\lambda_\parallel$ as shown in Fig: 7.4. As for the simulations shown by Fig. 7.3 the standard parameter as listed in Tab. 6.1 were used, for the initial energy in particular $E^{init} = 6$ MeV. In contrast to the trajectories as shown in Fig. 6.8a, the distribution of exit times in Fig. 7.4a concentrates for lower values of $\lambda_\parallel$, leading simultaneously to a shorter peak and a longer minimum duration. This is explained by the fact that shorter mean free paths cause more scattering which increases the amount of timesteps needed to reach the Jovian boundary even on a more or less optimal trajectory. With increasing time on the other hand the possibility to cross the Jovian boundary enhances due to the smaller step size. This behaviour of course is related to the size of the time increment in the way that a decreased time increment balances out the increase of the step size by an increased mean free path. Compared with Fig. 7.4b, which shows the corresponding distributions of the contribution to the resulting residence times, these effects are reflected in the broadening distribution towards higher values of $\lambda_\parallel$ as well in the shorter maxima of the weighted distributions.

The influence of χ as shown in Fig. 7.5 shows a similar behaviour in case of bad magnetic connection as discussed regarding $\lambda_\parallel$ in the range of lower values. As $\chi = \lambda_\perp/\lambda_\parallel$ determines

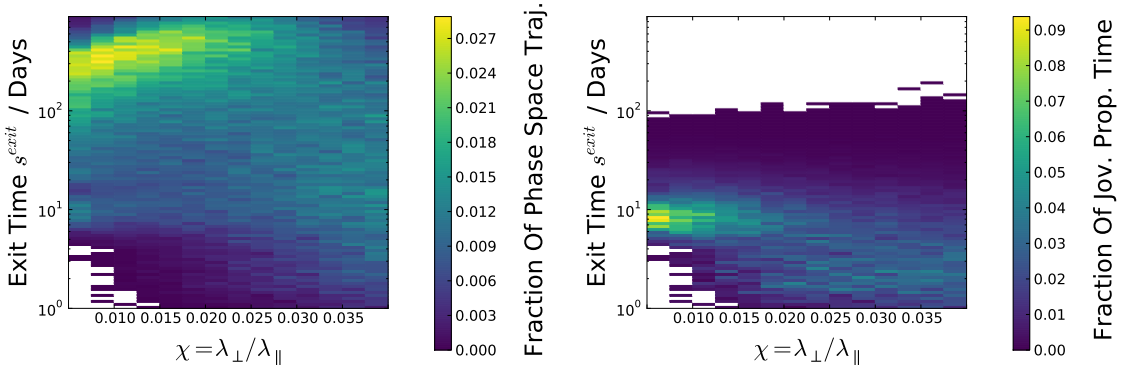

(a) **(b)**

Figure 7.5: *Binned distribution of exit times s_i^{exit} for simulations performed for different values of χ (see the range invesigated in Section 6.4.2) and an initial energy of $E_i^{init} = 6$ MeV. Similar to Fig. 6.10 the significant distribution broadens for larger values of χ. In contrast to Fig. 7.4 the case of bad magnetic connection is shown.*

the value of the perpendicular mean free path $\lambda_\perp$ with respect to $\lambda_\parallel(1\text{ AU}) = 0.125$ AU, this further supports the argument above. For higher values of $\chi \geq 0.02$ Fig. 7.5a the distributions become increasingly flattened out, an effect also present in Fig. 7.5b. Due to the magnetic alignment of Jovian source and observational point this is not accompanied with decreasing maxima for the distribution as the more effective perpendicular diffusion increased the possibility to reach the Jovian boundary from magnetically separated locations.

7.3 Physical Interpretation

Having discussed in detail how the boundary conditions determine the probability of phase-space trajectories as the individual solutions of the SDEs modelling scheme and the implications of the difference between considering the correct boundary conditions or not to the modelling results, it is necessary to discuss the physical implication of these findings, too. As the Jovian boundary condition weights the contribution of the individual phase-space trajectories by convolution with the source spectrum via the exit energies, the main purpose of the subsequent Section is to investigate the relation between adiabatic energy changes and charged particle diffusion. Based on this, also the relation between the analytical and numerical estimates for the residence times will be re-evaluated. Subsequently the considerations given in this Section will results in a revised analytical approach for the residence times in Section 7.3.3 which will be shown to be self consistent with the new numerical estimations as given by Eq. (7.25).

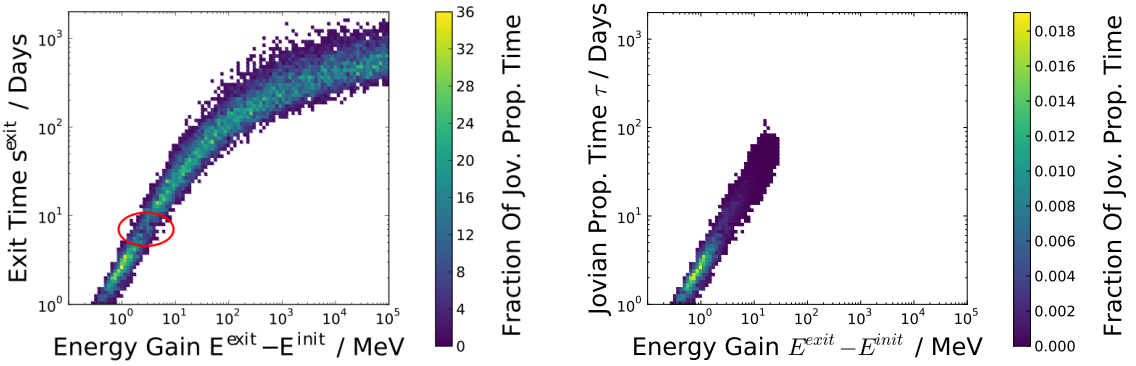

(a) **(b)**

Figure 7.6: *The relation between the energy gain (or loss, in the normal time-forward scenario) as a function of the corresponding exit time (left panel) or propagation time (right panel). Shown is the case of good magnetic connectivity as published by Vogt et al. (under rev.). The intensity sink again is marked in red.*

7.3.1 The Influence of Adiabatic Energy Changes

As discussed already in context of deriving both the differential intensities in Section 6.3 (see especially Fig. 6.6 in Section 6.3.2) and the new approach to the residence times above in Section 7.2.1, the adiabatic energy changes provide the measure to weight the contribution of the individual phase-space trajectories according to their physical significance. Considering their role for the calculation of residence times which highlights an interdependence between the adiabatic energy changes and the trajectories simulation times it is essential to investigate them further. As shown by Vogt et al. (under rev.) the understanding of the relation between adiabatic energy changes and the treatment of diffusion within the TPE not only questions the accuracy of the analytical treatment of residence times by Parker (1965), O'Gallagher (1975) and Strauss et al. (2011b) but also provides the necessary insight in order to offer an updated and presumably correct analytical estimation in Section 7.3.3.

Fig. 7.6 previously published by Vogt et al. (under rev.) shows the relation between the energy gain and the unweighted simulation times (Fig. 7.6a) and in the right panel (Fig. 7.6b) the corresponding relation in case the simulation times are weighted according to Eq. (7.25). Note further that Fig. 7.6 shows the case of good connection between the Jovian source and the observer at Earth orbit, as it was previously established within this work that the main difference between cases of good and bad connection is the present of a population of phase-space trajectories which are dominated by parallel transport. This assessment is supported by Fig. 7.6a as it shows the same intensity sink separating the diffusive background population from the parallel transport dominated one as identified e. g. in Figs. 6.7 and 7.3.

In order to interpret these effects correctly, it seems reasonable to address how energy changes are implemented within the modelling framework - and by that means also within the TPE. Because the IPM is almost empty particle-to-particle interactions are insignificant and their effect is therefore negligible within the TPE. This means that all energy changes depicted in Fig. 7.6 are caused by the effects described in Section 5.4. Because

these adiabatic energy changes only depend on the particle energy and its radial position according to Eq. (5.53) the implementation as given by 6.13 leads to the following situation: For each step of the random walk the particle gains energy depending on the time increment Δs, its kinetic energy before the step E_{n-1}, and its radial position after the step r_n. Thereby the radial direction of the step as wells as its spatial size appears to be irrelevant. As stated by Vogt et al. (2020), this leads to particles spending more simulation time at small radii losing more energy and implicitly to a statistical connection between the average energy losses and the particle's mean free paths.

Figure 7.6 shows these adiabatic energy gains on the x-axis against the exit times s^{exit} on the y-axis. Whereas the relation between the energy gains and the number of random walk steps perform by the trajectory is non-linear, the relation between the simulations times and the number of random walk steps is, according to Eq. (7.19). The distribution shown by Fig. 7.6a reflects this as especially for higher simulation times phase-space trajectories of the same (time) length can be related to different rates of adiabatic energy changes $E^{exit} - E^{init}$ according to Vogt et al. (under rev.). The relation between the residence times and the energy gains shown in Fig. 7.6b, however, is almost linear in the double logarithmic display. By means of weighting the phase-space trajectory according to their physical significance the upper right tail of the distribution vanishes in Fig. 7.6b. This can be explained by the assumption above that there is a connection between large energy gains and perpendicular diffusion dominated phase-space trajectories which cause the particles to remain at relatively small radial distances for a long time. The comparison between Fig. 7.6a and 7.6b therefore proves the implicit assessment that large adiabatic energy gains are connected to long simulation times which are physically insignificant.

7.3.2 The Relation Between Analytical and Numerical Estimations

The large discrepancy between both the maxima of the exit energy and exit times distributions on the one side and the maxima of the fractional contributions to the resulting differential intensities and residence times as shown by Figs. 6.6 and 7.2, respectively, raises the question whether this is an effect caused by the method of solving the TPE by means of SDEs or by the mathematical treatment of diffusion itself. Therefore it is necessary to compare the analytical estimations of residence times by Parker (1965) and Strauss et al. (2011b) as discussed in Section 7.1 to the corresponding numerical estimations by means of applying Eq. (7.25). The main restriction of any analytical approach to solve the TPE is the necessity to estimate the radial and energy dependent diffusion tensor $\hat{\kappa}$ as one constant value κ, independent of radius and energy. Another necessary assumption made by Parker (1965) and all following approaches as well is a constant value for the Solar wind speed u_{SW}, which furthermore is assumed to be directed radially outward. Other assumptions needed as discussed above in Section 7.1.1 is the isotropic diffusion of particles as well as the central position of the observational point. Since of course these assumption are not able to be applied to Jovian electron transport, the comparison between numerical and analytical estimations has to be applied to GCR electron residence times. As discussed by Vogt et al. (under rev.), this can be meaningfully done because although the same transport processes also govern the propagation of GCR electrons, their isotropic influx allows allows to estimate parallel and perpendicular diffusion into one value of κ (i.e. assume an isotropic diffusion tensor according) to e.g.Parker (1965).

Figure 7.7 therefore shows the distributions of GCR electron exit times (Fig. 7.7a) and their fractional contribution to the resulting residence times (Fig. 7.7b) over the whole

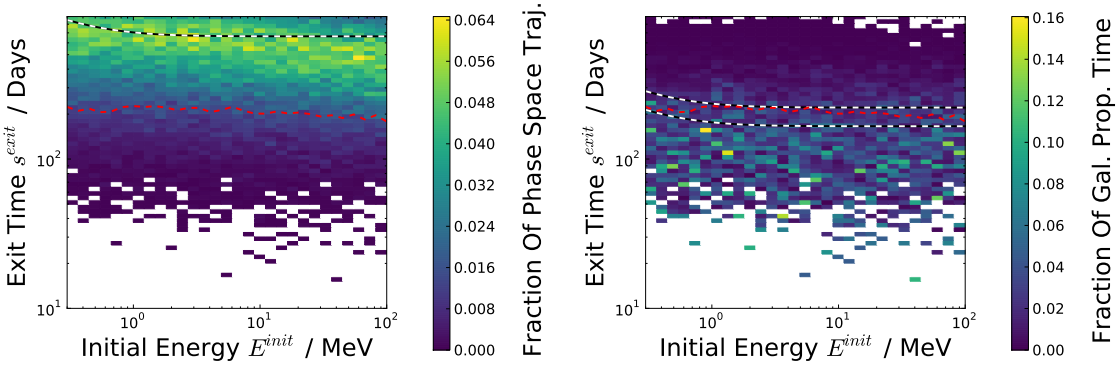

(a) **(b)**

Figure 7.7: *Similar to Fig. 7.3 but instead of the Jovian magnetosphere, trajectories exiting at the outer boundary are shown. Therefore no distinguishing between good and bad magentic connection is needed. The left panel shows the unweighted distribution of exit times alongside the numerical estimate according to Eq. (7.25) (red) as well as the analytical estimate for the diffusion limit according to Eq. (7.3) in dashed white and black. The right panel correspondingly shows the exit times contribution to the numerical estimate as well as an upper and lower limit for the new analytical estimate according to Eqs. (7.33) and (7.31). Both Figures are included in Vogt et al. (under rev.).*

energy range. Compared with the corresponding figures showing the distributions for Jovian electrons (Figs. 7.3a, 7.3c and 7.3b 7.3d, respectively) the GCR electrons show an even more pronounced behaviour equivalent to the case of bad connection to the Jovian source. This similarity is caused by the fact that of course the Galactic source is isotropic. Combined with a large distance to cover this leads for trajectories which are dominated by parallel transport to become as insignificant as unlikely due to the fact that in order to propagate effectively inwards a particle would have to diffuse perpendicular to the magnetic field lines.

This leads directly to the problem, how to compare the analytical estimation which assumes a globally constant value for the diffusion coefficient κ to a simulation setup which distinguishes between radial dependent values for perpendicular and parallel diffusion. In order to estimate how significant parallel diffusion is compared to perpendicular diffusion in case of GCRs electrons it seem reasonable to look at both the effectiveness and minimal path length of parallel and perpendicular diffusion. The relative effectiveness of parallel and perpendicular diffusion is defined by the factor of $\chi = 0.0125$ according to Eq. (6.16) and discussed in Section 6.4 in detail. Explicitly the values given by Tab.6.1 lead to a range between $\lambda_{\parallel} = 0.125$ AU and $\lambda_{\perp} = 0.001875$ AU at $r_0 = 1$ AU. Within this range of values an average, global value of λ to describe the diffusion of GCRs inward has to be estimated. As indicated above, although transport by parallel diffusion is much more effective it is tight to the Parker spiral. In contrast the much less effective perpendicular transport can (in the optimal case) lead (under idealised circumstances) to a radial trajectory. Therefore the ratio between the path length of the Parker spiral and the radial distance is taken as a proxy to estimate the relative significance of parallel to perpendicular transport. In case of the parameter as listed in Tab. 6.1 and used for the simulations shown in Fig. 7.7 this leads to a ratio of $L_P/R \approx 20$ between the path-length of the nominal Parker spiral L_P and outer boundary R. Since the parallel diffusion is about 80 times more effective than perpendicular diffusion, however, the 20 times longer distance to cover still indicates an effective value of $\bar{\lambda}$ near the one for the parallel mean free path $\lambda_{\parallel}$. Combined with the

fact that the adiabatic energy changes are most effective for small values of the heliocentric radius according to Eq. (5.52) and therefore in the inner Heliosphere it seems reasonable to apply the simplistic approach to use the value of the parallel mean free path at 1 AU in order to estimate a globally constant diffusion coefficient κ.

Applying this value in order to calculate the analytical estimates according to Eqn.7.3, supports these considerations by comparison with the maxima of the unweighted distribution of exit times in Fig. 7.7a. In both panels of Fig. 7.7 the numerical estimate of the residence times as developed in this work is shown by a red dashed line, whereas the analytical ones are shown in dashed white and black. Focusing first at Fig. 7.7a it is obvious that although the red dashed line is not in agreement with the maxima of the exit times distributions (as expected), the white and black dashed line which represents the analytical estimates apparently is. This of course raises the question why the analytical estimate according to Eq. (7.3) rather resembles the behaviour of phase-space trajectories without weighting than the actual physical solutions. Because all parameters are the same (or a least chosen equivalent in case of κ) it seems natural to assume that the analytical estimate indeed is equivalent to the averaged simulation times. This suggestion is further supported by the fact that the analytical estimates specifically describe the propagation of the probability density (without being convoluted with the boundary condition) and not the differential intensity according to Parker (1965). Therefore instead of an analytical result equivalent to the new approach given by Eq. (7.25) the analytical estimation provided by Parker (1965) and Strauss et al. (2011b) rather provides an expectation value for τ according to Eq. (7.20) with respect to the probability distribution. By applying a SDE based simulation approach and specifically investigating the effect of the boundary conditions on the distributions of exit energies and exit times, therefore this thesis was able to show, that the difference caused by the fact that Parker (1965), O'Gallagher (1975) and Strauss et al. (2011b) neglect the boundary conditions are too severe in order to ensure reliable solutions. Consequently in the next Chapter this thesis will attempt to derive a new analytical estimation which - at least qualitatively as a prove of concept - is able to avoid these simplifications and includes the effect of the boundary conditions on the mathematical solution for the probability density function.

7.3.3 A Revised Analytical Approach

As shown and discussed above, to derive an analytical estimation for the actual physical residence time, the convolution with the source spectrum as applied via e.g. Eq. (6.27) and Eq. (7.25) has to be applied to the analytical estimates too. This raises the problem, that instead of simulation times of individual trajectories, the expectation value for the probability density as a whole has to be weighted by the source spectrum. Since the energy difference between source and observer is the determining quantity by which the trajectories are weighted according to their physical significance as discussed in Section 6.3, it is therefore necessary to estimate a characteristic energy loss[1]. As already discussed by Vogt et al. (under rev.) the approach to assume a characteristic energy change which is depending on the initial energy is supported by Parker (1965) who assumed a time dependent energy loss of

$$E(t) \approx E_0 \exp\left(-\frac{u_{sw} t}{R}\right). \tag{7.26}$$

[1]In the time-backward frame as used for the simulation setup, this would be characteristic energy gain.

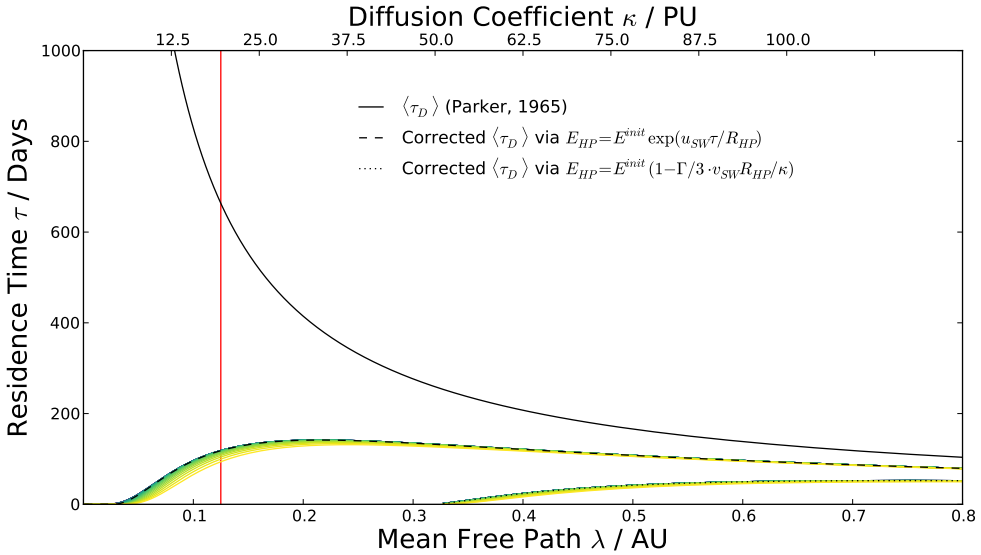

Figure 7.8: *The analytical estimate of the diffusion limit according to Parker (1965) as discussed in Section 7.1.1 alongside two possible corrected variants. These utilise the two estimations for the expected energy changes during the propagation inward according to Parker (1965) and Parker (1966) as discussed in Section 7.3.3. Thereby the dashed black lines show the estimated energy changes for energies of* 6 *MeV at the observation point. The colour coding indicated the variability of these results for different observed energies throughout the Jovian electron energy range. The mean free path at* 1 *AU as assumed by this thesis according to the results obtained in Section 6.4.1 and revisited for the purpose of estimating the residence times in Section 7.3.3 is indicated by the vertical red line.*

According to e.g. Parker (1965, 1966), Jokipii and Parker (1970) and Strauss et al. (2011b) the avarage fractional loss can be calculated by deconvoluting

$$\omega(r,t) = \int_0^\infty j(r,E,t)dE \tag{7.27}$$

under the assumption of a constant particle stream entering the Heliosphere at R with an energy of E_{HP}[2]. The average energy $\langle E_0 \rangle$ then can be derived as the expectation value at $r_0 = 0$ AU as

$$\langle E_0 \rangle = \frac{\int_0^{E_{HP}} E j(0,E,t)dE}{\int_0^{E_{HP}} j(0,E,t)dE} \tag{7.28}$$

Parker (1966) solved Eq. (7.28) in case of $u_{SW}R_{HP}/\kappa \ll 1$ as

$$\langle E_0 \rangle - E_{HP} = -\frac{\Gamma}{3} E_{HP} \frac{u_{SW}R}{\kappa} \quad \text{with} \quad \Gamma = \frac{E_0 + 2E_{rest}}{E_0 + E_{rest}} \tag{7.29}$$

which leads to an expression of the average fractional energy loss as

$$\frac{E_{HP}}{\langle E_0 \rangle} = \left\langle \frac{E_{HP}}{E_0} \right\rangle = \left(1 - \frac{\Gamma}{3}\frac{u_{SW}R}{\kappa}\right)^{-1}. \tag{7.30}$$

In order to apply these estimation, however, it has to be discussed whether all applied transport parameters are in the range of definition. As shown in Fig. 7.1 in Section 7.1.1 the analytical estimation $\langle \tau_{CD} \rangle$ derived by Strauss et al. (2011b) which considers both convection and diffusion is not reasonable defined for $\lambda \leq 0.175$ AU. Therefore only the

[2]This would be the exit energy E^{exit} in case of the simulation results shown in Fig. 7.7.

diffusion limit given by Eq. (7.3) as derived by Parker (1965) can be applied in this case, which suggest slightly smaller values for the residence times. Furthermore, as noted by Vogt et al. (under rev.), Eq. (7.30) was derived by Parker (1966) under the assumption that $R/\kappa \ll 1$. Due to the rather small value of the mean free path, however this does not hold true in case of GCR electrons as shown in Fig. 7.8 as indicated by the behaviour of the dotted line.

As discussed by Vogt et al. (under rev.), Fig. 7.8 shows the analytical estimate of the diffusion limit τ alongside its corrected value according to both estimates for the adiabatic energy changes Eqs. (7.26) and (7.30). Therefore we estimated the effect of the boundary conditions as the relation between the source spectrum intensity $j_{LIS}(E)$ of the initial energy E^{init} versus the exit energy E^{exit} to be

$$\langle \tau_D \rangle = \frac{R^2}{6\kappa} \cdot \left\langle \frac{j_{LIS}(E^{exit})}{j_{LIS}(E^{init})} \right\rangle . \tag{7.31}$$

Following the initial discussion, this approach is equivalent to Eq. (7.25) in Section 7.2. However, it does not consider the individual exit times and weights them according to their exit energies but interprets (in agreement with the results shown by Fig. 7.7a) the analytical estimate τ_D as a equivalent to the maximum of the exit times distribution. Consequently this reduces the sum in Eq. (7.25) to only one factor which is multiplied with its corresponding weight according to the expected energy changes. Thereby the numerator $j_{LIS}(E^{exit})$ serves as the boundary weight equivalent to the Jovian source spectrum in Eq. (7.25), whereas the denominator $j_{LIS}(E^{init})$ represents the weight for which τ_D originally has been calculated as the approach by Parker (1965) neglects the adiabatic energy changes. As argued e.g. by Vogt et al. (2020, under rev.) this neglection implicitly assumes an energy independent source spectrum, which appears to be an oversimplification only applicable in cases of small distances and/or focused transport for which only minor adiabatic energy changes are expected.

In order to calculate the exit energy E^{exit} via the time dependent estimation Eq. (7.26), the approach to interpret the original analytical estimate Eq. (7.3) by Parker (1965) as a measure for the maximum of the exit times distribution, suggests to use Eq. (7.3) to calculate the energy changes. Therefore Eq. (7.26) has to be rewritten first in order to resemble the time-backward integration scheme

$$E(t) \approx E^{init} \exp(u_{SW} t/R). \tag{7.32}$$

Subsequently applying the diffusion limit Eq. (7.3) then leads to

$$E^{exit}(\tau_D) \approx E^{init} \exp\left(\frac{R u_{SW}}{6\kappa}\right). \tag{7.33}$$

The corrected analytical estimates shown in Fig. 7.8 are derived via applying Eq. (7.31). As mentioned above it becomes obvious that Eq. (7.30) can not be used in case of MeV-electrons. Indicated by the red vertical line the mean free path and diffusion coefficient, respectively, are too small to comply with the condition that $u_{SW} R_{HP}/\kappa \ll 1$. Although also the corrected residence times in case of applying Eq. (7.26) (or its explicit derivation Eq. (7.33)) is arguably at the lower edge of its definition range, Fig. 7.8 offers the possibility to estimate the effect of applying Eq. (7.31) within a reasonable range of error. Thereby the corrected values of $\langle \tau_D \rangle$ in black are representing an initial energy of $E^{init} = 6$ MeV whereas the colour coded lines show the different results for 30 initial energies ranging logarithmically spaced over the whole energy range of interest.

This new and improved analytical estimation as shown in Fig. 7.7b by the two dashed black and white lines is in agreement with the new numerical approach to the residence

time in red. In order to cover the uncertainties of estimating κ globally throughout the Heliosphere, however, as well as the uncertainties due the estimation of the energy changes, the result for the average fractional energy loss according to Eq. (7.33) is rounded up and down to $3 \leq \langle E^{exit}/E^{init} \rangle \leq 4$ for global isotropic values of the mean free path in the range considered here for low-MeV electrons. These two solutions for the upper and lower limit of the energy changes (which can also be estimated by a graphic analysis of Fig. 7.8) are indicated by the dashed and dotted white and black lines in Fig. 7.7b and envelope the new numerical estimation according to Eq. (7.25) over almost the entire energy range of interest with the exception of the lower edge. Furthermore Fig. 7.7b indicates that the analytical estimate of the average fractional energy changes are in agreement with the distributions of the fractional contribution of the phase-space trajectories to the resulting differential intensities. The poor statistic, however, is caused by the limited resources of the simulation approach. As discussed above in Section 7.2.2 and 7.3.1, small exit times and small adiabatic energy changes are interlinked as shown by Fig. 7.6. Whereas in case of Jovian electrons during times of good magnetic connection but also else-wise the radial distance is small enough to provide a reasonable statistic also for very short exit times and small energy changes, the amount of random walk steps needed in order to cover the distances between the observational points at Earth orbit and the outer boundary at $R = 120\ AU$ makes this kind of trajectories much less likely. Therefore in order to provide an equivalent statistic as e.g. s given by Fig. 7.3 the amount of simulated trajectories would had to be increased in a way that demanded computational resources beyond the scope of this work. Nevertheless as a prove of concept Fig. 7.7 confirms the interpretation laid out above, that the previous analytical estimates describe the propagation of the probability density function and not the corresponding differential intensities of (physical) particles. Furthermore the comparison of the new numerical and the analytical estimations prove that the adiabatic energy changes have to be considered in order to analytically estimate residence times in order to obtain a physically reasonable result.

7.3.4 Consequences for the Interpretation of Diffusion

The results presented in this Section demand a discussion about the mathematical and physical treatment of diffusion. As shown already for the differential intensities and via the derivation of the new numerical estimation of residence times, it is the influence of the adiabatic energy changes that allow to differentiate the pseudo-particles phase-space trajectories according to their physical significance. Whereas this notion was discussed entirely with respect to the nature of the solution of the SDE modelling approach in Secs. 6.3 and 7.2, it has been shown in this Section that this interpretation is not correct.

In order to understand this, it is important to remember what diffusion is mathematically and what physical processes are described with it. As discussed in Secs. 4.1 and 4.2 the model case for diffusion is Brownian motion. Although first mathematically described by physicists, Brownian motion is a rather untypical physical phenomenon even in statistical physics as it appears to be rather chaotic than stochastic.[3] This is in contrast to the physics that appear to govern the "diffusion" of charged particles through the Heliosphere. As discussed in Section 5.1 charged particles are assumed to gyrate along magnetic field

[3]For an overview from the mathematical perspective see e.g. Dürr and Spohn (1998). The chaotic nature of Brownian motion is also highlighted by the mean square displacement (MSD) $\alpha = 1$ indicating that it can be described as a "memoryless" random walk. See Section 4.1 and Metzler and Klafter (2000) for further details.

lines according to the Lorentz force. What is described as "diffusion" by the TPE is the effect of irregularities of the magnetic field, mostly turbulences. These are assumed to cause short-lived kind of magnetic bottle effects resulting in changes of the particles pitch angles, the so-called pitch-angle diffusion. This effect, explicitly considered in focused transport equations such like the one by Roelof (1969) as mentioned in Section 5.5, is assumed to by isotropic by Parker (1965) and therefore modelled by the concept of spatial diffusion parallel and perpendicular to the nominal HMF.

As discussed in Section 5.3 the derivation of mean free paths to estimate the effectiveness of parallel and perpendicular diffusion quantitatively is an ongoing topic of research. It includes scatter theory (see Section 5.3.1) and turbulence theory as sketched in Section 5.3.2. Although an in-depth discussion on how derive theoretical estimations such as those given by Eqs. 5.35 and 5.36 would be beyond the scope of this work, the examples given and outlined in Section 5.3.3 illustrate, that these are derived and entirely theoretical physical quantities, which offer a mathematical representation of a stochastic process. In other words: describing charged particle transport by means of diffusion bears the same dilemma as the wave-particle duality in quantum mechanics or even more explicit the Schrödinger Equations which describes the probability density by means of a wave equation. Comparable to poetry also the mathematical language we use to describe physics by therefore does not describe the actual behaviour of light or subatomic particles but uses more accessible mathematical concepts in the way common language uses metaphors.

This can be interpreted as the reason, why it is necessary to transform the results of diffusion based simulations to physical meaningful quantities by applying sufficient boundary conditions as discussed in Section 6.2 and derived in Section 6.3.1 for differential intensities and in Section 7.2.1 for residence times. The derivation of an new analytical estimate for the residence times in Section 7.3.3 and the fact that this new analytical estimation seems to agree with the new numerical one as well as it is self consistent with the calculation of differential intensities, further supports these considerations. Therefore the inclusion of adiabatic energy changes gets the significance of being the means of transforming mathematical results into physical quantities. At least in case of charged particle propagation modelling they serve as the physical process which links the description of stochastic particle motion in space by the means of diffusion and the corresponding framework to the physics estimated by this mathematical model.

7.4 Jovian Corotation as a Possible Validation

The effect of the corotation of the HMF as discussed in Section 6.4.6 and demonstrated by Fig. 6.15 offers the possibility to examine these considerations by comparison with spacecraft data. Therefore first it will be re-examined how the corotation of the HMF influences the longitudinal position of both the maximum and the minimum of the 13 month periodic variation of the Jovian electron counting rate. Subsequently the possibility is discussed to compare these theoretical considerations with simulation results and spacecraft data, thereby utilizing two electron channels of the EPHIN instrument onboard *SOHO* as discussed in Section 3.3.4. Finally it will be shown that the electron count rates obtained by *SOHO* between 2006 and 2011 support the results of this thesis and that the simulation setup utilised realistic transport parameters as established in Section 6.4 and allows to calculate residence times whose effects are in agreement with *in situ* observations.

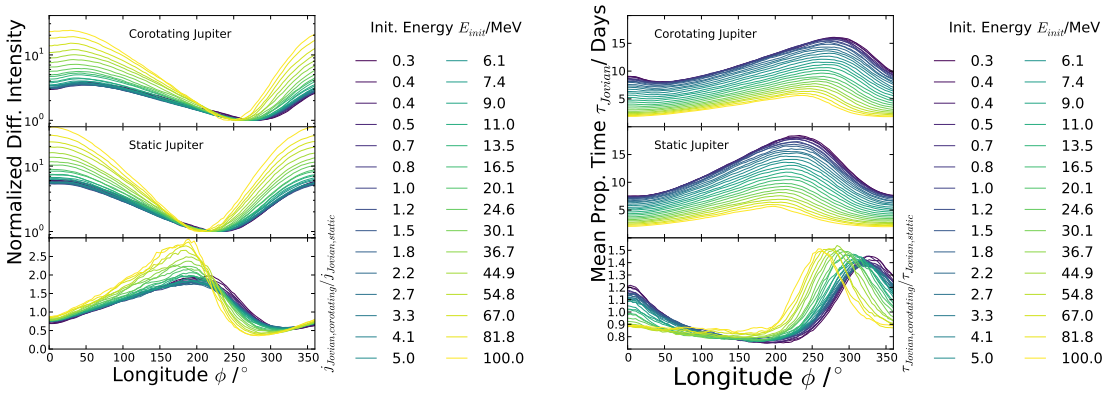

(a) **(b)**

Figure 7.9: *The effect of considering the corotation of the HMF on the Jovian differential intensities (left panel) and the corresponding residence times (right panel). Taken from Vogt et al. (under rev.) the colour coding refers to the same logarithmicaly spaced energies as utilised to show the energy dependence in Figs. 6.7 and 7.3, amongst others.*

7.4.1 The Effect of Corotation on Residence Times

As discussed by Vogt et al. (under rev.), comparing simulations over the whole longitudinal range with both a static Jovian source and a corotating one reveals a significant deviation of about 50° from the nominally best-connected longitude. This effect as shown by Fig. 6.15 in Section 6.4.6 is large enough to also be seen in spacecraft data, as it ranges around 50° even for cases of good connection. A version of Fig. 6.15 which includes the whole range of energies for which the Jovian source spectrum is defined is given by Fig. 7.9a. The left panel highlights further the energy dependence of the corotation effect which is cause by the energy-dependence of the Jovian residence times as discussed in Section 7.2.2 and illustrated by e. g. Figs. 7.2 and 7.3. As argued by Vogt et al. (under rev.) and mentioned above in Section 6.4.6 two different effects influence the magnetic connection between Jupiter and a possible observer:

1. The synodic period, in case of Earth the characteristic ≈ 13 months first discussed by McDonald et al. (1972) and given by Eq. (3.1) in Section 3.1.

2. The corotation of the HMF due to the Sun's rotational period of ≈ 27 days

Of these two corotations relative to the position of an observer at Earth orbit the synodic corotation does not cause an detectable effect. As discussed by Vogt et al. (under rev.) the expected angular shift between Earth and Jupiter in case of good magnetic connectivity is about $\Delta\phi \lessapprox 4°$ and therefore is supposedly within the margin of error. However, the angular speed of the HMF causes a much faster corotation with a periodicity of $\Omega_S \approx$ 27 days. This leads to an expected angular deviation of $\Delta\phi \gtrapprox 50°$ as it was found via simulation too by Vogt et al. (2020, under rev.) and shown within this work by Fig. 6.15 and 7.9. As shown by Vogt et al. (under rev.), this effect is large enough to be possibly resolved by spacecraft data and therefore could serve as an (indirect) measure for the residence time via

$$\tau_\phi = \frac{\Delta\phi}{\Omega_{Sun}}. \tag{7.34}$$

Thereby $\Delta\phi$ is the longitudinal shift between the detected maximum of the 13 month periodicity and the longitudinal position expected from the calculation of the trajectory point which is best connected to the Jovian source. Eq. (7.34) can be derived from the longitudinal convection speed discussed in Section 6.4.6 given by Eq. (6.28). Conceptually therefore the effect caused by the convection speed should be visible in the $\approx$ 13 month periodicity of the electron counting rates as a longitudinal shift away from the nominal position of best magnetic connection. The shift thereby can be explicitly predicted by means of Eq. (7.34) as both the numerical estimation of the residence time via Eq. (7.25) and the new approach to an analytical estimation given by Eq. (7.31) consistently suggest that in case of good connectivity the residence time for Jovian electrons is about $\tau \approx 5-6$ days corresponding to longitudinal shift of about $\approx 70°$. This is an upper theoretical limit as the comparison with the simulation results in Fig. 7.9a shows. Because the relative motion of Jupiter is directed against the rotation of the HMF (Jupiter rotates much slower around the Sun than the Sun around its own axis as mentioned above) the longitudinal shift is shortened by it. As the Jovian synodical period is of about $\Omega^{syn.} \approx 399$ days one would expect that Jupiter's relative motion decreases the angular separation by the equivalent of the residence time of about $6-7$ days, which results in reduction of $\approx 6°$.

7.4.2 Comparison with Spacecraft Data

Although this approach appears to be conceptually simple, the required data analysis bears some difficulties. As already discussed by Vogt et al. (under rev.), electrons are not only generally difficult to detect (for the technical aspects see e. g. Heber et al., 2005, amongst others), electron counting rates are also often highly influenced by SEP events and CIRs. As this thesis aims to compare simulation results for idealised quite time conditions to data, these effects have to be carefully discussed and eliminated as good as possible. Another obstacle is the fact, that the HMF as defined by Parker (1958) and used for the modelling setup within this thesis (see Section 6.1 as well as Dunzlaff et al., 2015; Vogt et al., 2020) demands the assumption of a globally constant Solar wind velocity. Even disregarding SEP events and CIRs, this is a strong simplification even in Solar minima with extremely low Solar activity.

However, it is possible to minimise the effect of these simplification by restricting the selection of data. Therefore EPHIN electron data covering four synodic periods between 2006-2011 were used and analysed with regard to their longitudinal separation from the nominal angle of best connectivity. As discussed by Vogt et al. (under rev.), the HMF for this matter was assumed to be frozen into a Solar wind with a radial speed of $u_{SW} = 400$ km/s and in order to constrain the database to the boundaries given by means of the simulation setup, the daily differential electron intensities were only included if all hourly averages of the Solar speed by SOHO-CELIAS were within the range of $[300, 400]$ km/s.

The lower panel of Fig. 7.10 shows the daily averages of Solar wind speeds and the corresponding electron intensities of the E300 (blue) and E1300 (orange) are shown in the upper panel. These data still show a large range of variation but, as argued by Vogt et al. (under rev.), the envelope appears to be in agreement with the simulation results. The reason why this agreement with the envelope is the important feature to validate the theoretical and numerical prediction of the Jovian residence times can be understood by the relationship between Solar wind speed variations and the propagation between the Jovian source and the observer. If only days with Solar wind speeds with hourly averages below $u_{SW} = 400$ km/s are considered, the variations of the Solar wind speed only change

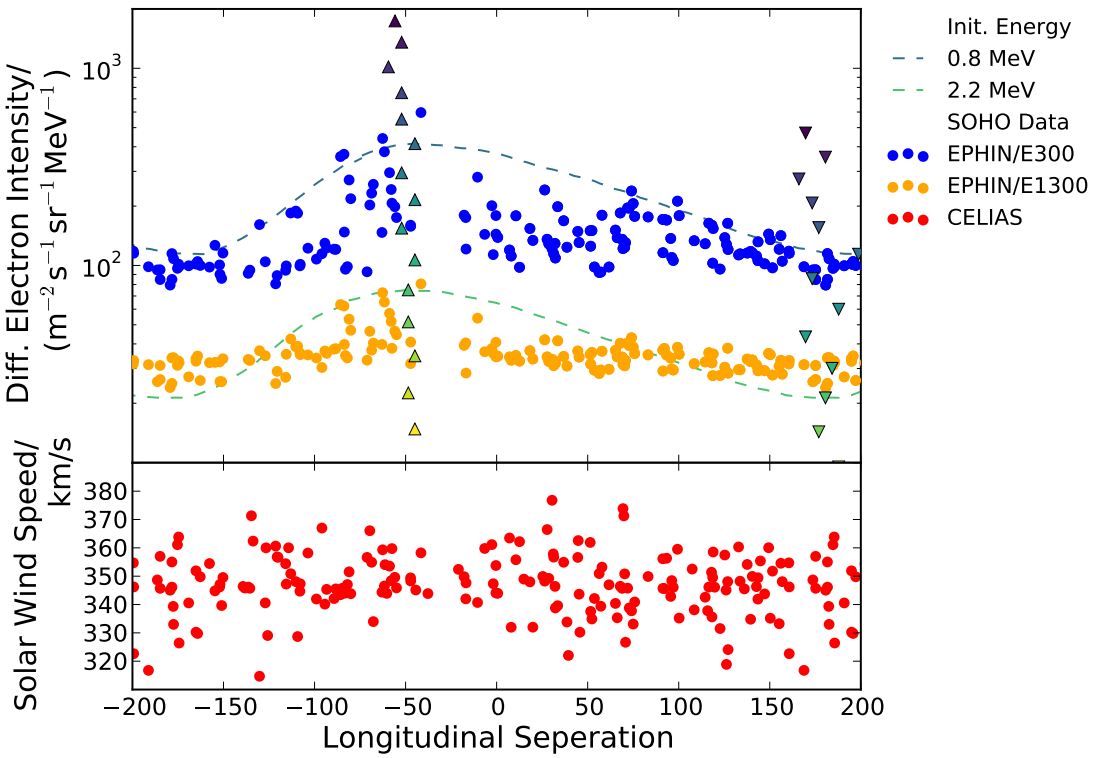

Figure 7.10: *The effect of corotation as detected by SOHO-EPHIN according to Vogt et al. (under rev.). Whereas the upright (▲) and down right triangles (▼) mark the positions of the maxima and minima of the* ~ 13 *month periodicity of the simulated Jovian fluxes for* $E^{init} \in [0.3, 0.37, 0.45, 0.55, 0.70, 0.82, 1.0, 1.22, 1.50, 1.82, 2.22, 2.71, 3.32, 4.06, 5.0]$ *MeV from top to bottom, the two electron channels are shown in blue and orange as daily averages sampled over four synodic periods during the 2006-2011 Solar minimum. The simulation results corresponding for initial energies corresponding to the electron channels are shown to match to the envelope of the data. In the lower panel the corresponding SOHO-CELIAS data points are given for the daily averages of the Solar wind speed. Both panels show their data with respect to the longitudinal separation to the nominal point of best magnetic connection.*

the longitude of best connectivity only due to lower Solar wind speeds. This would result in a shift to the right within the depiction in Fig. 7.10, as discussed by Vogt et al. (under rev.) and causes a change of the corresponding electron intensity. In cases of relatively good connection to the source the measured intensity would be expected to be lower than the simulation results and in case of bad connection, higher, Vogt et al. (under rev.) concludes. For example, if the observer was well connected with the Jovian source by a HMF corresponding to $u_{SW} = 400$ km/s, a decrease of the Solar wind speed would lead to a loss of connectivity and the Jovian electron intensity would decrease likewise. Thus only the upper envelope of the data is comparable to the simulations with an undisturbed HMF.

To validate the agreement between the simulated differential intensities and the spacecraft data, the representative energy for the two energy channels were calculated. Therefor the detector responses (Kühl, private communications) are convoluted with the new Jovian source spectrum. As shown in the lower panel of Fig. 7.11, the initial energy which fitted best with the data, $E^{init} = 0.8$ MeV is in agreement with the maximum of the normalised

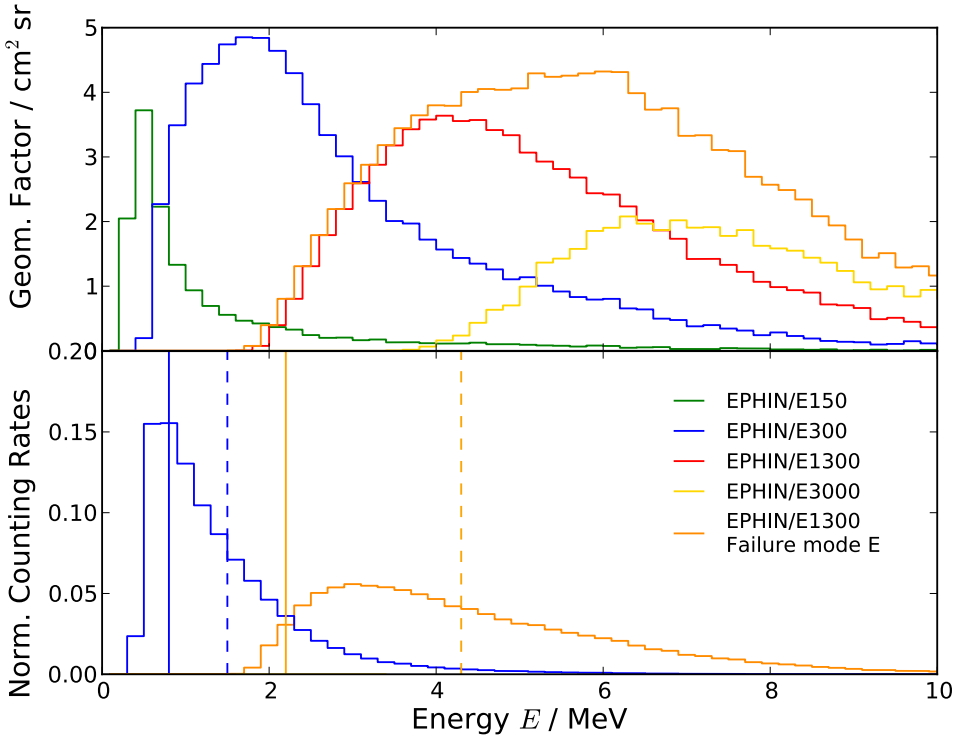

Figure 7.11: *Geometry factors of the SOHO-EPHIN electron channels according to Kühl (private communication) with respect to the corresponding electrons energies. The upper panels shows the geometry factors of the four electron channels as well as the the E1300 channel according to failure mode E (orange) being the combination of the original E1300 and E3000. The lower panel shows the E300 and E1300 convoluted with the source spectrum in order to obtain the normalised counting rates corresponding to the channels and determine the most likely observed energies. The simulated initial energies compared to the two electron channels in Fig. 7.10 are indicated by vertical lines whereas the dashed lines show the nominal median energies.*

counting rates of the E300 electron channel. However, the median energy of the distributions appears to be at $\approx$ 1.5 MeV, an energy which - if used as an initial energy for the simulation - would result in fluxes about a factor of three higher than measured. But although the median is often considered as a reliable and stable representative measure it depends on the assumption that statistical uncertainties are symmetrically distributed. In the case of the geometry factors which are convoluted with the Jovian source spectrum i.e. the normalised counting rates expected for the electron channels as shown in the lower panel of Fig. 7.11, however, the significance of the individual entries (and therefor of possible errors due to statistics, electronic noise and thresholds) is exponentially higher for lower energies. Therefore the calculation of the median energy suggests a false impression of reliability as not only the significantly greater influence of possible errors but also the fact that the low energy flank of the geometry factors of the E300 is very steeply increasing, indicates that the uncertainty area for the median energy of the E300 ranges into significantly lower energies. Thus, considering the fact that the energy which is best comparable with the measured intensities is located at the steeply increasing flank of the geometry factors, the deviation from the median energy seems to be in the margin of error unavoidable due to the various uncertainties connected to charged particle transport modelling on the one hand and the statistics of *in situ* measurements of electrons on the other

hand. Especially as the propagation parameters used to obtain the differential intensities shown by the dashed lines in Fig. 7.10 are benchmarked against the spectral measurements of four spacecraft (see Section 6.4.1) which themselves show a comparable deviation from each other.

For the E1300 electron channel according to failure mode E under which EPHIN operates since November 1996[4], however, the deviation between the median energy and the best fitting initial energy is more severe. Assuming that the highest observed differential intensity is best suitable for benchmarking with the simulation results due to the least relative influence of the GCR background, suggest an initial energy for the simulation of $E^{init} \approx 2.2$ MeV which appears much to low in order to be in agreement with a possible median of the E1300. Concluding, whereas the fluxes of the E300 channel are in agreement with the simulation results, the fluxes provided by E1300 are higher than expected from the simulation results. There are two possible reasons for this divergence. Apart from these technical difficulties, also the Galactic component could contribute more significantly at the measured energies than expected despite the results of Nndanganeni and Potgieter (2018) who suggest that there is no significant Galactic electron contribution up to measured energies of ≈ 25 MeV. Additionally, another reason for the deviation could be the fact, that due to smaller Jovian electron fluxes for higher energies the unstable HMF conditions as described above could cause a larger impact on the data resulting in higher electron fluxes than expected. Nevertheless the fact that the envelopes of both electron channels plotted in Fig. 7.10 are in agreement with both the simulation results and the theoretical expectation can be considered as a proof of concept.

In contrast to the uncertainties connected to the qualitative argument that the envelope of the spacecraft data is in agreement with the simulation results, the quantitative argument that the angular separation between the expected and measured maxima of the ~ 13 periodicity is energy independent. As shown by the triangles showing the simulation maxima (▲) and minima (▼) the longitudinal position of the highest and lowest measured intensities by E300 and E1300 are (regardless which possible initial energy of the simulation setup they represent best) in agreement with the predictions of the corotating simulation approach. For example, a deviation of the predicted residence time of 1 day would result in a longitudinal deviation of $\approx 13°$. Therefore a confidence range of ± 1.5 days for the residence times would result a longitudinal range of uncertainty of 40°. Regarding the simulated maxima and minima as well as with the data obtained by *SOHO* in Fig. 7.10 this estimations provides a good impression of the reliability of this data comparison.

Despite the limitation described above is therefore seems reasonable to assume that Fig. 7.10 indicates that under more stable propagation conditions, without the uncertainties tied to the fluctuation in the Solar wind speed and therefore the HMF the observational data would match the predictions of theory even better. Further it is important to note that three different approaches to estimate residence times - numerical, analytical (see Section 7.3.3) and observational - have been shown to agree with each other within a reasonable margin of error. Viewed in this context the results demonstrated by Fig. 7.10 serve as an encouragement to investigate this approach further when future spacecraft missions may provide data of higher statistics.

[4]A documentation on the coincidence conditions for the different electron channels can be found at `http://www.ieap.uni-kiel.de/et/ag-heber/costep/ephin_sensor.php` according to Müller-Mellin et al. (1995), a more detailed description of the detector at `http://ulysses.physik.uni-kiel.de/sun-360/data/L2_spec_ephin.pdf`

Chapter 8

Summary and Outlook

The present study covers different parts of the broad field of charged particle transport physics in the inner Heliosphere. In the following an overview will be given of the accomplishments together with an outlook on how future studies may benefit from the results of this work. Thereby the discussions in the corresponding Chapters and Sections will be references, the papers published as a result of this work are given therein and attached in the appendix.

8.1 Jovian Electrons

The first topic to mention is the re-evaluation of the Jovian electron flux at Earth, most importantly the development of a new approach to estimate the Jovian source spectrum. As discussed in Section 3.4.3 and Vogt et al. (2018), for the first time only flyby spectra were taken into account. Thus it was possible to present a spectrum as given by Eq. (3.10) with no implicit assumption regarding transport conditions as inevitable if Earth orbit data had been taken into account. Furthermore the spectral shape of this new approach meets the expectation from acceleration and transport theory following one single power law with an exponential cutoff.

8.1.1 Summary

In order to develop the new source spectrum, the available spectral data of electrons in the energy range of interest as given by Tab. 3.1 had to be re-evaluated. Two major discoveries have to be pointed out in this regard. First that the final data product published by Moses (1987), who tried to reconstruct the shape at Jupiter based on Earth orbit data obtained by *ISEE* 3, is based on outdated assumptions on the effectiveness of electrons transport and the strength of a possible additional significant Solar source in the low-MeV energy range. Therefore in this work, as well as by Vogt et al. (2018), the uncorrected Earth orbit data by Moses (1987) are used for validation purposes. Second the overestimation of the Jovian source strength by the flyby spectrum based on *Pioneer* 10 data as published by Teegarden et al. (1974). On the day on which the data was obtained a strong Jovian jet crossed the trajectory of *Pioneer* 10 as identified by Dunzlaff et al. (2009). Utilizing this information it could be shown by means of Fig. 3.14 that the source strength according to the *Pioneer* 10 data had to be corrected by a factor of 1/20 in order to match the supposed quiet-time intensity of Jovian electrons.

8.1.2 Outlook

Because these two spectra in particular were the basis of many past approaches to estimate the Jovian source (see Section 3.4.1 and reference therein) this re-evaluation of the *Pioneer* 10 and *ISEE* 3 data puts parts of the past research based on Jovian electrons into question. Therefore the new approach for the source spectrum promises new insights in various scientific topics associated with Jovian electron transport modelling. Apart from revisiting the transport parameters as included in the TPE by Parker (1965) (see Section 5.5 for details) as discussed in the following Section 8.2, the importance for GCR modelling has to be mentioned. As discussed by Nndanganeni and Potgieter (2018) utilizing a slightly different source spectrum (developed according to private communication with the author of this thesis), it becomes possible to estimate the ratio between Jovian and GCR electrons more precisely with the corresponding effect of allowing also more reliable simulations of GCR electrons transport and modulation.

8.2 Transport Modelling

Although limited, a demonstration of how and why Jovian electrons and especially the knowledge of their spectral shape and strength are important for charged particle transport research is given in Section 6.4. Due to its decentral position the Jovian source changes its magnetic connection to any observer a Earth orbit within a ~ 13 month period. Therefore as argued e.g. by Vogt et al. (2020) the dominant process of particle transport between the Jovian source and the observer changes too, in case of good magnetic connection it

can be assumed that parallel and in case of bad magnetic connection that perpendicular diffusion dominates. This unique possibility of a long-term stable and continuous source allows to almost separately investigate parallel and perpendicular diffusion and to compare its effectiveness.

8.2.1 Summary

Expanding the results by by Vogt et al. (2020), in Section 6.4.1 and 6.4.2 the corresponding magnetic connections as well as Earth orbit data obtained through times of good and bad magnetic connection, respectively, were utilised in order to perform a parameter study on the parallel and perpendicular mean free paths. This is possible due to the discovery as shown in Section 6.3 by e.g. Fig. 6.6, that the simulated differential intensities mostly rely on a phase-space trajectories corresponding to pseudo-particles with source (or exit) energies close to the observed (or initial) ones. Therefore it could be shown by this thesis that a possible energy dependence of the parallel and perpendicular mean free paths (in contrast to the numerical estimation included in the modelling setup) would not significantly effect the results due to the narrow energy range (less than two times the observed or initial energy) they depend on. Furthermore as discussed in Section 6.3.2 according to Fig. 6.7, a detailed investigation of how the phase-space trajectories are transformed by the boundary conditions into a measure of the Jovian differential intensity revealed that in fact the population of phase-space trajectories dominating in case of good magnetic connections are not present in case of a bad magnetic connection between the observer and the source. Based on these findings, Fig. 6.9 compares the results of simulation Jovian electron differential intensities at Earth orbit in case of good connection to the source for a vast range of possible values for the parallel mean free path with the Earth orbit electron spectra obtained by several spacecraft over the last decades. Equivalently Fig. 6.11 compared for two realistic choices of the parallel mean free path the different possibilities to assume the corresponding perpendicular mean free paths.

As discussed in Section 6.4.1 thereby it is possible to investigate parallel and perpendicular mean free path almost independently from each other. The suggestion for both the parallel and perpendicular mean free path are slightly lower than in previous studies, also in comparison with theoretical suggestions. Regarding the difference in shape in strength of the new Jovian source spectrum as shown e.g. by Fig. 3.13 this becomes understandable as a consequence of a larger than previously expected difference between the source strength and the intensities at Earth. Together with these more reliable estimations of the diffusion parameters, the advantage of a fast code written in CUDA (Dunzlaff et al., 2015) also made it possible to investigate more technical parameters such as the extent of the model Heliosphere (see Section 6.4.4), the size of the time increment as well as the maximal duration set for the simulation (see Section 6.4.5) and the influence of including the corotation of the HMF during the propagation of the pseudo-particles. As shown in the corresponding Section as well as discussed in Vogt et al. (2020) and Vogt et al. (under rev.) it could be shown that the corotation of the HMF has a significant effect on the periodicity of the Jovian electron intensities at Earth and could be even be detected in spacecraft data as proven by Fig. 7.10 in Section 7.4. Likewise the parameter studies investigating the radial extent and the time increment showed that only above certain values as discussed in Section 6.4.4 and 6.4.5 the modelling results convert against an asymptotic solution. In case of the radial extent these results for presented by Vogt et al. (2015) question previous

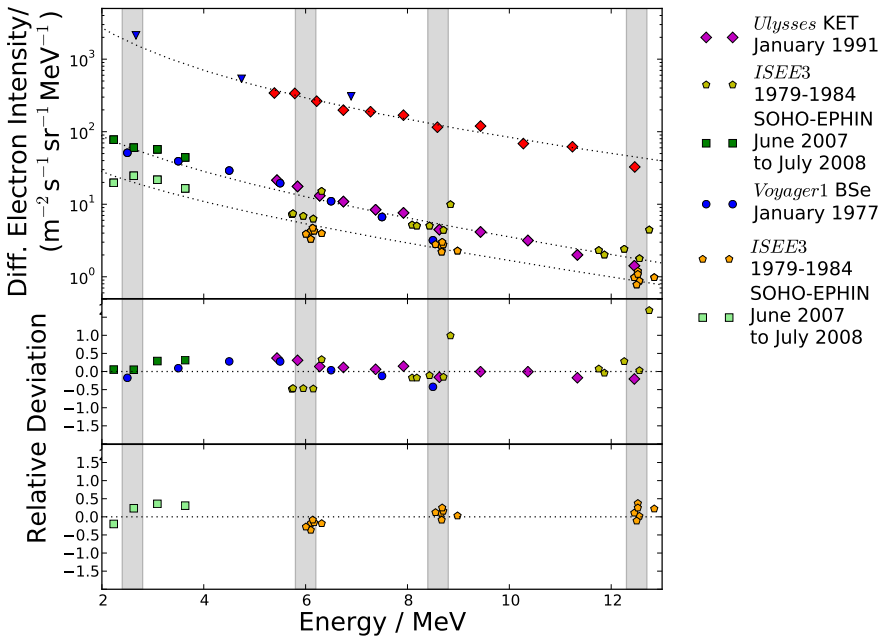

Figure 8.1: *The spectral data of Jovian electrons within the low-MeV range as listed in Tab. 3.1. The top panel shows the flyby data together with the data at Earth orbit obtained during times of good and bad magnetic connection to the Jovian source, respectively. The dashed lines show the source spectrum according to Eq. (3.10) and fits to the Earth orbit spectra in order to derive the relative deviations as shown in the second panel (good connections) and third panel (bad connection). The four grey shaded areas show four energy ranges in which the spectral data coverage is exceptionally good and which are therefor used for the parameter study investigating the approach presented by Eq. (8.1) by Engelbrecht et al. (in prep.).*

approaches which restricted the simulation setup to the most inner Heliosphere to increase the efficiency.

8.2.2 Outlook

Based on the considerations and results for the parallel and perpendicular mean free path as presented by this thesis, Engelbrecht et al. (in prep.) performed a more advanced parameter study utilising four energies for which the Jovian electron source strengths as well as the intensities at Earth during times of good and bad magnetic connection are well restricted by spacecraft data. This approach to restrict the data as shown by Fig. 8.1 is met by an approach to estimate the dependences of the mean free paths on the rigidity P, the radius r and their corresponding values at 1 AU as

$$\begin{aligned} \lambda_{\parallel} &= \lambda_{0,\parallel} P^{\alpha} r^{\beta} \\ \lambda_{\perp} &= \lambda_{0,\perp} P^{\gamma} r^{\delta} \end{aligned} \tag{8.1}$$

with the parameters ranging as $\lambda_{0,\parallel} \in [0.05, 1.0]$ AU, $\alpha \in [-0.1, 0.67]$, $\beta \in [0.5, 1.5]$, $\lambda_{0,\perp} \in [0.001, 0.5]$ AU, $\gamma \in [-0.1, 0.33]$ and $\delta \in [0.5, 1.5]$. The corresponding parameter

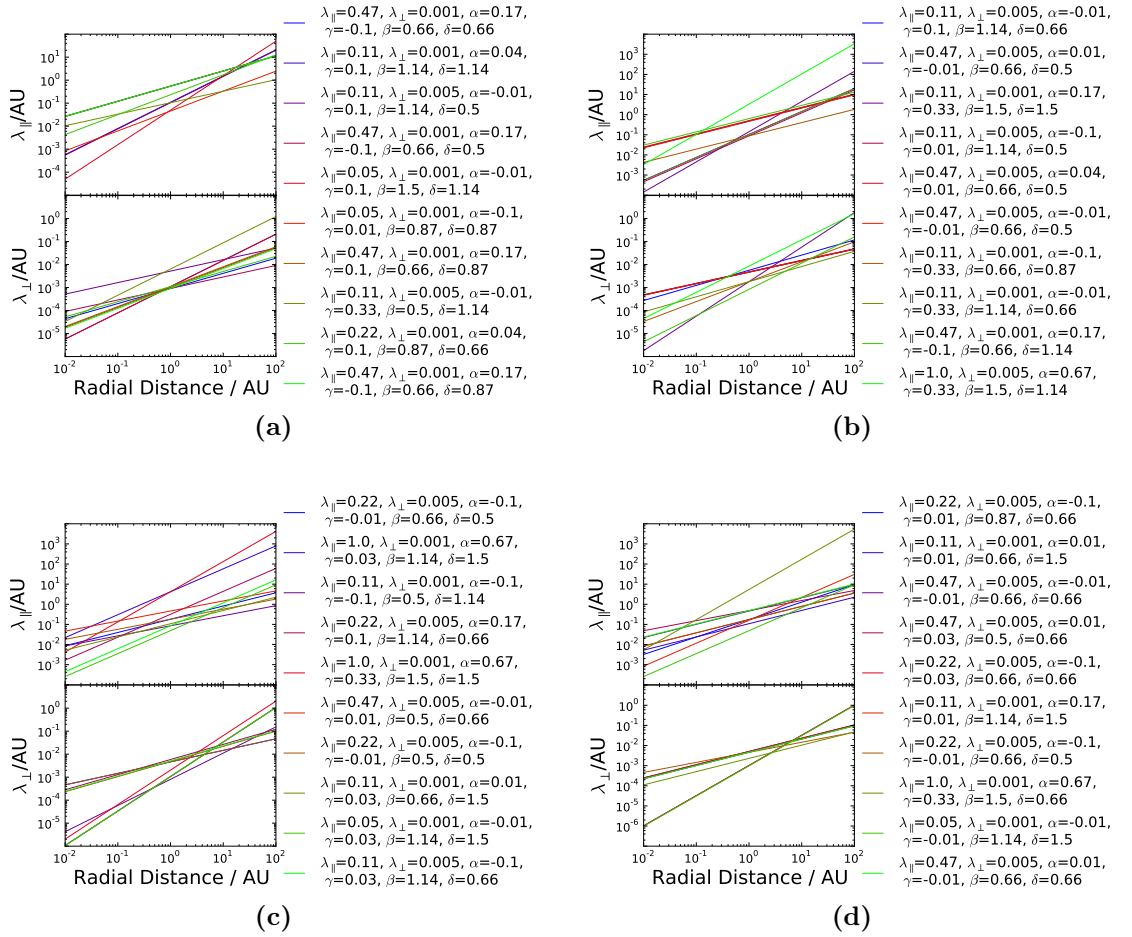

Figure 8.2: *Preliminary results by Engelbrecht et al. (in prep.) showing for the four energies E^{init} = 2.5 MeV (Fig. 8.2a), E^{init} = 6.0 MeV (Fig. 8.2b), E^{init} = 8.5 MeV (Fig. 8.2c) and E^{init} = 12.5 MeV (Fig. 8.2d) the ten best fitting parameter settings each.*

study consisting of over 60 000 individual simulations, offers the possibility to compare the dependences of the most fitting parameter settings with the theoretical estimations of the parallel and perpendicular mean free path as discussed in Section 5.3.3. Preliminary results are shown in Fig. 8.2 for the four different initial energies as illustrated by Fig. 8.1. Due to the dependence on the accuracy of the parallel mean free path (a phenomenon also visible and discussed in Section 6.4.2) the radial dependences of the ten best fits for each energy differ more than the parallel estimations which show a more general trend. Despite these unavoidable uncertainties these results show the possibility to test different parameter setting against *in situ* data which reflect different propagation conditions. Thereby offering the potential to actually distinguish between the different models of turbulence as discussed in Section 5.3.2.

Apart from potentially helping to provide indirect measures to test turbulence theories regarding the HMF, improved parameter setting could contribute to question whether Jovian electrons are detectable at the Mercury orbit as claimed by Eraker and Simpson (1979) based on measurements by *Mariner 10*. This of course would contribute to the ongoing research on the ratio between GCR and Jovian electrons in the inner Heliosphere. A question which (amongst others) also motivated this work as discussed by Vogt et al. (2018) [1]. Distinguishing between these two major electron populations in the low-MeV

[1] For a recent study which partly incorporates the results discussed by this work see Nndanganeni and Potgieter (2018)

range is the precondition to compare simulations of GCR electron modulation to data.

From a much broader scientific perspective the ultra-high vacuum of the interplanetary space provides qualities of the HMF that can not be reproduced under laboratory conditions up to this date. Therefore investigating the qualities of the HMF via transport simulation of Jovian electrons in the way discussed above also offers the possibilities to test theories within plasma physics under extreme conditions beyond the scope of space physics.

8.3 Residence Times

The third scientific topic, this work contributes to, is the question how to estimate the residence times of charged particles in the Heliosphere. Although developed explicitly by utilising Jovian electrons transport via the TPE by Parker (1965) as a test population the estimation demands to be valid for all particle populations and TPEs based on a similar FPE approach such as the TPE by Roelof (1969).

8.3.1 Summary

As shown by comparison with previous analytical and numerical estimations by Parker (1965); O'Gallagher (1975); Florinski and Pogorelov (2009); Strauss et al. (2011b), amongst others, in Section 7.1.4 as listed in Tab. 7.1 this work proves that diffusive transport tends to be way more effective than thought of before, decreasing the estimated residence times by a factor of 2 (GCRs) to almost 100 in case of Jovian electrons. This finding as confirmed by Fig. 7.2 is connected to the investigation of the influence of boundary conditions in Section 6.5 as discussed above. The new approach to estimate residence times as derived in Section 7.2 and published and discussed by Vogt et al. (2020) thereby for the first time considering the simulation times of the individual phase-space trajectories self consistently with the calculation of the differential intensities. Explicitly Eq. (7.25) assigns to each pseudo-trajectory the same significance for the resulting residence times, as it has for the resulting differential intensities according to Eq. (6.27).

Investigating the effect of weighting the individual trajectory durations thereby lead to equivalent results as discussed for the differential intensities. Again, as shown by Fig. 7.3 the distributions of phase-space trajectories over their corresponding length in time have a second minor maximum in case of good magnetic connection to the source. The relation between adiabatic energy gain and duration as hinted by this finding is confirmed by Fig. 7.6 and discussed in Section 7.3.1 as well as by Vogt et al. (under rev.). Re-examining the analytical approaches in that regard it could be shown that they agree with the maximum of the phase-space trajectories duration distribution as illustrated by Fig. 7.7a. This however raises the question whether the analytical estimates which also predict rather high residence times (see Section 7.1.1) need to re-evaluated in an equivalent manner. The discussion of the theoretical approaches used by Parker (1965) and all subsequent studies on analytical estimation of residence times showed that these analytical estimations are more precisely the expectation value for the propagation of the phase-space density itself rather than a measure corresponding to the derived (physical) quantity of the differential

intensity of GCRs. In Section 7.3.3 as well as by Vogt et al. (under rev.) it could be shown that rather simply approach to analytically estimate the effect of convoluting the durations of the phase-space trajectories with the boundary conditions (see Eq. (7.25) as well as its derivation) by convoluting the expectation values instead, is able to produce realistic values which agree with the numerical estimation as shown by Fig. 7.7b.

Although the new numerical and analytical estimations for the residence time are both (for the first time) self consistent with the approach to calculate the propagation of GCRs via phase-space densities in FPE approaches, they need to be experimentally examined in order to test their validity. In contrast to Strauss et al. (2013) who suggested a rather complicated method to measure Jovian electron residence times via the effect of QTIs, this thesis suggest to use the effect of the corotating HMF as described in Section 6.4.6. This method which is made possible by the discovery of how much the corotation of the HMF effects the longitudinal position of the maximum of the ~ 13 month Jovian electron intensity periodicity exploit the fact that this shift in longitude is only depending on two parameters: the residence time itself and the Solar wind speed which determines via the bending of the Parker spiral the expected longitude of the best connections. As discussed in Section 7.4.2 in detail the possible uncertainties caused by the variation of the Solar wind speed are covered by sampling over four ~ 13 periods of daily electron counting rates by *SOHO*/EPHIN and only considering data of days on which the hourly averages of the Solar wind speed did not exceed 400 km/s. Thereby comparing the envelope of the data with the simulations results for corresponding initial energies as well as with the expected longitudinal shifts as shown by Fig. 7.10 indicates an agreement between the data and the theoretical expectations. Thus, considering the large deviations of the previous attempts to estimate the residence times numerically and analytically, confirming the general accuracy of the approach presented by this thesis.

8.3.2 Outlook

Comparable to the results concerning transport modelling the new approaches to estimate the residence times of Jovian electrons become significant by applying the underlying physical discoveries to other topic of space physics. Since the results of this studies are not based on particular qualities of TPE by Parker (1965) but on the mathematics of the more general FPEs, it is possible to apply the considerations made by this thesis to other FPE type TPEs. Alhough beyond the scope of this work, the possibility to apply these results to TPEs such as the one by Roelof (1969) which considers pitch-angle diffusion rather than spatial diffusion could contribute to the attempts to model and predict the effects of SEP events at Earth.

The importance of this aspect is emphasised by several recent studies on SEP events, their modelling and space weather forecast such as Dumbović et al. (2020); Posner and Strauss (2020); Steyn et al. (2020); Veronig (2020), amongst others, just in the last year. As alredy discussed in the introduction to Chapter 7, this development builds on a long tradition to analyse and mathematically describe SEP events. Notable examples being e.g. Gopalswamy et al. (2001); Vršnak et al. (2013); Möstl et al. (2014) and more recently Möstl et al. (2017); Temmer et al. (2017); Green et al. (2018); Guo et al. (2018) as well as forecasting tools including e.g. REleASE (Posner, 2007), PPS (Kahler et al., 2007), SPARX (Marsh et al., 2015) and HESPERIA (Núñez et al., 2018). Of course, a more advanced understanding of residence times and how to estimate them based on FPE transport models could contribute to make forecast more precisely in time and as a consequence also in space.

That an estimation of residence times can contribute to understand the magnetic qualities of an SEP event was shown in concept by e.g. Dresing et al. (2016). The urgency of SEP event forecast further is shown by the fact that two spacecraft mission have been dedicated to close-up Solar investigation in recent years, NASA's *Parker Solar Probe* (see e.g. Fox et al., 2016) and ESA's *Solar Orbiter* (see e.g. Müller et al., 2013).

A main prospect thereby is the safety of manned spacecraft mission into outer space, emphasised by spacecraft mission such as the *Mars Science Laboratory (MSL)* which includes among others the Radiation Assessment Detector (RAD) (see e.g. Hassler et al., 2012) in order to measure GCR intensities on the Martian surface as well as investigating how the radiation would effect possible future manned missions. Further important aspects of Space Weather research are the influence on communication systems and the electronic infrastructure. Therefore an improved understanding of residence times and the possibility to forecast the timely evolution of events more precisely could benefit short term alarm systems as the ones discussed above.

Again, apart from these more straight forward aspects and possibilities to apply the results of this work regarding residence times directly, the consequences for the interpretation of diffusive processes are far wider reaching. As sketched e.g. in Section 7.3 this work's results emphasise the difference between a mathematical model and its physical interpretation and show the possible consequences of oversimplifying mathematical estimations. Therefore the time scales for diffusive processes in the inner Heliosphere could be shown to be much smaller than previous estimations of residence times suggested, bearing possible consequences for the interpretation of the efficiency of diffusive processes within the HMF and the modulation of GCR electrons. Without overstating the significance of the results presented herein, they further prove the usefulness of Jovian electrons as test particles for transport processes and contribute to secure the mathematical and observational foundations of future studies within this broad and still evolving field of space science.

List of Figures

List of Tables

Bibliography

H. Alfvén. Existence of Electromagnetic-Hydrodynamic Waves. *Nature*, 150(3805):405–406, Oct 1942. doi: 10.1038/150405d0.

H. Alfvén. On the theory of comet tails. *Tellus*, 9:92 – 96, 03 1957. doi: 10.1111/j.2153-3490.1957.tb01855.x.

H. Alfvén. Electric currents in cosmic plasma. *Reviews of Geophysics and Space Physics*, 15:271–284, August 1977. doi: 10.1029/RG015i003p00271.

M. J. Aschwanden. *Physics of the Solar Corona. An Introduction.* Springer Verlag, Berlin, Heidelberg, New York, 2004.

H. W. Babcock. The Topology of the Sun's Magnetic Field and the 22-YEAR Cycle. *The Astrophysical Journal*, 133:572, March 1961. doi: 10.1086/147060.

L. Bachelier. Théorie de la spéculation. *Annales scientifiques de l'École Normale Supérieure*, 3e série, 17:21–86, 1900. doi: 10.24033/asens.476.

L. Bachelier, M. Davis, A. Etheridge, and P.A. Samuelson. *Louis Bachelier's Theory of Speculation: The Origins of Modern Finance.* Princeton University Press, 2011. ISBN 9781400829309.

D. N. Baker and J. A. van Allen. Energetic electrons in the Jovian magnetosphere. *Journal of Geophysical Research*, 81:617–632, February 1976. doi: 10.1029/JA081i004p00617.

A. Balogh, E. J. Smith, B. T. Tsurutani, D. J. Southwood, R. J. Forsyth, and T. S. Horbury. The Heliospheric Magnetic Field Over the South Polar Region of the Sun. *Science*, 268(5213):1007–1010, May 1995. doi: 10.1126/science.268.5213.1007.

G. K. Batchelor. *The Theory of Homogeneous Turbulence.* Cambridge University Press, 1982.

H. N. Becker, D. Santos-Costa, J. L. Jørgensen, T. Denver, A. Adriani, A. Mura, J. E. P. Connerney, S. J. Bolton, S. M. Levin, R. M. Thorne, J. W. Alexander, V. Adumitroaie, E. A. Manor-Chapman, I. J. Daubar, C. Lee, M. Benn, J. Sushkova, A. Cicchetti, and R. Noschese. Observations of mev electrons in jupiter's innermost radiation belts and polar regions by the juno radiation monitoring investigation: Perijoves 1 and 3. *Geophysical Research Letters*, 44(10):4481–4488, 2017. ISSN 1944-8007. doi: 10.1002/2017GL073091. 2017GL073091.

H. Bethe. Zur Theorie des Durchgangs schneller Korpuskularstrahlen durch Materie. *Annalen der Physik*, 397(3):325–400, January 1930. doi: 10.1002/andp.19303970303.

J. W. Bieber and W. H. Matthaeus. Cosmic Ray Pitch Angle Scattering in Dynamical Magnetic Turbulence. In *International Cosmic Ray Conference*, volume 3 of *International Cosmic Ray Conference*, page 248, August 1991.

J. W. Bieber, W. H. Matthaeus, C. W. Smith, W. Wanner, M.-B. Kallenrode, and G. Wibberenz. Proton and electron mean free paths: The Palmer consensus revisited. *The Astrophysical Journal*, 420:294–306, January 1994. doi: 10.1086/173559.

J. W. Bieber, W. H. Matthaeus, A. Shalchi, and G. Qin. Nonlinear guiding center theory of perpendicular diffusion: General properties and comparison with observation. *Geophysical Research Letters*, 31(10):L10805, May 2004. doi: 10.1029/2004GL020007.

L. Biermann. Kometenschweife und solare Korpuskularstrahlung. *Zeitschrift für Astrophysik*, 29:274, Jan 1951.

K. Birkeland. *The Norwegian Aurora Polaris Expedition, 1902-1903: Volume I. On the Cause of Magnetic Storms and the Origin of Terrestrial Magnetism.* Number Bd. 1, in The Norwegian Aurora Polaris Expedition, 1902-1903: Volume I. On the Cause of Magnetic Storms and the Origin of Terrestrial Magnetism. H. Aschehoug & Company, 1908.

D. Bisschoff and M. S. Potgieter. Implications of Voyager 1 Observations beyond the Heliopause for the Local Interstellar Electron Spectrum. *The Astrophysical Journal*, 794:166, October 2014. doi: 10.1088/0004-637X/794/2/166.

F. Bloch. Zur Bremsung rasch bewegter Teilchen beim Durchgang durch Materie. *Annalen der Physik*, 408(3):285–320, January 1933. doi: 10.1002/andp.19334080303.

J. G. Blom and J. G. Verwer. VLUGR3: A Vectorizable Adaptive Grid Solver for PDEs in 3D. I. Algorithmic Aspects and Applications. *Appl. Numer. Math.*, 16:129–156, 1994.

J. G. Blom and J. G. Verwer. VLUGR3: A Vectorizable Adaptive Grid Solver for PDEs in 3D. II. Code Description. *ACM Trans. Math. Softw.*, 22:329–347, 1996.

P. Bobik, M. J. Boschini, S. Della Torre, M. Gervasi, D. Grandi, G. La Vacca, S. Pensotti, M. Putis, P. G. Rancoita, D. Rozza, M. Tacconi, and M. Zannoni. On the forward-backward-in-time approach for Monte Carlo solution of Parker's transport equation: One-dimensional case. *Journal of Geophysical Research (Space Physics)*, 121(5):3920–3930, May 2016. doi: 10.1002/2015JA022237.

S. J. Bolton, S. Gulkis, M. J. Klein, I. de Pater, and T. J. Thompson. Correlation studies between solar wind parameters and the decimetric radio emission from Jupiter. *Journal of Geophysical Research*, 94:121–128, January 1989. doi: 10.1029/JA094iA01p00121.

S. J. Bolton, M. Janssen, R. Thorne, S. Levin, M. Klein, S. Gulkis, T. Bastian, R. Sault, C. Elachi, M. Hofstadter, A. Bunker, G. Dulk, E. Gudim, G. Hamilton, W. T. K. Johnson, Y. Leblanc, O. Liepack, R. McLeod, J. Roller, L. Roth, and R. West. Ultra-relativistic electrons in Jupiter's radiation belts. , 415:987–991, February 2002. doi: 10.1038/415987a.

M. Born. Quantenmechanik der Stoßvorgänge. *Zeitschrift fur Physik*, 38(11-12):803–827, Nov 1926. doi: 10.1007/BF01397184.

A. L. Broadfoot, B. R. Sandel, D. E. Shemansky, J. C. McConnell, G. R. Smith, J. B. Holberg, S. K. Atreya, T. M. Donahue, D. F. Strobel, and J. L. Bertaux. Overview of the Voyager ultraviolet spectrometry results through Jupiter encounter. *Journal of Geophysical Research*, 86(A10):8259–8284, September 1981. doi: 10.1029/JA086iA10p08259.

B. Bru and M. Yor. ´Comments on the life and mathematical legacy of Wolfgang Doeblin. *Finance and Stochastics*, 6(1):3–47, Jan 2002. ISSN 0949-2984. doi: 10.1007/s780-002-8399-0.

R Brun, F Bruyant, M Maire, A C McPherson, and P Zanarini. *GEANT 3: user's guide Geant 3.10, Geant 3.11; rev. version*. CERN, Geneva, 1987.

R. A. Burger, M. S. Potgieter, and B. Heber. Rigidity dependence of cosmic ray proton latitudinal gradients measured by the Ulysses spacecraft: Implications for the diffusion tensor. *Journal of Geophysical Research*, 105:27447–27456, December 2000. doi: 10.1029/2000JA000153.

R. A. Burger, T. P. J. Krüger, M. Hitge, and N. E. Engelbrecht. A Fisk-Parker Hybrid Heliospheric Magnetic Field with a Solar-Cycle Dependence. *The Astrophysical Journal*, 674(1):511–519, February 2008. doi: 10.1086/525039.

L. F. Burlaga. Interplanetary stream interfaces. *Journal of Geophysical Research*, 79(25):3717, January 1974. doi: 10.1029/JA079i025p03717.

R. A. Caballero-Lopez, H. Moraal, K. G. McCracken, and F. B. McDonald. The heliospheric magnetic field from 850 to 2000 AD inferred from ^{10}Be records. *Journal of Geophysical Research (Space Physics)*, 109(A12):A12102, December 2004a. doi: 10.1029/2004JA010633.

R. A. Caballero-Lopez, H. Moraal, and F. B. McDonald. Galactic cosmic ray modulation: Effects of the solar wind termination shock and the heliosheath. *Journal of Geophysical Research (Space Physics)*, 109(A5):A05105, May 2004b. doi: 10.1029/2003JA010358.

S. Chandrasekhar. Stochastic Problems in Physics and Astronomy. *Reviews of Modern Physics*, 15:1–89, January 1943. doi: 10.1103/RevModPhys.15.1.

D. L. Chenette. The propagation of Jovian electrons to earth. *Journal of Geophysical Research*, 85(A5):2243–2256, May 1980. doi: 10.1029/JA085iA05p02243.

D. L. Chenette, T. F. Conlon, and J. A. Simpson. Bursts of relativistic electrons from Jupiter observed in interplanetary space with the time variation of the planetary rotation period. *Journal of Geophysical Research*, 79(25):3551, January 1974. doi: 10.1029/JA079i025p03551.

G. Clark, B. H. Mauk, C. Paranicas, D. Haggerty, P. Kollmann, A. Rymer, L. Brown, S. Jaskulek, C. Schlemm, C. Kim, J. Peachey, D. LaVallee, F. Allegrini, F. Bagenal, S. Bolton, J. Connerney, R. W. Ebert, G. Hospodarsky, S. Levin, W. S. Kurth, D. J. McComas, D. G. Mitchell, D. Ranquist, and P. Valek. Observation and interpretation of energetic ion conics in jupiter's polar magnetosphere. *Geophysical Research Letters*, 44(10):4419–4425, 2017. ISSN 1944-8007. doi: 10.1002/2016GL072325. 2016GL072325.

T. F. Conlon. The interplanetary modulation and transport of Jovian electrons. *Journal of Geophysical Research*, 83:541–552, February 1978. doi: 10.1029/JA083iA02p00541.

E. I. Daibog, K. Kecskemety, and Yu. I. Logachev. Jovian electrons and the solar wind during the minimum of the 23rd–24th solar activity cycle. *Bulletin of the Russian Academy of Sciences: Physics*, 77(5):551–553, May 2013. ISSN 1934-9432. doi: 10.3103/S1062873813050158.

S. Dalla, A. Balogh, S. Krucker, A. Posner, R. Müller-Mellin, J. D. Anglin, M. Y. Hofer, R. G. Marsden, T. R. Sanderson, C. Tranquille, B. Heber, M. Zhang, and R. B. McKibben. Properties of high heliolatitude solar energetic particle events and constraints

on models of acceleration and propagation. *Geophysical Research Letters*, 30(19):8035, October 2003. doi: 10.1029/2003GL017139.

S. Dasso, L. J. Milano, W. H. Matthaeus, and C. W. Smith. Anisotropy in Fast and Slow Solar Wind Fluctuations. *The Astrophysical Journall*, 635(2):L181–L184, December 2005. doi: 10.1086/499559.

I. de Pater and C. K. Goertz. Radial diffusion models of energetic electrons and Jupiter's synchrotron radiation. I - Steady state solution. *Journal of Geophysical Research*, 95: 39–50, January 1990. doi: 10.1029/JA095iA01p00039.

A. J. Dessler and J. A. Fejer. Interpretation of K_p index and M-region geomagnetic storms. *Planetary and Space Science*, 11(5):505–511, May 1963. doi: 10.1016/0032-0633(63)90074-6.

W. Doeblin. Sur l'équation de Kolmogoroff. *Pli cacheté déposé le 26 février 1940, ouvert le 18 mai 2000. Comptes-Rendus à l'Académie des sciences de Paris*, 331:1031–118, 1940.

A. Dosch, A. Shalchi, and B. Weinhorst. Relation between different theories for cosmic ray cross field diffusion. *Advances in Space Research*, 44(11):1326–1336, December 2009. doi: 10.1016/j.asr.2009.07.007.

N. Dresing, R. Gómez-Herrero, B. Heber, M. A. Hidalgo, A. Klassen, M. Temmer, and A. Veronig. Injection of solar energetic particles into both loop legs of a magnetic cloud. *Astronomy and Astrophysics*, 586:A55, February 2016. doi: 10.1051/0004-6361/201527347.

C. Drews, L. Berger, R. F. Wimmer-Schweingruber, P. Bochsler, A. B. Galvin, B. Klecker, and E. Möbius. Inflow direction of interstellar neutrals deduced from pickup ion measurements at 1 au. *Journal of Geophysical Research: Space Physics*, 117(A9), 2012. doi: 10.1029/2012JA017746.

W. Dröge. The Rigidity Dependence of Solar Particle Scattering Mean Free Paths. *Astrophysical Journal*, 537(2):1073–1079, July 2000. doi: 10.1086/309080.

W. Dröge. Solar Particle Transport in a Dynamical Quasi-linear Theory. *Astrophysical Journal*, 589(2):1027–1039, June 2003. doi: 10.1086/374812.

W. Dröge. Probing heliospheric diffusion coefficients with solar energetic particles. *Advances in Space Research*, 35(4):532–542, Jan 2005. doi: 10.1016/j.asr.2004.12.007.

W. Dröge, Y. Y. Kartavykh, B. Klecker, and G. A. Kovaltsov. Anisotropic Three-Dimensional Focused Transport of Solar Energetic Particles in the Inner Heliosphere. *Astrophysical Journal*, 709(2):912–919, February 2010. doi: 10.1088/0004-637X/709/2/912.

W. Dröge, Y. Y. Kartavykh, N. Dresing, and A. Klassen. Multi-spacecraft Observations and Transport Modeling of Energetic Electrons for a Series of Solar Particle Events in August 2010. *The Astrophysical Journal*, 826(2):134, Aug 2016. doi: 10.3847/0004-637X/826/2/134.

M. Dumbović, B. Vršnak, J. Guo, B. Heber, K. Dissauer, F. Carcaboso, M. Temmer, A. Veronig, T. Podladchikova, C. Möstl, T. Amerstorfer, and A. Kirin. Evolution of Coronal Mass Ejections and the Corresponding Forbush Decreases: Modeling vs. Multi-Spacecraft Observations. *Solar Physics*, 295(7):104, July 2020. doi: 10.1007/s11207-020-01671-7.

P. Dunzlaff. *Analysis of Anisotropic Jovian Electron Events*. PhD thesis, Christian-Albrechts-Universität zu Kiel, 2012.

P. Dunzlaff, B. Heber, A. Kopp, O. Rother, R. Müller-Mellin, A. Klassen, R. Gómez-Herrero, and R. Wimmer-Schweingruber. Observations of recurrent cosmic ray decreases during solar cycles 22 and 23. *Annales Geophysicae*, 26(10):3127–3138, October 2008a. doi: 10.5194/angeo-26-3127-2008.

P. Dunzlaff, B. Heber, O. Sternal, R. Müller-Mellin, R. Gomez-Herrero, H. Kunow, O. Rother, R. Wimmer-Schweingruber, and W. Dröge. Recurrent Modulation of Jovian Electron intensities: Ulysses KET measurements. In *International Cosmic Ray Conference*, volume 1 of *International Cosmic Ray Conference*, pages 363–366, January 2008b.

P. Dunzlaff, A. Kopp, B. Heber, and O. Sternal. Comparison of Jovian jets observed by Ulysses and Pioneer 10. *Proceedings oft he 31st International Cosmic Ray Conference (ICRC) 2009*, 2009.

P. Dunzlaff, R. D. Strauss, and M. S. Potgieter. Solving Parker's transport equation with stochastic differential equations on GPUs. *Computer Physics Communications*, 192: 156–165, July 2015. doi: 10.1016/j.cpc.2015.03.008.

D. Dürr and H Spohn. Brownian motion and microscopic chaos. *Nature*, 394:831–833, 1998. doi: https://doi.org/10.1038/29650.

J. A. Earl. The diffusive idealization of charged-particle transport in random magnetic fields. *Astrophysical Journal*, 193:231–242, October 1974. doi: 10.1086/153152.

F. Effenberger, H. Fichtner, K. Scherer, S. Barra, J. Kleimann, and R. D. Strauss. A Generalized Diffusion Tensor for Fully Anisotropic Diffusion of Energetic Particles in the Heliospheric Magnetic Field. *Astrophysical Journal*, 750(2):108, May 2012. doi: 10.1088/0004-637X/750/2/108.

A. Einstein. Über die von der molekularkinetischen Theorie der Wärme geforderte Bewegung von in ruhenden Flüssigkeiten suspendierten Teilchen. *Annalen der Physik*, 322: 549–560, 1905. doi: 10.1002/andp.19053220806.

N. E. Engelbrecht. *On the development and applications of a three–dimensional ab initio cosmic–ray modulation model*. PhD thesis, North-West University, 2012.

N. E. Engelbrecht. On the Effects of Pickup Ion-driven Waves on the Diffusion Tensor of Low-energy Electrons in the Heliosphere. *The Astrophysical Journall*, 849:L15, November 2017. doi: 10.3847/2041-8213/aa9372.

N. E. Engelbrecht and R. A. Burger. Effects of various dissipation range onset models on the 26-day variations of low-energy galactic cosmic-ray electrons. *Advances in Space Research*, 45(8):1015–1025, April 2010. doi: 10.1016/j.asr.2009.12.012.

N. E. Engelbrecht and R. A. Burger. An Ab Initio Model for the Modulation of Galactic Cosmic-ray Electrons. *The Astrophysical Journal*, 779:158, December 2013. doi: 10.1088/0004-637X/779/2/158.

N. E. Engelbrecht and R. A. Burger. Sensitivity of Cosmic-Ray Proton Spectra to the Low-wavenumber Behavior of the 2D Turbulence Power Spectrum. *The Astrophysical Journal*, 814(2):152, Dec 2015. doi: 10.1088/0004-637X/814/2/152.

N. E. Engelbrecht, A. Vogt, K. Herbst, and R. D. Strauss. Revisiting the revisited palmer consensus: New insights from jovian electron transport. in prep.

J. H. Eraker. Origins of the low-energy relativistic interplanetary electrons. *The Astrophysical Journal*, 257:862–880, June 1982. doi: 10.1086/160036.

J. H. Eraker and J. A. Simpson. Jovian electron propagation close to the sun ($\lessapprox$ 0.5 AU). *The Astrophysical Journall*, 232:L131–L134, September 1979. doi: 10.1086/183050.

P. Ferrando, R. Ducros, C. Rastoin, and A. Raviart. Jovian electron jets in interplanetary space. *Planetary and Space Science*, 41:839–849, November 1993. doi: 10.1016/0032-0633(93)90091-F.

P. Ferrando, A. Raviart, L. J. Haasbroek, M. S. Potgieter, W. Droege, B. Heber, H. Kunow, R. Mueller-Mellin, H. Sierks, G. Wibberenz, and C. Paizis. Latitude variations of ~7MeV and >300MeV cosmic ray electron fluxes in the heliosphere: ULYSSES COSPIN/KET results and implications. *Astronomy and Astrophysics*, 316:528–537, December 1996.

S. E. S. Ferreira. The Heliospheric Transport of Galactic Cosmic Rays and Jovian Electrons. *Ph.D. thesis, North-West University , South Africa*, 2002.

S. E. S. Ferreira and M. S. Potgieter. The modulation of 4- to 16-MeV electrons in the outer heliosphere: Implications of different local interstellar spectra. *Journal of Geophysical Research (Space Physics)*, 107:1221, August 2002. doi: 10.1029/2001JA000226.

S. E. S. Ferreira, M. S. Potgieter, R. A. Burger, B. Heber, and H. Fichtner. Modulation of Jovian and galactic electrons in the heliosphere: 1. Latitudinal transport of a few MeV electrons. *Journal of Geophysical Research*, 106:24979–24988, November 2001a. doi: 10.1029/2001JA000082.

S. E. S. Ferreira, M. S. Potgieter, R. A. Burger, B. Heber, H. Fichtner, and C. Lopate. Modulation of Jovian and galactic electrons in the heliosphere: 2. Radial transport of a few MeV electrons. *Journal of Geophysical Research*, 106:29313–29322, December 2001b. doi: 10.1029/2001JA000170.

S. E. S. Ferreira, M. S. Potgieter, D. M. Moeketsi, B. Heber, and H. Fichtner. Solar Wind Effects on the Transport of 3-10 MeV Cosmic-Ray Electrons from Solar Minimum to Solar Maximum. *The Astrophysical Journal*, 594:552–560, September 2003. doi: 10.1086/376869.

H. Fichtner. Anomalous Cosmic Rays: Messengers from the Outer Heliosphere. *Space Sc. Rev.*, 95:639–754, February 2001.

H. Fichtner, M. Potgieter, S. Ferreira, and A. Burger. On the propagation of Jovian electrons in the heliosphere: Transport modelling in 4-D phase space. *Geophysical Research Letters*, 27:1611–1614, June 2000. doi: 10.1029/2000GL003765.

H. M. Fischer, E. Pehlke, G. Wibberenz, L. J. Lanzerotti, and J. D. Mihalov. High-Energy Charged Particles in the Innermost Jovian Magnetosphere. *Science*, 272:856–858, May 1996. doi: 10.1126/science.272.5263.856.

L. A. Fisk. Motion of the footpoints of heliospheric magnetic field lines at the Sun: Implications for recurrent energetic particle events at high heliographic latitudes. *Journal of Geophysical Research*, 101(A7):15547–15554, July 1996. doi: 10.1029/96JA01005.

L. A. Fisk and G. Gloeckler. The case for a common spectrum of particles accelerated in the heliosphere: Observations and theory. *Journal of Geophysical Research (Space Physics)*, 119:8733–8749, November 2014. doi: 10.1002/2014JA020426.

V Florinski and N Pogorelov. Four-dimensional transport of galactic cosmic rays in the outer heliosphere and heliosheath. *The Astrophysical Journal*, 701:642, 07 2009.

A. D. Fokker. Die mittlere Energie rotierender elektrischer Dipole im Strahlungsfeld. *Annalen der Physik*, 348:810–820, 1914. doi: 10.1002/andp.19143480507.

H. Föllmer. On Kiyoshi Itˆo's Work and its Impact. *Proceedings of the International Congress of Mathematician, Madrid*, 1:109–124, 2006.

N. J. Fox, M. C. Velli, S. D. Bale, R. Decker, A. Driesman, R. A. Howard, J. C. Kasper, J. Kinnison, M. Kusterer, D. Lario, M. K. Lockwood, D. J. McComas, N. E. Raouafi, and A. Szabo. The Solar Probe Plus Mission: Humanity's First Visit to Our Star. *Space Science Reviews*, 204(1-4):7–48, December 2016. doi: 10.1007/s11214-015-0211-6.

M. Gammon and A. Shalchi. Simple Analytical Forms of the Perpendicular Diffusion Coefficient for Two-component Turbulence. III. Damping Model of Dynamical Turbulence. *The Astrophysical Journal*, 847(2):118, Oct 2017. doi: 10.3847/1538-4357/aa8950.

C. Gardiner. *Stochastic Methods: A Handbook for the Natural and Social Sciences*. Springer Series in Synergetics. Springer Berlin Heidelberg, 2009. ISBN 9783540707127.

H. B. Garrett, S. M. Levin, S. J. Bolton, R. W. Evans, and B. Bhattacharya. A revised model of Jupiter's inner electron belts: Updating the Divine radiation model. *Geophysical Research Letters*, 32(4):L04104, February 2005. doi: 10.1029/2004GL021986.

P. R. Gazis, A. Barnes, J. D. Mihalov, and A. J. Lazarus. Solar wind velocity and temperature in the outer heliosphere. *Journal of Geophysical Research*, 99(A4):6561–6574, April 1994. doi: 10.1029/93JA03144.

J. Geiss, G. Gloeckler, R. von Steiger, H. Balsiger, L. A. Fisk, A. B. Galvin, F. M. Ipavich, S. Livi, J. F. McKenzie, K. W. Ogilvie, and B. Wilken. The Southern High-Speed Stream: Results from the SWICS Instrument on Ulysses. *Science*, 268(5213):1033–1036, May 1995.

L. J. Gleeson and W. I. Axford. Solar Modulation of Galactic Cosmic Rays. *Astrophysical Journal*, 154:1011, December 1968. doi: 10.1086/149822.

M. L. Goldstein, D. A. Roberts, and W. H. Matthaeus. Magnetohydrodynamic Turbulence In The Solar Wind. *Annual Review of Astronomy and Astrophysics*, 33:283–326, January 1995. doi: 10.1146/annurev.aa.33.090195.001435.

Nat Gopalswamy, Alejandro Lara, Seiji Yashiro, Mike L. Kaiser, and Russell A. Howard. Predicting the 1-AU arrival times of coronal mass ejections. *Journal of Geophysical Research*, 106(A12):29207–29218, December 2001. doi: 10.1029/2001JA000177.

J. T. Gosling, A. J. Hundhausen, and S. J. Bame. Solar wind stream evolution at large heliocentric distances: Experimental demonstration and the test of a model. *Journal of Gephysical Research*, 81(13):2111, May 1976. doi: 10.1029/JA081i013p02111.

L. M. Green, T. Török, B. Vršnak, W. Manchester, and A. Veronig. The Origin, Early Evolution and Predictability of Solar Eruptions. *Space Science Reviews*, 214(1):46, February 2018. doi: 10.1007/s11214-017-0462-5.

K. I. Gringauz, V. V. Bezrokikh, V. D. Ozerov, and R. E. Rybchinskii. A Study of the Interplanetary Ionized Gas, High-Energy Electrons and Corpuscular Radiation from the Sun by Means of the Three-Electrode Trap for Charged Particles on the Second Soviet Cosmic Rocket. *Soviet Physics Doklady*, 5:361, September 1960.

J. Guo, M. Dumbović, R. F. Wimmer-Schweingruber, M. Temmer, H. Lohf, Y. Wang, A. Veronig, D. M. Hassler, L. M. Mays, C. Zeitlin, B. Ehresmann, O. Witasse, J. L. Freiherr von Forstner, B. Heber, M. Holmström, and A. Posner. Modeling the Evolution and Propagation of 10 September 2017 CMEs and SEPs Arriving at Mars Constrained by Remote Sensing and In Situ Measurement. *Space Weather*, 16(8):1156–1169, August 2018. doi: 10.1029/2018SW001973.

J. Gurav, J. In-Keun, H. Park, E. Kang, and D. Nadargi. Silica aerogel: Synthesis and applications. *Journal of Nanomaterials*, 2010, 01 2010. doi: 10.1155/2010/409310.

D. A. Gurnett, W. S. Kurth, L. F. Burlaga, and N. F. Ness. In Situ Observations of Interstellar Plasma with Voyager 1. *Science*, 341(6153):1489–1492, Sep 2013. doi: 10.1126/science.1241681.

L. J. Haasbroek, M. S. Potgieter, and J. A. Le Roux. Acceleration of galactic and Jovian electrons at the heliospheric solar wind termination shock. *Advances in Space Research*, 19:953–956, May 1997. doi: 10.1016/S0273-1177(97)00311-6.

D. K. Haggerty and S. Livi. Monte Carlo simulations of CASSINI/LEMMS. *Advances in Space Research*, 33:2303–2308, January 2004. doi: 10.1016/S0273-1177(03)00464-2.

K. Hasselmann and G. Wibberenz. Scattering of charged particles by random electromagnetic fields. *Z. Geophys.*, 34:353, 1968.

D. M. Hassler, C. Zeitlin, R. F. Wimmer-Schweingruber, S. Böttcher, C. Martin, J. Andrews, E. Böhm, D. E. Brinza, M. A. Bullock, S. Burmeister, B. Ehresmann, M. Epperly, D. Grinspoon, J. Köhler, O. Kortmann, K. Neal, J. Peterson, A. Posner, S. Rafkin, L. Seimetz, K. D. Smith, Y. Tyler, G. Weigle, G. Reitz, and F. A. Cucinotta. The Radiation Assessment Detector (RAD) Investigation. *Space Science Reviews*, 170(1-4): 503–558, September 2012.

B. Heber. *Modulation galaktischer kosmischer Protonen und α-Teilchen in der inneren dreidimensionalen Heliospähre - Band B: Technische Aspekte.* PhD thesis, Christian-Albrechts-Universität zu Kiel, 1997.

B. Heber, W. Droege, P. Ferrando, L. J. Haasbroek, H. Kunow, R. Mueller-Mellin, C. Paizis, M. S. Potgieter, A. Raviart, and G. Wibberenz. Spatial variation of >40MeV/n nuclei fluxes observed during the ULYSSES rapid latitude scan. *Astronomy and Astrophysics*, 316:538–546, December 1996.

B. Heber, A. Kopp, H. Fichtner, and S. E. S. Ferreira. On the determination of energy spectra of MeV electrons by the Ulysses COSPIN/KET. *Advances in Space Research*, 35:605–610, 2005. doi: 10.1016/j.asr.2005.01.054.

V. F. Hess. Über Beobachtungen der durchdringenden Strahlung bei sieben Freiballonfahrten. *Phys. Z.*, 13:1084–1091, 1912.

M. Hitge and R. A. Burger. Cosmic ray modulation with a Fisk-type heliospheric magnetic field and a latitude-dependent solar wind speed. *Advances in Space Research*, 45(1):18–27, January 2010. doi: 10.1016/j.asr.2009.07.024.

J. T. Hoeksema and P. H. Scherrer. Solar magnetic field, 1976 through 1985: an atlas of photospheric magnetic field observations and computed coronal magnetic fields from the John M. Wilcox Solar Observatory at Sanford, 1976-1985. *NASA STI/Recon Technical Report N*, 86:29760, January 1986.

R. B. Horne, R. M. Thorne, S. A. Glauert, J. Douglas Menietti, Y. Y. Shprits, and D. A. Gurnett. Gyro-resonant electron acceleration at Jupiter. *Nature Physics*, 4:301 – 304, 2008. doi: 10.1038/nphys897.

K. Ito. Stochastic Integral. *Proc. Imperial Acad. Tokyo*, 20:519–524, 1944.

M. Jastrow Jr. *Aspects of Religious Belief and Practice in Babylonia and Assyria*. G.P. Putnam's Sons: New York and London, 1911.

J. R. Jokipii. Cosmic-Ray Propagation. I. Charged Particles in a Random Magnetic Field. *Astrophysical Journal*, 146:480, November 1966. doi: 10.1086/148912.

J. R. Jokipii. Latitudinal heliospheric magnetic field: Stochastic and causal components. *Journal of Geophysical Research*, 106(A8):15841–15848, August 2001.

J. R. Jokipii and J. Kota. The polar heliospheric magnetic field. *Geophysical Research Letters*, 16(1):1–4, January 1989.

J. R. Jokipii and E. N. Parker. on the Convection, Diffusion, and Adiabatic Deceleration of Cosmic Rays in the Solar Wind. *The Astrophysical Journal*, 160:735, May 1970. doi: 10.1086/150465.

S. W. Kahler, E. W. Cliver, and A. G. Ling. Validating the proton prediction system (PPS). *Journal of Atmospheric and Solar-Terrestrial Physics*, 69(1-2):43–49, February 2007.

May-Britt Kallenrode. *Space physics : an introduction to plasmas and particles in the heliosphere and magnetospheres*. Springer Verlag, Berlin, Heidelberg, New York, 2004.

S. G. Kanekal, D. N. Baker, J. B. Blake, M. D. Looper, R. A. Mewaldt, and C. A. Lopate. Modulation of Jovian electrons at 1 AU during solar cycles 22-23. *Geophysical Research Letters*, 30(15):1795, August 2003. doi: 10.1029/2003GL017502.

E. Kappler. Versuche zur Messung der Avogadro-Loschmidtschen Zahl aus der Brownschen Bewegung einer Drehwaage. *Annalen der Physik*, 403(2):233–256, January 1931. doi: 10.1002/andp.19314030208.

J. Kelly, S. Dalla, and T. Laitinen. Cross-field Transport of Solar Energetic Particles in a Large-scale Fluctuating Magnetic Field. *Astrophysical Journal*, 750(1):47, May 2012. doi: 10.1088/0004-637X/750/1/47.

K. K. Khurana, M. G. Kivelson, V. M. Vasyliunas, N. Krupp, J. Woch, A. Lagg, B. H. Mauk, and W. S. Kurth. The configuration of Jupiter's magnetosphere. In Fran Bagenal, Timothy E. Dowling, and William B. McKinnon, editors, *Jupiter. The Planet, Satellites and Magnetosphere*, volume 1, pages 593–616. Cambridge University Press, 2004.

R. Kippenhahn and C. Möllenhoff. *Elementare Plasmaphysik*. Mannheim: Bibliographisches Institut, 1975, 1975.

R Kissmann, H. Fichtner, B. Heber, S.E.S. Ferreira, and M.S. Potgieter. First results of a new 3-d model of the time-dependent modulation of electrons in the heliosphere. *Advances in Space Research*, 32(4):681 – 686, 2003. ISSN 0273-1177. doi: https://doi.org/10.1016/S0273-1177(03)00346-6. Heliosphere at Solar Maximum.

R. Kissmann, Fichtner, H., and Ferreira, S. E. S. The influence of cirs on the energetic electron flux at 1 au. *Astronomy and Astrophysics*, 419(1):357–363, 2004. doi: 10.1051/0004-6361:20040072.

L. W. Klein, L. F. Burlaga, and N. F. Ness. Radial and latitudinal variations of the interplanetary magnetic field. *Journal of Geophysical Research*, 92(A9):9885–9892, September 1987. doi: 10.1029/JA092iA09p09885.

P. E. Kloeden and E. Platen. *Numerical Solution of Stochastic Differential Equations*. Stochastic Modelling and Applied Probability. Springer Berlin Heidelberg, 2011. ISBN 9783540540625.

M. Kojima, H. Washimi, H. Misawa, and K. Hakamada. Solar wind observed within 0.3 AU with interplanetary scintillation. In E. Marsch and R. Schwenn, editors, *Solar Wind Seven Colloquium*, pages 201–204, January 1992.

A. Kolmogorov. The Local Structure of Turbulence in Incompressible Viscous Fluid for Very Large Reynolds' Numbers. *Akademiia Nauk SSSR Doklady*, 30:301–305, January 1941.

A. Kopp, I. Büsching, R. D. Strauss, and M. S. Potgieter. A stochastic differential equation code for multidimensional Fokker-Planck type problems. *Computer Physics Communications*, 183:530–542, March 2012. doi: 10.1016/j.cpc.2011.11.014.

A. Kopp, T. Wiengarten, H. Fichtner, F. Effenberger, P. Kühl, B. Heber, J. Raath, and M. S. Potgieter. Cosmic-Ray Transport in Heliospheric Magnetic Structures. II. Modeling Particle Transport through Corotating Interaction Regions. *Astrophysical Journal*, 837 (1):37, March 2017. doi: 10.3847/1538-4357/aa603b.

Andreas Kopp and Yuri A. Shchekinov. A gedankenexperiment for anomalous diffusion in a charge-fluctuating dusty plasma. *Physics of Plasmas*, 21(2):023702, February 2014. doi: 10.1063/1.4865408.

A. S. Krieger, A. F. Timothy, and E. C. Roelof. A Coronal Hole and Its Identification as the Source of a High Velocity Solar Wind Stream. *Solar Physics*, 29(2):505–525, April 1973. doi: 10.1007/BF00150828.

S. M. Krimigis, D. G. Mitchell, D. C. Hamilton, S. Livi, J. Dandouras, S. Jaskulek, T. P. Armstrong, J. D. Boldt, A. F. Cheng, G. Gloeckler, J. R. Hayes, K. C. Hsieh, W.-H. Ip, E. P. Keath, E. Kirsch, N. Krupp, L. J. Lanzerotti, R. Lundgren, B. H. Mauk, R. W. McEntire, E. C. Roelof, C. E. Schlemm, B. E. Tossman, B. Wilken, and D. J. Williams. Magnetosphere Imaging Instrument (MIMI) on the Cassini Mission to Saturn/Titan. *Space Science Reviews*, 114:233–329, September 2004. doi: 10.1007/s11214-004-1410-8.

S. M. Krimigis, R. B. Decker, E. C. Roelof, M. E. Hill, T. P. Armstrong, G. Gloeckler, D. C. Hamilton, and L. J. Lanzarotti. Search for the Exit: Voyager 1 at Heliosphere's Border with the Galaxy. *Science*, 341, July 2013.

N. Krupp, J. Woch, A. Lagg, S. A. Espinosa, S. Livi, S. M. Krimigis, D. G. Mitchell, D. J. Williams, A. F. Cheng, B. H. Mauk, R. W. McEntire, T. P. Armstrong, D. C. Hamilton, G. Gloeckler, J. Dandouras, and L. J. Lanzerotti. Leakage of energetic particles from Jupiter's dusk magnetosphere: Dual spacecraft observations. *Geophysical Research Letters*, 29:1736, August 2002. doi: 10.1029/2001GL014290.

M. Kruse, V. Heidrich-Meisner, R. F. Wimmer-Schweingruber, and M. Hauptmann. An elliptic expansion of the potential field source surface model. *Astronomy and Astrophysics*, 638:A109, June 2020.

P. Kühl and B. Heber. Revising More Than 20 Years of EPHIN Ion Flux Data—A New Data Product for Space Weather Applications. *Space Weather*, 17(1):84–98, January 2019. doi: 10.1029/2018SW002114.

P. Kühl, N. Dresing, P. Dunzlaff, F. Effenberger, H. Fichtner, J. Gieseler, R. Gómez-Herrero, B. Heber, A. Klassen, J. Kleimann, A. Kopp, M. Potgieter, R. D. Strauss, and T. Wiengarten. Spectrum of galactic and Jovian electrons. *Proceedings of 33th International Cosmic Ray Conference (ICRC 2013)*, 2013a.

P. Kühl, N. Dresing, P. Dunzlaff, H. Fichtner, J. Gieseler, R. Gómez-Herrero, B. Heber, A. Klassen, J. Kleimann, A. Kopp, M. Potgieter, K. Scherer, and R. D. Strauss. Simultaneous Analysis of Recurrent Jovian Electron Increases and Galactic Cosmic Ray Decreases. *Central European Astrophysical Bulletin*, 37:643–648, January 2013b.

H. Kunow, W. Dröge, B. Heber, R. Müller-Mellin, K. Röhrs, H. Sierks, G. Wibberenz, R. Ducros, P. Ferrando, C. Rastoin, A. Raviart, and C. Paizis. High energy cosmic-ray nuclei results on Ulysses: 2. Effects of a recurrent high-speed stream from the southern polar coronal hole. *Space Science Reviews*, 72(1-2):397–402, April 1995. doi: 10.1007/BF00768811.

Valéry Lainey, Jean-Eudes Arlot, Özgür Karatekin, and Tim van Hoolst. Strong tidal dissipation in Io and Jupiter from astrometric observations. *Nature*, 459(7249):957–959, June 2009. doi: 10.1038/nature08108.

D. Lange and H. Fichtner. Are there Kronian electrons in the inner heliosphere? *Astronomy and Astrophysics*, 482:973–979, May 2008. doi: 10.1051/0004-6361:20079069.

D. Lange, H. Fichtner, and R. Kissmann. Time-dependent 3D modulation of Jovian electrons. Comparison with Ulysses/KET observations. *Astronomy and Astrophysics*, 449:401–410, April 2006. doi: 10.1051/0004-6361:20054061.

P. Langevin. Sur la théorie du mouvement brownien. *C. R. Acad. Sci. Paris.*, 146:530–533, 1908.

R. J. Leamon, C. W. Smith, N. F. Ness, W. H. Matthaeus, and H. K. Wong. Observational constraints on the dynamics of the interplanetary magnetic field dissipation range. *Journal of Geophysical Research*, 103(A3):4775–4788, March 1998. doi: 10.1029/97JA03394.

R. J. Leamon, W. H. Matthaeus, C. W. Smith, G. P. Zank, D. J. Mullan, and S. Oughton. MHD-driven Kinetic Dissipation in the Solar Wind and Corona. *Astrophysical Journal*, 537(2):1054–1062, July 2000. doi: 10.1086/309059.

D. S. Lemons and A. Gythiel. Paul langevin's 1908 paper "on the theory of brownian motion" ["sur la théorie du mouvement brownien," c. r. acad. sci. (paris) 146, 530–533 (1908)]. *American Journal of Physics*, 65(11):1079–1081, 1997. doi: 10.1119/1.18725.

G. A. Lentz, J. McCarthy, J. J. O'Gallagher, and J. A. Simpson. Anisotropies of Galactic Cosmic Rays Outside the Orbit of Earth Measured on Pioneer 10. In *International Cosmic Ray Conference*, volume 5 of *International Cosmic Ray Conference*, page 3145, January 1973.

A. von Lieven. *Grundriss des Laufes der Sterne – Das sogenannte Nutbuch.* The Carsten Niebuhr Institute of Ancient Eastern Studies, Kopenhagen, 2007.

T. Lindvall. W. Doeblin, 1915-1940. *Ann. Probab.*, 19(3):929–934, 07 1991. doi: 10.1214/aop/1176990329.

R. Lionello, J. A. Linker, Z. Mikić, and P. Riley. The Latitudinal Excursion of Coronal Magnetic Field Lines in Response to Differential Rotation: MHD Simulations. *The Astrophysical Journal*, 642(1):L69–L72, May 2006. doi: 10.1086/504289.

M. S. Longair. *High energy astrophysics. Vol.1: Particles, photons and their detection.* Cambridge Universtiy Press, 1992.

C. Lopate. Jovian and Galactic Electrons (2-30 MeV) in the Heliosphere from 1 to 50AU. *Proceedings of the 22nd International Cosmic Ray Conference (ICRC 1991)*, 2:149, August 1991.

I. H. Malitson and M. J Dodge. Refraction and dispersion of lead fluoride. *J. Opt. Soc. Am.*, 500A, 1969.

M. S. Marsh, S. Dalla, M. Dierckxsens, T. Laitinen, and N. B. Crosby. SPARX: A modeling system for Solar Energetic Particle Radiation Space Weather forecasting. *Space Weather*, 13(6):386–394, June 2015.

G. Maruyama. Continuous markov processes and stochastic equations. *Rendiconti del Circolo Matematico di Palermo*, 4(1):48, Jan 1955. ISSN 1973-4409.

G. M. Mason, R. von Steiger, R. B. Decker, M. I. Desai, J. R. Dwyer, L. A. Fisk, G. Gloeckler, J. T. Gosling, M. Hilchenbach, R. Kallenbach, E. Keppler, B. Klecker, H. Kunow, G. Mann, I. G. Richardson, T. R. Sanderson, G. M. Simnett, Y.-M. Wang, R. F. Wimmer-Schweingruber, M. Fränz, and J. E. Mazur. Origin, Injection, and Acceleration of CIR Particles: Observations Report of Working Group 6. *Space Science Reviews*, 89:327–367, July 1999.

B. H. Mauk, D. K. Haggerty, S. E. Jaskulek, C. E. Schlemm, L. E. Brown, S. A. Cooper, R. S. Gurnee, C. M. Hammock, J. R. Hayes, G. C. Ho, J. C. Hutcheson, A. D. Jacques, S. Kerem, C. K. Kim, D. G. Mitchell, K. S. Nelson, C. P. Paranicas, N. Paschalidis, E. Rossano, and M. R. Stokes. The jupiter energetic particle detector instrument (jedi) investigation for the juno mission. *Space Science Reviews*, Nov 2013. ISSN 1572-9672. doi: 10.1007/s11214-013-0025-3.

E. W. Maunder. The solar origin of the disturbances of terrestrial magnetism. *Astronomische Nachrichten*, 167(11):177, February 1905. doi: 10.1002/asna.19041671102.

J. McCarthy and J. J. O'Gallagher. The Time and Spatial Behavior of Solar Flare Proton Anisotropies Observed in Deep Space on Pioneer 10 and 11. In *International Cosmic Ray Conference*, volume 4 of *International Cosmic Ray Conference*, page 1526, August 1975.

D. J. McComas, H. A. Elliott, N. A. Schwadron, J. T. Gosling, R. M. Skoug, and B. E. Goldstein. The three-dimensional solar wind around solar maximum. *Geophysical Research Letters*, 30(10):1517, May 2003. doi: 10.1029/2003GL017136.

D. J. McComas, F. Allegrini, P. Bochsler, M. Bzowski, M. Collier, H. Fahr, H. Fichtner, P. Frisch, H. O. Funsten, S. A. Fuselier, G. Gloeckler, M. Gruntman, V. Izmodenov, P. Knappenberger, M. Lee, S. Livi, D. Mitchell, E. Möbius, T. Moore, S. Pope, D. Reisenfeld, E. Roelof, J. Scherrer, N. Schwadron, R. Tyler, M. Wieser, M. Witte, P. Wurz, and G. Zank. IBEX—Interstellar Boundary Explorer. *Space Science Reviews*, 146(1-4):11–33, August 2009. doi: 10.1007/s11214-009-9499-4.

D. J. McComas, D. Alexashov, M. Bzowski, H. Fahr, J. Heerikhuisen, V. Izmodenov, M. A. Lee, E. Möbius, N. Pogorelov, N. A. Schwadron, and G. P. Zank. The Heliosphere's

Interstellar Interaction: No Bow Shock. *Science*, 336(6086):1291, June 2012. doi: 10.1126/science.1221054.

F. B. McDonald, T. L. Cline, and G. M. Simnett. Multivarious temporal variations of low-energy relativistic cosmic-ray electrons. *Journal of Geophysical Research*, 77:2213, 1972. doi: 10.1029/JA077i013p02213.

A. S. McEwen, M. J. S. Belton, H. H. Breneman, S. A. Fagents, P. Geissler, R. Greeley, J. W. Head, G. Hoppa, W. L. Jaeger, T. V. Johnson, L. Keszthelyi, K. P. Klaasen, R. Lopes-Gautier, K. P. Magee, M. P. Milazzo, J. M. Moore, R. T. Pappalardo, C. B. Phillips, J. Radebaugh, G. Schubert, P. Schuster, D. P. Simonelli, R. Sullivan, P. C. Thomas, E. P. Turtle, and D. A. Williams. Galileo at Io: Results from High-Resolution Imaging. *Science*, 288(5469):1193–1198, May 2000. doi: 10.1126/science.288.5469.1193.

R. B. McKibben, M. Zhang, B. Heber, H. Kunow, and T. R. Sand erson. Localized "Jets" of Jovian electrons observed during Ulysses' distant Jupiter flyby in 2003 2004. *Planetary and Space Science*, 55(1-2):21–31, January 2007.

R. Metzler and J. Klafter. The random walk's guide to anomalous diffusion: a fractional dynamics approach. *Physical Reports*, 339(1):1–77, December 2000. doi: 10.1016/S0370-1573(00)00070-3.

P. Meyer and P. Evenson. The University of Chicago cosmic ray electrons and nuclei experiment on the H spacecraft. *IEEE Transactions on Geoscience Electronics*, 16:180–185, July 1978. doi: 10.1109/TGE.1978.294542.

N. Meyer-Vernet. *Basics of the Solar Wind*. Cambridge Universtiy Press, 2007.

D. M. Moeketsi, M. S. Potgieter, S. E. S. Ferreira, B. Heber, H. Fichtner, and V. K. Henize. The heliospheric modulation of 3 10 MeV electrons: Modeling of changes in the solar wind speed in relation to perpendicular polar diffusion. *Advances in Space Research*, 35: 597–604, 2005.

D. Moses. Jovian electrons at 1 AU - 1978-1984. *Astrophysical Journal, Part 1*, 313: 471–486, February 1987.

C. Möstl, K. Amla, J. R. Hall, P. C. Liewer, E. M. De Jong, R. C. Colaninno, A. M. Veronig, T. Rollett, M. Temmer, V. Peinhart, J. A. Davies, N. Lugaz, Y. D. Liu, C. J. Farrugia, J. G. Luhmann, B. Vršnak, R. A. Harrison, and A. B. Galvin. Connecting Speeds, Directions and Arrival Times of 22 Coronal Mass Ejections from the Sun to 1 AU. *The Astrophysical Journal*, 787(2):119, June 2014.

C. Möstl, A. Isavnin, P. D. Boakes, E. K. J. Kilpua, J. A. Davies, R. A. Harrison, D. Barnes, V. Krupar, J. P. Eastwood, S. W. Good, R. J. Forsyth, V. Bothmer, M. A. Reiss, T. Amerstorfer, R. M. Winslow, B. J. Anderson, L. C. Philpott, L. Rodriguez, A. P. Rouillard, P. Gallagher, T. Nieves-Chinchilla, and T. L. Zhang. Modeling observations of solar coronal mass ejections with heliospheric imagers verified with the Heliophysics System Observatory. *Space Weather*, 15(7):955–970, July 2017. doi: 10.1002/2017SW001614.

D. Müller, R. G. Marsden, O. C. St. Cyr, and H. R. Gilbert. Solar Orbiter . Exploring the Sun-Heliosphere Connection. *Solar Physics*, 285(1-2):25–70, July 2013.

R Müller-Mellin, H Kunow, V Fleißner, E Pehlke, E Rode, N Röschmann, C Scharmberg, H Sierks, P Rusznyak, S McKenna-Lawlor, I Elendt, J Sequeiros, D Meziat, S Sanchez, J Medina, L Del Peral, M Witte, R Marsden, and J Henrion. COSTEP - Comprehensive

Suprathermal and Energetic Particle Analyser. *Solar Physics*, 162(1):483–504, December 1995.

M. Neugebauer and C. W. Snyder. Solar Plasma Experiment. *Science*, 138(3545):1095–1097, December 1962. doi: 10.1126/science.138.3545.1095-a.

R. R. Nndanganeni and M. S. Potgieter. The energy range of drift effects in the solar modulation of cosmic ray electrons. *Advances in Space Research*, 58:453–463, August 2016. doi: 10.1016/j.asr.2016.04.020.

R. R. Nndanganeni and M. S. Potgieter. The global modulation of galactic and jovian electrons in the heliosphere. *Astrophysics and Space Science*, 363(7):156, Jun 2018.

M. Núñez, K.-L. Klein, B. Heber, O. E. Malandraki, P. Zucca, J. Labrens, P. Reyes-Santiago, P. Kuehl, and E. Pavlos. HESPERIA Forecasting Tools: Real-Time and Post-Event. In O. E. Malandraki and N. B. Crosby, editors, *Solar Particle Radiation Storms Forecasting and Analysis*, volume 444 of *Astrophysics and Space Science Library*, pages 113–131, 2018.

J. J. O'Gallagher. A time-dependent diffusion-convection model for the long-term modulation of cosmic rays. *The Astrophysical Journal*, 197:495–507, April 1975.

J. A. C. Oudemans and J. Bosscha. Galilee et Marius. *Archives Nederlandaises des Sciences Exactes et Naturelles, La Haye*, Serie II, Band VIII:115–189, 1903.

S. Oughton, E. R. Priest, and W. H. Matthaeus. The influence of a mean magnetic field on three-dimensional magnetohydrodynamic turbulence. *Journal of Fluid Mechanics*, 280: 95–117, January 1994. doi: 10.1017/S0022112094002867.

S. Oughton, W. H. Matthaeus, M. Wan, and K. T. Osman. Anisotropy in solar wind plasma turbulence. *Philosophical Transactions of the Royal Society of London Series A*, 373(2041):20140152–20140152, April 2015. doi: 10.1098/rsta.2014.0152.

B. Palmaerts, E. Roussos, N. Krupp, W. S. Kurth, D. G. Mitchell, and J. N. Yates. Statistical analysis and multi-instrument overview of the quasi-periodic 1-hour pulsations in Saturn's outer magnetosphere. , 271:1–18, June 2016. doi: 10.1016/j.icarus.2016.01.025.

I. D. Palmer. Transport coefficients of low-energy cosmic rays in interplanetary space. *Reviews of Geophysics and Space Physics*, 20:335–351, May 1982. doi: 10.1029/RG020i002p00335.

E. N. Parker. Dynamics of the Interplanetary Gas and Magnetic Fields. *The Astrophysical Journal*, 128:664, Nov 1958.

E. N. Parker. *Interplanetary dynamical processes.* John Wiley & Sons Inc, 1963.

E. N. Parker. The passage of energetic charged particles through interplanetary space. *Planetary and Space Science*, 13:9–49, January 1965. doi: 10.1016/0032-0633(65)90131-5.

E. N. Parker. The effect of adiabatic deceleration on the cosmic ray spectrum in the solar system. , 14(4):371–380, Apr 1966. doi: 10.1016/0032-0633(66)90074-2.

C. Pei, J. W. Bieber, R. A. Burger, and J. Clem. A general time-dependent stochastic method for solving parker's transport equation in spherical coordinates. *Journal of Geophysical Research: Space Physics*, 115(A12), 2010. doi: 10.1029/2010JA015721.

T. Peleikis, M. Kruse, L. Berger, and R. F. Wimmer-Schweingruber. Origin of the solar wind: A novel approach to link in situ and remote observations. A study for SPICE and SWA on the upcoming Solar Orbiter mission. *Astronomy and Astrophysics*, 602:A24, June 2017. doi: 10.1051/0004-6361/201629727.

A. Petrosyan, A. Balogh, M. L. Goldstein, J. Léorat, E. Marsch, K. Petrovay, B. Roberts, R. von Steiger, and J. C. Vial. Turbulence in the Solar Atmosphere and Solar Wind. *Space Science Reviews*, 156(1-4):135–238, October 2010. doi: 10.1007/s11214-010-9694-3.

M. Planck. Über einen Satz der statistischen Dynamik und seine Erweiterung in der Quantentheorie. *Sitzungsberichte der K¨oniglich-Preussischen Akademie der Wissenschaften zu Berlin*, 24:324–341, 1917.

A. Posner. Up to 1-hour forecasting of radiation hazards from solar energetic ion events with relativistic electrons. *Space Weather*, 5(5):05001, May 2007. doi: 10.1029/2006SW000268.

A. Posner and R. D. Strauss. Warning Time Analysis From SEP Simulations of a Two-Tier REleASE System Applied to Mars Exploration. *Space Weather*, 18(4):e02354, April 2020. doi: 10.1029/2019SW002354.

M. S. Potgieter. Heliospheric modulation of galactic electrons: Consequences of new calculations for the mean free path of electrons between 1 MeV and ˜10 GeV. *Journal of Geophysical Research*, 101:24411–24422, November 1996. doi: 10.1029/96JA02445.

M. S. Potgieter. Solar cycle variations and cosmic rays. *Journal of Atmospheric and Solar-Terrestrial Physics*, 70(2-4):207–218, February 2008. doi: 10.1016/j.jastp.2007.08.023.

M. S. Potgieter and S. E. S. Ferreira. Effects of the solar wind termination shock on the modulation of Jovian and galactic electrons in the heliosphere. *Journal of Geophysical Research (Space Physics)*, 107(A7):1089, jul 2002. doi: 10.1029/2001JA009040.

M. S. Potgieter and R. R. Nndanganeni. A local interstellar spectrum for galactic electrons. *Astroparticle Physics*, 48:25–29, August 2013. doi: 10.1016/j.astropartphys.2013.06.008.

M. S. Potgieter and E. E. Vos. Difference in the heliospheric modulation of cosmic-ray protons and electrons during the solar minimum period of 2006 to 2009. *Astronomy and Astrophysics*, 601:A23, 2017. doi: 10.1051/0004-6361/201629995.

M. S. Potgieter, E. E. Vos, R. Munini, M. Boezio, and V. Di Felice. Modulation of Galactic Electrons in the Heliosphere during the Unusual Solar Minimum of 2006-2009: A Modeling Approach. *The Astrophysical Journal*, 810:141, September 2015. doi: 10.1088/0004-637X/810/2/141.

P. L. Prinsloo, M. S. Potgieter, and R. D. Strauss. The Re-acceleration of Galactic Electrons at the Heliospheric Termination Shock. *The Astrophysical Journal*, 836:100, February 2017. doi: 10.3847/1538-4357/836/1/100.

K. R. Pyle and J. A. Simpson. The Jovian relativistic electron distribution in interplanetary space from 1 to 11 AU - Evidence for a continuously emitting 'point' source. *Astrophysical Journal, Part 2 - Letters to the Editor*, 215:L89–L93, July 1977. doi: 10.1086/182486.

J. L. Raath, M. S. Potgieter, R. D. Strauss, and A. Kopp. The effects of magnetic field modifications on the solar modulation of cosmic rays with a SDE-based model. *Advances in Space Research*, 57(9):1965–1977, May 2016. doi: 10.1016/j.asr.2016.01.017.

O. Rømer. Démonstration touchant le mouvement de la lumière trouvé par M. Rømer de l'Académie royale des sciences. *Le Journal des Sçavans. Paris*, page 233–236, 1676.

E. C. Roelof. Propagation of Solar Cosmic Rays in the Interplanetary Magnetic Field. In H. Ögelman and J. R. Wayland, editors, *Lectures in High-Energy Astrophysics*, page 111, 1969.

E. Roussos, N. Krupp, D. G. Mitchell, C. Paranicas, S. M. Krimigis, M. Andriopoulou, B. Palmaerts, W. S. Kurth, S. V. Badman, A. Masters, and M. K. Dougherty. Quasi-periodic injections of relativistic electrons in Saturn's outer magnetosphere. , 263:101–116, January 2016. doi: 10.1016/j.icarus.2015.04.017.

M. Savopulos and J. J. Quenby. Anomalous He Acceleration, the Particle Source and the Transport Coefficient. *Solar Physics*, 176(1):185–199, November 1997. doi: 10.1023/A:1004935311605.

M. Savopulos and J. J. Quenby. Ambiguity in Determining the Diffusion Coefficient from Shock-Associated Energetic Particle Increases. *Solar Physics*, 180:479–485, June 1998. doi: 10.1023/A:1005078122718.

W. Schachermayer and J. Teichmann. Wie K. It den stochastischen Kalkül revolutionierte. *IMN 61*, 205:11–22, 2007. doi: 10.1007/BF00146478.

K. H. Schatten, J. M. Wilcox, and N. F. Ness. A model of interplanetary and coronal magnetic fields. *Solar Physics*, 6:442–455, March 1969. doi: 10.1007/BF00146478.

K. Scherer, H. Fichtner, R. D. Strauss, S. E. S. Ferreira, M. S. Potgieter, and H. J. Fahr. On Cosmic Ray Modulation beyond the Heliopause: Where is the Modulation Boundary? , 735(2):128, July 2011. doi: 10.1088/0004-637X/735/2/128.

R. Schlickeiser. Particle acceleration in active galactic nuclei - coexistence of monoenergetic, power law and Maxwell-Boltzmann electron energy spectra. In J. E. Dyson, editor, *Active Galactic Nuclei*, pages 355–360. Manchester University Press, 1985.

R. Schlickeiser. Cosmic-ray transport and acceleration. I - Derivation of the kinetic equation and application to cosmic rays in static cold media. II - Cosmic rays in moving cold media with application to diffusive shock wave acceleration. *ApJ*, 336:243–293, January 1989. doi: 10.1086/167009.

N. A. Schwadron. An explanation for strongly underwound magnetic field in co-rotating rarefaction regions and its relationship to footpoint motion on the the sun. *Geophysical Research Letters*, 29(14):1663, July 2002. doi: 10.1029/2002GL015028.

N. A. Schwadron and D. J. McComas. Heliospheric "FALTS": Favored Acceleration Locations at the Termination Shock. *Geophysical Research Letters*, 30(11):1587, June 2003. doi: 10.1029/2002GL016499.

R. Schwenn. Large-Scale Structure of the Interplanetary Medium. In Rainer Schwenn and Eckart Marsch, editors, *Physics of the Inner Heliosphere I*, page 99. Springer Verlag, Berlin, Heidelberg, New York, 1990.

P. Kenneth Seidelmann, B. A. Archinal, M. F. A'Hearn, A. Conrad, G. J. Consolmagno, D. Hestroffer, J. L. Hilton, G. A. Krasinsky, G. Neumann, J. Oberst, P. Stooke, E. F. Tedesco, D. J. Tholen, P. C. Thomas, and I. P. Williams. Report of the IAU/IAG Working Group on cartographic coordinates and rotational elements: 2006. *Celestial Mechanics and Dynamical Astronomy*, 98(3):155–180, July 2007. doi: 10.1007/s10569-007-9072-y.

A. Shalchi, editor. *Nonlinear Cosmic Ray Diffusion Theories*, volume 362 of *Astrophysics and Space Science Library*, 2009. doi: 10.1007/978-3-642-00309-7.

J. V. Shebalin, W. H. Matthaeus, and D. Montgomery. Anisotropy in MHD turbulence due to a mean magnetic field. *Journal of Plasma Physics*, 29(3):525–547, June 1983. doi: 10.1017/S0022377800000933.

H. Sierks. Auswertung der Eichmessungen der Kieler Elektronenteleskops zur Erstellungvon Energiespektren an Bord der Raumsonde Ulysses (International Solar PolarMission). *Diploma thesis, Christian-Albrechts-Universität zu Kiel*, 1988.

J. A. Simpson, J. D. Anglin, A. Balogh, M. Bercovitch, J. M. Bouman, E. E. Budzinski, J. R. Burrows, R. Carvell, J. J. Connell, R. Ducros, P. Ferrando, J. Firth, M. Garcia-Munoz, J. Henrion, R. J. Hynds, B. Iwers, R. Jacquet, H. Kunow, G. Lentz, R. G. Marsden, R. B. Mckibben, R. Meuller-Mellin, D. E. Page, M. Perkins, A. Raviart, T. R. Sanderson, H. Sierks, L. Treguer, A. J. Tuzzolino, K. P. Wenzel, and G. Wibberenz. The ULYSSES Cosmic Ray and Solar Particle Investigation. *Astronomy and Astrophysics Supplement Series*, 92(2):365–399, January 1992.

J. A. Simpson, J. D. Anglin, V. Bothmer, J. J. Connell, P. Ferrando, B. Heber, H. Kunow, C. Lopate, R. G. Marsden, R. B. McKibben, R. Muller-Mellin, C. Paizis, C. Rastoin, A. Raviart, T. R. Sanderson, H. Sierks, K. J. Trattner, K. P. Wenzel, G. Wibberenz, and M. Zhang. Cosmic Ray and Solar Particle Investigations Over the South Polar Regions of the Sun. *Science*, 268(5213):1019–1023, May 1995. doi: 10.1126/science.268.5213.1019.

J. A. Simpson, M. Zhang, and S. Bame. A Solar Polar North-South Asymmetry for Cosmic-Ray Propagation in the Heliosphere: The ULYSSES Pole-to-Pole Rapid Transit. *Astrophysical Journal Letters*, 465:L69, July 1996. doi: 10.1086/310127.

C. W. Smith and John W. Bieber. Solar Cycle Variation of the Interplanetary Magnetic Field Spiral. *Astrophysical Journal*, 370:435, March 1991. doi: 10.1086/169830.

C. W. Smith, John W. Bieber, and William H. Matthaeus. Cosmic-Ray Pitch-Angle Scattering in Isotropic Turbulence. II. Sensitive Dependence on the Dissipation Range Spectrum. *Astrophysical Journal*, 363:283, November 1990. doi: 10.1086/169340.

C. W. Smith, W. H. Matthaeus, Gary P. Zank, Norman F. Ness, Sean Oughton, and John D. Richardson. Heating of the low-latitude solar wind by dissipation of turbulent magnetic fluctuations. *Journal of Geophysical Research*, 106(A5):8253–8272, May 2001. doi: 10.1029/2000JA000366.

C. W. Smith, K. Hamilton, B. J. Vasquez, and R. J. Leamon. Dependence of the Dissipation Range Spectrum of Interplanetary Magnetic Fluctuationson the Rate of Energy Cascade. *The Astrophysical Journall*, 645(1):L85–L88, July 2006a. doi: 10.1086/506151.

C. W. Smith, Philip A. Isenberg, William H. Matthaeus, and John D. Richardson. Turbulent Heating of the Solar Wind by Newborn Interstellar Pickup Protons. *The Astrophysical Journal*, 638(1):508–517, February 2006b. doi: 10.1086/498671.

E. J. Smith, B. T. Tsurutani, and R. L. Rosenberg. Observations of the interplanetary sector structure up to heliographic latitudes of 16°: Pioneer 11. *Journal of Geophysic*, 83(A2):717–724, February 1978. doi: 10.1029/JA083iA02p00717.

H. B. Snodgrass. Magnetic rotation of the solar photosphere. *Astrophysical Journal*, 270: 288–299, July 1983. doi: 10.1086/161121.

O. Sternal. *Transport of galactic cosmic rays in different heliospheric magnetic field configurations*. PhD thesis, Christian-Albrechts-Universität zu Kiel, 2010.

O. Sternal, N. E. Engelbrecht, R. A. Burger, S. E. S. Ferreira, H. Fichtner, B. Heber, A. Kopp, M. S. Potgieter, and K. Scherer. Possible Evidence for a Fisk-type Heliospheric Magnetic Field. I. Analyzing Ulysses/KET Electron Observations. *The Astrophysical Journal*, 741(1):23, November 2011. doi: 10.1088/0004-637X/741/1/23.

R. Steyn, D. T. Strauss, F. Effenberger, and D. Pacheco. The soft X-ray Neupert effect as a proxy for solar energetic particle injection. A proof-of-concept physics-based forecasting model. *Journal of Space Weather and Space Climate*, 10:64, November 2020. doi: 10.1051/swsc/2020067.

D. E. Stilwell, R. M. Joyce, B. J. Teegarden, J. H. Trainor, G. Streeter, and J. Bernstein. The Pioneer 10/11 and Helios A/B cosmic ray instruments. *IEEE Transactions on Nuclear Science*, 22:570–574, February 1975. doi: 10.1109/TNS.1975.4327705.

E. C. Stone, A. C. Cummings, F. B. McDonald, B. C. Heikkila, N. Lal, and W. R. Webber. Voyager 1 Explores the Termination Shock Region and the Heliosheath Beyond. *Science*, 309(5743):2017–2020, September 2005. doi: 10.1126/science.1117684.

E. C. Stone, A. C. Cummings, F. B. McDonald, B. C. Heikkila, N. Lal, and W. R. Webber. An asymmetric solar wind termination shock. *Nature*, 454(7200):71–74, July 2008. doi: 10.1038/nature07022.

E. C. Stone, A. C. Cummings, B. C. Heikkila, and N. Lal. Cosmic ray measurements from Voyager 2 as it crossed into interstellar space. *Nature Astronomy*, 3:1013–1018, November 2019. doi: 10.1038/s41550-019-0928-3.

R. D. Strauss, M. S. Potgieter, I. Büsching, and A. Kopp. Modeling the Modulation of Galactic and Jovian Electrons by Stochastic Processes. *The Astrophysical Journal*, 735:83, July 2011a. doi: 10.1088/0004-637X/735/2/83.

R. D. Strauss, M. S. Potgieter, A. Kopp, and I. Büsching. On the propagation times and energy losses of cosmic rays in the heliosphere. *Journal of Geophysical Research (Space Physics)*, 116:A12105, December 2011b.

R. D. Strauss, M. S. Potgieter, and S. E. S. Ferreira. Modelling and observing Jovian electron propagation times in the inner heliosphere. *Advances in Space Research*, 51:339–349, February 2013. doi: 10.1016/j.asr.2012.09.035.

R. D. T. Strauss and F. Effenberger. A Hitch-hiker's Guide to Stochastic Differential Equations. Solution Methods for Energetic Particle Transport in Space Physics and Astrophysics. *Space Sciences Reviews*, 212:151–192, October 2017. doi: 10.1007/s11214-017-0351-y.

R. C. Tautz and A. Shalchi. Simulated energetic particle transport in the interplanetary space: The Palmer consensus revisited. *Journal of Geophysical Research (Space Physics)*, 118:642–647, February 2013. doi: 10.1002/jgra.50155.

B. J. Teegarden, F. B. McDonald, J. H. Trainor, W. R. Webber, and E. C. Roelof. Interplanetary Mev electrons of Jovian origin. *Journal of Geophysical Research*, 79:3615, 1974. doi: 10.1029/JA079i025p03615.

M. Temmer, M. A. Reiss, L. Nikolic, S. J. Hofmeister, and A. M. Veronig. Preconditioning of Interplanetary Space Due to Transient CME Disturbances. *The Astrophysical Journal*, 835(2):141, February 2017.

A. Teufel and R. Schlickeiser. Analytic calculation of the parallel mean free path of heliospheric cosmic rays. I. Dynamical magnetic slab turbulence and random sweeping slab turbulence. *Astronomy and Astrophysics*, 393:703–715, October 2002. doi: 10.1051/0004-6361:20021046.

A. Teufel and R. Schlickeiser. Analytic calculation of the parallel mean free path of heliospheric cosmic rays. II. Dynamical magnetic slab turbulence and random sweeping slab turbulence with finite wave power at small wavenumbers. *Astronomy and Astrophysics*, 397:15–25, January 2003. doi: 10.1051/0004-6361:20021471.

J. H. Trainor, B. J. Teegarden, D. E. Stilwell, F. B. McDonald, E. C. Roelof, and W. R. Webber. Energetic Particle Population in the Jovian Magnetosphere: A Preliminary Note. *Science*, 183(4122):311–313, January 1974. doi: 10.1126/science.183.4122.311.

J. A. van Allen and L. A. Frank. Radiation Around the Earth to a Radial Distance of 107,400 km. *Nature*, 183(4659):430–434, February 1959. doi: 10.1038/183430a0.

P. A. Čerenkov. Visible Radiation Produced by Electrons Moving in a Medium with Velocities Exceeding that of Light. *Physical Review*, 52(4):378–379, August 1937. doi: 10.1103/PhysRev.52.378.

Astrid M. Veronig. Can we predict solar flares? *Science*, 369(6503):504–505, July 2020. doi: 10.1126/science.abb6150.

A. A. Vlasov. Reviews of Topical Problems: the Vibrational Properties of AN Electron Gas. *Soviet Physics Uspekhi*, 10(6):721–733, June 1968. doi: 10.1070/PU1968v010n06ABEH003709.

A. Vogt. Modellierung des einflusses korotierender wechselwirkungsregionen auf 7 mev-jupiterelektronen. *Institut für Experimentelle und Angewandte Physik, Mathematisch-Naturwissenschaftliche Fakultät*
der Christian-Albrechts-Universität zu Kiel, Master Thesis, 2013.

A. Vogt, B. Heber, P. Kuehl, A. Kopp, and R. D. Strauss. Jovian Electrons In The Inner Heliosphere: A Parameter Study On Intensity Profiles Near Earth. *Proceeding of the 34th International Cosmic Ray Conference (ICRC 2015)*, 2015.

A. Vogt, B. Heber, A. Kopp, M. S. Potgieter, and R. D. Strauss. Jovian electrons in the inner heliosphere - Proposing a new source spectrum based on 30 years of measurements. *Astronomy and Astrophysics*, 613:A28, 2018. doi: 10.1051/0004-6361/201731736.

A. Vogt, N. E. Engelbrecht, R. D. Strauss, B. Heber, A. Kopp, and K. Herbst. The residence-time of Jovian electrons in the inner heliosphere. *Astronomy and Astrophysics*, 642:A170, October 2020. doi: 10.1051/0004-6361/201936897.

A. Vogt, N. E. Engelbrecht, B. Heber, A. Kopp, and K. Herbst. Numerical and experimental evidence for a new interpretation of residence times in space. *Astronomy and Astrophysics*, under rev.

R. von Steiger, J. Geiss, and G. Gloeckler. Composition of the Solar Wind. In *Cosmic Winds and the Heliosphere*, page 581, January 1997.

B. Vršnak, T. Žic, D. Vrbanec, M. Temmer, T. Rollett, C. Möstl, A. Veronig, J. Čalogović, M. Dumbović, S. Lulić, Y. J. Moon, and A. Shanmugaraju. Propagation of Interplanetary Coronal Mass Ejections: The Drag-Based Model. *Solar Physics*, 285(1-2):295–315, July 2013. doi: 10.1007/s11207-012-0035-4.

C.-P. Wang, L. R. Lyons, T. Nagai, J. M. Weygand , and R. W. McEntire. Sources, transport, and distributions of plasma sheet ions and electrons and dependences on interplanetary parameters under northward interplanetary magnetic field. *Journal of Geophysical Research (Space Physics)*, 112(A10):A10224, October 2007. doi: 10.1029/2007JA012522.

G. M. Webb and L. J. Gleeson. Green's Theorem and Green's Functions for the Steady-State Cosmic-Ray Equation of Transport. *Astrophysics and Space Science*, 50(1):205–223, August 1977. doi: 10.1007/BF00648532.

G. M. Webb and L. J. Gleeson. On the Equation of Transport for Cosmic-Ray Particles in the Interplanetary Region. *Astrophysics and Space Science*, 60(2):335–351, February 1979. doi: 10.1007/BF00644337.

E. J. Weber and Jr. Davis, L. The Angular Momentum of the Solar Wind. *Astrophysical Journal*, 148:217–227, Apr 1967. doi: 10.1086/149138.

J. M. Weygand, W. H. Matthaeus, S. Dasso, M. G. Kivelson, L. M. Kistler, and C. Mouikis. Anisotropy of the Taylor scale and the correlation scale in plasma sheet and solar wind magnetic field fluctuations. *Journal of Geophysical Research (Space Physics)*, 114(A7): A07213, July 2009. doi: 10.1029/2008JA013766.

J. M. Weygand, W. H. Matthaeus, S. Dasso, and M. G. Kivelson. Correlation and Taylor scale variability in the interplanetary magnetic field fluctuations as a function of solar wind speed. *Journal of Geophysical Research (Space Physics)*, 116(A8):A08102, August 2011. doi: 10.1029/2011JA016621.

G. Wibberenz. Propagation of Cosmic Rays in Interplanetary Space. In Anton Bruzek and Hartmut Pilkuhn, editors, *Lectures on Space Physics 1: Cosmic Rays and Space Biophysics*, page 81, January 1973.

T. Wiengarten, J. Kleimann, H. Fichtner, R. Cameron, J. Jiang, R. Kissmann, and K. Scherer. MHD simulation of the inner-heliospheric magnetic field. *Journal of Geophysical Research (Space Physics)*, 118(1):29–44, January 2013. doi: 10.1029/2012JA018089.

T. Wiengarten, J. Kleimann, H. Fichtner, P. Kühl, A. Kopp, B. Heber, and R. Kissmann. Cosmic Ray Transport in Heliospheric Magnetic Structures. I. Modeling Background Solar Wind Using the CRONOS Magnetohydrodynamic Code. *Astrophysical Journal*, 788(1):80, June 2014. doi: 10.1088/0004-637X/788/1/80.

D. J. Williams, R. W. McEntire, S. Jaskulek, and B. Wilken. The Galileo Energetic Particles Detector. *Space Science Reviews*, 60:385–412, May 1992. doi: 10.1007/BF00216863.

R. F. Wimmer-Schweingruber, R. von Steiger, and R. Paerli. Solar wind stream interfaces in corotating interaction regions: SWICS/Ulysses results. *Journal of Geophysical Research*, 102(A8):17407–17418, August 1997. doi: 10.1029/97JA00951.

Xu Zhen-tao. The hexagram "feng" in "the book of changes" as the earliest written record of sunspot. *Chinese Astronomy*, 4(4):406, 1980. ISSN 0146-6364. doi: https://doi.org/10.1016/0146-6364(80)90034-1.

C. F. Yoder. How tidal heating in Io drives the galilean orbital resonance locks. *Nature*, 279(5716):767–770, June 1979. doi: 10.1038/279767a0.

J Yu. *Measurements of Suprathermal Particles at 1 AU and in the inner Heliosphere*. PhD thesis, Christian-Albrechts-Universität zu Kiel, 2018.

J. Yu, L. Berger, R. Wimmer-Schweingruber, P. Bochsler, B. Klecker, M. Hilchenbach, and R. Kallenbach. Suprathermal helium in corotating interaction regions: combined observations from SOHO/CELIAS/STOF and ACE/SWICS. *Astronomy and Astrophysics*, 599:A13, March 2017. doi: 10.1051/0004-6361/201628641.

M. Zhang. A Linear Relationship between the Latitude Gradient and 26 Day Recurrent Variation in the Fluxes of Galactic Cosmic Rays and Anomalous Nuclear Components. I. Observations. *Astrophysical Journal*, 488(2):841–853, October 1997. doi: 10.1086/304732.

M. Zhang. A Markov Stochastic Process Theory of Cosmic-Ray Modulation. *The Astrophysical Journal*, 513(1):409–420, March 1999.

M. Zhang, G. Qin, H. Rassoul, B. McKibben, C. Lopate, and B. Heber. Ulysses observations of Jovian relativistic electrons in the interplanetary space near Jupiter: Determination of perpendicular particle transport coefficients and their energy dependence. *Planetary and Space Science*, 55:12–20, January 2007. doi: 10.1016/j.pss.2005.11.004.

X.-J. Zhang, R. M. Thorne, Q. Ma, W. Li, B. H. Mauk, C. Paranicas, D. K. Haggerty, J. E. P. Connerney, and S. J. Bolton. Searching for low-altitude magnetic field anomalies by using observations of the energetic particle loss cone on juno. *Geophysical Research Letters*, 44(10):4472–4480, 2017. ISSN 1944-8007. doi: 10.1002/2017GL072902. 2017GL072902.

L. L. Zhao, L. Adhikari, G. P. Zank, Q. Hu, and X. S. Feng. Influence of the Solar Cycle on Turbulence Properties and Cosmic-Ray Diffusion. *Astrophysical Journal*, 856(2):94, April 2018. doi: 10.3847/1538-4357/aab362.

[toc,page]appendix pdfpages

Appendices

Chapter A

Vogt et al. (2018)

A&A 613, A28 (2018)
https://doi.org/10.1051/0004-6361/201731736

Astronomy & Astrophysics

Jovian electrons in the inner heliosphere

Proposing a new source spectrum based on 30 years of measurements

A. Vogt[1], B. Heber[1], A. Kopp[2,3], M. S. Potgieter[3], and R. D. Strauss[3]

[1] Institut für Experimentelle und Angewandte Physik, Christian-Albrechts Universität zu Kiel, Leibnizstraße 11, 24118 Kiel, Germany
e-mail: vogt@physik.uni-kiel.de
[2] Université Libre de Bruxelles, Service de Physique Statistique et des Plasmas, CP 231, 1050 Brussels, Belgium
[3] Centre for Space Research, North-West University, 2520 Potchefstroom, South Africa

Received 8 August 2017 / Accepted 20 December 2017

ABSTRACT

Context. Since the Pioneer 10 flyby of Jupiter it has become well known that electrons of Jovian origin dominate the lower MeV range of charged energetic particles in the inner heliosphere.
Aims. Because the Jovian source can be treated as point-like in numerical models, many attempts to investigate charged particle transport in the inner heliosphere have utilized Jovian electrons as test particles. The reliability of the derived parameters for convective and diffusive transport processes are therefore highly dependent on an accurate estimation of the Jovian source spectrum. In this study we aim to provide such an estimation .
Methods. In this study we have proposed a new electron source spectrum, specified at the boundary of the Jovian magnetosphere, fitted to flyby measurements by Pioneer 10 and *Ulysses*, with a spectral shape also in agreement with measurements at Earth's orbit by *Ulysses*, Voyager 1, ISEE and SOHO.
Results. The proposed spectrum is consistent with all previous theoretical suggestions, but deviates considerably in the lower MeV range which was inaccessible to those studies.

Key words. convection – astroparticle physics – Sun: heliosphere – interplanetary medium – methods: numerical – diffusion

1. Introduction

Cosmic rays (CRs), as charged particles, are continuously scattered by turbulent irregularities embedded in the heliospheric magnetic field. To correctly characterize the level of scattering, as quantified by the parallel and perpendicular diffusion coefficients (or, equivalently the corresponding mean-free-paths), still remains one of the biggest challenges in heliospheric physics. In the past, two different approaches have been followed. One approach is to specify the underlying level and structure of the turbulence and to calculate the diffusion coefficients by assuming some theoretical formulation (e.g., Engelbrecht & Burger 2013). The other, more phenomenological and practical approach, is to determine and constrain the diffusion coefficients by comparing numerical model solutions with observations, thus establishing the spatial and rigidity dependence and the magnitude of the diffusion coefficients (e.g., Zhang et al. 2007).

A frequently used test case to determine transport parameters is the propagation of Jovian electrons, where the Jovian magnetosphere can the treated as a quasi-continuously emitting point-like source (see Pyle & Simpson 1977). A first analytical model to study energetic particle propagation by means of Jovian electrons was introduced by Conlon (1978). Since then, various numerical models have been applied to study Jovian electron propagation in the inner heliosphere (see e.g., Fichtner et al. 2000; Ferreira et al. 2001; Strauss et al. 2011a, amongst others). A large uncertainty in these transport models is, however, the Jovian source function, that is, the magnitude and energy dependence of the Jovian electron distribution released from the Jovian magnetosphere. In order to produce satisfying and consistent model results, the source function must be constrained by in situ electron observations close to the Jovian magnetosphere. Previous attempts to construct a Jovian source function were at least partly based on measurements obtained at the Earth's orbit and therefore depend on transport effects. In this paper we propose a new Jovian source function which is based on spacecraft measurements obtained and published over the last 30 years. We will show that when temporal anomalies are ignored, the in situ observations of the source function by the Pioneer 10, Voyager 1 and *Ulysses* spacecraft are consistent with each other, while, when this new source function is introduced into a transport model, the resulting intensities are also consistent with various observations at the Earth's orbit.

2. The Jovian source

The first hint that Jupiter could serve as a dominant source of low-energy electrons in the inner heliosphere was given by McDonald et al. (1972) who pointed out that the characteristic ~13 month counting rate periodicities found in spacecraft data near Earth are in phase with Jupiter's synodical period. This hypothesis was confirmed by Teegarden et al. (1974), based on Pioneer 10 measurements, and since then by all spacecraft equipped with a particle detector that flew by Jupiter. The point-like nature of the Jovian source, at least on scales used for numerical simulation purposes was discovered by Pyle & Simpson (1977), who disproved the earlier hypothesis that Jovian

electrons are emitted through the planet's long magnetotail (see e.g., Pesses & Goertz 1976). Furthermore they showed via the interaction of Jovian electrons and corotating interaction regions (CIRs) that each time Pioneer 10 was magnetically connected with the Jovian source the expected electron counting rate increase appeared, concluding that the source should be more or less continuous.

Regarding the question of how electrons could be accelerated up to several MeV within the Jovian magnetosphere, the evidence that these electrons originate in the solar wind and diffuse inward (see e.g., Bolton et al. 1989), suggests an acceleration via conservation of the first and second adiabatic invariant as shown by de Pater & Goertz (1990). In situ observations by the Pioneer 11, *Galileo* and *Cassini* spacecraft (see van Allen et al. 1975; Fischer et al. 1996; Bolton et al. 2002) give a hint that additional processes such as wave particle interactions have to take place inside Jupiter's radiation belt, as discussed by Horne et al. (2008). Whether or not the findings of Simpson et al. (1992), indicating low-MeV electrons bursts with a quasi-periodicity of ~40 min throughout the dusk-side magnetosphere, are connected to these acceleration processes or even support theories of further acceleration outside the radiation belts, still needs to be clarified. Contributing to these issues, *Juno* measured MeV electrons in both the inner radiation belt and intense particle bursts at high latitudes outside the radiation belts (Becker et al. 2017), together with other observations of MeV and sub-MeV electrons in the Jovian polar region, which were detected while crossing magnetic field lines presumably mapping to the outer magnetosphere or even open field lines (see e.g., Clark et al. 2017; Zhang et al. 2017, amongst others). These findings therfore also revive the exploration of the release mechanism and contrast the findings of *Galileo* and *Cassini* which provided strong evidence that Jovian ions and electrons leak into interplanetary space despite a closed magnetic field topology, as stated by Krupp et al. (2002).

In recent years *Cassini* has also made corresponding observations within the Kronian magnetosphere, suggesting the acceleration of electrons up to relativistic and ultrarelativistic energies, as well as quasi-periodic one-hour pulsations in the outer magnetosphere according to Palmaerts et al. (2016) and Roussos et al. (2016), respectively. These findings add to the ongoing discussion whether there is a population of Kronian electrons in the inner heliossphere as stated by Lange & Fichtner (2008). An improved understanding of the Jovian source and the corresponding electron spectrum would therefore also help to distinguish between Galactic, Jovian and a possible weaker Kronian electron population.

3. Electron measurements in the inner heliosphere

A major challenge for any attempt to study Jovian electrons is the limited amount of in situ observations of low energy electrons near the Jovian magnetosphere. For this reason, this study combines electron spectra obtained by several spacecraft missions since 1973, both at the Earth's orbit and near to the Jovian magnetosphere. Thereby the flyby spectra were used to derive our proposed source spectrum, while the Earth orbit spectra were taken into account to check the consistency. These observations as listed in Table 1 are briefly discussed below.

3.1. Flyby observations

Figure 1 shows energy spectra obtained outside of Jupiter's magnetosphere during the Pioneer 10 and *Ulysses* flybys (for details, see Table 1). The COsmic and Solar Particle INvestigation Kiel Electron Telescope (COSPIN-KET) on board *Ulysses* measured electron counting rates in three energy channels during the entire mission from October 1990 until June 2009. Using a detailed data analysis utilizing GEANT 3 simulations Heber et al. (2005) could provide two electron spectra: one measured in the early cruise phase still near Earth's orbit and a second one capturing the electron fluxes during the first Jupiter encounter in February 1992. Both COSPIN-KET spectra are consistent with spectra obtained by the Voyager 1 BSe detector, for equivalent energies both at the Earth and for the Jupiter encounter in 1977. These observations were made available to Nndanganeni (2015), through private communication between W. R. Webber and M. S. Potgieter, but are otherwise not yet published. Therefore, the BSe spectra were only taken into account for comparison to and evaluation of COSPIN-KET data.

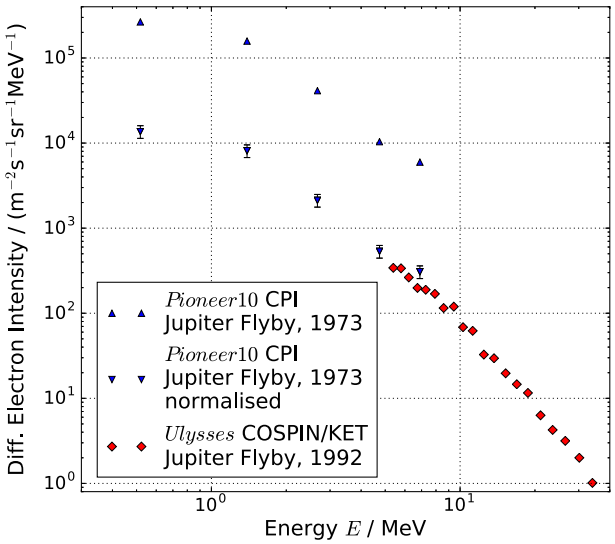

Fig. 1. Electron energy spectra measured by Pioneer 10 and *Ulysses* KET. The Pioneer 10 spectrum is shown both with and without the renormalization illustrated in Fig. 2 and described in Sect. 3.1.

While the COSPIN-KET and BSe data are found to be consistent with each other, the Pioneer 10 spectrum differs by a factor of more than one order of magnitude. Teegarden et al. (1974) determined their energy spectrum from measurements obtained on 11 May 1973, a day with extraordinary high fluxes. Due to statistical measures, this spectrum as shown in Fig. 1 and another one based on measurements inside the outer Jovian magnetosphere, were the only electron spectra published by the Pioneer 10 CPI team. No spectra covering the quiet times while Pioneer 10 was approaching and/or leaving Jupiter are available. The reason for this observation of high electron fluxes which made it possible to obtain a statistically trustworthy spectrum, lies in the occurrence of a so-called Jovian electron jet, a phenomena discovered first in the data of the *Ulysses* spacecraft (Ferrando et al. 1993) and later also during the Pioneer 10 period (Dunzlaff et al. 2009): such electron events can be identified as Jovian jets by three matching criteria. A short-duration increase in the electron flux is observed together with a significant anisotropy and a local interplanetary magnetic field aligned to the direction toward Jupiter. Furthermore, the spectral slope is the same as the one observed inside the Jovian magnetosphere. Due to this same spectral slope despite varying intensities, the spectral slope of Jovian jets is also believed

Table 1. Overview of the electron spectra used in this study.

Location of observation	Spacecraft mission/instrument	Source
Flyby spectra	Pioneer 10 Charged Particle Instrument (CPI)	Teegarden et al. (1974)
	Ulysses Kiel Electron Telescope (KET)	Heber et al. (2005)
Earth orbit spectra	SOHO/EPHIN	Kühl et al. (2013)
	Ulysses Kiel Electron Telescope (KET)	Heber et al. (2005)
	ISEE 3 (ICE) Chicago electron spectrometer	Moses (1987)

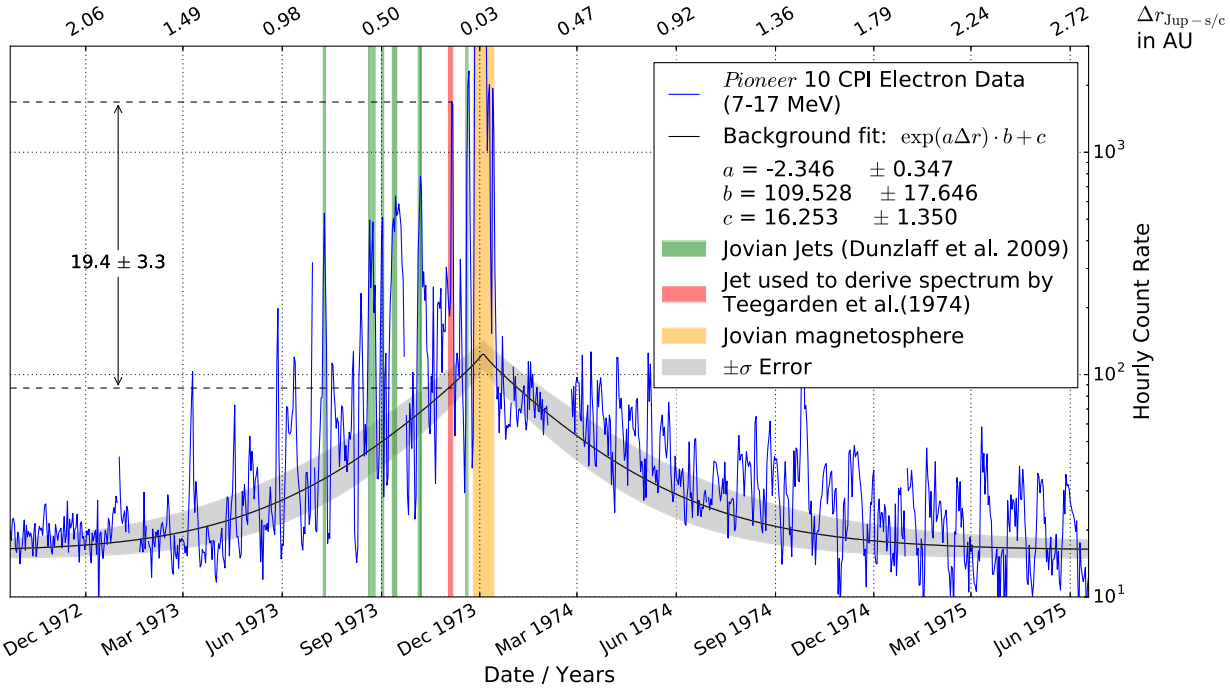

Fig. 2. Pioneer 10's CPI counting rates of the 7–17 MeV electron channel (blue), are displayed together with the result of an exponential background fit (black with a gray shaded region showing a 1 σ uncertainty). In order to estimate the increase of the electron flux in the Jovian jet used to determine the Pioneer spectrum by Teegarden et al. (1974; shaded in red) all other jets identified by Dunzlaff et al. (2009; green) were also excluded from the background, along with the fluxes obtained inside the Jovian magnetosphere (orange).

to be similar to the quiet time Jovian population's without significant effects of the possibly different release mechanisms. This assumption of Ferrando et al. (1993) is supported by the agreement with the COSPIN-KET data in the energy range covered by both spacecraft, as well as by our check for consistency with Earth-orbit observations in Sect. 5. Because the electron event, which Teegarden et al. (1974) used to obtain their source spectrum, is actually included in the list of electron jets by Dunzlaff et al. (2009), it can be normalized to the quiet-time background flux to be used in a meaningful manner.

Figure 2 shows the daily Pioneer 10 electron fluxes measured by the Charged Particle Instrument (CPI)[1] together with the result of an exponential background fit (black with a gray shaded region showing a 1 σ uncerntainty). In order to estimate the increase of the electron flux in the Jovian jet used to determine the Pioneer spectrum by Teegarden et al. (1974) all other jets identified by Dunzlaff et al. (2009) were also excluded from the background, along with the fluxes obtained inside the Jovian magnetosphere. The comparison between the measured flux and the fitted background gives a hint that the intensity of the Pioneer 10 spectrum has to be renormalized and reduced by a factor of about 20, which agrees quite well with the *Ulysses* COSPIN-KET spectrum as shown in the lower panel of Fig. 1. The $\pm\sigma$ uncertainty was computed by multiplying the Jacobian matrix with the residual variances, estimated by the mean square errors, according to the documentation of the fitting routine[2]. The resulting covariance matrix has been used to derive the standard error and therefore the $\pm\sigma$ uncertainty. Applying this renormalization factor to the Teegarden et al. (1974) data leads to a convincing agreement between the Pioneer 10, *Ulysses* and Voyager data (not shown here) as displayed in Fig. 1.These consistent observations can now be used to derive a Jovian source function, as it is shown by the fit in Fig. 3. Because of their spatial and temporal constraints, Jovian jets are not likely to influence the strength of the Jovian source. Temporal varitions due to the passing of a jet are only to expected inside a radius of ~0.8 AU around Jupiter, further inside the interplanetary space jets have not been detected yet.

[1] Taken from: ftp://spdf.gsfc.nasa.gov/pub/data/pioneer/pioneer10/particle/cpi/ip_1day_ascii/p10cpi.h24

[2] Provided at https://docs.scipy.org/doc/scipy-0.19.0/reference/generated/scipy.optimize.leastsq.html

Although three other spacecraft visited the Jovian magnetosphere in recent years, namely *Galileo*, *Cassini* and *Juno*, no flyby spectra suitable for this study have been published yet. Considering the instrumentation of all three missions, the energetic particle detector (EPD) onboard *Galileo* (see Williams et al. 1992), the Low Energy Magnetospheric Measurement System (LEMMS) onboard *Cassini* (see Krimigis et al. 2004; Haggerty & Livi 2004) as well as Juno's Jupiter Energetic particle Detector Instrument (JEDI) discussed by Mauk et al. (2013), the energy range of interest seems to be well covered. Observations inside the Jovian and Kronian magnetosphere, respectively, as briefly discussed in Sect. 2 suggest also the possibility of deriving such electron spectra close to but not inside the Jovian magnetosphere. Regarding the well known difficulties obtaining such spectra due to the complexity of the corresponding response function, as detailed in Heber et al. (2005) and Kühl et al. (2013), amongst others, deriving these spectra from the published counting rates is beyond the scope of this study. Nevertheless any flyby spectrum of *Galileo*, *Cassini* or *Juno* would contribute to constrain the Jovian source spectrum further in this energy range.

3.2. Observations at Earth's orbit

Although commonly used in studies on this subject, electron spectra at the Earth's orbit will not be used in this study to obtain a Jovian source spectrum. The more detailed measurements at 1 AU are however important in order to validate our findings.

In addition to the already mentioned *Ulysses* COSPIN-KET and Voyager 1 BSe data, the electron spectral data of SOHO-SEPT cover roughly the same energy range in more detail as the flyby data by Pioneer 10. As described by Kühl et al. (2013) two electron spectra were derived from SOHO-EPHIN (Müller-Mellin et al. 1995) data to investigate the effect of parallel and perpendicular diffusive transport on Jovian electron fluxes. In our work, we chose the spectrum which corresponds to time periods of undisturbed magnetospheric conditions between Jupiter and the spacecraft, as well as an (assumed) magnetic connection. Therefore, it is reasonable to neglect perpendicular diffusion in order to compare the spectrum to the flyby spectra in the relevant energy range. This reduces the probability that other effects, apart from adiabatic deceleration (energy loses), influence the spectral shape and intensity.

The same decision to take only data of best magnetic connectivity into account was made for the electron spectra derived by Moses (1987) from the data obtained by the Chicago electron spectrometer on board ISEE 3 (ICE). The data set used for our validation in Sect. 5 consists of six energy spectra obtained between 1978 and 1984 in time intervals with a period (length) up to 200 days when ISEE 3 was believed to be magnetically connected with the Jovian source

- 1978 November 4 to 1979 April 10;
- 1979 September 7 to 1980 April 9;
- 1980 October 26 to 1981 April 20;
- 1981 October 27 to 1982 June 19;
- 1982 November 28 to 1983 may 20;
- 1983 December 6 to 1984 July 18.

The variations in the different energy channels are due to the long averaging periods in connection with the variability of both the connectivity and the solar activity during that time, although flares identified by IMP 8 were excluded. In contrast to previous studies on Jovian electrons observed at Earth, the data product derived from these six previously discussed spectra (which was an assumption of the source itself) was disregarded in favor of the original data as shown in Fig. 8. of Moses (1987). We will revisit this matter in Sect. 5 when discussing previous attempts to estimate the Jovian source spectrum.

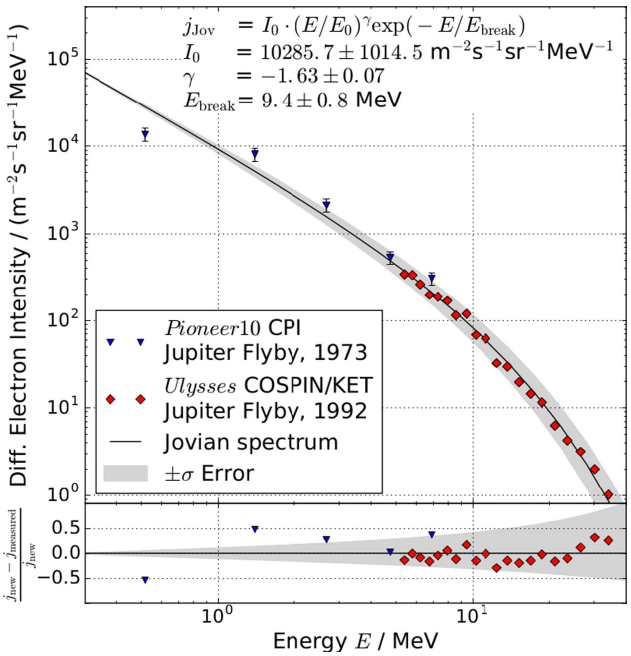

Fig. 3. Proposed new Jovian spectrum according to Eq. (11) together with the Pioneer 10 CPI and *Ulysses* COSPIN-KET data. The $\pm\sigma$ uncertainty has been derived by the same method as detailed in Fig. 2.

4. The new source spectrum

A first attempt to estimate a Jovian source spectrum was made by Teegarden et al. (1974) who suggested a power law with an exponent of about −1.5, in terms of kinetic energy, based on their own Pioneer 10 data, as shown in Fig. 1, and the findings of McDonald et al. (1972) who analyzed electron spectra at the Earth's orbit. This first, mostly qualitative suggestion

$$j(E) \propto \left(\frac{E}{E_0}\right)^{-1.5}, \tag{1}$$

normalized to $E_0 = 1$ MeV, was expanded by Baker & van Allen (1976) by adding a second power law for the steepening of the spectrum at higher energies. These two approaches were elaborated on as more data became available. In the following we present a selection of the most significant suggestions based mainly on these two assumptions before discussing the reasons that lead us to propose a new Jovian spectrum with a different mathematical expression.

Following the initial approach by Teegarden et al. (1974), Eraker (1982) presented a first quantitative analysis of the Jovian source and concluded the source function as

$$J(E) = 3\,10^{25}\left(\frac{E}{E_0}\right)^{-1.7}, \tag{2}$$

in units of electrons s^{-1} MeV^{-1} , taking into account the data of Pioneer 10, IMP 8 and *Mariner 10* as well as the results of the first Jovian electron propagation model developed by Conlon (1978). This work was continued by Lopate (1991), who investigated the spectral index during the whole Pioneer 10 mission up

to 1991 and found that the ratio between the 27-day averages of 2–7 MeV and 7–17 MeV electrons was quite stable during the flight, and showed only minor fluctuations with a slight decrease during the 1987 solar minimum period when the spacecraft was already at a radial distance of 40 AU.

Also relying on Pioneer 10 and IMP 8, but regarding Pioneer 8/9 data as well, Haasbroek et al. (1997) specified the approach of Baker & van Allen (1976) quantitatively and concluded

$$j(E) = c \left(\frac{E}{E_0} \right)^{-1.5} \left(1 + \frac{E}{5\,E_0} \right)^{-3.5}, \tag{3}$$

again with $E_0 = 1$ MeV and in units of electrons m^{-2} s^{-1} sr^{-1} MeV^{-1} to simulate the Jovian electron contribution on electron counting rates throughout the heliosphere. The normalization factor c was obtained via the Jovian electron data of Pioneer 10 and ISEE 3 and given indirectly by referring to corresponding measurements. Reconstruction this normalization suggest that $c = 4 \cdot 10^4$, the value which was used to compare the spectrum in Fig. 4, provides the least deviation to the data the spectrum is based on.

Also, based on the spectral shape concluded according to the ISEE 3 data by Moses (1987) and the flyby data of the Pioneer 10 mission, Ferreira et al. (2001) expanded this approach of utilizing a soft and a hard power law to describe the Jovian source function, as displayed in Fig. 4 by the orange line. In addition to the first power law which is in agreement with the previous suggestions

$$j(E)_{1.5} = 5 \cdot 10^3 \left(\frac{E}{E_0} \right)^{-1.5}, \tag{4}$$

with

$$E_0 = 1 \text{ GeV}, \tag{5}$$

the second power law added to cover the steepening at higher energies was much harder than the earlier approach by Haasbroek et al. (1997):

$$j(E)_{6.0} = 10^9 \left(\frac{E}{E_0} \right)^{-6.0} \tag{6}$$

matching the normalized ISEE 3 (ICE) spectral data by Moses (1987), mentioned in Sect. 3.2. These two power laws are combined in a spectral function as

$$j(E)_{\text{Jovian}} = 1.5 \left(\frac{c_k \cdot j_{1.5} \cdot d_k \cdot j_{6.0}}{c_k \cdot j_{1.5} + d_k \cdot j_{6.0}} \right), \tag{7}$$

again in units of electrons m^{-2} s^{-1} sr^{-1} MeV^{-1} and with the fitting parameters

$$c_k = 0.6, \tag{8}$$

and

$$d_k = 5.0. \tag{9}$$

The Jovian source spectrum by Ferreira et al. (2001) was used in several numerical modeling studies in the subsequent years, covering many aspects and issues of charged particle physics in the inner heliosphere. See for example, Ferreira & Potgieter (2002); Ferreira et al. (2003) and the review by Ferreira (2005).

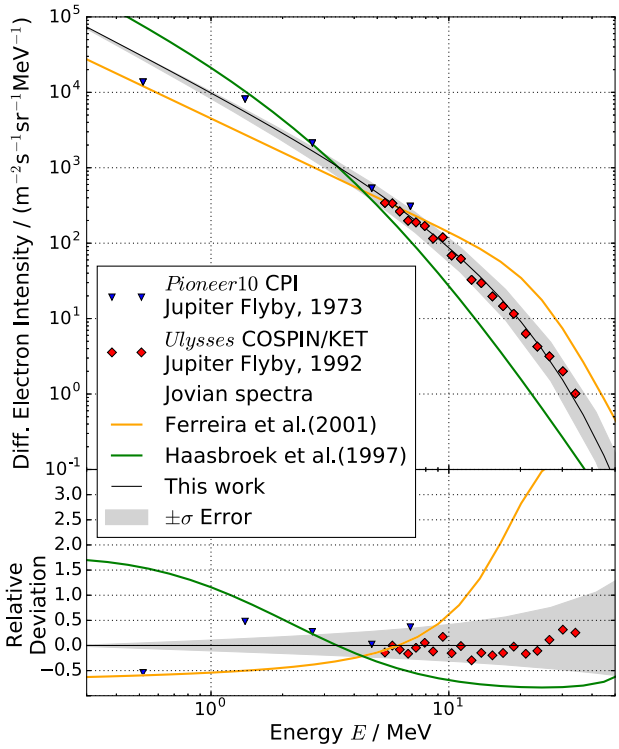

Fig. 4. New source spectrum alongside that by Ferreira et al. (2001) in orange and the suggestion by Haasbroek et al. (1997; green) as discussed in Sect. 4. In the *upper panel* all three spectra are shown alongside the Jovian flyby data and the 1 σ error region surrounding our estimation. The *lower panel* shows the relative deviation of the estimations, calculated as $(j_{\text{previous}} - j_{\text{new}})/j_{\text{new}}$. Especially in the energy range above $E_{\text{break}} = 9.4$ MeV the *lower panel* shows how the deviation increases up to over 100% and even far more for the spectrum by Ferreira et al. (2001).

However, with more and more electron data made available, it has become an important and relevant task to revisit the question whether the source function could be simply updated or if it would be possible and necessary to establish a new one. A main scientific goal to understand cosmic ray modulation and transport has been to establish a local interstellar spectrum (LIS) and compare its shape with the corresponding particle spectrum measured in the inner heliosphere. In order to do so, it is necessary to distinguish between the Jovian and the Galactic components but with new computations of the electron LIS by Potgieter & Nndanganeni (2013), Potgieter et al. (2015), Bisschoff & Potgieter (2014) and Potgieter & Vos (2017), see also the overview by Potgieter (2014), based on measurements by Voyager 1 in the very local interstellar medium, the suspicion raised that the Jovian source spectrum overestimated the amount of electrons in the low-MeV range; see for example, the discussion by Nndanganeni & Potgieter (2016). Also the data from the *Ulysses* flyby and the knowledge of the Voyager BSe spectral data suggested that the spectrum had to be corrected to cover the spectral shape in that same energy range correctly.

Therefore, the decision was made to combine the most significant measurements of electron spectra in the Jovian electron energy range, both at Jupiter and at the Earth's orbit, as listed in Table 1 and as discussed before. In order to make our result self consistent the flyby spectra were used to obtain the spectral shape and the quantitative fit, while the Earth orbit data provided the possibility of a fully independent check for consistency check at 1 AU.

Regarding the general shape we follow neither of the introduced approaches but the combination of a power-law with an exponential cut-off

$$j(E)_{\rm jov} \propto \left(\frac{E}{E_0}\right)^{\gamma} {\rm e}^{-E/E_{\rm break}}, \tag{10}$$

as particle acceleration theory suggests; see for example, the discussion of diffusive shock acceleration by Prinsloo et al. (2017).

This approach, again normalized with $E_0 = 1$ MeV was fitted via the least-square method taking only the flyby data of Pioneer 10 CPI and *Ulysses* COSPIN-KET into account. The result is displayed in Fig. 3 together with the detailed uncertainties of the fit and in Fig. 4 compared with the estimates of Eqs. (3) and (7) and has the following mathematical expression for the Jovian source function:

$$j(E)_{\rm jov} = 1.029 \cdot 10^4 \left(\frac{E}{E_0}\right)^{-1.63} {\rm e}^{-E/E_{\rm break}}, \tag{11}$$

with

$$E_{\rm break} = 9.4 \text{ MeV}. \tag{12}$$

5. Discussion

In order to check for consistency, we simulated the resulting electron fluxes at the Earth orbit for times with the best magnetic connection and compared them to the corresponding spacecraft data as listed in Table 1. The result is shown in Fig. 5 together with the source spectrum and the flyby data. For our simulation we used the stochastic differential equation method as described in detail by Kopp et al. (2012). The numerical model by Dunzlaff et al. (2015), used in this study, implements the parallel mean free path

$$\lambda_{\parallel}(r) = \frac{\lambda_0}{2}\left(1 + \frac{r}{r_0}\right), \tag{13}$$

depending on a mean free path λ_0 at a point of reference r_0, which is in this case the Earth orbit at 1 AU. The parallel mean free and the particle's speed v then scale the parallel diffusion coefficient as

$$\kappa_{\parallel}(r) = \frac{v\lambda_{\parallel}(r)}{3}, \tag{14}$$

and the perpendicular diffusion coefficient via the proportional factor χ

$$\kappa_{\perp}(r) = \chi\kappa_{\parallel}(r). \tag{15}$$

As input parameters we choose a constant value for the solar wind speed of $u_{SW} = 400$ km S^{-1} and a ratio between the parallel and perpendicular diffusion coefficient of $\kappa_{\parallel}/\kappa_{\perp} = 0.02$, The value for the parallel mean free path at 1 AU was set to $\lambda_0 = 0.1$ AU, as suggested theoretically by Palmer (1982) and implemented successfully by Strauss et al. (2011b) in a comparable model setup. Despite the necessity that future work has to further investigate the chosen transport parameters with a more elaborated approach, the simulated electron spectrum at the Earth's orbit confirms that the proposed source spectrum can reproduce the observed data.

Comparing our proposed expression for the Jovian source function qualitatively with the previous suggestions, as shown in Fig. 4, our value for the exponent $\gamma = -1.63$ ranges in between the values given in Eq. (2) by Eraker (1982) and Eq. (3) by Haasbroek et al. (1997) or Eq. (7) by Ferreira et al. (2001), respectively. In contrast to the approach in Eq. (7), where the softening of the spectrum is treated by an additional power with exponents of -3.5 or -6 in the second case, applying an exponential cut-off creates a much smoother transition between the harder and softer ranges of the spectrum. The even smoother spectral shape given by Haasbroek et al. (1997) in Eq. (3) seems to be too steep in the lower energy range and to flat in the higher energy range.

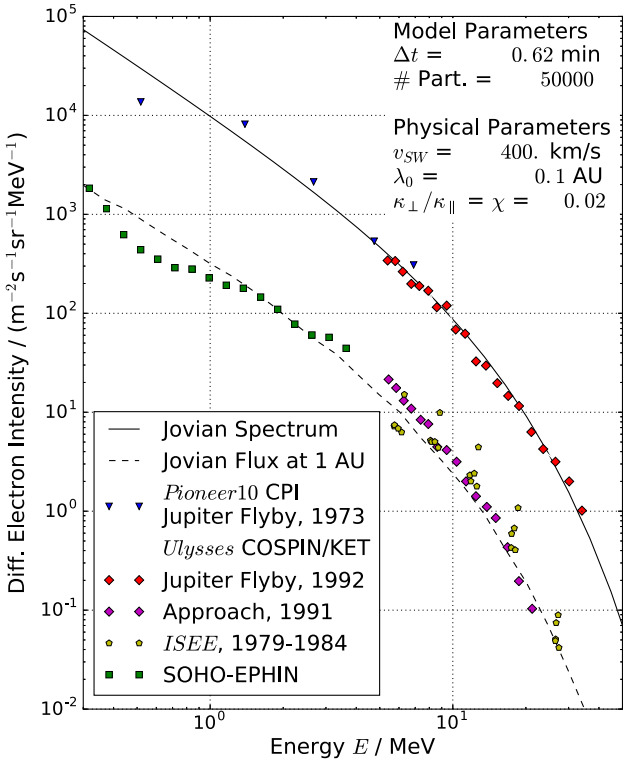

Fig. 5. New Jovian source spectrum (solid line) and the corresponding simulated intensities at the Earth's orbit (dashed line) at times of good magnetic connectivity to the source. Additional to the flyby spectra obtained by Pioneer 10 CPI and *Ulysses* COSPIN-KET which were introduced to derive the source, here also the spectral data by SOHO-EPHIN (green), ISEE 3 (yellow), and the *Ulysses* COSPIN-KET (violet) data measured shortly after the launch are displayed, as documented in Table 1. While the SOHO-EPHIN spectrum is sampled over several time periods of good magnetic connectivity with the source, due to reasons explained in Sect. 3.2 the spectra obtained by ISEE 3 have to be included separately.

Furthermore the value of $\gamma = -1.63$ for the exponent in our findings contribute to the discussion about a common acceleration process throughout the heliosphere as introduced by Fisk & Gloeckler (2014). By that means the newly established source function provides a benchmark to study and explain electron acceleration, being more consistent with contemporary theory, if one would not assume two equally effective acceleration processes within the Jovian magnetosphere to create the spectral overlap.

The quantitative comparison with the older estimates, especially with the spectrum proposed by Ferreira et al. (2001) in Fig. 4, shows that the new source function gives higher electron intensities in the lower energy range of the spectrum, up to one or two MeV. This can easily be explained by the fact that up to our renormalization of the Pioneer 10 CPI data no reliable

flyby measurements were available in that spectral range. Also, the SOHO-EPHIN data at the corresponding energy range show an unexplained spectral break at 0.5 MeV, which either could be caused by instrumental effects or even a different energy dependence of the electron mean free path in this energy range, as stated by Kühl et al. (2013). To avoid assumptions which are not clearly supported by statistical evidence, the functional form was limited to the chosen approach. Due to the poor data coverage at the Jovian magnetosphere and the uncertainties of the Earth orbit data, the keV and low MeV range therefore has to be treated carefully, until further flyby measurements become available, as already discussed in Sect. 3.1. Despite these concerns, the convincing consistency check and the fact, that the break energy $E_{\mathrm{break}} = 9.4$ MeV is located in an well covered energy range, both suggest that only minor changes are to be expected regarding the intensity or the exponent $\gamma = -1.63$.

Therefore, in the spectral range above 4–5 MeV, we expect lower fluxes than previously thought, as supported by the *Ulysses* COSPIN-KET flyby data, which also were not available at the times the older estimates were published. In this energy range, especially of 30–50 MeV, the second power law of the Ferreira et al. (2001) approach would give an overestimation of electrons up to 60% and even more. In particular, the second panel of Fig. 4 illustrates these differences, caused by the different data sets used to constrain the spectra. As briefly mentioned in Sect. 3.2 we did not consider the final data product of Moses (1987), on which Ferreira et al. (2001) based their assumption in the low MeV range, in favor of the uncorrected spectra. The deviation of this finally published spectrum to the corresponding data obtained by *Ulysses* COSPIN-KET and Voyager 1 BSe becomes reasonable considering that and how Moses (1987) estimated the Jovian source spectrum. The Moses (1987) data was corrected in both absolute intensity and spectral shape, due to the estimation of a dominant solar component and the results of Monte Carlo transport simulations with a strong influence of adiabatic deceleration. An inspection of current approximations of adiabatic energy changes, following the suggestion of Fichtner et al. (2000), indicate that significant changes in the spectral shape are expected at much higher energies, casting doubt on this approach. Furthermore, with the spectral data of *Ulysses* COSPIN-KET and Voyager 1 BSe, flyby measurements became available, which are by definition independent of any assumptions on particle transport.

Taking into account that the most prominent deviations from previous works, both in shape and intensity, are located in the MeV range suggests to revisit past simulations concerning Jovian electrons, because mostly MeV electron counting rates were used for evaluation. Normalizing the simulation results by an overestimated source intensity thereby would have lead to correspondingly higher fluxes. Concluding that past simulations which seemed to match the measured counting rates could have actually produced fluxes lower than observed, one would expect that the transport parameters have to be changed in order to allow a more efficient transport to reproduce the measurements.

Another consequence could be that estimates on the ratio between the Galactic and the Jovian contribution to electron fluxes at the Earth (see e.g., Strauss et al. 2013) would have to be reconsidered based on the effects the new source function has on the computer modeled Jovian electron intensities.

6. Conclusion

In contrast to previous attempts the newly developed Jovian source function as formulated in Eq. (11) is derived only from flyby data without taking Earth orbit measurements into account. Because our new source spectrum is essentially independent on any assumptions regarding charged particle transport, Jovian electron simulations based on our source spectrum can be considered more self-consistent than was possible before. The consistency check shown in Fig. 5 suggests that more elaborated model set-ups and parameter studies can reproduce the measurements at Earth orbit as listed for the spectral data in Table 1 with more accuracy and reliability.

Looking at the theoretical implications of our findings, the new source spectrum agrees with the assumptions about charged particle acceleration theory. Therefore we could provide an orientation for investigations focused on the acceleration and transport processes inside the Jovian magnetosphere (as referred to briefly in Sect. 2) to constrain their models to a comparable spectral slope and intensity outside the magnetosphere or inside a Jovian jet.

Another possible outcome for related research fields is to address the efficiency of perpendicular diffusion with respect to field line random walk. Because the continuous outflow is assumed as perpendicular diffusion through a closed field line topology (see Krupp et al. 2002), comparing the background of Jovian electrons to the peak intensities during Jovian jets which are magnetically connected to the Jovian magnetosphere would provide an estimate.

Most importantly, the new Jovian source spectrum established in this work allows future studies to investigate charged particle transport and all it's intricate effects with much improved reliability. In particular, the ratio of Galactic to Jovian electron intensities in the inner heliosphere below about 50 MeV can now be done more convincingly so that a better estimate of how many low-energy Galactic cosmic ray electrons actually reach the Earth is possible, as discussed in Sect. 5. Also the influence of the latitudinal transition between fast and slow solar wind and the different propagation conditions during solar minima and maxima could be revisited. By continuing the investigations of investigations as done by Moeketsi et al. (2005), modeling the low MeV electron counting rates obtained by *Ulysses* COSPIN-KET addresses both the efficiency of perpendicular diffusion up to the polar regions and the effects of the changing solar wind speed on particle transport.

Regarding the influence of the source function, not only on computed intensities, but also on the estimated propagation time as shown in Vogt et al. (2015), it seems promising that after more than 30 years of measurements the investigation of Jovian electron transport can still lead to new insights on the propagation of low-energy electron in the heliosphere.

Acknowledgements. The work was partly carried out within the framework of the bilateral BMBF-NRF-project "Astrohel" (01DG15009) as supported by the Bundesministerium für Bildung und Forschung (BMBF) and the South African National Research Foundation (NRF), grant UID93132.

References

Baker, D. N., & van Allen, J. A. 1976, J. Geophys. Res., 81, 617
Becker, H. N., Santos-Costa, D., Jørgensen, J. L., et al. 2017, Geophys. Res. Lett., 44, 4481
Bisschoff, D., & Potgieter, M. S. 2014, ApJ, 794, 166
Bolton, S. J., Gulkis, S., Klein, M. J., de Pater, I., & Thompson, T. J. 1989, J. Geophys. Res., 94, 121
Bolton, S. J., Janssen, M., Thorne, R., et al. 2002, Nature, 415, 987
Clark, G., Mauk, B. H., Paranicas, C., et al. 2017, Geophys. Res. Lett., 44, 4419
Conlon, T. F. 1978, J. Geophys. Res., 83, 541
de Pater, I., & Goertz, C. K. 1990, J. Geophys. Res., 95, 39

Dunzlaff, P., Kopp, A., Heber, B., & Sternal, O. 2009, Proc. 31st Int. Cosmic Ray Conf.
Dunzlaff, P., Strauss, R. D., & Potgieter, M. S. 2015, Comput. Phys. Commun., 192, 156
Engelbrecht, N. E., & Burger, R. A. 2013, ApJ, 772, 46
Eraker, J. H. 1982, ApJ, 257, 862
Ferrando, P., Ducros, R., Rastoin, C., & Raviart, A. 1993, Planet. Space Sci., 41, 839
Ferreira, S. E. S. 2005, Adv. Space Res., 35, 586
Ferreira, S. E. S., & Potgieter, M. S. 2002, J. Geophys. Res. (Space Phys.), 107, 1221
Ferreira, S. E. S., Potgieter, M. S., Burger, R. A., Heber, B., & Fichtner, H. 2001, J. Geophys. Res., 106, 24979
Ferreira, S. E. S., Potgieter, M. S., Moeketsi, D. M., Heber, B., & Fichtner, H. 2003, ApJ, 594, 552
Fichtner, H., Potgieter, M., Ferreira, S., & Burger, A. 2000, Geophys. Res. Lett., 27, 1611
Fischer, H. M., Pehlke, E., Wibberenz, G., Lanzerotti, L. J., & Mihalov, J. D. 1996, Science, 272, 856
Fisk, L. A., & Gloeckler, G. 2014, J. Geophys. Res. (Space Phys.), 119, 8733
Haasbroek, L. J., Potgieter, M. S., & Le Roux, J. A. 1997, Adv. Space Res., 19, 953
Haggerty, D. K., & Livi, S. 2004, Adv. Space Res., 33, 2303
Heber, B., Kopp, A., Fichtner, H., & Ferreira, S. E. S. 2005, Adv. Space Res., 35, 605
Horne, R. B., Thorne, R. M., Glauert, S. A., et al. 2008, Nat. Phys., 4, 301
Kopp, A., Büsching, I., Strauss, R. D., & Potgieter, M. S. 2012, Comput. Phys. Commun., 183, 530
Krimigis, S. M., Mitchell, D. G., Hamilton, D. C., et al. 2004, Space Sci. Rev., 114, 233
Krupp, N., Woch, J., Lagg, A., et al. 2002, Geophys. Res. Lett., 29, 1736
Kühl, P., Dresing, N., Dunzlaff, P., et al. 2013, Proc. 33rd Int. Cosmic Ray Conf.
Lange, D., & Fichtner, H. 2008, A&A, 482, 973
Lopate, C. 1991, Proc. 22th Int. Cosmic Ray Conf.
Mauk, B. H., Haggerty, D. K., Jaskulek, S. E., et al. 2013, Space Sci. Rev.
McDonald, F. B., Cline, T. L., & Simnett, G. M. 1972, J. Geophys. Res., 77, 2213
Moeketsi, D. M., Potgieter, M. S., Ferreira, S. E. S., et al. 2005, Adv. Space Res., 35, 597
Moses, D. 1987, Astrophys. J., Part 1, 313, 471
Müller-Mellin, R., Kunow, H., Fleißner, V., et al. 1995, Solar Phys., 162, 483
Nndanganeni, R. R. 2015, PhD thesis, North-West University, South Africa
Nndanganeni, R. R., & Potgieter, M. S. 2016, Adv. Space Res., 58, 453
Palmaerts, B., Roussos, E., Krupp, N., et al. 2016, Icarus, 271, 1
Palmer, I. D. 1982, Rev. Geophys. Space Phys., 20, 335
Pesses, M. E., & Goertz, C. K. 1976, Geophys. Res. Lett., 3, 228
Potgieter, M. S. 2014, Braz. J. Phys., 44, 581
Potgieter, M. S., & Nndanganeni, R. R. 2013, Astrophys. Space Sci., 345, 33
Potgieter, M. S., & Vos, E. E. 2017, A&A, 601, A23
Potgieter, M. S., Vos, E. E., Munini, R., Boezio, M., & Di Felice, V. 2015, ApJ, 810, 141
Prinsloo, P. L., Potgieter, M. S., & Strauss, R. D. 2017, ApJ, 836, 100
Pyle, K. R., & Simpson, J. A. 1977, AJ, 215, L89
Roussos, E., Krupp, N., Mitchell, D. G., et al. 2016, Icarus, 263, 101
Simpson, J. A., Anglin, J. D., Balogh, A., et al. 1992, Science, 257, 1543
Strauss, R. D., Potgieter, M. S., Büsching, I., & Kopp, A. 2011a, ApJ, 735, 83
Strauss, R. D., Potgieter, M. S., Kopp, A., & Büsching, I. 2011b, J. Geophys. Res. (Space Phys.), 116, A12105
Strauss, R. D., Potgieter, M. S., & Ferreira, S. E. S. 2013, Adv. Space Res., 51, 339
Teegarden, B. J., McDonald, F. B., Trainor, J. H., Webber, W. R., & Roelof, E. C. 1974, J. Geophys. Res., 79, 3615
van Allen, J. A., Randall, B. A., Baker, D. N., et al. 1975, Science, 188, 459
Vogt, A., Heber, B., Kuehl, P., Kopp, A., & Strauss, R. D. 2015, Proc. 34th Int. Cosmic Ray Conf.
Williams, D. J., McEntire, R. W., Jaskulek, S., & Wilken, B. 1992, Space Sci. Rev., 60, 385
Zhang, M., Qin, G., Rassoul, H., et al. 2007, Planet. Space Sci., 55, 12
Zhang, X.-J., Thorne, R. M., Ma, Q., et al. 2017, Geophys. Res. Lett., 44, 4472

Chapter B

Vogt et al. (2020)

A&A 642, A170 (2020)
https://doi.org/10.1051/0004-6361/201936897

Astronomy & Astrophysics

The residence-time of Jovian electrons in the inner heliosphere

A. Vogt[1], N. E. Engelbrecht[2], R. D. Strauss[2], B. Heber[1], A. Kopp[2,3], and K. Herbst[1]

[1] Institut für Experimentelle und Angewandte Physik, Christian-Albrechts Universität zu Kiel, Leibnizstraße 11, 24118 Kiel, Germany
e-mail: vogt@physik.uni-kiel.de
[2] Centre for Space Research, North-West University, 2520 Potchefstroom, South Africa
[3] Theoretische Physik IV, Ruhr-Universität Bochum, Universitätsstr. 150, 44801 Bochum, Germany

Received 11 October 2019 / Accepted 21 May 2020

ABSTRACT

Context. Jovian electrons serve an important role in test-particle distribution in the inner heliosphere. They have been used extensively in the past to study the (diffusive) transport of cosmic rays in the inner heliosphere. With new limits on the Jovian source function, that is, the particle intensity just outside the Jovian magnetosphere, and a new set of in-situ observations at 1 AU for cases of both good and poor magnetic connection between the source and observer, we revisit some of these earlier simulations.
Aims. We aim to find the optimal numerical set-up that can be used to simulate the propagation of 6 MeV Jovian electrons in the inner heliosphere. Using such a setup, we further aim to study the residence (propagation) times of these particles for different levels of magnetic connection between Jupiter and an observer at Earth (1 AU).
Methods. Using an advanced Jovian electron propagation model based on the stochastic differential equation approach, we calculated the Jovian electron intensity for different model parameters. A comparison with observations leads to an optimal numerical setup, which was then used to calculate the so-called residence (propagation) times of these particles.
Results. Through a comparison with in-situ observations, we were able to derive transport parameters that are appropriate for the study of the propagation of 6 MeV Jovian electrons in the inner heliosphere. Moreover, using these values, we show that the method of calculating the residence time applied in the existing literature is not suited to being interpreted as the propagation time of physical particles. This is due to an incorrect weighting of the probability distribution. We applied a new method, where the results from each pseudo-particle are weighted by its resulting phase-space density (i.e. the number of physical particles that it represents). We thereby obtained more reliable estimates for the propagation time.

Key words. methods: numerical – Sun: heliosphere – diffusion – interplanetary medium – astroparticle physics – turbulence

1. Introduction

Over the last decade, solving particle transport equations by means of stochastic differential equations (SDEs) has become an increasingly popular tool due to increasing computational power. Whereas many of these studies are focused on galactic cosmic rays (GCRs), this work builds upon recent research regarding Jovian electrons (see Vogt et al. 2018; Nndanganeni & Potgieter 2018, and references therein). Since Jupiter is essentially a "steady state point source" of MeV electrons, Jovian electrons present a unique opportunity to study particle transport in the inner heliosphere. Detailed computational parameter studies have also become more feasible due to the enhanced computational capabilities acquired by utilising Nvidia's Compute Unified Device Architecture (CUDA) as described by Dunzlaff et al. (2015). Here we study the residence time of energetic Jovians in the heliosphere (see e.g. McKibben et al. 2005, and references therein). Since Jupiter is assumed to release electrons continuously, these times are not directly measurable, and therefore have to be derived from theory or modelling. In order to develop a reliable estimation of the residence or propagation time, it is therefore necessary to (1) determine if the computational setup is realistic and to (2) validate the transport parameters against spacecraft data. This work will address both.

As for modulation studies of GCRs, an essential constraint for such an investigation is the knowledge of the source spectrum. The Jovian electron source spectrum was recently determined by Vogt et al. (2018) and is shown in Fig. 1. Knowledge of this spectrum allows us to estimate the effects of various physical parameters on computed Jovian intensities, which can also be compared to spacecraft observations of the same at Earth taken during periods of good and bad magnetic connection with the Jovian source. These comparisons can then provide insights with regard to the behaviour of quantities such as the low-energy electron diffusion coefficients parallel and perpendicular to the heliospheric magnetic field, as well as an optimised, realistic parameter set for further model computations as proposed in Table 2, which is used to study the residence times of Jovian electrons. We focussed our simulations on 6 MeV electrons during quiet-time conditions. This choice is in agreement with most prior investigations on Jovian electrons (see e.g. Kissmann et al. 2004; Nndanganeni & Potgieter 2018, and references therein) as it covers the detection range of several particle detection instruments such as Ulysses/KET, Voyager 1/TET, ISEE 3/ICE, IMP-8/CRNC, and SOHO/EPHIN.

In order to estimate the residence times, we propose a similar formalism as the one used to transform the probability densities resulting from the transport equation (TPE) into differential intensities. As this is done by a convolution with the source spectrum (see e.g. Strauss & Effenberger 2017, and references therein), an equivalent convolution is applied to the simulation times provided by the SDEs code. It has been demonstrated that the method of calculating residence times employed by, e.g., Florinski & Pogorelov (2009) and Strauss et al. (2013), cannot be interpreted as the propagation time of physical particles. We

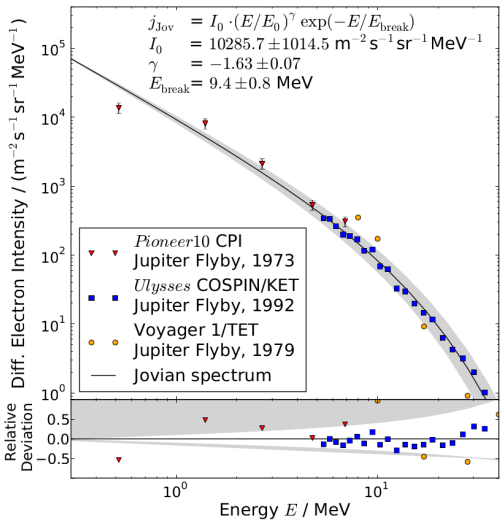

Fig. 1. Jovian source spectrum according to Vogt et al. (2018). *Upper panel*: source spectrum as fitted to the Pioneer 10 CPI and *Ulysses* COSPIN/KET data. The Voyager 1 TET data added in this plot appears to be in agreement as well. *Lower panel*: relative deviation of the spacecraft data from the fit. The shaded area covers the $\pm\sigma$ uncertainty.

propose a novel approach in which the results from each pseudo-particle are weighted by its resulting phase-space density (i.e. the number of physical particles that it represents) to obtain estimates for the propagation time that are more consistent with the limited observational constraints, but also more representative of the propagation time of the physical particles themselves.

2. Scientific background

2.1. Jovian electrons as test particles

The scientific discussion of Jovian electrons dates back to the early 1970s when McDonald et al. (1972) proposed the existence of a dominant Jovian source by addressing the correlation of the ∼13 month periodicity in low-MeV electron counting rate measurements at Earth orbit with Jupiter's synodic period. Following the Jupiter flyby of Pioneer 10, Teegarden et al. (1974) were able to confirm this hypothesis based on data obtained by the Charged Particle Instrument (CPI). Pyle & Simpson (1977) showed through an analysis of the electron fluxes as a function of distance and their dependence on the occurrence of corotating interaction regions (CIRs), that the Jovian source is not only quasi-continuous but also point-like. This refers to the observation that no electron emission could be detected from Jupiter's magneto-tail, which extends up to over 1 AU into the heliosphere.

As the dominant particle population, from a few to several tens of MeV in the inner heliosphere, Jovian electrons soon became the subject of charged particle transport modelling (Conlon 1978; Zhang et al. 2017). Due to Jupiter's decentralised position, the magnetic connection by means of the Parker spirals determines whether the electrons reach the observer primarily via motion along the field or by diffusion perpendicular to it. Thus, Jovian electrons are ideal candidates to probe the electron diffusion coefficients in the inner heliosphere.

Jovian electrons were used as test particles to model the charged-particle transport computationally (see e.g. Chenette et al. 1977; Conlon 1978; Fichtner et al. 2000; Zhang et al. 2007, and references therein) to ascertain the diffusion coefficients parallel and perpendicular to the Heliospheric Magnetic Field (HMF). This was usually done by comparing computed with measured electron intensities at Earth during periods of good or bad magnetic connection. Furthermore, given the demonstrated sensitivity of computed low-energy galactic electron intensities to various turbulence quantities (see Engelbrecht & Burger 2010, 2013; Engelbrecht 2019), it may be possible to draw conclusions from Jovian electrons to better understand the behaviour of those quantities in regions of the heliosphere where spacecraft observations of this character do not exist (see, e.g., Engelbrecht 2017). Since these transport parameters and the diffusion coefficients they depend on are spatially dependent, the time that particles reside in a certain part of the heliosphere may yield significant insights to the modulation of GCRs as well. Florinski & Pogorelov (2009) showed this dependency for GCR protons, investigating the time they spend in the heliotail, in the heliosheath, and in the solar wind within the termination shock, respectively. Utilising both galactic electrons and protons, Strauss et al. (2011a) focussed on the connection between the total propagation time and energy losses. They find a significant non-linear dependency on the total propagation times, which is strong enough to influence also the observations of Jovian electrons. These energy losses are entirely caused by adiabatic effects as other possible influences such as particle-particle interactions are negligible in the TPE due to a lack of significance in the interplanetary medium. As the adiabatic energy changes $\mathrm{d}E/\mathrm{d}t \sim -2/3 \cdot E u_{SW}/r$ are connected to the radial position, the corresponding energy loss rate per step only depends on the temporal step size Δs and the radial position after the step. The radial direction of the step is thereby irrelevant. This leads to particles spending more simulation time at small radii losing more energy and implicitly to a statistical connection between the average energy losses and the particle's mean free paths.

2.2. The Jovian electron spectrum

Parallel to the efforts of studying Jovian electron transport, the Jovian source itself has been investigated intensively. The main unknowns are the energy spectrum of the source and the way in which the particles are accelerated.

Source energy spectrum. Although it is widely considered to be dominant in its energy range, the shape and exact strength of the Jovian source remains a topic of debate. A preliminary suggestion was published as soon as Pioneer 10 confirmed the existence of the source by Teegarden et al. (1974), but the limited amount of flyby data and the general difficulties related to measuring electrons, especially electron spectra, made it difficult to further constrain both the magnitude and the shape. Suggestions were published by Baker & van Allen (1976), Eraker (1982), Haasbroek et al. (1997) and Ferreira et al. (2001) based on both Pioneer 10 CPI flyby and Earth orbit data. The two Voyagers and Ulysses are the only spacecraft equipped with particle instruments that could resolve the electron spectra above a few MeV (see Heber et al. 2005; Vogt et al. 2018; Nndanganeni & Potgieter 2018, and references therein). The latter two published source energy spectra $j_{\rm jov}(E)$ shown in Fig. 1 on the basis of these flyby data. Vogt et al. (2018) proposed

$$j_{\rm jov}(E) = \frac{1.029 \times 10^4}{\mathrm{m^2 s\ sr\ MeV}} \left(\frac{E}{E_0}\right)^{-1.63} \mathrm{e}^{-E/E_b}, \quad (1)$$

with E, and E_0 the kinetic and rest energy of the electron, and E_b = 9.4 MeV the spectral break energy. The exponent of

Table 1. Overview of the electron spectra used in this study.

Location of observation	Spacecraft mission/instrument	Source
Flyby	Pioneer 10/CPI	Teegarden et al. (1974)
	Ulyssses/KET	Heber et al. (2005)
	Voyager 1/TET	Nndanganeni & Potgieter (2018)
Earth orbit (well connected)	SOHO/EPHIN	Kühl et al. (2013)
	Ulyssses/KET	Heber et al. (2005)
	ISEE 3/ICE	Moses (1987)
	Voyager 1/TET	Nndanganeni & Potgieter (2018)
Earth orbit (badly connected)	ISEE 3/ICE	Moses (1987)

$\alpha = -1.63$ is very much in agreement with the findings of Ferreira et al. (2001) and Baker & van Allen (1976), the shape proposed in Eq. (1) is more similar to that suggested by Teegarden et al. (1974) and Eraker (1982), and acceleration theory in itself, as Ferreira et al. (2001) proposed a combination of two spectra to fit the spectral break. The Voyager 1 flyby spectrum, as published by Nndanganeni & Potgieter (2018), is included in Fig. 1 and supports these results. An overview of the electron spectral data utilised for this study, obtained both during the flybys and at Earth's orbit, is listed in Table 1. Previous studies derived the spectra by solving the particle transport equation and fitting the results to measurements close to Earth (see, for example Moses 1987, and references therein).

Acceleration processes. Since the findings of Bolton et al. (1989) were published, it has been widely accepted that Jovian electrons originate in the solar wind, then they are picked up by the Jovian magnetosphere and diffuse inwards. In situ data has been obtained by spacecraft such as Pioneer 10, *Galileo,* and *Cassini* and found to suggest acceleration via wave-particle interaction within the radiation belts, as discussed by Horne et al. (2008), alongside adiabatic processes suggested by de Pater & Goertz (1990). Because the existence of the Jovian source seems to be linked to the planet's extended and strong magnetic field, the question as to whether these processes also apply close to Saturn is relevant as well (see e.g Lange & Fichtner 2008). Recently, *Cassini* measurements (as reported by Palmaerts et al. 2016; Roussos et al. 2016) revived this discussion and provide support, together with *Galileo* data, for the dominant role of adiabatic processes within both planets' magnetospheres in order to accelerate MeV electrons (see Kollmann et al. 2018, and references therein).

Due to the recent measurements of electrons outside the heliosphere (Stone et al. 2013), the question of how to distinguish the Jovian population from the Galactic background, based on suggestions for the very local interstellar spectrum (VLIS) has been discussed in Bisschoff et al. (2019, and references therein). Apart from its implications regarding the modulation of GCRs, Nndanganeni & Potgieter (2018) find the Jovian population dominating the spectrum up to energies of about $E \sim 25$ MeV, followed by an energy range of 25 MeV $\leq E \leq 40$ MeV where the spectrum consists of a mixture of Jovian and Galactic electrons varied by the co-longitudinal dependency of the Jovian intensities. Regarding the radial dependency, Jovian electrons were found to be the dominant populations up to radial distances of $R \sim 15$ AU, based on simulations of the 6 MeV Jovian and Galactic electron intensities.

3. Calculating differential intensities

For the purpose of this study, the SDE code as discussed by Dunzlaff et al. (2009) was utilised, which is based on previous codes by e.g. Strauss et al. (2011b,a). This SDE solver is written in CUDA to optimise on performance time, and therefore incorporates a simplified analytical approach for both the solar wind velocity as well as for the HMF. The solar wind velocity is chosen to be $u_{\mathrm{SW}} = 400\ \mathrm{km\,s^{-1}}$ and directed radially outwards. The HMF is assumed to be Parker-like and included geometrically within the diffusion tensor according to Burger et al. (2000). Therefore, the results of this study are applicable to solar minimum conditions.

It has been established, based on models (e.g. Potgieter 1996; Burger et al. 2000; Ferreira & Potgieter 2002) as well as from a theoretical perspective (e.g. Bieber et al. 1994; Engelbrecht & Burger 2010) that drift effects can be neglected when studying the transport of electrons with energies of a few MeV. In order to optimise the performance time of the code, the energy-independent approach of Dunzlaff et al. (2015) and Strauss et al. (2011b) is used to include the parallel and perpendicular mean free paths: $\lambda_{\parallel}$ is normalised to a value of the parallel mean free path λ_0 at 1 AU, such that:

$$\lambda_{\parallel}(r) = \frac{\lambda_0}{2}\left(1 + \frac{r}{r_0}\right). \tag{2}$$

This value of the parallel mean free path, together with the particle speed v, scales the parallel diffusion coefficient as $\kappa_{\parallel}(r) = v\lambda_{\parallel}(r)/3$ and the perpendicular diffusion coefficient via the proportional factor χ such that:

$$\kappa_{\perp}(r) = \chi\kappa_{\parallel}(r). \tag{3}$$

Although the above expressions represent an essentially ad hoc approach to modelling diffusion parameters, the radial dependency of the parallel diffusion coefficient does reproduce the corresponding behaviour of the quasi-linear theory electron parallel diffusion coefficient employed by Engelbrecht & Burger (2013), between 1 and 5 AU. Perpendicular mean free path expressions from theory, however, can behave in a manner quite different from what is assumed in this study (see, e.g. Shalchi 2009; Engelbrecht & Burger 2015; Gammon & Shalchi 2017). For a preliminary study, however, the above expression for $\kappa_{\perp}$ should provide a reasonable approximation that meets the requirements for the scientific tasks investigated herein. This assumption is confirmed later within this study as the approach leads to reasonable results for the limited energy range considered.

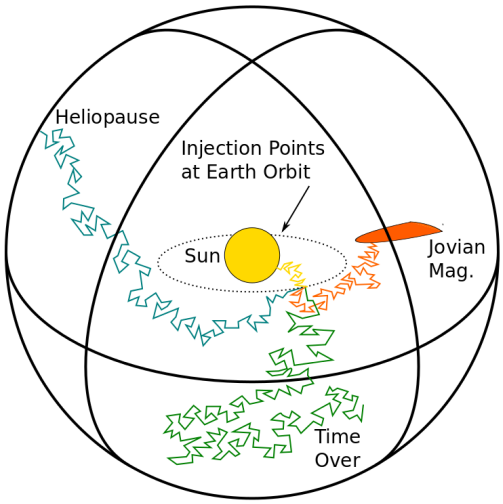

Fig. 2. Sketch of the simulation setup as detailed in Dunzlaff et al. (2015). The four different exit possibilities are colour-coded: the Sun (yellow), the Jovian magnetosphere (orange), the Heliopause (blue), as well as the option that the phase space trajectory is terminated by reaching a predefined end time (green). We note that the figure is not to scale.

As described in great detail by e.g. Kloeden & Platen (2011), the stochastic nature of diffusion is treated within the SDE method as a Wiener process $\mathrm{d}W_t = \zeta \sqrt{\mathrm{d}t}$ with ζ being a vector of Gaussian distributed random numbers. The resulting set of four integral equations, as they are derived by Strauss et al. (2011b), is solved iteratively by applying the Euler-Maruyama scheme. This leads to a random walk type solution which is terminated if a spatial or temporal boundary is reached, as shown in Fig. 2 for various possible exit positions. A time-backward phase-space trajectory can either terminate at the assumed position of the heliopause (blue line), the Jovian magnetosphere (orange line), or after a pre-specified number of steps have been made without an encounter with either of the formerly mentioned structures (green line). As discussed in Sect. 2.2, in the low-MeV energy range Jovian electrons dominate the spectrum. The solar population therefore can be assumed to be negligible during quiet times, and thus trajectories exiting at the Sun are discarded. Galactic electrons, on the other hand are considered via the local interstellar spectrum according to Potgieter & Vos (2017), although the transport of the Galactic population into the inner heliosphere is much more sensitive to the drift effect, which is not considered here.

Instead of solving Parker's TPE directly to obtain a time-dependent distribution function $f(\boldsymbol{r}, t)$ covering the whole phase space, the SDE method provides a chain of point-like solutions both in space and time. The solutions must be sampled at a large number of phase-space points to approximate a spatial solution covering the phase space of interest. In order for the computational results to be comparable with spacecraft data, the time-backward setup is solved as derived and discussed by e.g. Kopp et al. (2012). A comparison between the time-forward and time-backward setup, made using a simpler 1D model, can be found in the review by Strauss & Effenberger (2017).

The left panel of Fig. 5 shows histograms of the so called exit energy[1] (i.e. the energy of which pseudo-particles leave the computational domain) at times of good magnetic connection between the Jovian magnetosphere and the observational point, in contrast to Fig. 5b, which illustrates the energy distribution for an observational point in opposition to the Jovian source. The distributions in Fig. 5b are much broader. This, of course, is in agreement with Fig. 5a being dominated by the much more efficient parallel diffusion along the nominal Parker spirals, while pseudo-particles reaching the Jovian magnetosphere in Fig. 5b must do so via the more inefficient perpendicular diffusion process. These particles suffer much more scattering, leading to a more diffuse distribution.

Taking the integral distributions (dashed lines) into account, it shows that these extreme particle trajectories corresponding to high exit energies contribute very little to the total differential intensity. In the case of good connection, Fig. 5a suggest that the pseudo-particles with exit energies below 10 MeV contribute about 90% to the total differential intensity, whereas Fig. 5b shows that in the case of bad connection, they still make up about 80%. Therefore, we conclude that although the trajectory of each pseudo-particle is (mathematically) equally likely, they do not contribute equally towards the differential intensity. This is equivalent to stating that different pseudo-particles represent different amounts of physical particles corresponding to their physical significance.

The concern is now to consider that if each pseudo-particle represents a different number of real particles, is it necessary to weigh the pseudo-particles equally when calculating physical quantities, such as the residence time, from their distribution.

3.1. Model parameter dependencies

A major aspect of modelling physical processes is simplifying the computational setup in order to save resources and time without affecting the physical validity of the results. Therefore, the variability of our results was tested against various model setups in order to find the most optimal modelling scenario.

The choice of time increment Δs has the most obvious influence on the simulation results due to its association with the Wiener process and, hence, with the mathematical representation of diffusion. Both the effects of the size of the time increments and the influence of the maximal simulation time have been tested. For Δs a high sensitivity to the magnetic connection was observed as expected since the time increment (which is related to the adiabatic energy changes) influences the duration of the random walk. Therefore, it is important to note that the effect is more significant for observation points of good magnetic connections. As the trajectories for bad connections are much more diffusion-dominated, the effect of the size of the time increment is more likely to be cancelled out by the number of timesteps. For good connections, however, the trajectories are much more dominated by the geometry of the underlying HMF. Therefore, larger time increments cause larger abbreviations and subsequently longer simulation times. It was found that the simulated differential intensity converges for values of $\Delta s \leq 0.001$ in programme units (about 0.004 days). The numerical dependence on the maximal duration of simulation appears to be very weak (above a certain limit), with a required duration of about 700 to 800 programm units in order to avoid deviations of more than 20. This leads to a total time of simulations of $\sum \Delta s \geq 300$ days. As the numerical step sizes of the pseudo-particles are ultimately dependent on the choice of the energy transport parameters (which influences the diffusive step size), there is a slight energy dependence on the optimal size of the timestep.

[1] We note that the term exit energy refers to a time-backward simulation setup. Therefore, the exit energy describes the energy the particle would have been emitted with at its source – which is in the case of this study the Jovian magnetosphere.

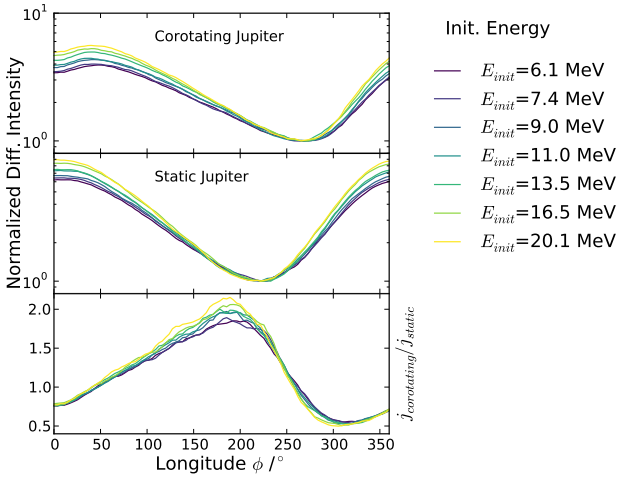

Fig. 3. Differential intensities of Jovian electrons for different initial energies E^{init}. *Top panel*: longitudinal variation due to varying connection for a co-rotating Jovian source, *middle panel*: case of a static Jupiter. *Bottom panel*: ratio of the results of the two approaches.

Due to the fact that Jovian electrons originate in and populate mainly the inner heliosphere, it seems natural to raise the question as to whether a model heliosphere could be restricted in size so that calculation results remain unaffected. It was found that results become insensitive to the size of the model heliosphere if $R_{\text{HP}} \geq 80$ AU is used. For smaller radii, the resulting differential intensities increase exponentially, regardless of magnetic connection. Therefore, we use a value of $R_{\text{HP}} = 120$ AU in order to assure convergence, and, as reported by e.g. Gurnett et al. (2013), this is the radial distance at which Voyager 1 crossed the heliopause.

A more physical question is whether a co-rotating coordinate system is necessary. To keep the setup mathematically as simple as possible, the code is designed in a way that both the Sun and the Jovian source are kept fixed. The position of the observer as the starting point of the time-backward phase space trajectories is calculated in a coordinate system relative to the slow orbital motion of Jupiter. These relative position can be kept static during the random walk or include the further co-rotation of the Jovian source by means of an additional longitudinal advection velocity $V_\phi = \Omega_{\text{Sun}} \cdot r$. Figure 3 shows the calculated Jovian electron intensities, at Earth, for different energies as a function of longitude. Simulations were performed for both a co-rotating coordinate system (top panel) and for the case of a static Jupiter (bottom panel). The bottom panel shows the ratio of these two scenarios and proves that the ratio between the differential intensities for a co-rotating and a static approach appears to be significant. We conclude that Jovian co-rotation must be included in the model to produce reasonable results. We also conclude that the co-rotation of the Jovian source is an important effect that should be incorporated into the numerical model.

3.2. Deriving an estimation for the mean free paths

Figure 5 shows that only lower-energy pseudo particles (with exit energies near the initial energy) contribute significantly to particle intensity at Earth. As this energy range only covers an order of magnitude, the energy dependence of the mean free paths both parallel and perpendicular can be neglected for the means of this study. We note, however, that the resulting diffusion coefficients, which are the parameters used in the model, might still have some energy dependence due to their dependence on the particle speed v.

Thus, to estimate λ_0, the Jovian spectral data at Earth orbit as listed in Table 1 were compared to the results of a parameter study covering the parameter space in question, namely $\lambda_\parallel$ and $\lambda_\perp$. As already discussed in Sect. 2.1, the decentralised position of the Jovian source allows us to estimate the effectiveness of parallel and perpendicular transport dependent on the observational point's magnetic connection with Jupiter. In order to ensure consistency, $\lambda_\parallel$ was determined when investigating the case of the best magnetic connection between the observational point and the source before determining χ which scales $\lambda_\perp$ with respect to $\lambda_\parallel$ according to Eq. (3) and this, therefore, dominates the results in case of magnetic opposition.

The upper panel of Fig. 4a shows the available Jovian electron spectral data at Earth orbit during times of good magnetic connection. For a more detailed discussion with regards to the Jovian source spectrum, see Vogt et al. (2018) or the individual publications listed in Table 1. The black dashed line marks the shape of the Jovian source as fitted to the Earth orbit data in order to have a measure to define the deviation. The results of the simulations are colour-coded in all three panels, with varying parallel mean free paths covering the range of $\lambda_\parallel = [0.05\text{ AU}, 0.4\text{ AU}]$ in steps of 0.05 AU, and a value of $\chi = 0.01$ in agreement with the suggestions by Palmer (1982) as well as Bieber et al. (1994) and succesfully implemented in previous studies by (e.g. Strauss et al. 2011a; Vogt et al. 2018, amongst others) is used. The results are shown in the two upper panels of Fig. 4a; the top panel depicting the simulated intensities, whereas the middle panel shows their relative deviation from the nominal spectrum provided by the fit. The grey area marks the range of a ±0.5 relative deviation in order to give an impression on the reliability of the results. As the errors related to the data appeared to be too small to be significant and it is way beyond the scope of this work to re-examine them, the choice was made to display the simulation results with respect to their relative deviation from the fit. In the bottom panel, the area between the lowest and the highest value of $\lambda_\parallel$, leading to simulation results within this ±0.5 relative deviation, is again marked in grey. Thereby it provides an estimation of the energy dependency of $\lambda_{\parallel/\perp}$. The energy range is chosen in order to cover the range of exit energies contributing to the total differential intensity for an inititial energy of 6 MeV according to Fig. 5. As it appears, a value of $\lambda_\parallel = 0.15$ AU seems to match the observations best over the whole energy range investigated herein. This is an additional motivation for our choice of an energy-independent mean free path.

Figure 4b shows the relative deviation of simulations with varying $\chi = [0.00, 0.04]$ and for two values for $\lambda_\parallel = [0.125, 0.15]$ AU. The uppermost panel of Fig. 4b shows the spectral data at Earth's orbit according to Table 1, specifically obtained during times of bad magnetic connection between the spacecraft and the Jovian magnetosphere. Similarly to Fig. 4a, the dashed line indicates the spectral shape of the source when fitted to the Earth orbit data. In this case the data are presumably dominated by the effects of perpendicular diffusion. As discussed above, larger values of $\lambda_\parallel$ lead to more effective diffusion and, therefore, to increased differential intensities at the observational point. This relation is also present in the results depicted by Fig. 4b, as higher values of $\lambda_\parallel$ demand smaller values of χ in order to fit the data. Although the estimation of parallel and perpendicular mean free paths based on turbulence theory is still an ongoing topic of research, previous studies suggest

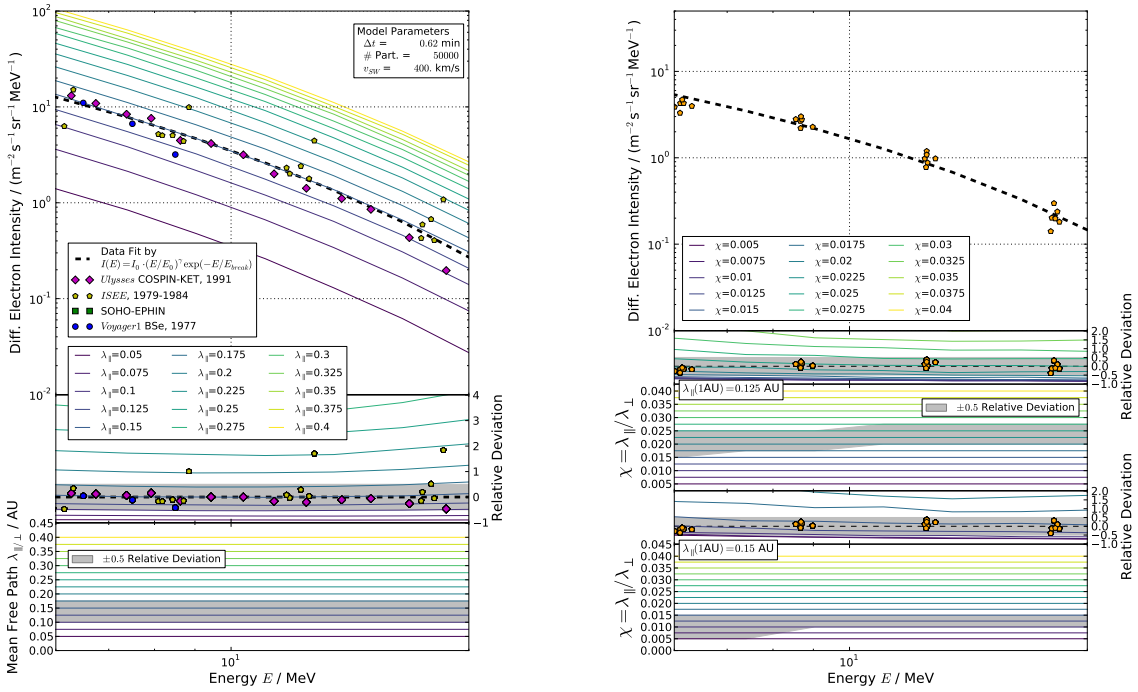

(a) (b)

Fig. 4. Simulated Jovian electron spectra used to optimize the values of $\lambda_\parallel$ and χ. *Top panel*: a data fit (dashed line) along with the simulations results and spacecraft data obtained during corresponding time periods at the longitudinal point of best effective magnetic connection for different values of $\lambda_\parallel$ = [0.05, 0.4] AU. *Panel b* does not show the simulated spectra for different values of for different values of χ = [0.005, 0.045] in the *upper panel* as the simulations are performed utilizing two different values for $\lambda_\parallel$. The fit (dashed line) was performed utilizing spacecraft data by ISEE 3, the only spectral data for magnetically poorly connected observation times as given by Table 1. *Lower panels*: corresponding relative deviations from the fit (dashed lines) together with the ±0.5 deviation area given in shaded grey and the spacecraft data. *Lowest panel*: shaded area marks the range of values for $\lambda_{\parallel/\perp}$ within the margin of less than ±0.5 relative deviation.

values between 0.09 and 0.3 AU for $\lambda_\parallel$ (Palmer 1982; Bieber et al. 1994) which were tested successfully for electrons in the inner heliosphere such by studies such as, for example, Ferreira et al. (2003), Ferreira (2005), Strauss et al. (2011b) and Dröge et al. (2016) amongst others. While values of just $\lambda_\parallel$ = 0.175 AU would would fit well within this range, they would demand values for χ that would be out of a realistic range (see e.g. Palmer 1982; Bieber et al. 1994; Strauss et al. 2011b; Dröge et al. 2016, amongst others) and, therefore, are considered unrealistic.

Taking the best fit χ for $\lambda_\parallel$ = 0.15 AU (as the best-fitting value for $\lambda_\parallel$ according to Fig. 4a) into account, a value of χ = 0.0125 seems to be justifiable within the margin of error for the energy range of interest. This value for the parallel mean free path is well within the Palmer (1982) consensus range, and reasonable for low-energy electrons (e.g. Bieber et al. 1994). The value for χ is somewhat smaller than the range expected from Palmer (1982), where $0.02 \leq \chi \leq 0.08$, but well within the range of values commonly used in numerical modulation studies (see, e.g. Ferreira et al. 2001; Engelbrecht & Burger 2013; Nndanganeni & Potgieter 2018). Therefore, unless otherwise indicated, these parameters were utilised throughout this study, as summarised in Table 2.

3.3. Interpretation of phase space trajectories

As already pointed out above, the phase space trajectories obtained by the SDE solver are mathematical solutions and, in contrast to a physical interpretation, each phase space trajectory is equally probable. However, not each phase space trajectory represents the same number of physical particles. Although they are often referred to as pseudo-particles, this term is slightly misleading because the phase space trajectories represent the evolution of the particle density distribution f along a curve through the heliosphere and has no connection with the trajectory of actual charged particles in a turbulent plasma.

Table 2. Computational and physical parameters used for the code (when not stated otherwise).

Computational parameters	
# Trajectories	50 000
Δt	0.0001
$T_{\rm End}$	800
Physical parameters	
$R_{\rm HP}$	120 AU
$u_{\rm SW}$	400 km s^{-1}
$\lambda_\parallel$(1 AU)	0.15 AU
$\chi = \lambda_\perp/\lambda_\parallel$	0.0125
$E^{\rm init}$	6 MeV

The TPE is solved by integrating the SDEs via the time-backward Euler-Maruyama scheme which leads to an increase of the pseudo-particle's energy E_i due to the inverse adiabatic processes (adiabatic energy losses treated in a time-backwards fashion). Therefore, applying the source spectrum $j_{\rm jov}(E)$ as the boundary weight (see, e.g., Strauss et al. 2011b; Kopp et al. 2012) leads to the expression

$$j(r^0, E^0) = \frac{\sum_{i=1}^{N} j_{\rm jov}(E_i^{\rm exit})}{N}, \quad (4)$$

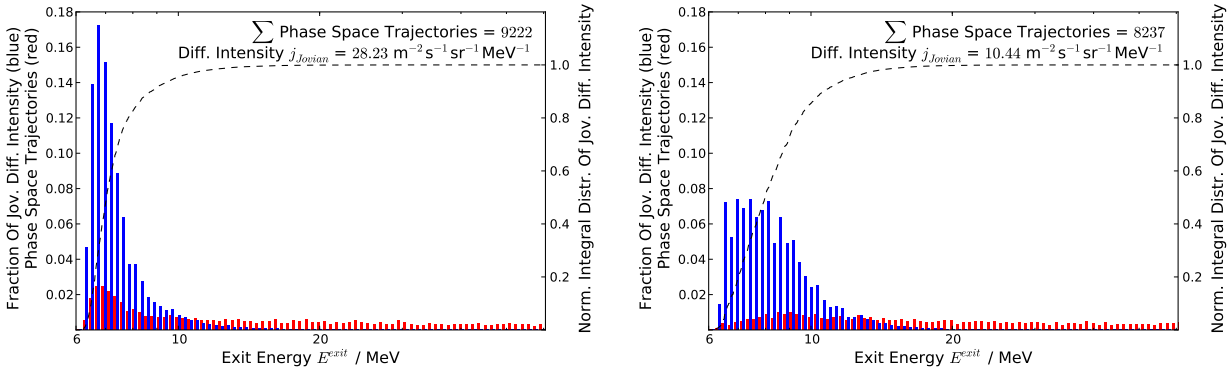

(a) (b)

Fig. 5. Binned distributions of the exit energies $E_i^{\rm exit}$ (red) and the binned contribution of each energy point to the total differential intensity, $j_{\rm jov}(E_i^{\rm exit})$ (blue), for an initial energy of $E_i^{\rm init} = 6$ MeV. Thereby *panel a* shows the distribution of exit times of pseudo-particles for a good magnetic connection between the observational point and the Jovian source and *panel b* for the case of poor magnetic connection. The dashed lines show the integral distribution of the trajectories' contribution to the total differential intensity as shown in blue.

with the distribution function f as the solution of the TPE related to the differential intensity $j = P^2 f$, with $P = pc/q$ being the particle rigidity, depending on the momentum p and the charge q.

Equation (4) can also be derived by calculating the Green's function $G(x_i, s = T)$ for any given boundary or initial condition in order to solve the convolution (see, e.g. Pei et al. 2010)

$$f(x,T) = \int_0^T \int_x G(x',t) f_b(x',t) \mathrm{d}x' \mathrm{d}t, \tag{5}$$

with $f_b(x',t)$ denoting the boundary value. As discussed by Strauss & Effenberger (2017), neglecting the initial condition simplifies Eq. (5) to

$$f(\boldsymbol{x}_0, t_0) = \int_0^{t_0} \int_{\boldsymbol{x}\in\Omega_b} f_b(\boldsymbol{x},t)\rho(\boldsymbol{x},t)\mathrm{d}\Omega\mathrm{d}t, \tag{6}$$

with $\boldsymbol{x} = (r, E)$, $f_b(\boldsymbol{x}, t)$ representing the boundary condition (i.e. the particle population's source distribution), $\rho(\boldsymbol{x}, t)$ being the conditional probability density and $f(\boldsymbol{x}_0, t_0)$ the distribution at the observational point. Focusing on steady state solutions where $t \to \infty \Rightarrow \rho(\boldsymbol{x}_i, t) :\to \rho(\boldsymbol{x}_i)$, as well as calculating $f_i(\boldsymbol{x}_0, t_0)$ for each phase space trajectory, ρ_i, individually reducing the spatial boundary of the integration domain Ω_b to the exit position, $r^{\rm exit}$, as well as the range of the energy coordinates to $E^{\rm exit}$ then leads to the expression given by Eq. (4).

Figure 5 shows the probability density (binned distribution of pseudo-particles, N_i/N; red) and the elements of Eq. (4) ($j_{jov}(E_i^{\rm exit})$; blue) for an initial energy of $E_0 = 6$ Mev at an observational point at Earth. Whereas each pseudo-particle is equally weighted in the calculation, they may contribute very differently to the total differential intensity; from the figure, it is evident that pseudo-particles may reach the Jovian magnetosphere with several tens of MeV (which implies significant energy loss in the normal time-forward scenario). However, the blue histogram hints that only pseudo-particles with up to 10 MeV contribute significantly to the total differential intensity. The integral distributions (dashed line) for both cases further support this assumption as they converge roughly at the exit energies for which the fractional contribution of the differential intensity gets lower than the fractional contribution of pseudo-particles. Looking at just the distribution of the pseudo-particles may, therefore, prove misleading if we are interested in deriving physical quantities from the SDE method. It is important to note that even if some pseudo-particles contribute very little to the differential intensity, they cannot be disregarded in the calculations as they still contribute to the denominator of Eq. (4).

4. Residence times

Because the Euler-Maruyama-Scheme (as well as alternative methods) utilises a well-defined time increment, ds, in order to solve for the system of integral equations, it is possible to derive a measure of τ as the time that the phase space trajectory takes to connect the source to the observational point. Thereby τ is calculated as the number of time steps needed for the phase space trajectory n_i multiplied by the time increment ds, if the latter time step is assumed to be constant. Generally, τ can be given as $\tau_i = |s_i^{\rm exit} - s_i^0|$, with $s_i^{\rm exit} = n_i \cdot \mathrm{d}s$ and s_i^0 often being simply the start time of the calculation. Although τ_i is often referred to as the propagation time or as the residence time too, the more accurate description would be to call τ_i the trajectory duration or simulation time.

This estimation raises the question of how to interpret the individual phase space trajectories. As discussed in Sect. 3, phase space trajectories are equally mathematically possible but not equally physically significant. If we now want to derive physical quantities from these trajectories, how should we weigh the resulting distributions? We aim to address this question in the next paragraphs.

Traditionally, the residence or propagation time is assumed to be equivalent to the expectation value of the time, as weighed by a probability density ρ,

$$\tau = \frac{\int \rho(\boldsymbol{x},t) t \mathrm{d}t}{\int \rho(\boldsymbol{x},t)\mathrm{d}t}. \tag{7}$$

Typically, in previous works, ρ is constructed from the SDE solutions as the (normalised) distribution of the pseudo-particles' exit time (see e.g. Florinski & Pogorelov 2009; Strauss et al. 2013). For 6 MeV Jovian electrons, these distributions are shown in Fig. 6, as the red histogram, for the case of good (left) and bad (right) magnetic connection to the source. From the red distribution, a propagation time of ~550−600 days is calculated, and from the figure itself, we note that most pseudo-particles only reach the observer within ~100−1000 days. This seems

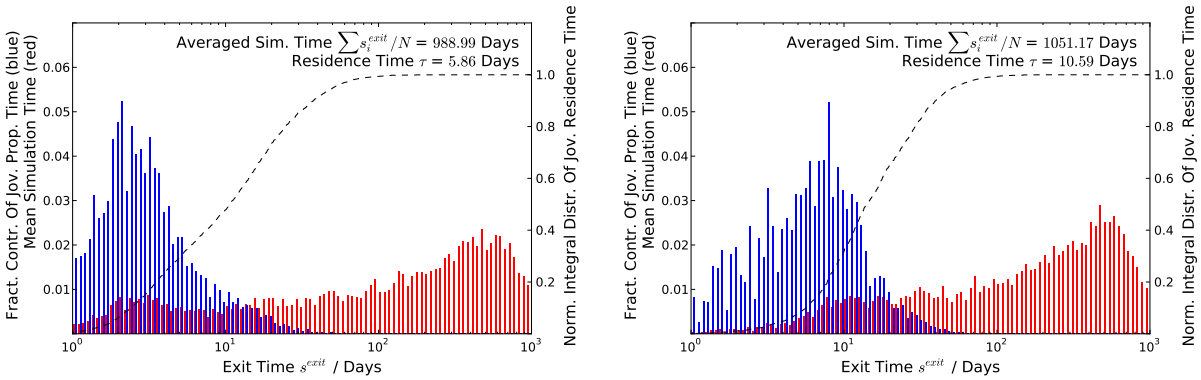

Fig. 6. Binned distributions of the Jovian electron propagation time using the normal (red) and new (blue) way of defining the probability distribution. Thereby *panel a* shows the distribution of exit times of pseudo-particles for a good magnetic connection between the observational point and the Jovian source and *panel b* for the case of poor magnetic connection. The blue distribution shows the weighted exit times, which we refer to as the propagation (residence) time of Jovian electrons. Again the integral distribution of the pseudo-trajectories contribution to τ is shown by the dashed line. The residence times are obtained via Eq. (10).

very long for relativistic electrons diffusing only a radial distance of ∼ 4 AU towards Earth.

An observational estimate to compare with is discussed by Strauss et al. (2013). Investigating quiet-time increases (QTIs) (see e. g. McDonald et al. 1972; Chenette 1980), which relate to a diffusion barrier between Earth and Jupiter, these authors find that it takes ≈5 days after the diffusion barrier has passed Jupiter for the Jovian electrons to be detected again.

The numerical definition of τ according to Eq. (7) essentially weighs each pseudo-particle with the same probability. However, we have already seen earlier in this paper that each pseudo-particle does not represent the same number of physical particles. We therefore propose to rather use the distribution of particle density to calculate the propagation time by specifying

$$\rho(\boldsymbol{x}, t) = \frac{f(\boldsymbol{x}, t)}{f_0(\boldsymbol{x})}, \tag{8}$$

which is normalised by the total phase-space density,

$$f_0(\boldsymbol{x}) = \int f(\boldsymbol{x}, t)\mathrm{d}t. \tag{9}$$

Thereby $f(\boldsymbol{x}, t)$ represents the solution of the TPE and is calculated at the exit position $\boldsymbol{x}^{\mathrm{exit}}$ of the random walk. We note that $f_0(\boldsymbol{x}^{\mathrm{exit}})$ cancels in the calculation of τ, which in discrete form is read as:

$$\tau(r^0, E^0) = \frac{\sum_{i=1}^{N} s(E_i^{\mathrm{exit}}) \cdot f(E_i^{\mathrm{exit}})}{\sum_{i=1}^{N} f(E_i^{\mathrm{exit}})} \tag{10}$$

and s is the exit (integration) time of the pseudo-particles. Using this new definition, their weighted contribution to the propagation times are shown in Fig. 6 as the blue distribution. The parameters used for this simulation are listed in Table 2, as discussed in Sect. 3.2. These weighted propagation times are generally much shorter than those obtained by weighing the pseudo-particles equally. Similar values as the ones found by this study were only obtained using larger mean free paths (compare to e.g. Strauss et al. 2013) which would turn out to be unrealistic, as discussed in Sect. 3.2, because our findings are in agreement with prior studies on electron mean free paths such as (e.g. Palmer 1982; Bieber et al. 1994; Tautz & Shalchi 2013, amongst others) and modelling approaches by (e.g. Potgieter & Ferreira 2002; Dröge 2005; Strauss et al. 2011b, amongst others). By integrating the blue histograms, we find propagation times of ∼5−11 days, almost two orders of magnitude shorter than the traditional calculation. Again, the comparison with the red histogram showing the pseudo-particle trajectories' exit times makes this difference comprehensible. The integral distribution of the blue histograms (dashed lines) illustrate that the maximum of the exit times distribution (red) is almost a magnitude higher than the range of convergence. Normalised to the value of the residence time, the integral distributions (as for the differential intensities that are shown in Fig. 3) illustrate how little long exit times corresponding to large exit energies influence the residence times if calculated via Eq. (10). This leads to the disparity between the averaged exit or simulation times and our estimations of the residence time equivalent to the differences between the two distributions.

As we have shown and discussed in Sect. 3.3, this is caused by the diverging physical significance of the phase space trajectories. As Eq. (10) addresses and solves this problem, we consider our new calculation to be more representative of the propagation time of a physical particle. This is supported by the fact that Eq. (10) considers the exit or simulation times according to their representation of physical particles and therefore provides a measure consistent with the total differential intensity.

5. Discussion and conclusions

In this paper, we discuss a Jovian electron transport model that is used to study the propagation times (residence times) of 6 MeV electrons. We discuss the optimal numerical set-up, including the choice of time step, integration times, and the required size of the numerical domain. We also show that taking into account the co-rotation of the Jovian source leads to non-negligible effects. This is an important effect due to its influence on the finite propagation time of Jovian particles from the observer (assumed at Earth, but at different longitudes) to the source. Figure 7 shows how the calculation of, for example, the propagation time, changes due to the assumption of either a static, or a co-rotating source.

We have also used the unique magnetic geometry of the Jovian propagation problem to quantify the appropriate mean free paths. By reproducing the 1 AU intensity spectrum during times of good magnetic connection, we were able to show that $\lambda_{\parallel} \approx 0.1$ AU is appropriate for Jovian electrons in the energy

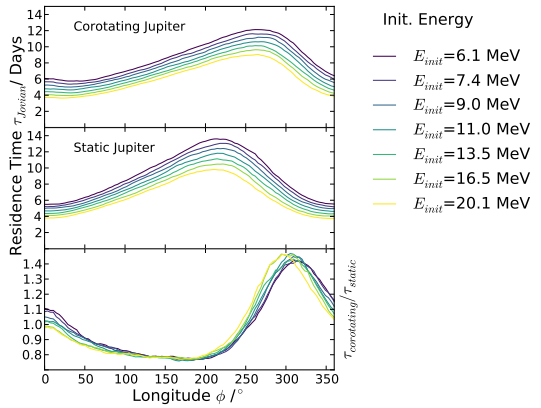

Fig. 7. Similarly to Fig. 3, the residence times (τ) of Jovian electrons are now shown in order to illustrate the influence of co-rotation of the Jovian source as compared to a static source. *Bottom panel*: ratio of the solutions. Different colours indicate different energies.

range under consideration. By doing the same during times of bad magnetic connection, we were able to show that a value of $\chi \approx 0.01$ is appropriate. Both these values fall within the range of what is expected from previous studies.

Using the optimal numerical set-up, we calculated the exit times of 6 MeV electrons using the traditional SDE formalism, where each pseudo-particle contributes equally to the final results. A value of ~600 days was found, which, while formally correct, does not seem physically consistent with relativistic particle propagating across a distance of ~4 AU. Therefore, we propose a new technique to weigh the resulting exit times with the particle intensity, leading to more realistic values of ~6 days. We propose to term these weighted exit times as the propagation (residence) time of Jovian electrons. The motivation for this weighing is as follows: although the trajectory of each pseudo-particle is equally probable, each pseudo-particle does not represent the same number of actual particles since the phase-space density of each pseudo-particle is different.

In the case of CIRs in particular, a more realistic measure of Jovian residence times could improve our understanding. As Jovian electron simulations successfully have been applied to this topic by Kissmann et al. (2003, 2004) the numerical set-up provided by this study provides the opportunity to revisit this approach with further insights. Simulations of residence times could also help to determine how much time Jovian electrons (and other particle populations) spend within structures like CIRs or magnetic flux tubes. More recently, Daibog et al. (2013) highlighted the role of Jovian electrons as test particles within this matter again, suggesting that deviations from their quiet time variations could serve as probes for the inner heliosphere's structure.

Acknowledgements. This work is based on the research supported in part by the National Research Foundation of South Africa (Grant Number 111731) and the Deutsche Forschungsgemeinschaft (Grant Number FI 706/14). Opinions expressed and conclusions arrived at are those of the author and are not necessarily to be attributed to the NRF or DFG, respectively.

References

Baker, D. N., & van Allen, J. A. 1976, J. Geophys. Res., 81, 617
Bieber, J. W., Matthaeus, W. H., Smith, C. W., et al. 1994, ApJ, 420, 294
Bisschoff, D., Potgieter, M. S., & Aslam, O. P. M. 2019, ApJ, 878, 59
Bolton, S. J., Gulkis, S., Klein, M. J., de Pater, I., & Thompson, T. J. 1989, J. Geophys. Res., 94, 121
Burger, R. A., Potgieter, M. S., & Heber, B. 2000, J. Geophys. Res., 105, 27447
Chenette, D. L. 1980, J. Geophys. Res., 85, 2243
Chenette, D. L., Conlon, T. F., Pyle, K. R., & Simpson, J. A. 1977, ApJ, 215, L95
Conlon, T. F. 1978, J. Geophys. Res., 83, 541
Daibog, E. I., Kecskemety, K., & Logachev, Y. I. 2013, Bull. Russ. Acad. Sci. Phys., 77, 551
de Pater, I., & Goertz, C. K. 1990, J. Geophys. Res., 95, 39
Dröge, W. 2005, Adv. Space Res., 35, 532
Dröge, W., Kartavykh, Y. Y., Dresing, N., & Klassen, A. 2016, ApJ, 826, 134
Dunzlaff, P., Kopp, A., Heber, B., & Sternal, O. 2009, Proceedings of the 31st International Cosmic Ray Conference (ICRC) 2009
Dunzlaff, P., Strauss, R. D., & Potgieter, M. S. 2015, Comput. Phys. Commun., 192, 156
Engelbrecht, N. E. 2017, ApJ, 849, L15
Engelbrecht, N. E. 2019, ApJ, 872, 124
Engelbrecht, N. E., & Burger, R. A. 2010, Adv. Space Res., 45, 1015
Engelbrecht, N. E., & Burger, R. A. 2013, ApJ, 779, 158
Engelbrecht, N. E., & Burger, R. A. 2015, ApJ, 814, 152
Eraker, J. H. 1982, ApJ, 257, 862
Ferreira, S. E. S. 2005, Adv. Space Res., 35, 586
Ferreira, S. E. S., & Potgieter, M. S. 2002, J. Geophys. Res. Space Phys., 107, 1221
Ferreira, S. E. S., Potgieter, M. S., Burger, R. A., Heber, B., & Fichtner, H. 2001, J. Geophys. Res., 106, 24979
Ferreira, S. E. S., Potgieter, M. S., Moeketsi, D. M., Heber, B., & Fichtner, H. 2003, ApJ, 594, 552
Fichtner, H., Potgieter, M., Ferreira, S., & Burger, A. 2000, Geophys. Res. Lett., 27, 1611
Florinski, V., & Pogorelov, N. 2009, ApJ, 701, 642
Gammon, M., & Shalchi, A. 2017, ApJ, 847, 118
Gurnett, D. A., Kurth, W. S., Burlaga, L. F., & Ness, N. F. 2013, Science, 341, 1489
Haasbroek, L. J., Potgieter, M. S., & Le Roux, J. A. 1997, Adv. Space Res., 19, 953
Heber, B., Kopp, A., Fichtner, H., & Ferreira, S. E. S. 2005, Adv. Space Res., 35, 605
Horne, R. B., Thorne, R. M., Glauert, S. A., et al. 2008, Nat. Phys., 4, 301
Kissmann, R., Fichtner, H., Heber, B., Ferreira, S., & Potgieter, M. 2003, Adv. Space Res., 32, 681
Kissmann, R., Fichtner, H., & Ferreira, S. E. S. 2004, A&A, 419, 357
Kloeden, P., & Platen, E. 2011, Numerical Solution of Stochastic Differential Equations, Stochastic Modelling and Applied Probability (Berlin: Springer)
Kollmann, P., Roussos, E., Paranicas, C., et al. 2018, J. Geophys. Res. Space Phys., 123, 9110
Kopp, A., Büsching, I., Strauss, R. D., & Potgieter, M. S. 2012, Comput. Phys. Commun., 183, 530
Kühl, P., Dresing, N., Dunzlaff, P., et al. 2013, Proceedings of 33th International Cosmic Ray Conference (ICRC 2013)
Lange, D., & Fichtner, H. 2008, A&A, 482, 973
McDonald, F. B., Cline, T. L., & Simnett, G. M. 1972, J. Geophys. Res., 77, 2213
McKibben, R. B., Anglin, J. D., Connell, J. J., et al. 2005, J. Geophys. Res. Space Phys., 110, A09S19
Moses, D. 1987, ApJ, 313, 471
Nndanganeni, R. R., & Potgieter, M. S. 2018, Astrophys. Space Sci., 363, 156
Palmaerts, B., Roussos, E., Krupp, N., et al. 2016, Icarus, 271, 1
Palmer, I. D. 1982, Rev. Geophys. Space Phys., 20, 335
Pei, C., Bieber, J. W., Burger, R. A., & Clem, J. 2010, J. Geophys. Res. Space Phys., 115
Potgieter, M. S. 1996, J. Geophys. Res., 101, 24411
Potgieter, M. S., & Ferreira, S. E. S. 2002, J. Geophys. Res. Space Phys., 107, 1089
Potgieter, M. S., & Vos, E. E. 2017, A&A, 601, A23
Pyle, K. R., & Simpson, J. A. 1977, ApJ, 215, L89
Roussos, E., Krupp, N., Mitchell, D. G., et al. 2016, Icarus, 263, 101
Shalchi, A., 2009, Nonlinear Cosmic Ray Diffusion Theories, Astrophysics and Space Science Library (Switzerland: Springer), 326
Stone, E. C., Cummings, A. C., McDonald, F. B., et al. 2013, Science, 341, 150
Strauss, R. D. T., & Effenberger, F. 2017, Space Sci. Rev., 212, 151
Strauss, R. D., Potgieter, M. S., Kopp, A., & Büsching, I. 2011a, J. Geophys. Res. Space Phys., 116, A12105
Strauss, R. D., Potgieter, M. S., Büsching, I., & Kopp, A. 2011b, ApJ, 735, 83
Strauss, R. D., Potgieter, M. S., & Ferreira, S. E. S. 2013, Adv. Space Res., 51, 339
Tautz, R. C., & Shalchi, A. 2013, J. Geophys. Res. Space Phys., 118, 642
Teegarden, B. J., McDonald, F. B., Trainor, J. H., Webber, W. R., & Roelof, E. C. 1974, J. Geophys. Res., 79, 3615
Vogt, A., Heber, B., Kopp, A., Potgieter, M. S., & Strauss, R. D. 2018, A&A, 613, A28
Zhang, M., Qin, G., Rassoul, H., et al. 2007, Planet. Space Sci., 55, 12
Zhang, X.-J., Thorne, R. M., Ma, Q., et al. 2017, Geophys. Res. Lett., 44, 4472

Chapter C

Vogt et al. (under rev.)

Astronomy & Astrophysics manuscript no. output
February 22, 2021

Numerical and experimental evidence for a new interpretation of residence times in space

A. Vogt[1], N. Eugene Engelbrecht[2], B. Heber[1], A. Kopp[2,3], and K. Herbst[1]

[1] Institut für Experimentelle und Angewandte Physik, Christian-Albrechts Universität zu Kiel, Leibnizstraße 11, D-24118 Kiel, Germany
e-mail: vogt@physik.uni-kiel.de
[2] Centre for Space Research, North-West University, 2520 Potchefstroom, South Africa
[3] Theoretische Physik IV, Ruhr-Universität Bochum, Universitätsstr. 150, 44801 Bochum, Germany

ABSTRACT

Aims. We investigate the energy dependence of Jovian electron residence times, which allows for a deeper understanding of adiabatic energy changes that occur during charged particle transport as well as of their significance for simulation approaches. Thereby we seek to further validate an improved approach to estimate residence times numerically by investigating the implications on previous analytical approaches and possible effects detectable by spacecraft data.
Methods. Utilizing a propagation model based on a Stochastic Differential Equation (SDE) solver written in CUDA, residence times for Jovian electrons are calculated over the whole energy range dominated by the Jovian electron source spectrum. We analyse the interdependences both with the magnetic connection between observer and the source as well as between the the distribution of the exit (simulation) times and the resulting residence times.
Results. We point out a linear relation between the residence time for different kinetic energies and the longitudinal shift of the 13 month periodicity typically observed for Jovian electrons and discuss the applicability of these findings to data. Furthermore we utilize our finding that the simulated residence times are approximately linearly related to the energy loss for Jovian and Galactic electrons and develop an improved analytical estimation in agreement with the numerical residence time and the longitudinal shift observed by measurements.

Key words. astroparticle physics – convection – diffusion – interplanetary medium – methods: numerical – Sun: heliosphere

1. Introduction

In order to estimate the residence times of charged particles in the context of Stochastic Differential Equation (SDE) modelling, Vogt et al. (2020) proposed a new approach with results more realistic than the ones by previous attempts. This study will investigate further the energy dependence of residence times regarding how they are related to adiabatic energy changes as modelled by the Parker Transport Equation (TPE) (see Parker 1965) in particular. Therefore, we will re-examine the suggested calculation of residence times with respect to the influence of adiabatic energy changes and investigate the relation between these two quantities. In the following we expand our considerations from the inter-dependence of residence times and adiabatic energy changes within the SDE modelling scheme and discuss the consequences of our results for the understanding of diffusion approaches within the physics of charged particle transport in general. Finally we compare prediction based on our results to spacecraft obtained by SOHO-EPHIN.

We will analyse the distribution of simulation or exit times as provided by the SDE approach with respect to their contribution to the residence times. As Vogt et al. (2020) focused on 6 MeV Jovian electrons, this work subsequently aims to expand the focus to energies covering the whole observed range of $E_{Jov} = [0.3, 100.0]$ MeV as indicated by the Jovian source spectrum according to Vogt et al. (2018). The goal is to gain further insights as to the role that adiabatic energy changes play relative to diffusion to mathematically model charged particle propagation. In order to do this, we implement a parallel and perpendicular mean free path independent from the particle's energy as discussed in Sec. 2.3 by Eq. (3).

In that regard we will also discuss the analytical attempts to estimate the residence times of Galactic Cosmic Rays (GCRs), namely by Parker (1965) and O'Gallagher (1975). In order to confirm our considerations , we discuss the possibility to validate our results via qualities of spacecraft data caused by the corotation of the Jovian source relative to the observer during the particles propagation. By that means we aim to establish that the estimation for the residence time as proposed by Vogt et al. (2020) is consistent both with the analytical treatment of the TPE as well as with observations of Jovian electrons.

2. Scientific Background

2.1. Jovian electrons

Jupiter has been known as a source of an electron population dominating the inner heliosphere in the low-MeV range since the early 1970s. After being proposed by McDonald et al. (1972), based on a characteristic 13 month periodicity in electron counting rates obtained at Earth orbit, the *Pioneer 10* flyby was able to prove the origin of this phenomenon at the Jovian magnetosphere. Teegarden et al. (1974), as well as Pyle & Simpson (1977), showed that the 13 month periodicity was indeed linked to the synodic period of Jupiter, and that the source could be approximated to be point-like.

These two unique qualities, the point-like nature of the source itself and its decentral position, led to ongoing efforts to model Jovian electron propagation, beginning with Conlon (1978). Since the decentral position causes changes in the magnetic connectivity between Jupiter and a possible observer, Jovian electrons are especially suited to serve as test particles to investigate parallel and perpendicular diffusion coefficients. Previous studies on this have been published by (e. g. Chenette et al. 1977; Fichtner et al. 2000; Zhang et al. 2007, and references therein). Furthermore, a significant influence of drift effects on low-MeV electron transport has been ruled out both from a modelling (e. g. Potgieter 1996; Burger et al. 2000; Ferreira & Potgieter 2002) as well as from a theoretical perspective (e. g. Bieber et al. 1994; Engelbrecht & Burger 2010, 2013).

The source spectrum itself remained a topic of research as well , due to the general difficulties in measuring electron spectra, as detailed by (e. g. Heber et al. 2005; Kühl et al. 2013). Based on both *Pioneer* 10 flyby and Earth orbit data (e. g. Teegarden et al. 1974; Baker & van Allen 1976; Eraker 1982; Ferreira et al. 2001a, amongst others) published suggestions on both the general shape of the spectrum and its strength. A recent estimation based on the *Pioneer* 10 and *Ulysses* flyby data, as published by Heber et al. (2005) in the meantime, has been given by Vogt et al. (2018) and is utilized for this study.

2.2. SDE based modelling

Knowing the shape and strength of the source as accurately as possible is important in order to normalize simulation results. In case of solving the TPE by Parker (1965) by the means of SDEs the relation appears as follows: instead of solving the TPE itself as a differential equation, a corresponding set of Langevin equations is solved as described, for instance, by Strauss et al. (2011a):

$$
\begin{aligned}
dr &= \left[\frac{1}{r^2}\frac{\partial}{\partial r}(r^2\kappa_{rr}) + \frac{1}{r\sin\theta}\frac{\partial \kappa_{r\phi}}{\partial \phi} - u_{SW}\right]ds \\
&\quad + \sqrt{2\kappa_{rr} - \frac{2\kappa_{r\phi}^2}{\kappa_{\phi\phi}}}d\omega_r + \frac{\sqrt{2\kappa_{r\phi}}}{\kappa_{\phi\phi}}d\omega_\phi \\
d\theta &= \left[\frac{1}{r^2\sin\theta}\frac{\partial}{\partial\theta}(\sin\theta\kappa_{\theta\theta})\right]ds + \frac{\sqrt{2\kappa_{\theta\theta}}}{r}d\omega_\theta \\
d\phi &= \left[\frac{1}{r^2\sin^2\theta}\frac{\partial\kappa_{\phi\phi}}{\partial\phi} + \frac{1}{r^2\sin\theta}\frac{\partial}{\partial r}(r\kappa_{r\phi})\right]ds + \frac{\sqrt{2\kappa_{\phi\phi}}}{r\sin\theta}d\omega_\phi \\
dE &= \left[\frac{1}{3r^2}\frac{\partial}{\partial r}(r^2 u_{SW})\Gamma E\right]ds, \qquad (1)
\end{aligned}
$$

with $\Gamma = (E + 2E_0)/(E + E_0)$, $\kappa_{rr/r\phi/\phi\phi/\theta\theta}$ being the entries of the diffusion tensor $\hat{\kappa}$ in spherical coordinates aligned to the Heliospheric Magnetic Field (HMF) as derived e.g. by Burger et al. (2000) and ds the time-backward time increment. In order to solve Eq. (1) an iterative Euler-Maruyama scheme is used which produces a set of random walk type solutions. This is due to the way the SDE approach treats the stochastic nature of diffusion by impementing a Wiener process $d\omega = \zeta\sqrt{dt}$ with ζ being a stochastic element as a vector of Gaussian distributed random numbers. The solutions can be described as point-like solutions of the time-dependent distribution function $f(\mathbf{r}, t)$ covering the whole phase space as described by the TPE. As illustrated in Fig. 1, the temporal evolution of the solutions form trajectories through the phase space. In case of a time-backward approach as utilised for this study (see e.g. Kopp et al. 2012; Strauss & Effenberger 2017) and depicted by Fig. 1, the injection point can be understood as the observational point and the phase-space trajectories follow a random walk to three possible sources, which are implemented as boundary conditions according to (Dunzlaff et al. 2015):

- The Sun, indicated in yellow (such trajectories are neglected in this study due to the lack of a significant Solar component in high-keV and low-Mev energy range of electrons)
- The Jovian magnetosphere, indicated in orange (source spectrum according to Vogt et al. (2018))
- The Heliopause, indicated in blue (the local interstellar spectrum of galactic cosmic-ray electrons)

Usually the point-like solutions of the SDEsin space and time are interpreted as a set of pseudo-particles. Thus, the phase-space trajectories as illustrated in Fig. 1 could be understood as describing the propagation of particle samples. But this interpretation bears the problem that the solutions of the SDEs are inherently of mathematical nature and could represent a varying number of physical particles (see Kopp et al. 2012; Strauss & Effenberger 2017; Vogt et al. 2020, amongst others). Therefore if we refer to the temporal evolution of the solutions in the following we will address them plainly as phase-space trajectories.

Since the phase space trajectories are mathematical solutions they are (and in contrast to a physical interpretation) equally probable. In order to be comparable with spacecraft data therefore a large number of phase space trajectories has to be sampled and weighted according to their physical significance in order to approximate a spatial solution. Thereby the corresponding source spectrum serves as a boundary weight (see, e. g., Strauss et al. 2011a; Kopp et al. 2012) in order to determine the contribution to the differential intensity as a physical quantity (or the physical likelihood of the phase space trajectory, respectively). As illustrated on the right side of Fig. 1 each radial step results in adiabatic energy losses (or gains in the time-backward approach) as obtained by the modelling approach according to Eq. (1) until the boundary is reached. Then the trajectories are weighted with the source spectrum of this exit energies E^{exit} and the number of phase-space trajectories N as since strength of the source indicates how likely a particle measured at the observational point with an initial energy E^{init} has left the source with E^{exit}. This means, as sketched by Fig. 1, that the phase-space trajectories effectively are weighted by the differential intensities at the source corresponding to their adiabatic energy gain. In case of the Jovian source spectrum $j_{jov}(E)$ this leads to the expression

$$
j_{jov} = \frac{\sum_{i=1}^{N} j_{jov}(E_i^{exit})}{N} \qquad (2)
$$

The distribution function f is the solution of the TPE, and is related to the differential intensity by $j = P^2 f$, where $P = pc/q$ is the rigidity of the electrons corresponding to the momentum p and the charge q, as well as to the speed of light c, , see e.g. Moraal (2013)

2.3. The numerical setup

In continuation of the work presented in Vogt et al. (2020), the same SDE code as discussed by Dunzlaff et al. (2015) was utilized in order to perform the simulations. Since it is written in CUDA in order to optimize the the performance time, several simplifications haven been made due to the limited internal memory on Graphic Processing Units (GPUs). The solar wind velocity is chosen to be directed radially outward and constant

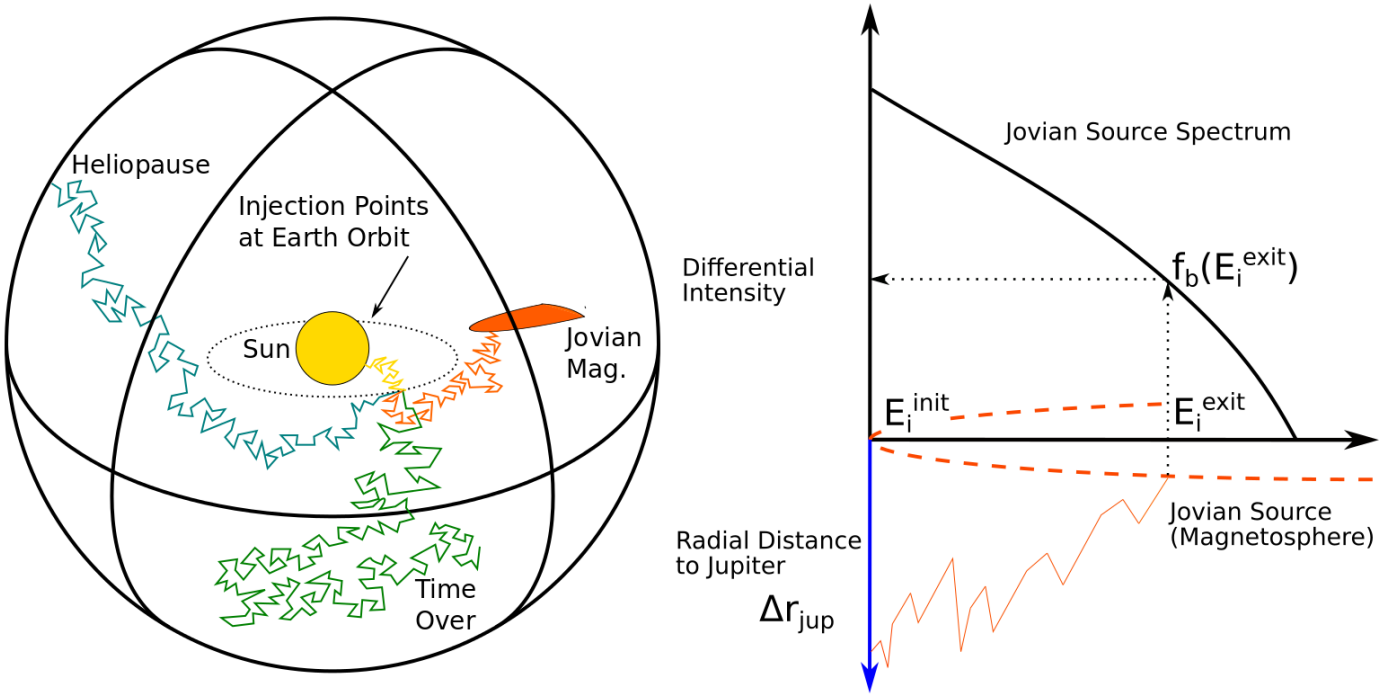

Fig. 1: The simulation setup according to Vogt et al. (2020). On the right side a visualisation is shown of how the Jovian source spectrum determines the resulting differential intensity. The sketch thereby is to be read from bottom to top. The pseudo-particle is injected with an initial energy E_i^{init} at a certain distance from the Jovian source. When the pseudo-particle's phase-space trajectory hits the source (the dashed representation of the Jovian magnetosphere) with an exit energy E_i^{exit} it is convoluted with the source spectrum as the boundary condition. Subsequently the differential intensity is calculated as $\sum_i f_b(E_i^{exit})$. The dashed representation of the Jovian magnetosphere only serves an illustrative purpose.

throughout the simulation setup. Following the deeper discussion on parameter setting by Vogt et al. (2020) the value is set to u_{SW} = 400 km/s, in agreement with solar minimum conditions. The corresponding HMF is assumed to be Parker-like. The HMF geometry enters into the transformation of the diffusion tensor, done here according to the approach of Burger et al. (2000).

The mean free paths determining the diffusion tensor are included and are based on the simplified, energy-independent approach applied successfully by (e. g. Strauss et al. 2011a,b, amongst others): $\lambda_\parallel$ is normalised at r_0 = 1 AU, such that

$$\lambda_\parallel(r) = \frac{\lambda_0}{2}\left(1 + \frac{r}{r_0}\right). \tag{3}$$

An energy dependence, however, does enter into the diffusion coefficient by way of its standard definition, viz. $\kappa = v\lambda/3$ (see, e.g., Shalchi 2009), with v being the particle speed . Again following previous studies, the perpendicular diffusion coefficient is assumed to be proportional to the parallel diffusion coefficient by a constant factor χ such that

$$\kappa_\perp(r) = \chi\kappa_\parallel(r). \tag{4}$$

For the purposes of the present study, these simplified transport parameters serve to qualitatively emulate the behaviour in the inner heliosphere of more theoretically-motivated expressions for the same employed in *ab initio* particle transport studies (see, e.g., Engelbrecht & Burger 2013; Engelbrecht 2019). For instance, the energy-independence of $\lambda_\parallel$ over the range of (low) energies considered in this study reflects the behaviour of electron parallel mean free paths derived from quasilinear theory (see, e.g., Teufel & Schlickeiser 2003; Engelbrecht & Burger 2010; Dempers & Engelbrecht 2020), as well as what is expected from observations (e.g. Bieber et al. 1994). The energy independent perpendicular mean free path is chosen to reflect the energy dependence expected from observational (e.g. Palmer 1982) and modulation studies (e.g. Burger et al. 2000) at the energies relevant to this study, and does not differ much from the relatively weak energy dependences of perpendicular mean free paths derived from theory (see, e.g., Shalchi 2009; Burger et al. 2008; Engelbrecht & Burger 2015; Engelbrecht 2019).

Tab. 1 shows the choice of parameters used within this framework as motivated and tested by Vogt et al. (2020). In order to do so the authors performed a set of parameter studies varying the 'computational' parameters. The set of values listed in Tab.1 was found to be a trustworthy compromise between the need to keep the simulation time low and to assure that the results are converging. Also the radius of the model setup R_{HP} is chosen specifically because a smaller setup can influence the simulation results, as demonstrated by that study. The parallel mean free path $\lambda_\parallel$ was determined by simulating the Jovian electron spectrum at Earth orbit during times of good magnetic connection at which the particle transport can be assumed to be dominated by parallel diffusion. Fig. 2 shows the results of this study over an extended energy range, covering the whole range of interest of the Jovian source spectrum, as opposed to the single energy considered by Vogt et al. (2020). In case of good magnetic connection to the source, the parallel mean free path $\lambda_\parallel$ seems to be only slightly energy dependent within the constraints of our modelling approach, although in contrast to the limited energy range investigated by (Vogt et al. 2020) $\lambda_\parallel$ = 0.125 AU appears to be more in agreement with the simulation results covering the extended energy range. Therefore, the value listed in Tab. 1 appears

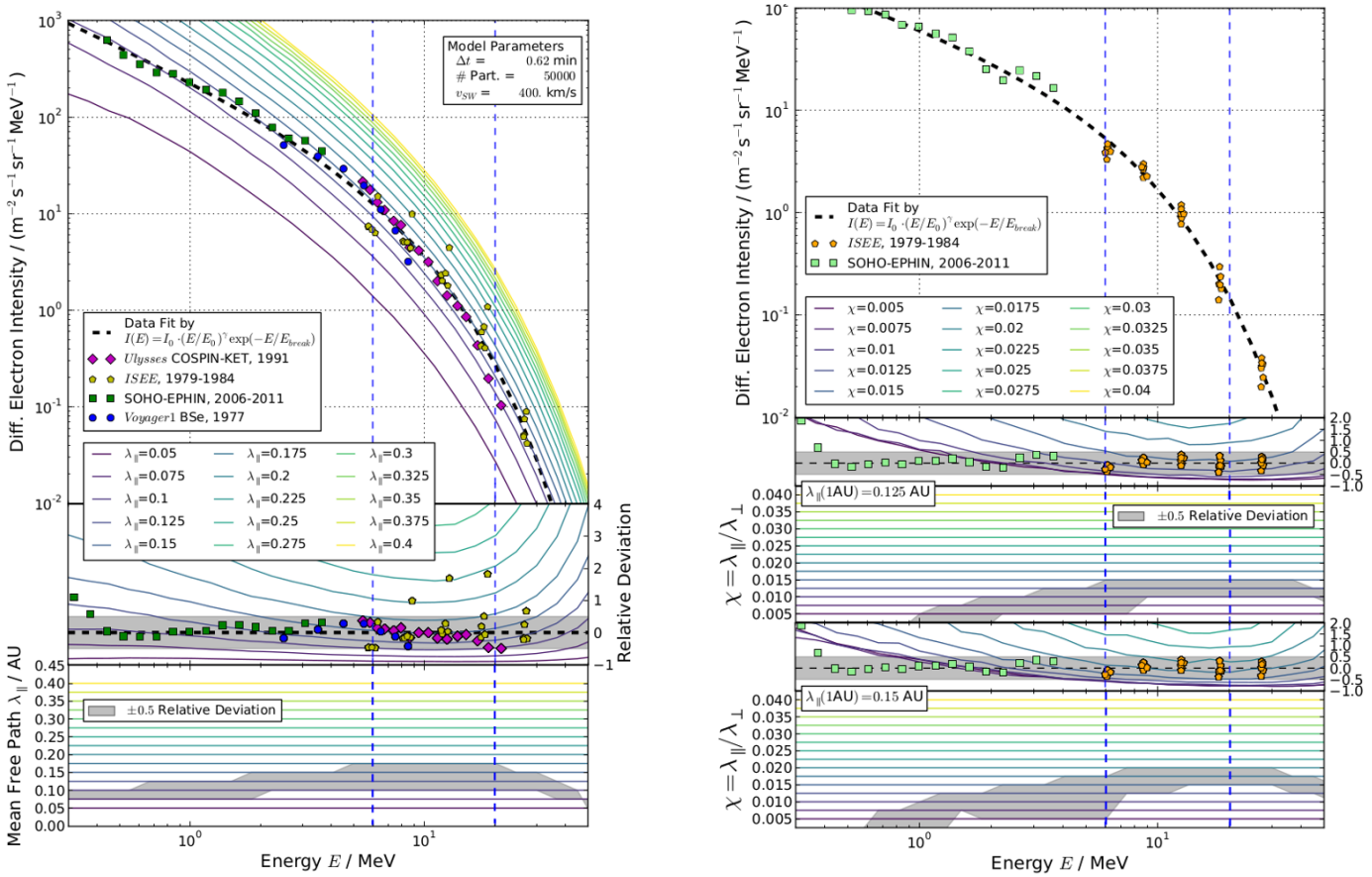

(a) (b)

Fig. 2: Simulated Jovian electron spectra, similar to the Figures by Vogt et al. (2020) but covering the whole energy range of the Jovian source where the energy range previously investigated by Vogt et al. (2020) is indicated by the two dashed blue lines. The left panel shows on top the Earth orbit spectral data in case of good connection to the source alongside with a data fit (dashed black line). The simulation results for different values of $\lambda_{\parallel} = [0.05, 0.4]$ AU are color coded. The middle panel of Fig. 2a shows the corresponding relative deviation to the source spectrum for both data and simulation results, with the area of ±0.5 deviation indicated in grey. The bottom panel shows the resulting energy dependence of the parallel mean free path. The right panel displays the corresponding results for different values of $\chi = [0, 0005, 0.045]$ in case of bad connection. Again, the top panels shows the Earth orbit spectral data alongside a data fit indicated in dashed black. The relative deviations and resulting energy dependencies are shown for $\lambda_{\parallel} = 0.125$ AU (second and third panel) and $\lambda_{\parallel} = 0.15$ AU (fourth and fifth panel).

to produce results that are most in agreement with spacecraft data at Earth orbit during comparable conditions. Likewise χ was determined by applying the result for $\lambda_{\parallel}$ and comparing the results of simulation runs with different values of χ to Jovian electron spectra obtained during times of poor magnetic connection as shown in Fig. 2b, where perpendicular diffusion is expected to be the predominant mechanism governing the transport of these electrons. As can be seen for both cases of $\lambda_{\parallel} = 0.125$ AU (second and third panel) and $\lambda_{\parallel} = 0.15$ AU (fourth and fifth panel) the energy dependence of χ is more prominent. It is worth noting that the decrease of χ is located in the keV-range. As discussed by Vogt et al. (2018), the Jovian source spectrum below the MeV range can only be determined by utilizing *Pioneer 10* flyby data by Teegarden et al. (1974), which has to be re-normalised, and *SOHO* data by Kühl et al. (2013) at Earth orbit, which shows a variation in its steepness below 1 MeV. These two uncertain influences on the source spectrum could translate into uncertainty of the behaviour of χ at these energies. Nevertheless regarding the whole energy range of the Jovian source spectrum serves the important purpose of clarifying whether or not effects seen in both the weighted and unweighted simulation results are caused by energy dependent effects. Regarding the choice of transport parameters, the broader energy range in which χ appears to be energy independent for $\lambda_{\parallel}$ further supports the choice of this slightly lower value relative to that used by Vogt et al. (2020). In order to maximise the energy range with a physical reasonable choice, $\chi = 0.0125$ was used for the simulation within this study as listed alongside the other parameters in Tab. 1.

2.4. The influence of boundary conditions

The effect of applying Eq. (2) is shown by Fig. 3. The panels on the left display the binned distribution of phase-space trajectories according to their exit energies for good (top panel) and bad magnetic connection to the source (middle panel) as well as the difference between them, assuming a Parker field. On the

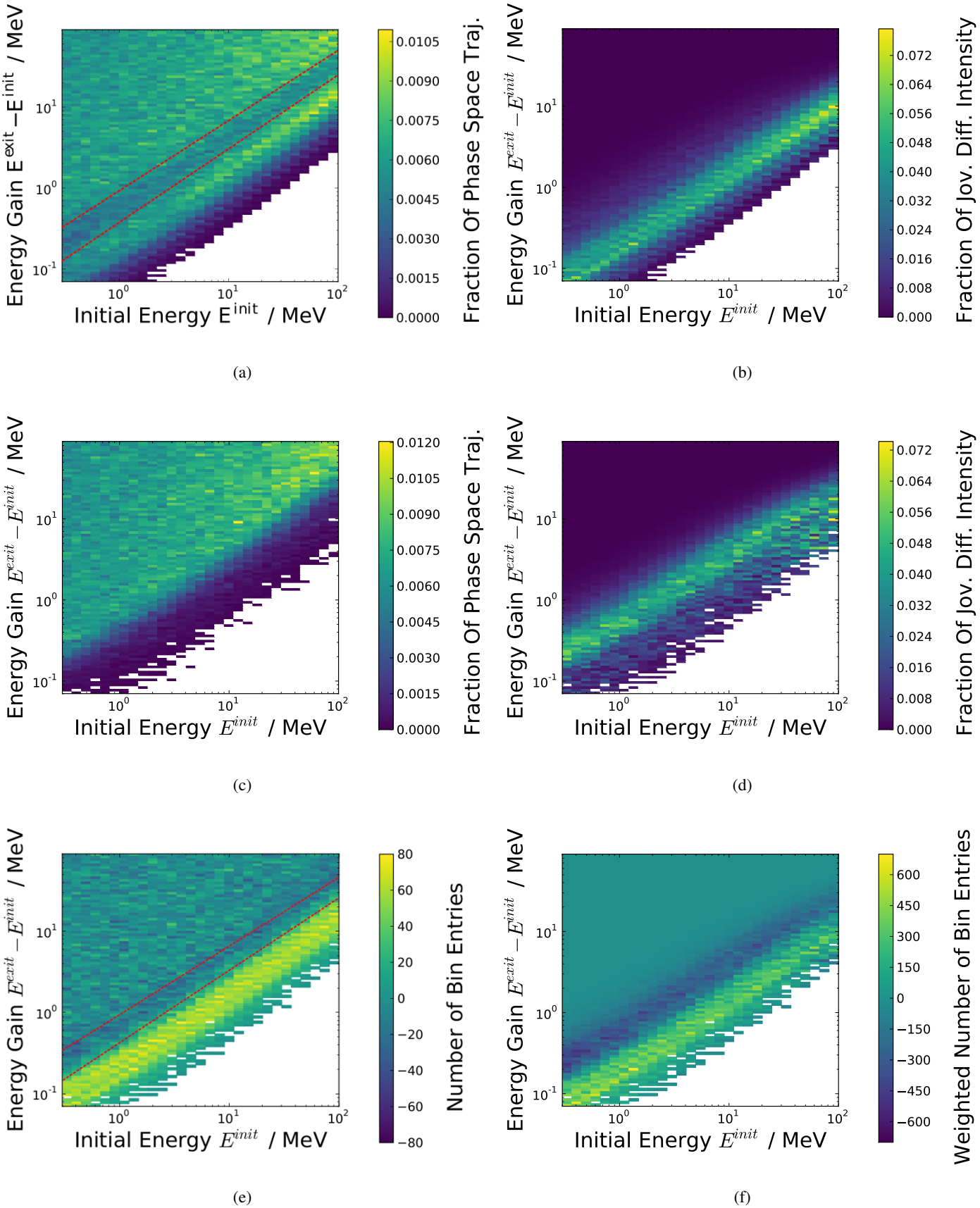

(a) (b) (c) (d) (e) (f)

Fig. 3: Binned distributions of exit energies E_i^{init} over the whole energy range dominated by Jovian electrons. Whereas the right panels show them weighted by their contribution according to Eq. (2), the left side displays the unweighted results of the simulation. The upper most panels Figs. 3a and 3b show the case of good magnetic connection to the source, whereas Figs. 3c and 3d show the case of bad magnetic connection. The differences between those distributions are depicted by the two lower panels, Figs. 3e and 3f.

Table 1: The computational and physical parameters used for the code (when not stated otherwise).

Computational Parameters	
# Trajectories	50000
Δt	0.0001
T_{End}	800
Physical Parameters	
R_{HP}	120 AU
u_{SW}	400 km/s
$\lambda_{\parallel}$(1 AU)	0.125 AU
$\chi = \lambda_{\perp}/\lambda_{\parallel}$	0.0125
E^{init}	6 MeV

right side the corresponding distributions are shown if Eq. (2) is applied and the phase-space trajectories are therefore weighted according to their physical significance. In both cases the distributions are normalized to one. In order to interpret the results in general, and in particular the relation between the distributions of the trajectories and the differential intensities, Fig. 3a displays an important feature. As marked by two dashed red lines, a sink in the intensity can be spotted throughout the whole energy range. It is important to note that it is directly located above the highest intensities shown by the phase-space trajectories, which are associated with very low energy gains. The comparison with Fig. 3c shows that the intensity sink in Fig. 3a appears where the phase-space distributions in the case of bad magnetic connection to the source become significant. This shift of the maximum of the distributions according to the magnetic connection to the source is also visible by Figs. 3b and 3d for the weighted contribution to the resulting differential intensities.

In order to interpret this behaviour the difference between the distribution for good and bad magnetic connection is shown by Figs. 3e and 3f. As noted above, both Figures display the differences between the distributions, Fig. 3e the number of trajectories in each bin and Fig. 3f the sum of the weight of these trajectories according to the source spectrum. For both Figures the color coding is defined symmetrically around zero. This highlights the important fact that despite some negative bins in the difference distributions which mostly located within the area of the intensity sink, there is either an equal amount of or more bin entries (and therefore phase-space trajectories attributed to Jovian electrons) for the case of good magnetic connection to the Jovian source. Whereas this in itself is not an unexpected result, it is remarkable that the distinct maximum of this difference distribution is located below the intensity sink in Fig. 3a which is indicated by two dashed red lines. Therefore the maximum below the intensity sink in Fig. 3a (which is identical with the population of phase-space trajectories responsible for almost the entire contribution to the resulting differential intensity according to Fig. 3b) has to be attributed to parallel diffusion-dominated transport. Since propagation parallel to the nominal Parker spiral is the most effective mechanism for charged particle transport, it can be expected as being related to both shorter simulation times (i.e. amounts of random walk steps to perform the corresponding phase-space trajectory) as well as lower energy gains. That explains why this population of trajectories is absent in Fig. 3c showing the phase-space trajectory distribution in case of bad magnetic connections.

We therefore can interpret the simulation results as displayed in Fig. 3 as follows: Since the left upper triangle of the panels showing the phase-space trajectory distributions seems to no vary with respect to the degree of magnetic connection, this population can be interpreted as a kind of diffusive background. By this we aim to describe the fact that these trajectories appear to represent a population which exists, in a sense, independently of the physical propagation conditions. This interpretation which is further supported by the fact that according to the corresponding panels on the right side of Fig. 3, this population has almost no physical significance with respect to the resulting differential intensities. Therefore it can be assumed that energy gains of more than half an order of magnitude most likely correspond to phase-space trajectories of low physical probability. With respect to Figs. 3e and 3f we can conclude that the (physical) variation of intensities is caused by the (mathematical) variation of the maximum of the distribution of the phase-space trajectories below the intensity sink.

3. Modelling of residence times

Within the mathematical framework of the Parker (1965) TPE, the residence time corresponding to the evolution of the particles probability density ρ is defined as the expectation value of the time according to

$$\tau = \frac{\int \rho(\mathbf{x}, t) t dt}{\int \rho(\mathbf{x}, t) dt}. \tag{5}$$

As Vogt et al. (2020) pointed out, this approach can not be transformed into SDE modelling by simply averaging over the pseudo-particles' exit times. Instead ρ is proposed to be the distribution of particle density as

$$\rho(\mathbf{x}, t) = \frac{f(\mathbf{x}^{exit}, t)}{f_0(\mathbf{x})} \tag{6}$$

and normalized by the total phase-space density

$$f_0(\mathbf{x}) = \int f(\mathbf{x}^{exit}, t) dt. \tag{7}$$

Thereby $f_0(\mathbf{x})$ cancels out in Eq. (5). Applied to the discrete case of phase space trajectories as the output of an SDE code, Eq. (5) reads as

$$\tau(r^0, E^0) = \frac{\sum_{i=1}^{N} s(E_i^{exit}) \cdot f(E_i^{exit})}{\sum_{i=1}^{N} f(E_i^{exit})}, \tag{8}$$

with s as the exit (integration) time corresponding to the different phase space trajectories. Compared to the calculation of differential intensities by applying Enq. 2, this approach appears to the self consistent as each phase space trajectory is attributed the same significance due to it's exit energy in both cases. For 6 MeV Jovian electrons, Vogt et al. (2020) shows further that the residence times obtained via Eq. (8) are between $\sim 5 - 11$ days, depending on magnetic connectivity, and are therefore shorter by almost two orders of magnitude when compared to previous estimations (see e.g. Strauss et al. 2011b; Vogt et al. 2020, and references therein).

3.1. Adiabatic energy changes and the role of the source spectrum

According to Eq. (8) the contribution of each phase-space trajectory depends on its exit time $s(E_i^{exit})$, more precisely on the differential intensity $f(E_i^{exit})$ corresponding to it within the source

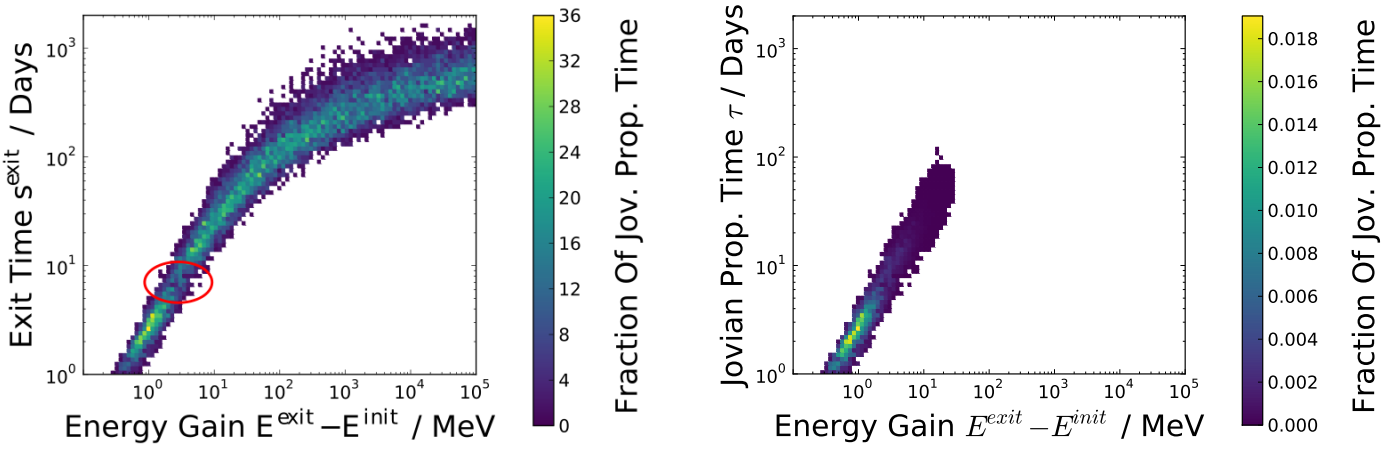

(a) (b)

Fig. 4: The relation between the energy gain $E_i^{exit} - E_i^{init}$ (or loss, in the normal time-forward scenario) as a function of the corresponding exit time s_i^{exit} (left panel) or propagation time (right panel), weighted by applying Eq. (8). The case of good magnetic connectivity is shown.

spectrum. Therefore it is necessary to investigate this relation further. Fig. 4 shows the relation between the energy gain and the exit times of the phase space trajectories unweighted by Eq. (8) (Fig. 4a) and weighted by their contribution to the residence time (Fig. 4b) for the case of good magnetic connectivity between the Jovian source and the observer. As discussed above by means of Fig. 3, the energy differences between the initial energies E_i^{init} and the exit energies E_i^{exit} are caused by adiabatic energy changes as given by Parker (1965) within the TPE. For the SDEs modelling approach as utilized here, the influence of this effect is included as follows: Whereas each subsequent iteration of the random walk increases the corresponding simulation time s_i by the the value of the time increment, the energy gain accompanying each step of the phase space trajectory is depending on energy and location. Therefore phase space trajectories of the same (time) length can be related to different rates of adiabatic energy changes $E^{exit} - E^{init}$ as illustrated in the right upper part of Fig. 4a. Given by

$$\frac{1}{E}\frac{dE}{dt} = -\frac{1}{3}\nabla u_{SW}, \tag{9}$$

according to Parker (1965) and Webb & Gleeson (1979), the relation of adiabatic energy changes to simulation times is almost linear in the logarithmic display within Fig. 4b. This is due to the fact that the divergence simplifies as $\nabla u_{SW} \approx 2u_{SW}/r$ for a constant radial solar wind speed and extremely relativistic particle such as the Jovian electron population. Since Fig. 4a consists of the simulation results displayed with respect to their initial energies E_i^{init} in Fig. 3b, the intensity sink discussed in Sec. 2.2 appears in Fig. 4a, too. The depiction (especially with respect to Fig. 4b) allows to deduce that according to the location of the intensity sink (red), phase-space trajectories corresponding to energy gains of more than half of an order of magnitude and a simulation time of more than eight days do not contribute significantly to the modelling results. This notion further supports the interpretation of Fig. 3 in Sec. 2.2 that this intensity sink segregates the physically significant population of phase-space trajectories from the (diffusive background) population which is shown in Fig.4a as a high energy gain and high exit time tail. The comparison with Fig. 4b validates this as the high energy gain and high exit time tail is shown to weighted down to effectively zero by the boundary conditions, i.e. the Jovian source spectrum.

These considerations suggest that the adiabatic energy changes implemented according to Eq. (9) always have to be considered in order to obtain physically reliable results as long as diffusive processes influence the particles propagation. As shown by Figs. 3 and 4 and discussed in detail in Sec. 2.2 the physical likeliness of mathematically equally possible phase-space trajectories is determined by the boundary conditions via the corresponding exit energy E_i^{exit}. Therefore, not considering adiabatic energy changes effectively assumes that the energy spectrum of the particle population of interest is flat and therefore each energy equally probable to occur. This relation is also shown on the right side of Fig. 1. The following Section investigates further the significant influence of the boundary conditions (and therefore adiabatic energy changes) on Jovian residence times over the whole Jovian energy range, as opposed to the results presented by Vogt et al. (2020) for only the low-MeV range. Subsequently these considerations and results will be applied to the analytical estimation of the GCR residence times as suggested by e.g. Parker (1965); O'Gallagher (1975); Strauss et al. (2011b).

3.2. Adiabatic Energy dependence of Jovian Residence Times

Taking also Fig. 5 into account in order to include the dependence of τ on the adiabatic energy changes, the intensity sink as indicated in red is confirmed over the whole energy range of interest. The right panels show the histograms for the exit times at the Jovian boundary considering each to be of equal probability, while the left panels show their contribution to the residence time according to Eqn 8. From top to bottom, first the case of good magnetic connectivity between observer and the source is shown, followed by the case of poor magnetic connectivity and the difference of the two sets of histograms. Similar to Fig. 3e which shows the difference of the phase-space trajectory distributions with respect to their corresponding exit energies, also

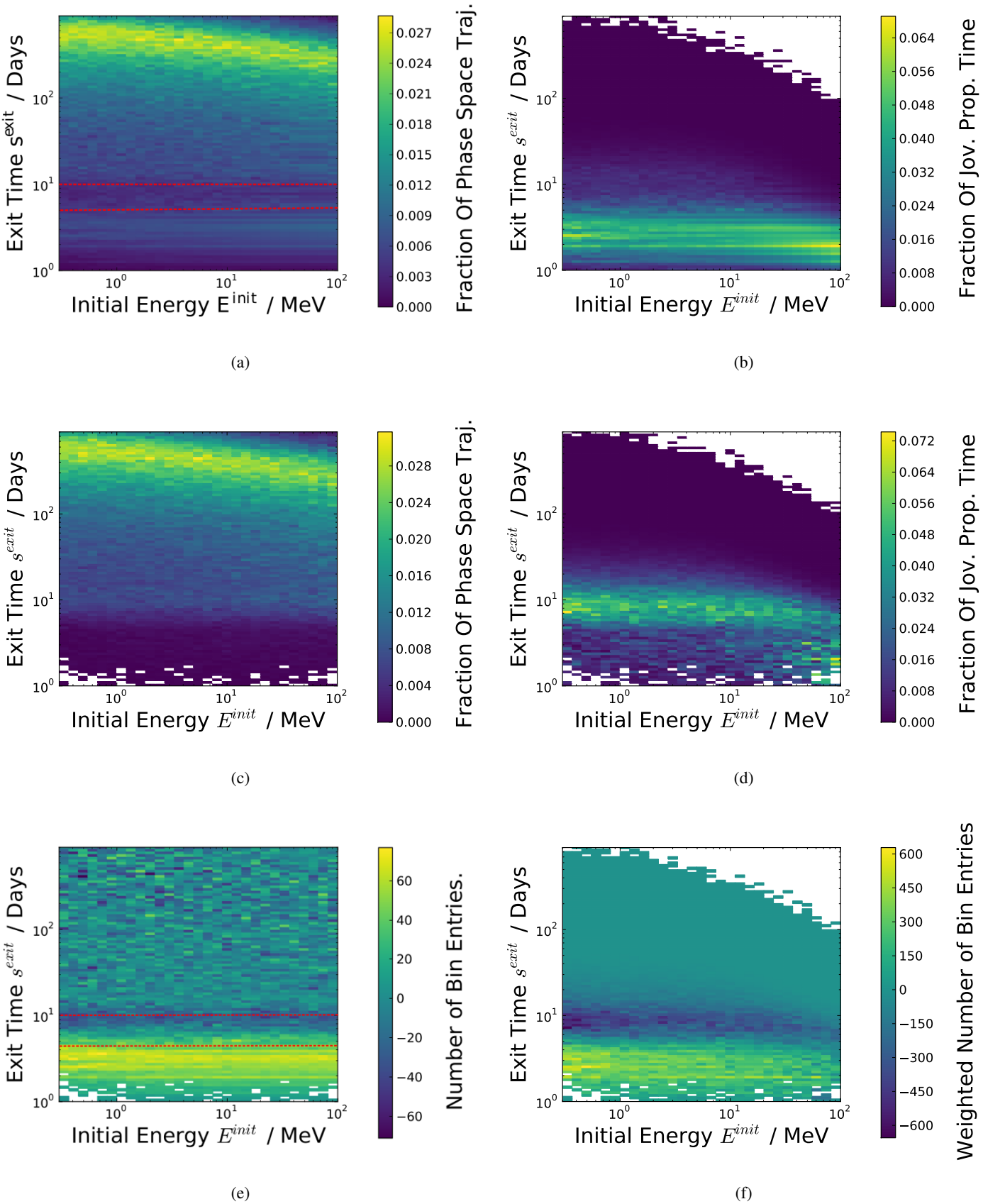

Fig. 5: Binned distributions of exit times over the whole energy range dominated by Jovian electrons, displayed similarly to Fig. 3. Whereas the right panels show them weighted by their contribution according to Eq. (8), the left side displays the unweighted results of the simulation. The first row (Figures 5a and 5b) shows the distributions in case of good the second in case of bad connection. Figures 5e and 5f show the differences between the distributions for good and bad connection, highlighting the influence of magnetic connectivity on the simulation results

the difference of the phase-space trajectory distributions with respect to their corresponding exit times (Fig. 5e) shows a significant maximum below the intensity sink (red). This reflects the relation shown by Fig. 4a. The comparison with Fig. 5f confirms that these trajectories indeed determine the residence time almost entirely. As discussed in detail above , this further supports that the population of pseudo-particles performing trajectories dominated by the perpendicular diffusion process exits almost independently from the magnetic connection between the source and the observer. The population corresponding to small exit times and low adiabatic energy gains however seems to determine the resulting residence times as it determines the resulting differential intensities. Since both small exit times and low adiabatic energy gains indicate a very effective particle transport, it is reasonable to identify this population as being dominated by particles whose transport is governed by the parallel diffusion process as suggested by Vogt et al. (2020).

In the case of poor magnetic connection however, Fig.5c lacks the parallel diffusion-dominated population, but otherwise shows a similar shape. This overall similarity seen both in case of exit energies (Fig. 3) and exit times strongly suggest that this population is dominated by perpendicular transport processes. Again, the comparison with the corresponding contribution to the total differential intensity, as shown by Fig. 5d, suggests that the trajectories dominated by perpendicular diffusion processes could be considered as a 'diffusive background' since they neither change according to the degree of magnetic connection nor do they influence the physical results significantly. This is due to the fact that the pseudo-particles' trajectories are the results of a Wiener Process as the mathematical representation of Brownian motion. Although the concept of parallel diffusion mimics the actual physical particle motion in the case of good connectivity and therefore shows the significance illustrated by Figs. 5a and 5b, nevertheless the results as a whole have to be transformed according to Eq. (2) in order to assign a physically significant number of real particles to the pseudo-particles trajectories. This, as discussed in detail by Vogt et al. (2020), is of course equally applicable to the relation between the phase space trajectories exit times and the residence time as a result of applying Eq. (8).

The bottom panels of Fig. 5 confirm these assumptions: As demonstrated by Fig. 5e and 5f the 'diffusive background' disappears almost entirely if only the differences between the histograms for good and bad connectivity are shown. Therefore the suggested interpretation would be that the possibility to reach the Jovian boundary via a perpendicular diffusion-dominated trajectory does not depend on the magnetic connectivity between the boundary and the start or observational point. But with increasingly good connectivity the probability increases that trajectories dominated by parallel diffusion reach the boundary as well.

This effect is almost independent of the particle's energy. Although Fig. 5a shows slightly shorter maxima of s^{exit} for higher initial energies E^{init}, this effect is almost entirely limited to the population of trajectories which do not significantly contribute. The most prominent energy-dependent effect appears to be the increasing density of the distributions in Fig. 5b, leading to more distinct maxima as also slightly visible in Fig. 5a for the same exit times and initial energies, respectively. The fact that the intensity sink is present over the whole energy range further supports the interpretation of a 'diffusive background' and trajectories reflecting the physical behaviour of charged particles within the heliospheric magnetic field – as indicated by the fact that in case of good magnetic connection only the latter population seems to contribute to the resulting differential intensity and residence times.

4. Comparison of numerical and analytical approaches

The large discrepancy between between the maxima of the distribution of the exit times s^{exit} and the calculated residence times as displayed by the comparison of the left and right panels of Fig. 5 seems to be caused by the mathematical nature of the diffusion approach. As already outlined by Vogt et al. (2020) and discussed in Sec. 2.2 and especially Sec. 3.2 focusing on the role of adiabatic energy changes , the solutions of the SDE modelling have to be transformed into physically meaningful quantities by the means of the source spectrum as a boundary condition . A probable consequence becomes apparent in contrast to the analytical approximations of Parker (1965) and O'Gallagher (1975). Comparing these analytical estimations to the results of our approach to simulate the residence times shows a pattern of deviations similar to the deviations of the exit time distributions.

As the solution of the TPE is a four-dimensional probability density function of time, space and rigidity (or energy, respectively), the residence time can be derived from it as the expectation value of the time as discussed at the beginning of Sec. 3 by means of Eq. (5). In order to solve the TPE analytically, however, it has to be simplified. Therefore the assumptions are made by Parker (1965) (and subsequently all other analytical estimation as well so far) that κ and u_{SW} are constant scalar values in time and space . Further assumptions are the isotropy of the particles diffusing inwards as well as that the observational point of τ_x as given by Eq. (5) is assumed to be the center of a spherical heliosphere. Solving Eq. (5) under these assumptions yields a diffusion and a convection limit $\tau_D = R^2/(6\kappa)$ (see Parker 1965)' and $\tau_C = R/u_{SW}$ (see O'Gallagher 1975) , respectively. For a more detailed description of the derivation see alsoStrauss et al. (2011a), and references therein. Evidently both estimations are independent of the particle energy. The diffusion limit τ_D, however, incorporates an indirect dependence via the overall average value of the diffusion coefficient κ. The assumption of a globally constant value of κ (which does not depend on the radial distance nor differentiates between parallel and perpendicular diffusion processes)of course is not realistic for the case of Jovian electrons, which have transport properties that depend strongly on whether parallel or perpendicular diffusion dominates. Therefore Galactic electrons have to be taken into account in order to compare these estimations with simulation results. Although the same transport processes also govern the propagation of GCR electrons, their isotropic influx allows to estimate parallel and perpendicular diffusion into one value of κ according to e.g.Parker (1965). Nevertheless the results of Strauss et al. (2011b, 2013) who benchmarked their numerical estimation in case of GCR electrons against the analytical diffusion limit τ_D by Parker (1965, 1966) and a combined estimation of $\tau = (1/\tau_D - 1/\tau_C)^{-1}$, show in the Jovian electron case, that values of $\lambda_\parallel = \lambda_\perp \approx 1$ AU are required in order to obtain realistic values for the Jovian residence times, a result which is contrast to values successfully employed in modulation studies by e.g. Ferreira et al. (2001a,b); Kissmann et al. (2004); Sternal et al. (2011); Strauss et al. (2011a); Nndanganeni & Potgieter (2016), amongst others, as well as in contrast with what is expected from theory (e.g. Engelbrecht & Burger 2013; Dempers & Engelbrecht 2020; Shalchi 2020) and numerical test-particle simulations of diffusion coefficients (e.g. Minnie et al. 2007; Heusen & Shalchi 2016; Dundovic et al. 2020).

This discrepancy is most likely caused by the fact that neither of the analytical estimates incorporate the adiabatic energy changes, and therefore also neglect the boundary condi-

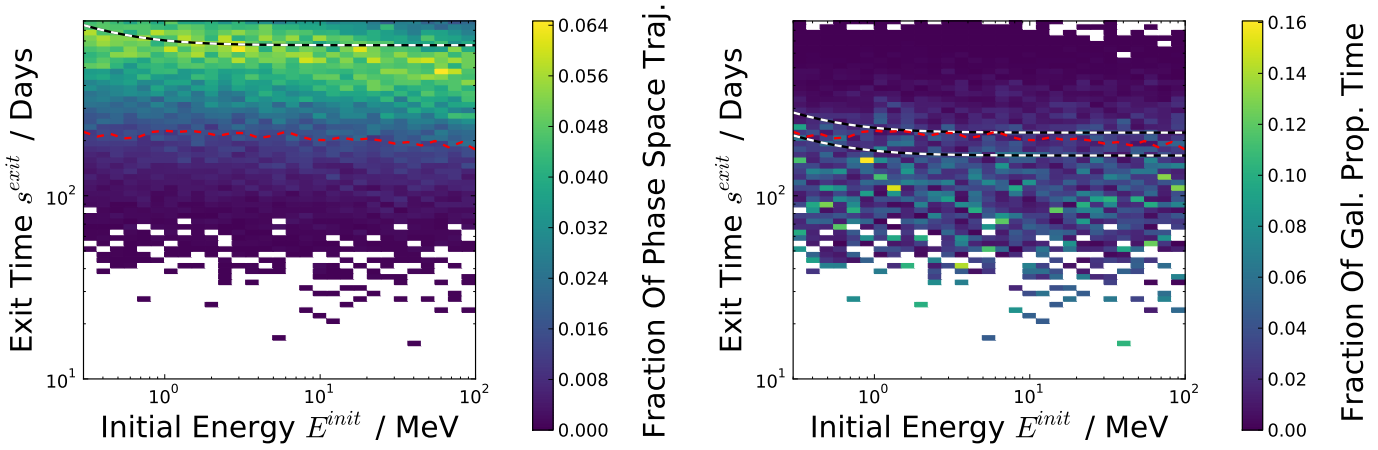

(a) (b)

Fig. 6: Similar to Fig. 5 but instead of the Jovian magnetosphere, trajectories exiting at the outer boundary are shown. Thereby the left panel shows the distribution of unweighted exit times s_i^{exit} of trajectories exiting at the outer boundary. Note that the maxima are in loose agreement with the analytical estimation as suggested by Parker (1965) given by the dashed white and black line . The right panel shows the influence of weighting with Eq. (8) together with numerical solution indicated in red and two estimations of the revised analytical solution given by Eq. (**??**).

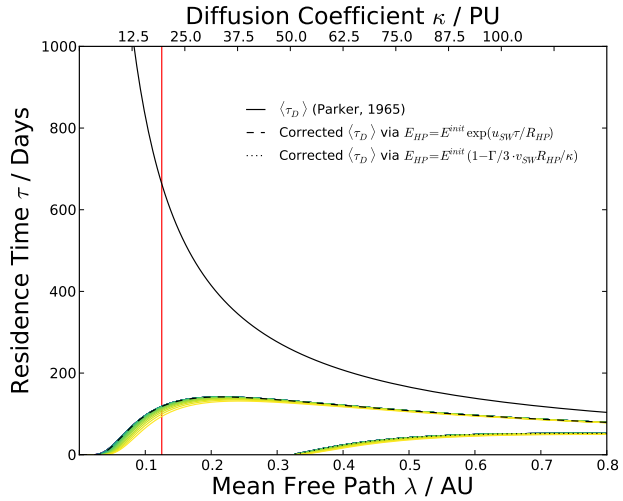

Fig. 7: The analytical estimate of the GCR residence time according to Parker (1965) with respect to the assumed mean free path λ (bottom x-axis) and the resulting diffusion coefficient κ (top x-axis). The two dashed lines show the corrected analytical estimates according to the estimations for the adiabatic energy loss by Eq. (10) and 11, respectively. Color coded from blue to yellow the resulting residence times are shown for the whole energy range of the Jovian spectrum (by 30 logarithmical spaced representive energies) as a measure of the uncertainty.

tions. As argued above in Sec. 3.1, the TPE is effectively solved for an isotropic diffusion approach with a flat energy spectrum. This simplification appears to be problematic because it neglects the physical constraints of charged particle transport theory. Most prominently the fact that the diffusive processes incorporated into the TPE describe stochastic processes associated with (pitch-angle) scattering at irregularities within the HMF as acknowledged by Parker (1965). Therefore the SDE method, as being mathematical equivalent, offers the possibility to depict the effect of the boundary conditions to the results of the TPE as visualised by Figs. 3 and 5. In order to avoid the consequences of over-simplifying within the analytical estimates, it therefore seems to be necessary to incorporate an analytical estimate of the boundary conditions as well.

For the purpose of these qualitative considerations, we used the galactic electron local interstellar spectrum (LIS) proposed by Potgieter et al. (2015) in order to apply Eq. (8) to the phase space trajectories exiting at the outer boundary equivalent to the way the Jovian residence times are calculated.

Indeed, Fig. 6 shows that the main effect of weighting the trajectories according to their contribution to the differential intensity determines the results for the Galactic population too. As one would expect, the analytical estimation of τ_d according to Parker (1965) (dashed white and black line) in Fig. 6a is in agreement with the unweighted distribution of exit times. The numerical estimation according to Vogt et al. (2020) , however, as shown by the red dashed line, strongly deviates similar to the case of the Jovian electron population . These findings confirm the our interpretation of adiabatic energy changes in order to transform the mathematical solution of the TPE into a physical and observationally meaningful one. Therefore, by neglecting any influence of adiabatic energy changes, implicitly one assumes an energy-independent source spectrum. Due to the adiabatic energy changes of particles, they are not detected with the energy they had a their source. In order to calculate the residence time of a particle detected with E^{init} = 6 MeV at the observational point one therefore would have to assume an energy of $E^{exit} = E^{init} + \Delta E$ at the source with ΔE being the average adiabatic energy change of the particle population. Since these two energies correspond to different intensities if the spectrum is not assumed to be flat (again, see the discussion in Sec. 3.1), the adiabatic energy changes can be transformed into intensity changes within this mathematical framework.

The approach to assume the characteristic energy change as being proportional to the initial energy is supported by Parker

(1965), who assumed the energy loss after a time t as being

$$E(t) \approx E_0 \exp(-tu_{SW}/R_{HP}) \tag{10}$$

and that t is not energy-dependent, or at least negligibly so. Solving a simplified TPE accordingly, this approach leads to an average fractional energy loss of

$$\left\langle \frac{E^{exit}}{E^{init}} \right\rangle = \left(1 - \frac{\Gamma}{3}\frac{Ru_{SW}}{\kappa}\right)^{-1} \quad \text{with} \quad \Gamma = \frac{E^{exit} + 2E^{rest}}{E^{exit} + E^{rest}} \tag{11}$$

as derived by Parker (1966). As pointed out by e.g. Strauss et al. (2011b), this expression is only valid for a constant stream of inflowing particles with a globally constant mean free path and diffusion tensor, respectively. Fig. 7 shows the analytical estimate of the diffusion limit τ alongside its corrected value according to both estimates for the adiabatic energy changes, Eqns. 10 and 11. As outlined above we therefore assumed the analytical estimate of the effect of the boundary conditions as the relation between the source spectrum intensity $j_{LIS}(E)$ of the initial energy E^{init} versus the exit energy E^{exit} to be:

$$\langle \tau_D \rangle = \frac{R^2}{6\kappa} \cdot \left\langle \frac{j_{LIS}(E^{init})}{j_{LIS}(E^{exit})} \right\rangle \tag{12}$$

A limitation of this approach is that only the diffusion limit τ_D is considered. The approach by Strauss et al. (2011b), which also considers the convection of the particles outward, is not defined for the small values of λ, and therefore of κ, we need to apply for Jovian electrons as shown and discussed in Sec. 2.3 and Vogt et al. (2020). Nevertheless the slightly lower values of τ_D (see Strauss et al. (2011b) for detailed discussion) seem to be in agreement with the exit times s^{exit} as displayed in Fig. 6a.

As illustrated by Fig. 7, the explicit analytical solution for the fractional adiabatic energy loss given by Eq. (11) is also not physically useful defined due to the assumption made in its derivation that $R_{HP}/\kappa \ll 1$.

Therefore, as indicated by the wider range of definition in Fig. 7, we chose to apply Eq. (10) in order to estimate the effect of the boundary conditions on the analytical estimate for the residence time. As the energy $E(t)$ in Eq. (10) is given as depending on the time t and the energy E_0 with which the particle enters the heliosphere, Eq. (10) has to be rewritten according to the time-backward approach and we have to compare our analytical estimate with:

$$E(t) \approx E^{init} \exp(tu_{SW}/R_{HP}). \tag{13}$$

Since we are interested in the total average energy gain for GCR electrons we substitute t with the diffusion limit $\tau = R_{HP}^2/(6\kappa)$ and obtain

$$E^{exit}(\tau_D) \approx E^{init} \exp\left(\frac{R_{HP}u_{SW}}{6\kappa}\right). \tag{14}$$

As indicated by Eq. (9) the adiabatic energy changes are the more effective the lower the radial distance of the particle is. Therefor, as we assume the value of κ as corresponding to $\lambda_\parallel = 0.125$ AU at Earth orbit (marked in red in Fig. 7). This choice is supported by Fig. 6a as it shows that the likewise calculated diffusion limit $\tau = R_{HP}^2/(6\kappa)$ is in agreement with the simulation results. Despite being located at the lower edge of the definition range and the uncertainties within the need to assume an effective global value of κ, Fig. 7 supports the notion that the effect of the boundary conditions can be estimated as a factor of 1/3 to 1/4 as shown by the black and white dashed lines in Fig. 6b.

We can demonstrate that this analytical estimation shifts to the same range of values as suggested by our numerical estimation. Whereas a more detailed treatment of how to define and derive a characteristic energy change is beyond the scope of this study, the approach sketched herein should be sufficient to qualitatively strengthen our point as to how diffusion and adiabatic energy changes are physically interlinked with each other within the theoretical treatment of charged particle transport. As described by Vogt et al. (2020) the approach to model diffusion via a Wiener process does not track the particle motion itself, leading to mathematical remnants such as the 'diffusive background' as discussed in Secs. 2.2 and 3.2 which have to be transformed into physically useful solutions by convolution with the source spectrum. The comparison between analytical and numerical estimations, however, suggests that these considerations apply to diffusion as a mathematical model to treat particle motion in general, rather than just to its numerical implementation by means of SDEs.

5. Corotational effects as possible measure

A possibility to examine these considerations is to utilize the corotational effects as described by Vogt et al. (2020). Comparing simulations over the whole longitudinal range with both a static Jovian source and a corotating one reveals a significant deviation of about 50° from the nominally best-connected longitude, an effect even larger in case of bad magnetic connection between observer and the Jovian source. Utilizing simulation results from Vogt et al. (2020), Fig. 8 sketches the physical mechanism behind this. Two different effects determine the magnetic connection between Jupiter and a possible observer:

1. The synodic period, in case of Earth the characteristic $\approx$ 13 months first discussed by McDonald et al. (1972).
2. The corotation of the HMF due to the Sun's rotational period of $\Omega_S \approx 27$ days

The synodic corotation of $\approx$ 13 months bears more or less no detectable effect since the expected angular shift between Earth and Jupiter in case of good magnetic connectivity is about $\Delta\phi \lessapprox 4°$. The angular speed of the HMF caused by the Solar rotation with $\Omega_S \approx 27$ days, however, suggests a much more significant angular deviation of $\Delta\phi \gtrapprox 50°$ confirmed via simulation by Vogt et al. (2020). This is indicated by the red shaded shift in Fig. 8. As sketched in the left panel of Fig. 8 the reason for this shift is the following: Due to the Sun's angular rotation, the nominal Parker-like HMF frozen into the radially outward streaming Solar wind also rotates with the same angular velocity. During the propagation of Jovian electrons (indicated for good and bad connections by the orange trajectories in Fig. 8) a Parker-spiral connecting the Jovian source with the Earth orbit (dashed black circle) would change its longitudinal position as indicated by the red arrow. Since the Jovian electron could follow the path of the nominal Parker-spiral by the more effective processes categorized as parallel diffusion (indicated by the larger step sizes in Fig. 8) the residence times in case of good magnetic connection are small and only cause small corotation effects. In case of bad magnetic connection, however, perpendicular diffusion dominates the propagation processes of Jovian electrons that happen to reach the observer at Earth orbit, and therefore leads to much longer residence times. As indicated by the blue arrow and the blue shades area in Fig. 8, respectively, the corresponding angular shift of the mininum of the 13 month periodicity of Jovian electron intensity is expected to be much larger. However,

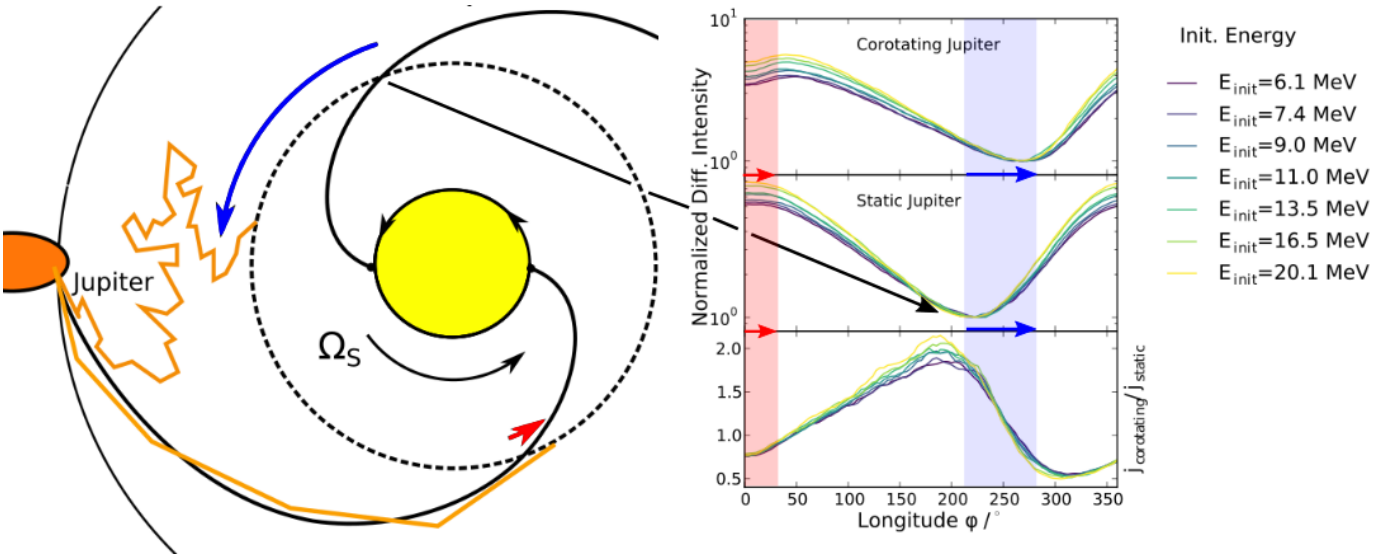

Fig. 8: Differential intensities of Jovian electrons for different initial energies E^{init}.The top panel shows the longitudinal variation due to varying connection for a co-rotatingJovian source, while the middle panel shows the case of a static Jupiter. The bottom panel shows the ratio of the results of the two approaches. Right panel taken from Vogt et al. (2020)

due to the longer residence times, the fluctuations in both Solar wind speed and the HMF can be expected to significantly interfere with this effect. But even in case of good magnetic connection, the angular shift due to the corotation is expected to belarge enough to be possibly resolved by spacecraft data and therefore could serve as an (indirect) measure for the residence time via

$$\tau = \frac{\Delta\phi}{\Omega_S} \tag{15}$$

with Ω_S being the Sun's angular speed. Although conceptually simple, this approach bears difficulties concerning the data analysis it requires. Despite being generally difficult to detect (see e. g. Heber et al. 2005, amongst others), electron counting rates are often highly influenced by Solar Energetic Particles (SEP) events and Corotating Interaction Regions (CIRs). Furthermore the HMF as defined by Parker (1958) and used by the modelling setup (see Sec. 2.3 as well as Dunzlaff et al. 2015; Vogt et al. 2020) assumes a globally constant solar wind velocity, which is a strong simplification even in times of low solar activity.

Fig.9 therefore shows SOHO-EPHIN electron data covering four synodic periods between 2006-2011, plotted with regard to their longitudinal separation from the nominal angle of best connectivity. The HMF for this matter was assumed to be frozen into a solar wind with a radial speed of u_{SW} = 400 km/s. In order to constrain the database to the boundaries given by means of the simulation setup, daily differential electron intensities were only included if all hourly averages of the solar speed by SOHO-CELIAS were within the range of $[300, 400]$ km/s. The remaining daily averages of solar wind speeds are plotted in the lower panel of Fig. 9. The corresponding electron intensities of the E300 (blue) and E1300 (orange) channels of the EPHIN instrument still show a large range of variation but an envelope in agreement with the simulation results. This can be understood by way of how solar wind speed variations influence the propagation between the Jovian source and the observer. By choosing only days with solar wind speeds with hourly averages not bigger than u_{SW} = 400 km/s, we assure that these variations change the longitude of best connectivity due to decreases of the solar wind speed, resulting in a shift to the right within the depiction in Fig. 9. The effect of these shifts of connectivity is a change of the corresponding electron intensity.

If the observer was well connected with the Jovian source by a HMF corresponding to u_{SW} = 400 km/s, a decrease of the solar wind speed would lead to a loss of connectivity and the Jovian electron intensity would decrease likewise. Thus only the upper envelope of the data is comparable to the simulations with an undisturbed HMF. Another reason to limit the focus on the envelope as a test of principle is the fact that the Solar wind takes several days to propagate across the 4 AU between Earth and Jupiter. Thus to be in complete agreement with the simulation we would have needed data corresponding to days of stable Solar wind conditions. Since Fig. 9 already displays five years of data during the most stable conditions measured by SOHO-EPHIN, this simply is a problem of statistics. But as shown in the upper panel of Fig. 9, both of the electron channels of EPHIN meet the theoretical and computational expectations within the restrictions described. Whereas the the E300 channel is in agreement with the simulation both qualitatively and quantitatively the intensities provided by E1300 are higher than expected. There are two possible reasons for this divergence. In order to calculate a representative energy for each channel, the detector responses (see Kühl et al. 2013) have to be convoluted with the electron spectrum. Apart from these technical difficulties, also the Galactic component could contribute more significantly at the measured energies than expected despite the results of Nndanganeni & Potgieter (2018) who suggest that there is no significant Galactic electron contribution up to measured energies of ≈ 25 MeV. Additionally to these possible statistical causes, another reason for the deviation could be the fact that due to smaller fluxes in general the unstable HMF conditions as described above could cause a larger impact on the data.

Nevertheless the fact that the envelopes of both electron channels plotted in Fig. 9 are in agreement with both the simulation results and the theoretical expectation can be considered as a confirmation of concept. Despite the uncertainties tied to the fluctuation in the propagation conditions this result serves as an encouragement to investigate this approach further when future spacecraft missions may provide data of higher statistics.

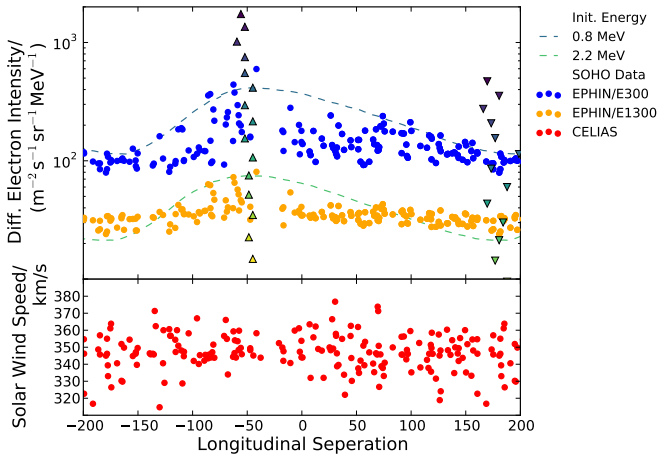

Fig. 9: The effect of corotation as shown by Figure 8 as detected by SOHO-EPHIN. Whereas the upright and down right triangles mark the positions of the maxima and minima of the simulated Jovian fluxes as shown in the upper panel of Figure 8, the two electron channels are shown in blue and orange as daily averages sampled over four synodic periods during the 2006-2011 Solar minimum. The simulation results corresponding for initial energies corresponding to the electron channels are shown to match to the envelope of the data. In the lower panel the corresponding SOHO-CELIAS data points are given for the daily averages of the Solar wind speed. Both panels show their data with respect to the longitudinal separation to the nominal point of best magnetic connection.

6. Discussion and conclusions

This paper investigated the energy dependence of residence times, especially focused on the effect that adiabatic energy changes have on the mathematical implementation of diffusion. We discussed how adiabatic energy changes and and simulation times are related within the framework of SDE modelling. These considerations in Sec. 3.2 were taken into account in order to investigate how different initial energies E^{init} influence the estimated residence times according to Figs. 5. The significant structures of the results (both weighted and unweighted for good and bad magnetic connection) were used to further explore how the mathematical results are related to physics.

This question initially lead to the suggestion to calculate residence times as proposed by Vogt et al. (2020) and outlined in Sec. 3, but appears to be of broader significance. As we showed by comparing the numerical and analytical approaches concerning the residence times of GCRs the prior analytical approaches to estimate residence times are equivalent to the approaches to take the simulation or exit times s^{exit} as a measure for τ. Therefore this study provides evidence to include a representative adiabatic energy changes into the analytical approach. As discussed in Secs. 3.2 and 4 it has long been established that the convolution with the source (or equivalent boundary conditions in a non time-backward SDE approach) is necessary in order to transform the results of a diffusion equation describing Brownian motion into a physically relevant solution of a more complex stochastic process. By means of Eq. (**??**) we suggest a simple but sufficient approximation which appears to reproduce the simulation results and could further serve as a more reliable first guess for residence times when simulation results are not available.

Utilizing the fact that the residence times result in a longitudinal shift of the best magnetic connection to the Jovian source due to the orbital motion as discussed in Sec. 5, we are able to show via Fig.9 that our estimations are in a general agreement with the observable longitudinal dependence of electron intensities. Since the estimation of residence times is connected both to adiabatic energy changes (and therefore spectral modulation) and the transport parameters within the TPE, this offers a further possibility to constrain charged particle transport simulations. An example is the investigations of CIRs and their effect on particle propagation. The question whether and how the considerations and results of this study can be generalized and applied to focused transport equations describing SEP events, amongst others, is beyond the scope of this work but appears to be a promising task for subsequent research.

Acknowledgements. This work is based on the research supported in part by the National Research Foundation of South Africa (Grant Number 111731). Opinions expressed and conclusions arrived at are those of the author and are not necessarily to be attributed to the NRF. KH acknowledges the International Space Science Institute and the supported International Team 464: *The Role Of Solar And Stellar Energetic Particles On (Exo)Planetary Habitability (ETERNAL, `http://www.issibern.ch/teams/exoeternal/`).*

References

Baker, D. N. & van Allen, J. A. 1976, Journal of Geophysical Research, 81, 617
Bieber, J. W., Matthaeus, W. H., Smith, C. W., et al. 1994, The Astrophysical Journal, 420, 294
Burger, R. A., Krüger, T. P. J., Hitge, M., & Engelbrecht, N. E. 2008, The Astrophysical Journal, 674, 511
Burger, R. A., Potgieter, M. S., & Heber, B. 2000, Journal of Geophysical Research, 105, 27447
Chenette, D. L., Conlon, T. F., Pyle, K. R., & Simpson, J. A. 1977, ApJ, 215
Conlon, T. F. 1978, Journal of Geophysical Research, 83, 541
Dempers, N. & Engelbrecht, N. E. 2020, Advances in Space Research, 65, 2072
Dundovic, A., Pezzi, O., Blasi, P., Evoli, C., & Matthaeus, W. H. 2020, Phys. Rev. D, 102, 103016
Dunzlaff, P., Strauss, R. D., & Potgieter, M. S. 2015, Computer Physics Communications, 192, 156
Engelbrecht, N. E. 2019, The Astrophysical Journal, 872, 124
Engelbrecht, N. E. & Burger, R. A. 2010, Advances in Space Research, 45, 1015
Engelbrecht, N. E. & Burger, R. A. 2013, ApJ, 779, 158
Engelbrecht, N. E. & Burger, R. A. 2015, ApJ, 814, 152
Eraker, J. H. 1982, The Astrophysical Journal, 257, 862
Ferreira, S. E. S. & Potgieter, M. S. 2002, Journal of Geophysical Research (Space Physics), 107, 1221
Ferreira, S. E. S., Potgieter, M. S., Burger, R. A., Heber, B., & Fichtner, H. 2001a, Journal of Geophysical Research, 106, 24979
Ferreira, S. E. S., Potgieter, M. S., Burger, R. A., et al. 2001b, Journal of Geophysical Research, 106, 29313
Fichtner, H., Potgieter, M., Ferreira, S., & Burger, A. 2000, Geophysical Research Letters, 27, 1611
Heber, B., Kopp, A., Fichtner, H., & Ferreira, S. E. S. 2005, Advances in Space Research, 35, 605
Heusen, M. & Shalchi, A. 2016, Ap&SS, 361, 308
Kissmann, R., Fichtner, H., & Ferreira, S. E. S. 2004, A&A, 419, 357
Kopp, A., Büsching, I., Strauss, R. D., & Potgieter, M. S. 2012, Computer Physics Communications, 183, 530
Kühl, P., Dresing, N., Dunzlaff, P., et al. 2013, Proceedings of 33th International Cosmic Ray Conference (ICRC 2013)
McDonald, F. B., Cline, T. L., & Simnett, G. M. 1972, Journal of Geophysical Research, 77, 2213
Minnie, J., Bieber, J. W., Matthaeus, W. H., & Burger, R. A. 2007, Astrophysical Journal, 663, 1049
Moraal, H. 2013, Space Sci. Rev., 176, 299
Ndanganeni, R. R. & Potgieter, M. S. 2016, Advances in Space Research, 58, 453
Ndanganeni, R. R. & Potgieter, M. S. 2018, Astrophysics and Space Science, 363, 156
O'Gallagher, J. J. 1975, The Astrophysical Journal, 197, 495
Palmer, I. D. 1982, Reviews of Geophysics and Space Physics, 20, 335
Parker, E. N. 1958, The Astrophysical Journal, 128, 664
Parker, E. N. 1965, Planetary and Space Science, 13, 9

Parker, E. N. 1966, Planet. Space Sci., 14, 371
Potgieter, M. S. 1996, Journal of Geophysical Research, 101, 24411
Potgieter, M. S., Vos, E. E., Munini, R., Boezio, M., & Di Felice, V. 2015, The Astrophysical Journal, 810, 141
Pyle, K. R. & Simpson, J. A. 1977, Astrophysical Journal, Part 2 - Letters to the Editor, 215, L89
Shalchi, A., ed. 2009, Astrophysics and Space Science Library, Vol. 362, Nonlinear Cosmic Ray Diffusion Theories
Shalchi, A. 2020, Space Sci. Rev., 216, 23
Sternal, O., Engelbrecht, N. E., Burger, R. A., et al. 2011, ApJ, 741, 23
Strauss, R. D., Potgieter, M. S., Büsching, I., & Kopp, A. 2011a, The Astrophysical Journal, 735, 83
Strauss, R. D., Potgieter, M. S., & Ferreira, S. E. S. 2013, Advances in Space Research, 51, 339
Strauss, R. D., Potgieter, M. S., Kopp, A., & Büsching, I. 2011b, Journal of Geophysical Research (Space Physics), 116, A12105
Strauss, R. D. T. & Effenberger, F. 2017, Space Sciences Reviews, 212, 151
Teegarden, B. J., McDonald, F. B., Trainor, J. H., Webber, W. R., & Roelof, E. C. 1974, Journal of Geophysical Research, 79, 3615
Teufel, A. & Schlickeiser, R. 2003, Astronomy and Astrophysics, 397, 15
Vogt, A., Engelbrecht, N. E., Strauss, R. D., et al. 2020, A&A, 642, A170
Vogt, A., Heber, B., Kopp, A., Potgieter, M. S., & Strauss, R. D. 2018, Astronomy and Astrophysics, 613, A28
Webb, G. M. & Gleeson, L. J. 1979, Astrophysics and Space Science, 60, 335
Zhang, M., Qin, G., Rassoul, H., et al. 2007, Planet. Space Sci., 55, 12

Danksagung/Acknowledgements

Zunächst gebührt mein Dank selbstverständlich meinem Doktorvater Herrn Prof. Dr. Bernd Heber und seinem Vertrauen in meine Fähigkeit diese Arbeit trotz organisatorischer Widrigkeiten zu einem erfolgreichen Ende zu bringen.

An zweiter Stelle möchte ich ausdrücklich Herrn PD Horst Fichtner danken, ohne dessen vielfältige Unterstützung und ohne dessen Rat diese Arbeit ebenfalls nicht möglich gewesen wäre.

Der Gründlichkeit, mit der Herr Dr. Andreas Kopp mit mir den hier verwendeten Simulationscode analysiert hat, verdanke ich viele der Ideen, die in diese Arbeit eingeflossen sind. Darüber hinaus möchte ich ihm für seine Hilfe und die Betreuung meines Werdeganges seit dem Bachelorstudium danken, die meine eigene Arbeitsweise sehr geprägt haben.

With heartfelt gratefulness I also want to thank my colleagues at Potchefstroom, South Africa, for their welcoming during three stays at the Campus of the North-West University, Prof. Dr. Marius Potgieter, Prof. Dr. Roelf Du Toit Strauss and Prof. Dr. N. Eugene Engelbrecht and their input and support, especially the suggestion to revisit the Jovian source spectrum and the electron mean free paths. Baie dankie!

Für Rat und Geduld mit meinen Fragen danke ich Dr. Konstantin Herbst und für die langjährige Bürogemeinschaft Dr Patrick Kühl und Henning Lohf.

Anregungen aus unterschiedlichsten Wissenschaftsgebieten verdanke ich dem Zentrum für Konstruktive Erziehungswissenschaft.

Stellvertretend für die vielen Menschen, die mich auch über schwere Zeiten hinweg getragen hat, möchte ich besonders Tina Dippe, Jenny Fischer und Helge Scheef, Paula Dieck-Roloff und Albrecht Roloff, Daria Bedulina und Jörg Roloff, sowie Alexander Scheel und Linda Zollitsch und Suzanna Wrzeszcz danken.

Und natürlich wäre ohne die Unterstützung meiner Familie und Johannas, die mich durch dieses Abenteuer begleitet, immer wieder aufgemuntert und motiviert haben, nicht nur die Fertigstellung dieses Manuskriptes kaum möglich gewesen!

Vielen Dank!

Eidesstattliche Erklärung

Ich versichere an Eides Statt, dass ich die vorliegende Promotion in Form und Inhalt eigenständig angefertigt habe. Abgesehen von der Beratung durch meine Kollegen und der angegebenen Literatur wurde die Arbeit ohne fremde Hilfe erstellt. Diese Versicherung bezieht sich auch auf alle in dieser Arbeit enthaltenen Grafiken und bildlichen Darstellungen. Darüber hinaus versichere ich ebenfalls, dass mir noch kein Akademischer Grad entzogen worden ist.

Die Arbeit als Ganzes wurde bisher keiner anderen Prüfungsbehörde vorgelegt. Teile der Arbeit wurden bereits in Fachzeitschrifften veröffentlicht oder für eine Veröffentlichung eingereicht und sind als solche gekennzeichnet. Die Quellennachweise der in den einzelnen Veröffentlichungen referenzierten Inhalte finden sich in der jeweiligen Veröffentlichung selbst und werden nicht zusätzlich im Quellennachweis dieser Arbeit aufgeführt. Für das Einbinden der Veröffentlichungen in diese Arbeit wurde die ausdrückliche Genehmigung der publizierenden Fachzeitschrifft eingeholt.

Ich erkläre abschließend, dass die Arbeit unter Einhaltung der Regeln guter wissenschaftlicher Praxis der Deutschen Forschungsgemeinschaft entstanden ist.

Kiel, den .....

Adrian Vogt